

Observations of a systematically selected  
sample of high frequency peaked BL Lac  
objects with the MAGIC telescope

Dissertation zur Erlangung des  
naturwissenschaftlichen Doktorgrades  
der Bayerischen Julius-Maximilians-Universität Würzburg



vorgelegt von  
Markus Meyer  
aus Dettelbach

Würzburg 2008

Eingereicht am 28.01.2008

bei der Fakultät für Physik und Astronomie

1. Gutachter: Prof. Dr. K. Mannheim
  2. Gutachter: Prof. Dr. W. Porod
  3. Gutachter: Prof. Dr. Dr. W. Rhode
- der Dissertation.

1. Prüfer: Prof. Dr. K. Mannheim
  2. Prüfer: Prof. Dr. W. Porod
  3. Prüfer: Prof. Dr. T. Trefzger
- im Promotionskolloquium

Tag des Promotionskolloquiums: 04.06.2008

Doktorurkunde ausgehändigt am:

# Contents

<b>Abstract</b>	<b>8</b>
<b>Zusammenfassung</b>	<b>10</b>
<b>Introduction</b>	<b>12</b>
<b>1 High energy astrophysics</b>	<b>15</b>
1.1 Cosmic rays . . . . .	15
1.1.1 The cosmic ray spectrum . . . . .	15
1.1.2 Cosmic accelerators - the Hillas plot . . . . .	17
1.1.3 Fermi acceleration . . . . .	19
1.2 Gamma-ray astronomy . . . . .	21
1.2.1 High energy: 500 keV - 100 GeV . . . . .	21
1.2.2 Very high energy: 100 GeV - 100 TeV . . . . .	23
1.3 Mechanisms of gamma-ray production . . . . .	28
1.3.1 Bremsstrahlung . . . . .	29
1.3.2 Synchrotron radiation . . . . .	29
1.3.3 Inverse Compton scattering . . . . .	30
1.3.4 Pion decay . . . . .	32
1.4 Absorption of gamma-rays . . . . .	33
1.5 Astrophysical sources of gamma radiation . . . . .	36
1.5.1 Galactic sources . . . . .	36
1.5.2 Active galactic nuclei . . . . .	39
1.5.3 Unidentified sources . . . . .	40
1.5.4 Gamma-ray bursts . . . . .	40
1.5.5 Dark matter annihilation . . . . .	41
<b>2 Active galactic nuclei</b>	<b>42</b>
2.1 Empirical classification . . . . .	43
2.2 The unified model . . . . .	45
2.2.1 The AGN paradigm . . . . .	45

2.2.2	Unified scheme for radio-loud AGN . . . . .	47
2.2.3	AGN jets . . . . .	48
2.3	Blazars . . . . .	49
2.3.1	Relativistic beaming . . . . .	49
2.3.2	Spectral energy distribution . . . . .	51
2.3.3	Emission models . . . . .	54
<b>3</b>	<b>The imaging air Cherenkov technique</b>	<b>58</b>
3.1	Air showers . . . . .	58
3.2	Cherenkov effect . . . . .	62
3.3	Imaging technique . . . . .	66
3.4	The MAGIC telescope . . . . .	68
3.4.1	Reflector . . . . .	69
3.4.2	Telescope structure and drive system . . . . .	70
3.4.3	Detector . . . . .	70
3.4.4	Data acquisition . . . . .	70
3.4.5	Trigger . . . . .	71
<b>4</b>	<b>The analysis chain</b>	<b>74</b>
4.1	Data preparation . . . . .	75
4.1.1	Calibration . . . . .	75
4.1.2	Pulse extraction . . . . .	76
4.1.3	Detector inhomogeneities . . . . .	77
4.1.4	Bad pixel treatment . . . . .	77
4.1.5	Software trigger . . . . .	77
4.1.6	Image cleaning . . . . .	78
4.1.7	Image parameters . . . . .	79
4.2	Background determination . . . . .	80
4.2.1	On-off mode . . . . .	80
4.2.2	Wobble mode . . . . .	80
4.3	Gamma-hadron separation . . . . .	81
4.3.1	Quality cuts . . . . .	81
4.3.2	Dynamical cuts . . . . .	82
4.3.3	Reconstruction of the shower origin . . . . .	83
4.4	Spectrum . . . . .	85
4.4.1	Monte Carlo simulations . . . . .	85
4.4.2	Energy reconstruction . . . . .	86
4.4.3	Effective collection area . . . . .	86
4.5	Observations of the Crab Nebula . . . . .	87
4.5.1	The Crab Nebula . . . . .	87
4.5.2	Observations with the MAGIC telescope . . . . .	88

4.5.3	Gamma-hadron separation . . . . .	88
4.5.4	Monte Carlo comparison . . . . .	91
4.5.5	Energy spectrum . . . . .	91
4.5.6	Lightcurve . . . . .	95
4.5.7	Sensitivity . . . . .	96
<b>5</b>	<b>Muons</b>	<b>98</b>
5.1	Muon image in the Cherenkov telescope . . . . .	98
5.1.1	Dependence on the impact parameter . . . . .	98
5.1.2	Width of muon ring images . . . . .	100
5.2	Analysis of single muon events . . . . .	101
5.2.1	Image reconstruction . . . . .	102
5.2.2	Monte Carlo simulation . . . . .	103
5.2.3	Monte Carlo comparison . . . . .	104
5.3	Calibration and point spread function . . . . .	105
5.3.1	Implementation in the automatic analysis . . . . .	106
5.3.2	Monitoring of the point spread function . . . . .	106
5.3.3	Calibration with muon ring images . . . . .	108
5.4	Muon background . . . . .	111
5.4.1	Gamma-background separation . . . . .	111
5.4.2	Estimated muon rate . . . . .	113
<b>6</b>	<b>Search for gamma-ray emission</b>	<b>116</b>
6.1	Sample selection . . . . .	116
6.2	Observations . . . . .	118
6.3	Analysis . . . . .	119
6.3.1	Method of upper limit calculation . . . . .	119
6.3.2	Analysis results . . . . .	121
6.3.3	1ES 1426+428 . . . . .	122
6.4	Detections and possible detections . . . . .	123
6.4.1	1ES 1011+496 . . . . .	124
6.4.2	1ES 1218+304 . . . . .	125
6.4.3	1ES 2344+514 . . . . .	130
<b>7</b>	<b>Overall spectral properties</b>	<b>135</b>
7.1	Multiwavelength data . . . . .	135
7.1.1	Upper limits at 200 GeV . . . . .	136
7.1.2	Simultaneous optical observations . . . . .	136
7.2	Corrections . . . . .	137
7.2.1	K-correction . . . . .	137
7.2.2	Absorption of gamma-rays . . . . .	139

7.3	Broad-band spectral indices . . . . .	139
7.3.1	Sample enlargement . . . . .	140
7.3.2	Discussion . . . . .	140
<b>8</b>	<b>Spectral energy distribution</b>	<b>144</b>
8.1	Single zone SSC model . . . . .	144
8.2	1ES 2344+514 . . . . .	148
8.2.1	Gamma-ray data . . . . .	149
8.2.2	Multiwavelength data - the X-ray properties . . . . .	151
8.2.3	Model fit . . . . .	151
8.3	1ES 1218+304 . . . . .	156
8.3.1	Gamma-ray data . . . . .	157
8.3.2	Multiwavelength data - the X-ray properties . . . . .	158
8.3.3	Model fit . . . . .	159
8.4	Summary and conclusions . . . . .	162
<b>9</b>	<b>Constraints on the luminosity function</b>	<b>165</b>
9.1	Complete BL Lac samples . . . . .	165
9.2	Redshift distribution . . . . .	167
9.3	Number counts . . . . .	169
9.4	Contribution to the extragalactic background . . . . .	171
<b>10</b>	<b>Conclusions</b>	<b>173</b>
<b>A</b>	<b>Observation log: Crab Nebula</b>	<b>176</b>
A.1	Observations in on-off mode . . . . .	176
A.2	Observations in wobble mode . . . . .	180
<b>B</b>	<b>Monte Carlo comparison</b>	<b>181</b>
B.1	Gamma initiated air showers . . . . .	181
B.2	Muons . . . . .	183
<b>C</b>	<b>Observation log: HBL objects</b>	<b>184</b>
C.1	1ES 0120+340 . . . . .	184
C.2	RX J0319.8+1845 . . . . .	185
C.3	1ES 0323+022 . . . . .	187
C.4	1ES 0414+009 . . . . .	188
C.5	1ES 0806+524 . . . . .	189
C.6	1ES 0927+500 . . . . .	190
C.7	1ES 1011+496 . . . . .	192
C.8	1ES 1218+304 . . . . .	194
C.9	1ES 1426+428 . . . . .	195

C.10 RX J1725.0+1152 . . . . .	196
C.11 1ES 2344+514 . . . . .	197
<b>D Spectral data points</b>	<b>199</b>
D.1 Spectrum of 1ES 1218+304 . . . . .	199
D.2 Spectrum of 1ES 2344+514 . . . . .	200
<b>E Parameters for the constraints on <math>B</math> and <math>\delta</math></b>	<b>201</b>
<b>List of figures</b>	<b>202</b>
<b>List of tables</b>	<b>206</b>
<b>Bibliography</b>	<b>208</b>
<b>List of publications</b>	<b>231</b>
<b>Abbreviations</b>	<b>235</b>
<b>Lebenslauf</b>	<b>237</b>
<b>Acknowledgements</b>	<b>238</b>

# Abstract

At the beginning of regular observations with the MAGIC telescope in December 2004, all but one extragalactic sources detected at very high energy (VHE) gamma-rays belonged to the class of high frequency peaked BL Lac (HBL) objects. This motivated a systematic scan of candidate sources to increase the number of known sources and to study systematically their spectral properties.

As candidate sources for VHE emission, X-ray bright HBLs were selected from a compilation of active galactic nuclei (Donato et al., 2001). The MAGIC observations took place from December 2004 to March 2006. The declination of the objects was restricted to values between  $-1.2^\circ$  and  $+58.8^\circ$  corresponding to a maximum zenith distance lower than  $30^\circ$  at culmination. Since gamma-rays are absorbed by photo-pair production in low energy background radiation fields, the redshift of the investigated objects was limited to  $z < 0.3$ . Under the assumption that HBLs generally emit the same energy flux at 1 keV as at 200 GeV, only the brightest X-ray sources were observed, leading to a cut in the X-ray flux of  $F(1 \text{ keV}) > 2 \mu\text{Jy}$ .

Of the fourteen sources observed, four have been detected: 1ES 1218+304 (for the first time at very high energies), 1ES 2344+514 (strong detection in a state of low activity), Mrk 421 and Mrk 501 (discussed in detail in Albert et al. (2007c) and Albert et al. (2007g), respectively). A hint of a signal on a  $3\sigma$ -level from the direction of 1ES 1011+496 has been observed. In the meantime the object has been confirmed as a source of VHE gamma-rays by a second MAGIC observation campaign triggered by an optical outburst (Albert et al., 2007e). For ten sources, upper limits on their integral fluxes above  $\sim 200 \text{ GeV}$  have been calculated on a 99% confidence level.

To cross calibrate the different data samples, collected during 14 months, bright muon ring images have been used, recorded as background events by the MAGIC telescope. Based on the development by Meyer (2004), the method has been improved and implemented into the automatic data analysis as a continuous monitor of the calibration and the point spread function of the optical system. While the ring images are generated by muons with small

impact parameters, it could be shown that the image parameter distributions for muons with large impact parameters and gamma showers completely overlap, revealing these muons as the dominant background for gamma-ray observations below energies of  $\sim 150$  GeV.

The sample of HBLs (including all HBLs detected at VHE so far) has been investigated for correlations between broad-band spectral indices as determined from simultaneous optical, archival X-ray and radio luminosities, finding that the VHE emitting HBLs do not differ from the non-detected ones. In general the absorption corrected HBL gamma-ray luminosities at 200 GeV are not higher than their X-ray luminosities at 1 keV. Based on a complete X-ray BL Lac sample, the Hamburg/ROSAT X-ray BL Lac sample (Beckmann et al., 2003), the number of expected VHE sources has been estimated for the performed scan, finding a consistent number under the assumption of a  $\sim 37\%$  completeness of the investigated sample and a 1 keV-to-200 GeV luminosity ratio of 1.4. An upper limit on the omnidirectional flux at 200 GeV has been calculated by interpolating the sum over the observed fluxes and upper limits. Within the uncertainties, the result is in agreement with the expectations derived from the X-ray luminosity function of BL Lacs.

For 1ES 1218+304 and 1ES 2344+514 the lightcurves have been derived, showing evidence for flux variability on a time scale of 17 days and 24 h, respectively. In the case of 1ES 1218+304 variability has been reported for the first time at VHEs. For both sources the energy spectra have been reconstructed and discussed in the context of their broad band spectral energy distribution (SED), using a single zone synchrotron self Compton model. The SEDs are well fitted by the simulation even though the very high peak frequencies at gamma-rays push the model to its limits. The parameters derived from the simulation are in good agreement with the parameters found for similar HBLs.

# Zusammenfassung

Zu Beginn der regulären Beobachtungen des MAGIC-Teleskops im Dezember 2004 gehörten alle extragalaktischen Quellen, bis auf eine, von denen sehr hochenergetische (VHE von engl. very high energy) Gammastrahlung detektiert wurde, zur Klasse der sogenannten "high frequency peaked BL Lac"-Objekte (HBL). Dies motivierte eine systematische Durchmusterung von Quellkandidaten mit dem Ziel die Anzahl der bekannten Quellen zu erhöhen und ihre spektralen Eigenschaften systematisch zu untersuchen.

Als Quellkandidaten für VHE-Emission wurden röntgen-helle HBLs aus einer Kompilation von aktiven galaktischen Kernen (Donato et al., 2001) ausgewählt. Die MAGIC-Beobachtungen fanden von Dezember 2004 bis März 2006 statt. Die Deklination der Objekte war begrenzt auf Werte zwischen  $-1.2^\circ$  und  $+58.8^\circ$ , entsprechend einer Zenitdistanz von weniger als  $30^\circ$  an der Kulmination. Da Gammastrahlung durch Photo-Paar-Produktion in niederenergetischen Hintergrundstrahlungsfeldern absorbiert wird, wurde die Rotverschiebung der untersuchten Objekte auf  $z < 0.3$  begrenzt. Unter der Annahme, dass HBLs generell den selben Energiefluss bei 1 keV wie bei 200 GeV emittieren, wurden nur die hellsten Röntgenquellen beobachtet, was zu einem Schnitt im Röntgenfluss von  $F(1 \text{ keV}) > 2 \mu\text{Jy}$  führte.

Von den vierzehn beobachteten Objekten konnten vier detektiert werden: 1ES 1218+304 (zum ersten Mal im VHE-Bereich), 1ES 2344+514 (klare Detektion in einem Zustand niedriger Aktivität), Mrk 421 und Mrk 501 (im Detail diskutiert in Albert et al. (2007c) beziehungsweise Albert et al. (2007g)). Ein Hinweis auf ein Signal auf einem  $3\sigma$ -Level wurde aus der Richtung von 1ES 1011+496 beobachtet. Inzwischen ist das Objekt als eine Quelle hochenergetischer Gammastrahlung in einer zweiten MAGIC-Beobachtungskampagne, die durch einen hohen optischen Flusszustand ausgelöst wurde, bestätigt worden (Albert et al., 2007e). Für die übrigen zehn Quellen wurden Obergrenzen an den integralen Fluss oberhalb von  $\sim 200 \text{ GeV}$  mit einer statistischen Sicherheit von 99% berechnet.

Um eine Kreuzkalibrierung verschiedener Datensätze, genommen innerhalb von 14 Monaten, durchzuführen, wurden helle Bilder von Myonenringen

verwendet, die als Hintergrundereignisse vom MAGIC Teleskop aufgenommen werden. Basierend auf der Entwicklung von Meyer (2004) wurde die Methode verbessert und als ein kontinuierlicher Monitor der Kalibrierung sowie der Punktbildfunktion des optischen Systems in die automatische Datenanalyse implementiert. Während die Ringbilder von Myonen mit kleinen Stoßparametern erzeugt werden, konnte gezeigt werden, dass die Verteilungen der Bildparameter von Myonen mit großen Stoßparametern und der von Gammascchauern sich vollständig überlappen, was diese Myonen zum dominierenden Hintergrund für die Beobachtung von Gammastrahlung unterhalb einer Energie von  $\sim 150$  GeV macht.

Das HBL-Sample (inklusive aller HBLs, die bisher bei sehr hohen Energien detektiert wurden) wurde nach Korrelationen zwischen den Breitband-Spektralindices untersucht, die durch simultane optische sowie durch Röntgen- und Radio-Leuchtkräfte aus früheren Beobachtungen bestimmt wurden, mit dem Ergebnis, dass die VHE-emittierenden HBLs sich nicht von den nicht-detektierten unterscheiden. Generell sind die absorptionskorrigierten Gammaleuchtkräfte der HBLs bei 200 GeV nicht höher als ihre Röntgenleuchtkräfte bei 1 keV. Basierend auf einem vollständigen Röntgen-BL Lac-Sample, dem Hamburg-ROSAT-Röntgen-BL Lac-Sample (Beckmann et al., 2003), wurde die Anzahl der zu erwartenden VHE-Quellen für die durchgeführte Durchmusterung abgeschätzt, wobei eine konsistente Anzahl erreicht wird, unter der Annahme einer Vollständigkeit des untersuchten Samples von  $\sim 37\%$  sowie ein 1 keV-zu-200 GeV Leuchtkraftverhältnis von 1,4. Eine Obergrenze an den gesamten Fluss pro Raumwinkel bei 200 GeV wurde durch eine Interpolation der Summe der beobachteten Flüsse und Fluss-Obergrenzen berechnet. Innerhalb der Ungenauigkeiten ist das Ergebnis in Übereinstimmung mit den Erwartungen die aus der Röntgen-Leuchtkraftfunktion der BL Lacs abgeleitet wurde.

Für 1ES 1218+304 und 1ES 2344+514 wurden die Lichtkurven bestimmt, welche Anzeichen von Flussvariabilität auf einer Zeitskala von 17 Tagen beziehungsweise 24 Stunden aufweisen. Im Falle von 1ES 1218+304 wurde zum ersten Mal zeitliche Variabilität bei sehr hohen Energien gesehen. Für beide Quellen wurden die Energiespektren rekonstruiert und im Kontext ihrer spektralen Energieverteilung (SED) diskutiert, wobei ein ein-Zonen-Synchrotron-selbst-Compton-Modell verwendet wurde. Die SEDs wurden von der Simulation gut beschrieben, auch wenn die sehr hohen Energien der Maxima im Gammabereich das Modell an seine Grenzen bringen. Die von der Simulation abgeleiteten Parameter stimmen gut mit den Parametern, die für ähnliche HBLs gefunden wurden überein.

# Introduction

Astronomy was restricted to observations of visible light until the mid 20th century. After the pioneer work of Karl Jansky in the 1930s and Grote Reber in the early 1940s, radio astronomy became more and more successful and established a new window to the universe. While visible light is mainly produced in stars by thermal processes, the bulk of the observed radio waves is produced by non-thermal processes, such as synchrotron radiation of non-thermal particle species.

The new insights in the non-thermal universe led to the discovery of new classes of objects. A landmark in this context was the optical identification of the radio sources 3C 273 and 3C 48 in 1963. The measurement of their redshift revealed that they are located at cosmological distances and by that the existence of very energetic objects with a star-like appearance, called quasi-stellar objects or quasars. The name of another new but very similar class discovered by radio observations is derived from BL Lacertae, the prototype of the BL Lac objects. Originally discovered in 1929 by Cuno Hoffmeister as a variable star in the constellation of Lacerta (lizard), it was identified with a variable radio source in 1968 by John Schmitt. Contrary to the formerly detected quasars, BL Lacertae showed neither absorption nor emission lines. Later the diffuse nebula around BL Lacertae could be identified as a giant elliptical galaxy which made the determination of the redshift possible.

In the 1960s a new observation window was opened in the X-ray regime. As the earth's atmosphere is opaque for X-rays, rocket flights were necessary which could lift scientific payloads above the earth's atmosphere. In the 1970s dedicated X-ray satellites, such as Uhuru, Ariel V, SAS-3, OSO-8 and HEAO-1 developed this new field of astronomy at an astounding pace. In 1976 an X-ray transient at high galactic latitude, observed by Ariel V, was identified with the BL Lac object Mrk 421. The total number of known BL Lacs at that time exceeded 30. Only two years later, with the identification of four more variable X-ray sources with BL Lac objects, it became clear that BL Lacs constitute a new class of X-ray emitters.

During the 1980s, the number of BL Lacs was growing to more than a hundred objects. Depending on the discovery in the radio or X-ray band, they were referred to as radio selected BL Lacs (RBL) and X-ray selected BL Lacs (XBL), respectively. At the same time models were developed to unify different types of active galactic nuclei, such as Seyfert galaxies or radio galaxies with BL Lacs and quasars, which are summarised as blazars. Today BL Lacs are understood as the bright active nuclei of elliptical galaxies with elongated radio jets closely aligned to the line of sight. The enormous energy output is thereby generated by mass accretion onto a supermassive black hole, like in all active galactic nuclei. The extreme apparent luminosities and the short time variability, typical for the blazar phenomenon, are explained by beaming effects, as the emission of the relativistic plasma is strongly boosted in forward direction. The differences between RBLs and XBLs were found to be related to intrinsic peaks in their broad-band spectrum, leading to the physically motivated classification in low frequency peaked BL Lacs (LBL) and high frequency peaked BL Lacs (HBL).

Another landmark in the study of BL Lac objects was the detection of TeV photons from Mrk 421 with the 10 m reflector of the Whipple observatory. With the newly developed imaging air Cherenkov technique for the detection of TeV gamma-rays from the ground the first TeV source has been discovered by the same group in 1989 with the observation of the Crab Nebula, a supernova remnant at a distance of 2 kiloparsecs. The technique uses the faint Cherenkov light flashes produced by secondary particles to derive an image of the particle shower initiated by the primary gamma-ray. During the 1990s, the EGRET instrument onboard the Compton Gamma-Ray Observatory discovered 271 sources above 100 MeV in an all-sky survey, with a large fraction of quasars and BL Lacs, including also Mrk 421. At the same time ground based Cherenkov telescopes discovered six extragalactic sources at much higher energies, all of them HBLs.

These observations revealed a population of objects in which the total energy output is dominated by the emission of TeV gamma-rays. The observed short time variability down to several minutes yields sizes of the emission region in the order of a few astronomical units. This makes them one of the most extreme objects among astrophysical sources. In the recent years, imaging air Cherenkov telescopes of the second generation, such as the H.E.S.S. array in Namibia or the MAGIC telescope on the Canary Island of La Palma, increased the number of extragalactic TeV sources to 20. This offers for the first time the possibility to perform population studies of TeV gamma-ray emitting BL Lacs. The next major step is expected from the GLAST satellite, to be launched in May 2008, which will perform an all sky survey above 100 MeV with a 50 times higher sensitivity than EGRET.

In the following work, observations of a systematically selected sample of X-ray bright HBL objects performed with the MAGIC telescope are reported. The goal was to investigate if TeV emission is a general characteristic of HBLs. Therefore the broad-band spectral properties of this sample are studied and compared to all HBLs detected at TeV-energies so far in a statistical way, including the radio, optical and X-ray fluxes. For two objects of the sample, detected clearly at gamma-rays, the spectral energy distribution is simulated with a state-of-the-art leptonic emission model and the intrinsic source parameters are derived. Finally, the luminosity function at gamma-rays is constrained by the comparison with a complete X-ray BL Lac sample and the expected omnidirectional flux at 200 GeV is estimated.

# Chapter 1

## High energy astrophysics

The starting point for high energy astrophysics was in 1912, when Victor Hess made his historical balloon flight to measure the dependence of ionising radiation on the altitude (Hess, 1912, Nobel prize in 1936). At that time radioactivity was a known phenomenon from matter. His results of an increasing intensity of ionising radiation with increasing altitude showed that there must be another contribution with extraterrestrial origin to the natural radioactivity, the cosmic rays. Later this radiation could be measured directly in cloud chambers.

In the following chapter first the field of cosmic rays is briefly introduced. In Section 1.2 an overview of the current status of gamma-ray astronomy and its future prospects is given. Section 1.3 describes the mechanisms of gamma-ray production. The absorption of gamma-rays in low energy background radiation fields is discussed in Section 1.4. The chapter closes with an overview of astrophysical gamma-ray sources in Section 1.5.

### 1.1 Cosmic rays

#### 1.1.1 The cosmic ray spectrum

The spectrum of cosmic rays ranges from  $10^6$  eV to  $\sim 10^{20}$  eV. Below a few TeV - where the composition is well understood - the cosmic rays consist mainly of protons (85%) and He-nuclei (12%), but also of heavy nuclei (1%) and electrons (2%). Below  $\sim 1$  GeV the spectrum is dominated by the solar wind and therefore shows an 11-years modulation. From GeV energies up to  $10^{15}$  eV the spectrum is well fitted by a power law with a spectral index of  $-2.75$  (e.g., Ghia, 2007). At  $4 \times 10^{15}$  eV, the so-called "knee", the spectrum becomes steeper (index  $\sim -3$ ) and it is softening further at the "second knee",

around  $4 \times 10^{17}$  eV, until it hardens at the "ankle" around  $5 \times 10^{18}$  eV (see Fig. 1.1). At the highest energies a cut-off is expected due to the interaction

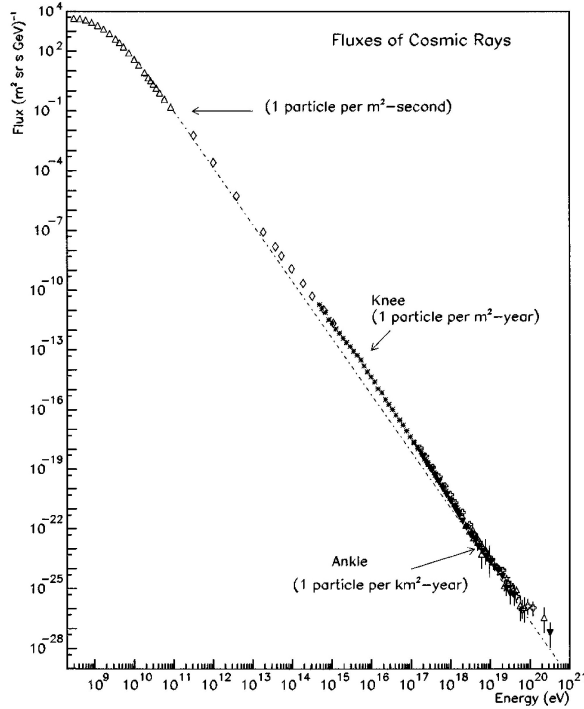


Figure 1.1: The cosmic ray spectrum from  $10^8$  eV up to  $\sim 10^{20}$  eV (www-01).

of cosmic rays with photons of the cosmic microwave background (CMB), the so-called Greisen-Zatsepin-Kuzmin (GZK) cut-off (Greisen, 1966; Zatsepin and Kuzmin, 1966). After contradictory results from different experiments, using different detection principles, a cut-off is now clearly seen in the first results of the Pierre Auger observatory, using both the fluorescence and the surface detection techniques (see Figure 1.2). For a recent review of ultra high energy cosmic rays see also Bergman and Belz (2007).

Due to the deflection of charged particles in the magnetic field of our galaxy, cosmic rays lose their direction information. Only for the highest energies, close to  $10^{20}$  eV, the effect of the magnetic field is small. Taking into account the limited range of  $\sim 75$  Mpc due to absorption in the CMB the search for point sources seems feasible. Recently the Pierre Auger collaboration reported the correlation of events above an energy of  $5.6 \times 10^{19}$  eV with nearby active galactic nuclei (Abraham et al., 2007). They rejected the hypothesis of isotropy in the distribution of the arrival directions of cosmic rays with the highest energies at a 99% confidence level.

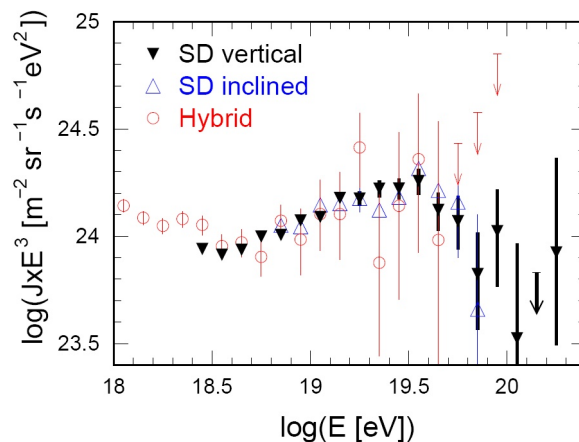


Figure 1.2: The high energy end of the cosmic ray spectrum as measured by the Pierre Auger Observatory (Yamamoto for the Pierre Auger collaboration, 2007). The flux is multiplied by  $E^3$ . The black triangles mark the measurement with the surface detector (SD) with angles of incidence below  $60^\circ$ , the blue ones are SD data with incidence above  $60^\circ$ . The red circles belong to events which are detected by the fluorescence and the surface detectors (Hybrid). The ankle is clearly visible at  $10^{18.5}$  eV as well the cut-off above  $10^{19.6}$  eV.

Below the knee, galactic accelerators like supernova remnants (SNR) are believed to be responsible for the bulk of cosmic rays. From an energetic point of view below  $10^{15}$  eV, a Supernova rate of 1 per 30 years would be sufficient to account for the observed cosmic ray energy density, assuming an efficiency of 10% for the transition of the total energy of the outburst to the cosmic ray acceleration. There are experimental indications that the chemical composition changes from a proton dominated one around the knee to a domination by iron and even heavier nuclei at the second knee. This is expected in any scenario where acceleration is caused by magnetic fields whose effects only depend on rigidity, the ratio of charge to rest mass. Above the ankle the origin is supposed to be extragalactic, as the cosmic rays at these energies are no longer confined by the magnetic field of our galaxy. There are also scenarios in which the extragalactic component already starts to dominate at lower energies around the second knee (Sigl, 2006).

### 1.1.2 Cosmic accelerators - the Hillas plot

A simple way to identify possible candidates for sources of cosmic rays was proposed by Hillas (1984) taking into account the lamor radius of the accelerated particles. He found out that the size  $L$  of the essential part of the accelerating region must be greater than two times the lamor radius  $r_L$ ,

yielding

$$B_{\mu\text{G}} L_{\text{pc}} > \frac{2E_{15}}{Z\beta}, \quad (1.1)$$

where  $L_{\text{pc}}$  is the size of the accelerator in units of parsecs,  $B_{\mu\text{G}}$  the magnetic field in units of  $\mu\text{G}$ ,  $E_{15}$  the energy in units of  $10^{15}$  eV,  $Z$  the atomic number of the accelerated particle and  $\beta$  its relativistic velocity in units of the speed of light. Figure 1.3 shows the magnetic field vs. the size of the accelerator together with the condition for protons ( $E = 10^{20}$  eV and  $10^{21}$  eV) as well as for iron nuclei ( $E = 10^{20}$  eV). It can be seen that several extragalactic sources would fulfill the criteria, while SNRs can be clearly excluded for the highest energies.

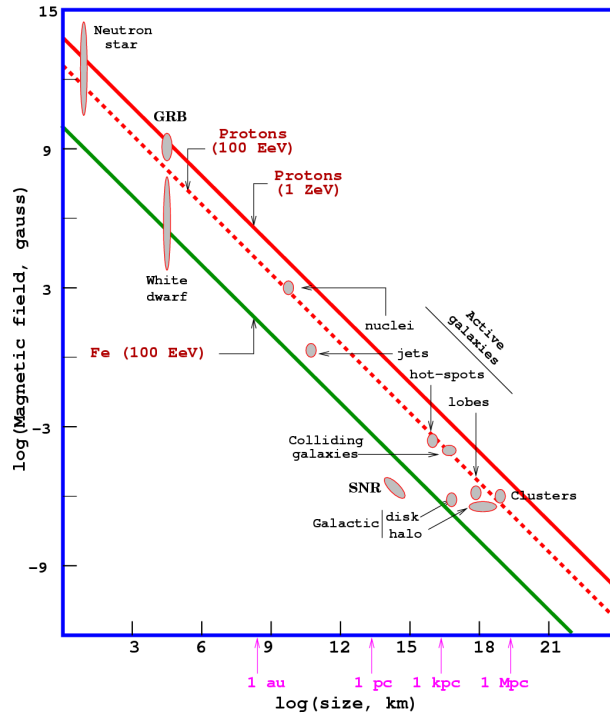


Figure 1.3: The Hillas plot: magnetic field strength vs. the size of the source. The red lines represent the required magnetic field depending on the source size for protons with an energy of  $10^{20}$  eV (dotted line) and  $10^{21}$  eV (solid line). Sources below the lines are not able to accelerate protons to these energies. The green line shows the same for iron nuclei, which requires a lower magnetic field for the same size due to the higher electric charge. The plot is taken from www-02.

### 1.1.3 Fermi acceleration

In the following a brief description is given about the most popular acceleration mechanism for cosmic rays: the first order Fermi acceleration on non-relativistic shocks (see also Ahn et al. (2001) for a more detailed description). The model makes the following assumptions.

- A thermal plasma in supersonic motion experiences an adiabatic shock with a supersonic upstream velocity  $u_1 > v_{s1}$  and a subsonic downstream velocity  $u_2 < v_{s2}$ ;  $v_{s1,2}$  are the sound speeds in the respective regions.
- A population of suprathermal particles is transported by the plasma flow.
- The plasma carries a frozen-in magnetic field with a regular and an irregular component. The irregular component causes elastic scatterings which result in an effective diffusion of the suprathermal particle velocity distribution.

The idea is that the fast particles, which pass the shock front, gain energy and get isotropised by scattering off the magnetic irregularities. Some particles move behind the shock front, where they gain energy again (Fig. 1.4). Since

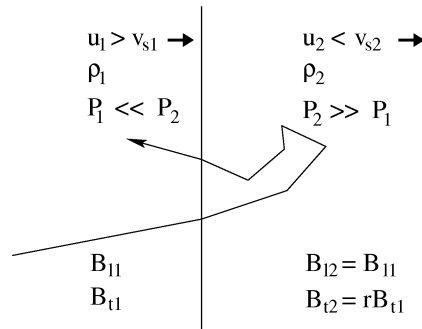


Figure 1.4: Schematic view of a first order Fermi acceleration on a non-relativistic plane shock front. On the left side is the upstream region (index 1), on the right side the downstream region (index 2):  $u$  is the velocity,  $\rho$  the density,  $P$  the pressure,  $B_l$  and  $B_t$  are the longitudinal and the transversal components of the magnetic field and  $r$  is the compression ratio (see text).

the flow is assumed stationary, the mass across the front is conserved, yielding

$$\rho_1 u_1 = \rho_2 u_2 \quad (1.2)$$

where  $\rho_{1,2}$  are the densities in the respective regions. An important quantity deduced from this relation is the compression ratio  $r$ :

$$r \equiv \frac{\rho_1}{\rho_2} = \frac{u_2}{u_1} = \frac{\gamma_a + 1}{\gamma_a - 1 + 2/M^2}, \quad (1.3)$$

where  $M \equiv u_1/v_{s1}$  is the Mach number and gives the strength of the shock and  $\gamma_a$  is the adiabatic index. For strong shocks ( $M \gg 1$ ) and non-relativistic plasma pressure ( $\gamma_a = 5/3$ ) the compression ratio yields  $r \approx 4$ .

A particle with velocity  $v$  is crossing the shock front from upstream, scattered downstream and coming back upstream. In each crossing the particle gains energy resulting in the average gain per Fermi cycle of

$$\Delta E_{\text{cycle}} = \frac{4}{3} \frac{u_1 - u_2}{v} E \quad (1.4)$$

due to  $v \gg u_1$  the energy gain per cycle is small. There is also the probability for the particle to escape in the downstream. The escape probability  $\eta$  is given as:

$$\eta = \frac{4u_2}{v} \quad (1.5)$$

The probability  $P$  for a particle to pass  $n$  cycles is then  $P_n = \prod_{k=1}^{k=n} (1 - \eta_k)$ . The resulting energy spectrum of the accelerated particles can be derived from the probability for a particle to reach an energy larger than  $E$ . The energy after  $n$  cycles is given as:

$$E_n = E_0 \prod_{k=1}^{k=n} \left( 1 + \frac{4}{3} \frac{u_1 - u_2}{v_k} \right) = E_0 \prod_{k=1}^{k=n} \left( 1 + \frac{r-1}{3} \eta_k \right) \quad (1.6)$$

From the following ratio

$$\frac{\ln P_n}{\ln(E_n/E_0)} = \frac{\sum_{k=1}^{k=n} \ln(1 - \eta_k)}{\sum_{k=1}^{k=n} \ln \left( 1 + \frac{r-1}{3} \eta_k \right)} \approx -\frac{3}{r-1} \quad (1.7)$$

one can obtain the probability for a particle to reach an energy larger than  $E$  as

$$P(\geq E) \propto \left( \frac{E}{E_0} \right)^{-3/(r-1)}. \quad (1.8)$$

After differentiation of Equation 1.8 one gets the energy spectrum as:

$$F(E) \propto E^{-\frac{r+2}{r-1}} \approx E^{-2}. \quad (1.9)$$

## 1.2 Gamma-ray astronomy

As a result of particle acceleration, photons are produced from the radio band up to very high energy gamma-rays as well as high energetic neutrinos (in case of pion production of relativistic protons). As these particles are not deflected by magnetic fields, they are suitable for the search of point sources.

While neutrinos from the sun (see Haxton, 1995, for a review) as well as from a nearby supernova explosion (SN1987A, Hirata et al., 1987) were detected in the MeV energy range, the search for cosmic neutrinos at higher energies resulted only in upper limits so far. By now the most stringent upper limit on the diffuse neutrino flux comes from AMANDA-II, an ice Cherenkov detector located at the south pole, in the energy range from several hundred GeV up to  $10^9$  GeV (Hoshina et al., 2007; Gerhardt et al., 2007). Currently IceCube, a neutrino detector with  $1 \text{ km}^3$  detector volume, is under construction at the same site, planned to be complete in 2011 (Karle et al., 2007). Since the southern neutrino telescopes observe the northern sky, there are also plans for a  $1 \text{ km}^3$  detector in the Mediterranean sea, called KM3NeT (Katz, 2006). The prototype Antares is currently under construction, expected to be complete in early 2008 (Kouchner et al., 2007).

The observation of gamma-rays challenge different kinds of detection principles depending on the energy. Therefore the following overview is separated in High Energy (HE) and Very High Energy (VHE) gamma-rays.

### 1.2.1 High energy: 500 keV - 100 GeV

At these energies the gamma-rays are detected directly in space experiments. From a few hundred keV up to several MeV Compton scattering is the dominant absorption process and the total interaction cross-section reaches its minimum. Above a few tens of MeV pair production becomes dominant, and the cross-section increases again.

The first evidence for a diffuse source of gamma-rays in the energy range from 0.1 MeV to 1 MeV was shown by experiments on the lunar probes Ranger 3 and Ranger 5 (Arnold et al., 1962). Between March 1967 and July 1968, the third Orbiting Solar Observatory (OSO-3) measured 621 gamma-rays above 50 MeV with cosmic origin. Although they could not find discrete sources, a clear excess was measured from the galactic plane with a broad maximum towards the galactic center together with an isotropic component, interpreted as an extragalactic origin (Kraushaar et al., 1972). At lower energies (0.25-6.0 MeV) diffuse emission was detected by the Environmental Research Satellite 18 (ERS-18, Vette et al., 1970). The first discrete sources at energies between 30 MeV and 200 MeV were discovered by the Second



Burst Monitor (GBM) and the Large Area Telescope (LAT). The GBM covers the energy range from 8 keV to 25 MeV with a field of view (FOV) of 9.5 steradians ( $\sim 80\%$  sky coverage) to detect very short transients like Gamma-ray bursts. The LAT has an energy range from 20 MeV up to 200 GeV with a FOV of 2.5 steradians. With its sensitivity of about 50 times that of EGRET at 100 MeV and even more at higher energies the detection of a few thousand of new gamma-ray sources is expected. Figure 1.6 compares the EGRET sky map with the simulated sky map as anticipated to be seen by the LAT. The simulated image includes several components like a diffuse galactic background model, the 3rd EGRET source catalogue, a galactic halo of unidentified sources, an additional distribution of unidentified sources about the galactic plane and a diffuse isotropic background represented as many faint sources with a flux distribution based on Stecker and Salamon (1996).

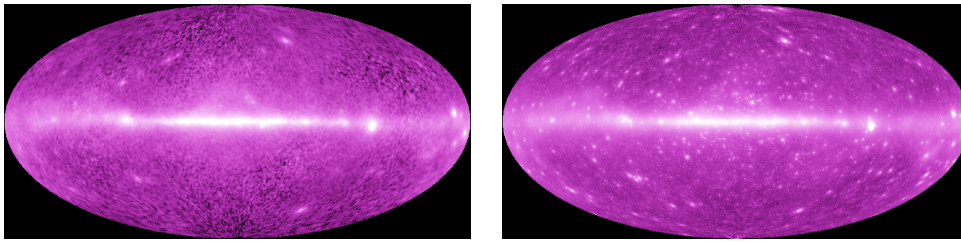


Figure 1.6: Left panel: The sky in galactic coordinates as seen by EGRET above 100 MeV. Right panel: A simulation of the sky as anticipated to be seen by the GLAST Large Area Telescope above 100 MeV (www-04).

### 1.2.2 Very high energy: 100 GeV - 100 TeV

Above  $\sim 30$  GeV a measurable amount of Cherenkov light from secondary particles, produced in electromagnetic cascades (so-called air showers, see Chapter 3), reaches the ground. At higher energies even the produced electrons and positrons can reach the observation level. Satellite experiments suffer from the low fluxes at VHE ( $\sim 10^{-6}$  photons  $\text{m}^{-2} \text{s}^{-1}$  for a strong point source at a few hundred GeV) because of their limited effective area. Also the detector mass and volume has to be larger to stop all the secondary particles produced in the detector. Ground based telescopes can be build as large arrays (if the secondary particles shall be detected directly) or make use of the atmosphere as a calorimeter like air Cherenkov telescopes. With the latter technique effective areas in the order of  $10^5 \text{m}^2$  can be reached by a single telescope.

### Imaging Cherenkov telescopes - the first generation

In 1989, gamma-rays above 700 GeV were detected from the Crab Nebula as the first VHE gamma-ray source by the Whipple 10 m imaging air Cherenkov telescope (IACT)<sup>1</sup> (Weekes et al., 1989), followed by the first extragalactic source, Mrk 421, in 1992 (Punch et al., 1992). The imaging air Cherenkov technique provides large effective areas ( $10^5 \text{ m}^2$ ), a good angular ( $\sim 0.1^\circ$ ) and energy ( $\sim 25\%$ ) resolution and low costs compared to space experiments. The drawbacks are the small FOV and a duty cycle of  $\sim 10\%$  as observations are restricted to clear moonless nights. During the 1990s an array of Cherenkov telescopes was built on the Canary Island of La Palma. They were part of the High Energy Gamma Ray Array (HEGRA) which included also particle detectors to enhance the accessible energy range up to  $10^{16}$  eV. The first prototype CT1 was operational in 1992, the second one (CT2) with a larger reflector of  $8.5 \text{ m}^2$  in 1993. In 1998 the system of 5 telescopes was complete (CT2 -CT6, CT1 was still used in single mode) and performed successfully observations above 700 GeV until 2002. It was the first time that the imaging technique was used in stereoscopic mode, which enhanced the sensitivity, as well as the spatial and energy resolution, by a coincidence trigger and the reconstruction of the impact parameter of the primary gamma-ray (Daum et al., 1997).

Also in 1992, CANGAROO-I (Collaboration of Australia and Nippon (Japan) for a GAMMA Ray Observatory in the Outback), the first Cherenkov telescope in the southern hemisphere equipped with an 3.8 m reflector, started operation in Woomera (Australia). It was complemented by a 7 m telescope in March 1999 (CANGAROO-II). Another southern telescope, the University of Durham Mark 6 gamma-ray telescope, was commissioned in 1995. It was equipped with three  $\sim 42 \text{ m}^2$  mirrors on a single mount (one camera per mirror).

Further IACTs on the northern hemisphere were the Cherenkov Array at Themis (CAT, France), operational since September 1996 with a  $18 \text{ m}^2$  reflector, the Utah Seven Telescope Array in Dugway, Utah (USA), which started observations in January 1997 with the first three telescopes (each with a  $6 \text{ m}^2$  reflector) and the TeV Atmospheric Cherenkov Telescope with Imaging Camera (TACTIC), located at Mt. Abu (India, since 2001 with a  $9.5 \text{ m}^2$  reflective area). Due to the small FOV of all these telescopes, observations are all performed in pointing mode. During the first 15 years of VHE gamma-ray astronomy, detections of ten extragalactic and eight galactic sources above several hundred GeV were claimed by different groups (Horan and Weekes, 2004), eight of them were confirmed by a second group at that time (see

---

<sup>1</sup>See Chapter 3.3 for a description of the detection principle.

Fig. 1.7). All discoveries were made by IACTs.

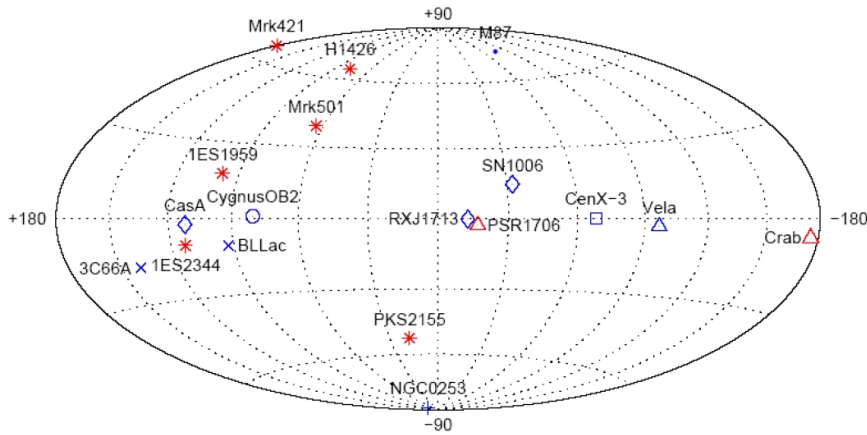


Figure 1.7: The VHE gamma-ray sky in 2003 (Horan and Weekes, 2004). Confirmed sources are drawn in red.

### Wave front sampling

Instead of imaging the air shower, it is also possible to sample the incoming wave front, using also the Cherenkov light of the secondary particles. By the end of the last century, solar plants were used for the first time as observatories, employing successfully the method of wave front sampling. CELESTE used a former solar plant at Themis in the eastern French Pyrenees, equipped with 40 heliostats with a total reflecting surface of  $2000 \text{ m}^2$  (de Naurois et al., 2002). The Solar Tower Atmospheric Cherenkov Effect Experiment (STACEE) is located at the National Thermal Test Facility near Albuquerque, New Mexico (USA). It consists of 64 heliostats with a surface of  $37 \text{ m}^2$  each and is fully operational since autumn 2002 (Hanna et al., 2002). Both experiments reach very low energy thresholds of below  $100 \text{ GeV}$  but suffer from a poor background rejection. Other heliostat arrays are the Solar-Two power plant, located at Barstow, California (USA) and GRAAL (Gamma Ray Astronomy at Almeria, Arqueros et al., 2002), located in Almeria, Spain. Another wave front sampling telescope, which makes no use of a solar plant is PACT (Pachmarhi Array of Cherenkov Telescopes), located at Pachmarhi, India (Bhat, 2002). It consists of an array of 25 telescopes, each with seven mirrors and one photomultiplier tube (PMT) per mirror, yielding an energy threshold of  $900 \text{ GeV}$ .

### Large field of view telescopes

At TeV energies (and high altitudes) a significant amount of secondary particles can reach the ground. Milagro, located in Jemez mountains of northern New Mexico (USA, 2630 m a.s.l.) uses the Cherenkov effect in water for the particle detection. It consists of a 4800 m<sup>2</sup> covered water pond surrounded by 175 instrumented water tanks resulting in a 40000 m<sup>2</sup> area with a FOV of 2 steradians. The clear advantages of this technique are the large FOV combined with a duty cycle of > 90%, while the main drawbacks are the high energy threshold and the poor background rejection. Recently the Milagro group reported new VHE sources after more than six years of scanning the northern hemisphere (Abdo et al., 2007b). Some of them are spatially extended. A future experiment, called HAWC, is currently planned to be built in Mexico at an altitude above 4000 m. The high altitude combined with a large covered water pond of 22500 m<sup>2</sup> will result in a 15 times higher sensitivity compared to Milagro.

Beside the water Cherenkov technique, the incoming particles can also be detected by a layer of resistive plate counters as successfully employed in ARGO, located in Yangbajing, Tibet (China, 4300 m a.s.l.). The 5800 m<sup>2</sup> detector is fully operational since February 2007, yielding a threshold of a few hundreds of GeV and a sensitivity 5 times higher than Milagro (Martello et al., 2007).

There is also a new instrument combining the Imaging Cherenkov Technique with a large FOV camera, using fresnel lenses instead of reflectors. GAW (Gamma Air Watch), located at the Calar Alto Observatory (Spain, 2150 m a.s.l.), will consist of three telescopes, 2.13 m in diameter each, with a FOV of the detector of 5° in phase I (later enhanced to 24°), providing an energy threshold of 700 GeV (Cusumano et al., 2007).

### Imaging Cherenkov telescopes - the second generation

With the completion of the fourth telescope of the H.E.S.S. (High Energy Stereoscopic System) array in 2003, the first IACT of the second generation started regular data taking. Each of the four telescopes consists of a 108 m<sup>2</sup> tessellated mirror and a camera with 960 PMTs. The array is located in Namibia (23° 16' S, 16° 30' O, 1800 m a.s.l.). In March 2004 CANGAROO-III started with an array of four 10 m telescopes. At the former site of HEGRA, the Major Atmospheric Gamma Imaging Cherenkov (MAGIC) telescope finished its commissioning in October 2004. It is currently the largest IACT with a 234 m<sup>2</sup> tessellated mirror, leading to a trigger threshold of 50 GeV. It operates in single mode (see more technical details in Chapter 3.4). With

the inauguration of the Very Energetic Radiation Imaging Telescope Array System (VERITAS) in August 2007 the last of the second generation IACTs went operational. It is located close to the Whipple site and consists of an array of four 12 m telescopes. Figure 1.8 shows the location of the current second generation IACTs.

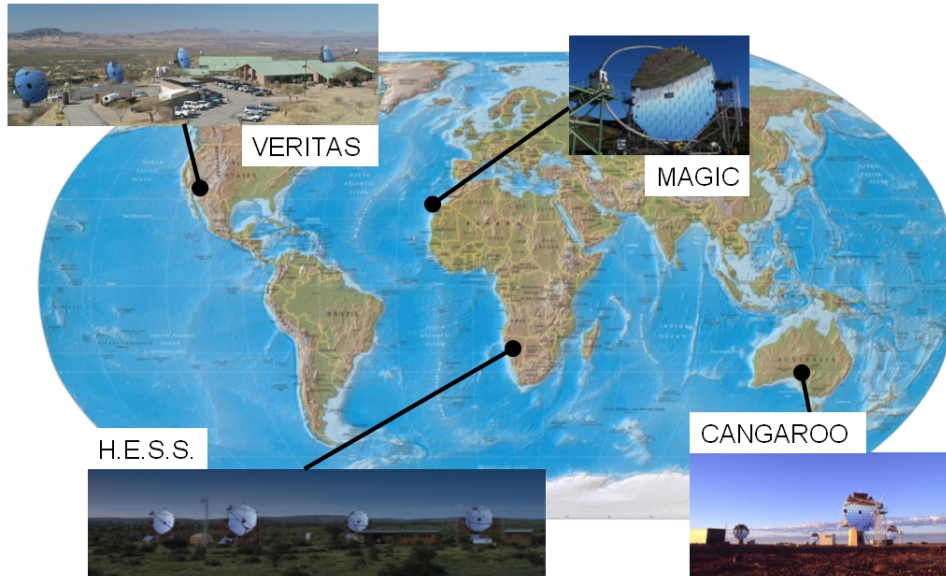


Figure 1.8: World map with the locations of the second generation imaging air Cherenkov telescopes.

Within the last four years the number of detected VHE gamma-ray sources increased to 52 galactic and 20 extragalactic objects<sup>2</sup>. While several objects, previously discovered, could be confirmed by the new experiments, the objects NGC 253 (the first starburst galaxy at VHEs) and 3C66A (the first Low-peaked BL Lac object at VHEs) as well as the supernova remnant SN 2006 are in conflict with recent measurements (Aharonian et al., 2005e; Itoh et al., 2007; Aharonian et al., 2005c; Horan and Weekes, 2004). The strong increase in the number of sources is mainly due to the lower energy threshold of the new instruments as the fluxes always decrease with increasing energy. In case of extragalactic objects the absorption of gamma-rays causes an additional softening of the spectra (see Section 1.4). In 2004 H.E.S.S. showed with a scan of the inner part of the galactic plane that this region is rich of VHE sources, some of them with no counterpart at other wavelengths (Aha-

<sup>2</sup>For an up-to-date list of VHE sources, see <http://www.mppmu.mpg.de/~rwagner/sources/>

ronian et al., 2005d). Figure 1.9 shows the current VHE gamma-ray sky with 72 objects in total.

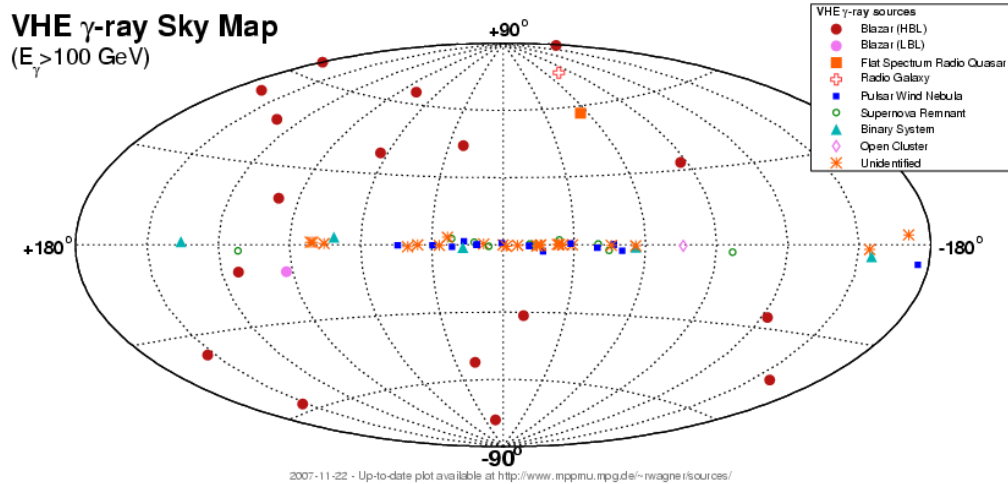


Figure 1.9: The VHE-sky: All VHE gamma-ray sources in galactic coordinates (status: 22.11.2007, www-05).

### Future prospects

Currently under construction are H.E.S.S.II, where the existing array will be complemented by a central very large telescope with a  $600\text{ m}^2$  reflecting surface and MAGIC II, where a second 17 m telescope for stereo observations is expected to be operational in autumn 2008. Both systems will then be able to make stereoscopic observations below 100 GeV, which will lead to a clear overlap with the upcoming GLAST mission. A Future project, currently under discussion, is the Cherenkov Telescope Array (CTA); it is planned to be an array of tens of large Cherenkov telescopes for highly sensitive observations above tens of GeV, supported by a large number of small telescopes, covering the higher energies up to 100 TeV (Bernlöhner et al., 2007).

## 1.3 Mechanisms of gamma-ray production

Exept for radioactivity, which can only account for emission lines in the MeV energy range, all production mechanisms of gamma-rays require highly relativistic charged particles.

### 1.3.1 Bremsstrahlung

When a charged particle is scattered in the Coulomb field of a charged target particle, bremsstrahlung is emitted. In case of non-relativistic particles, the energy loss due to ionisation is much larger than due to bremsstrahlung. For ultra-relativistic particles, the energy loss due to bremsstrahlung becomes dominant. It can be written as (Jackson, 1982):

$$-\frac{dE}{dx} = 4\alpha Z(1+Z) \frac{N_A}{A} \left( \frac{z^2 e^2}{4\pi\epsilon_0 m c^2} \right)^2 E \ln \left( \frac{233m}{Z^{1/3} M_e} \right) = \frac{E}{X_0} \quad (1.10)$$

with  $\alpha = e^2/(4\pi\epsilon_0\hbar c)$  being the finestructure constant,  $m$  the mass of the scattered particle and  $M_e$  the electron mass,  $N_A$  the Avogadro constant and  $A$  the molar mass of the target particles. The length  $X_0$  (given in g/cm<sup>2</sup>) where the energy of the scattered particle is  $1/e$  of its initial value is called the radiation length. For electrons in air the radiation length is  $X_0 = 33.66$  (g/cm<sup>2</sup>). For heavier particles the effect is suppressed by  $1/m^2$ , but as the energy loss increases linear with increasing energy it can also become dominant. On the one hand the radiation length decreases for target materials with higher atomic number due to the factor  $A/(Z(1+Z))$ , on the other hand the length of the path itself (given in cm) is strongly depending on the density of the material. Therefore the effect can be even negligible in astrophysical sources with low particle densities.

### 1.3.2 Synchrotron radiation

Synchrotron radiation is emitted when a charged particle travels through a magnetic field with a field component perpendicular to the path of the particle. The total emitted power of one particle is given as

$$P = \frac{2}{3} r_0^2 c \beta^2 \gamma^2 \frac{4\pi B^2}{\mu_0} \sin^2(\alpha), \quad r_0 = \frac{e^2}{4\pi\epsilon_0 m c^2}, \quad (1.11)$$

where  $B$  is the magnetic field,  $\beta = v/c$  the particle's velocity in units of the speed of light,  $\gamma$  the Lorentz factor of the particle and  $\alpha$  the angle between the velocity and the magnetic field, known as the pitch angle. This power is emitted in a narrow cone of opening angle  $\sim 1/\gamma$  around the velocity vector. The radiation is polarised. If the particles' velocities are distributed isotropically, the average emitted power is

$$P = \frac{4}{3} \sigma_T c \beta^2 \gamma^2 U_B, \quad (1.12)$$

where  $\sigma_T = (8\pi/3)(q^2/(4\pi\epsilon_0 mc^2))^2 = 6.652 \times 10^{-25} \text{ cm}^2$  is the Thomson scattering cross-section and  $u_B = B^2/(2\mu_0)$  is the energy density of the magnetic field. The spectrum appears to be continuous with a maximum at the critical frequency

$$\nu_c = \frac{3eB_\perp}{4\pi mc} \frac{1}{\sqrt{\epsilon_0\mu_0}} \left(\frac{E}{mc^2}\right)^2 = A \times \left(\frac{B_\perp}{\mu\text{G}}\right) \left(\frac{E}{\text{TeV}}\right)^2 \text{ Hz}, \quad (1.13)$$

with  $A = 1.61 \times 10^{13}$  for electrons and  $A = 2.58 \times 10^3$  for protons. It can be seen that synchrotron radiation of electrons will generate photons from the radio to the hard X-ray regime (assuming a magnetic field strength up to  $\sim \text{G}$  and electron energies up to  $\text{TeV}$ ). There is also the possibility for ultra high energy protons ( $E \sim 10^{19} \text{ eV}$ ) in strong magnetic fields ( $B \geq \text{G}$ ) to produce gamma-rays up to  $\text{TeV}$  energies. In Section 1.1 it has been shown that shock acceleration generates energy spectra, which follow a power law:

$$n(E) = CE^{-s}, \quad (1.14)$$

where  $n(E)$  is the number density of the particles and  $C$  and  $s$  are constants. The radiation spectrum, produced by particles having the energy  $E$ , peaks at the critical frequency  $\nu_c$ . It can be shown that the emitted spectrum will also follow a power law in the form of (e.g. Kembhavi and Narlika, 1999):

$$P(\nu) \propto \nu^{-\alpha}, \quad \alpha = \frac{s-1}{2} \quad (1.15)$$

### 1.3.3 Inverse Compton scattering

The scattering of photons by electrons is known as Compton scattering. If the electron is at rest, it will gain energy from the scattering as it requires a recoil velocity to satisfy momentum conservation. The total cross-section, obtained by using a quantum electrodynamic treatment, is given by the Klein-Nishina cross-section:

$$\sigma_{\text{KN}} = \frac{3\sigma_T}{4} \left\{ \frac{1+x}{x^3} \left[ \frac{2x(1+x)}{1+2x} - \ln(1+2x) \right] + \frac{\ln(1+2x)}{2x} - \frac{1+3x}{(1+2x)^2} \right\}, \quad (1.16)$$

with  $x = (h\nu\gamma)/(mc^2)$ . For  $x \ll 1$  Thomson scattering applies and the Klein-Nishina cross-section reduces to the classical Thomson cross-section. For  $x < 0.02$  a serial expansion up to the first order is in good agreement with the total cross-section:

$$\sigma = \sigma_T \left( 1 - \frac{2h\nu}{mc^2} \right) \quad (1.17)$$

In the extreme case ( $x > 10$ ) the Klein-Nishina limit holds:

$$\sigma = \frac{3}{8} \sigma_{\text{T}} \frac{mc^2}{h\nu} \left[ 0.5 + \ln \left( \frac{2h\nu}{mc^2} \right) \right] \quad (1.18)$$

Figure 1.10 shows the variation of the total cross-section with energy, together with the approximations for low and high values of  $x$ .

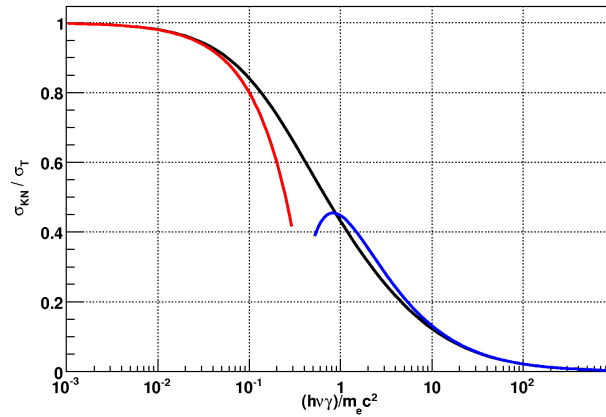


Figure 1.10: The variation of the Compton scattering cross-section with energy. The black line indicates the total cross-section, the red line a series expansion up to the first order and the blue line the Klein-Nishina limit for high values of  $x = (h\nu\gamma)/(mc^2)$ .

If the electron is already in motion before the scattering, energy can either pass from the electron to the photon or vice versa, depending upon the kinematical details of the collision. In case the photon gains energy, it is called inverse Compton scattering. This is always the case for highly relativistic electrons. For  $h\nu \ll mc^2/\gamma$  (Thomson limit) the energy of the photon after the scattering is approximately  $h\nu' \approx \gamma^2 h\nu$ , with  $\gamma$  being the Lorentz factor of the electron. Since the total energy has to be conserved, there is an upper limit to the increase of the photon energy of  $\Delta h\nu \leq \gamma mc^2$ . In the extreme Klein-Nishina limit ( $h\nu \gg mc^2/\gamma$ ) the energy of the scattered photon is  $h\nu' \approx \gamma mc^2$ ; the electron loses its energy already in one scattering process.

The power of a single Compton scattering is given as (e.g. Blumenthal and Gould, 1970)

$$P = \frac{4}{3} \sigma_{\text{T}} c \beta^2 \gamma^2 U_{ph}, \quad (1.19)$$

where  $U_{ph}$  is the total energy density of the electromagnetic radiation (target photons). This expression is strikingly similar to the synchrotron power output (Equ. 1.12). The similarity arises because synchrotron emission can

be considered to be the scattering by an electron off the virtual photons of the magnetic field. Since in realistic cases the cross-section is reduced, the Compton power from scattering in the Thomson regime can be seen as a maximum power. See also Blumenthal and Gould (1970) for a more general and detailed calculation of the Compton power, including thermal and isotropic target photon distributions.

### 1.3.4 Pion decay

Another source of high energy gamma-rays is the decay of neutral pions (mean life time  $\tau = 8.4 \cdot 10^{-17}$  s):

$$\pi^0 \rightarrow \gamma + \gamma$$

In the rest frame of the pion, both photons have the same energy of half of the pion mass. In the observer's frame, in case of a moving pion, the photon emitted in the same direction as the path of the pion gets more energy than the photon emitted to the opposite direction. This results in a flat spectrum with a minimum and a maximum energy, given as:

$$\begin{aligned} E_{\gamma}^{\max} &= \frac{1}{2}\gamma m_{\pi^0}(1 + \beta) \\ E_{\gamma}^{\min} &= \frac{1}{2}\gamma m_{\pi^0}(1 - \beta) \end{aligned} \quad (1.20)$$

For ultra-relativistic particles ( $\gamma \gg 1$ ,  $\beta \approx 1$ ) the maximum energy is equal to the total energy of the pion, while the minimum energy is zero. In a logarithmic scale, the energy distribution is symmetrically around  $1/2 m_{\pi^0} c^2$ . A spectrum of neutral pions therefore results in a gamma-ray spectrum with a maximum at  $E_{\gamma} = 1/2 m_{\pi^0} c^2$ .

Neutral pions can be produced in proton(neutron)-nucleon interaction or in proton(neutron)-photon interaction. As the astrophysical sites of pion production considered in this work are much more dominated by radiation instead of matter, the photo-pion production will be the more important process. The threshold for the nucleon energy is given as (e.g. Ahn et al., 2001):

$$E_{th} = \frac{m_{\pi}(m_p + m_{\pi}/2)}{h\nu} \simeq 6.8 \times 10^{16} \left( \frac{h\nu}{\text{eV}} \right)^{-1} \text{ eV}, \quad (1.21)$$

where  $h\nu$  is the energy of the corresponding photon. Close to the threshold energy, the cross-section is dominated by resonances (mainly the  $\Delta(1232)$ -resonance) and has a maximum. The incoming baryon is excited to a baryonic resonance due to the absorption of the photon. Such resonances have very

short life times and decay immediately into other hadrons. At higher energies the total interaction cross-section becomes almost energy independent while the contribution of resonances decreases. At these energies the photon-hadron interaction is dominated by inelastic multiple pion production (e.g. Mücke et al., 2000).

Another, indirect production of gamma-rays arises from the decay of charged pions into muons (or anti-muons), which can emit synchrotron radiation up to high energies before they decay into electrons (or positrons). These relativistic electrons and positrons can produce gamma-rays by inverse Compton scattering off low energy photons.

## 1.4 Absorption of gamma-rays

Gamma-radiation from cosmological distances is attenuated by pair production in photon-photon interactions with photons from low energy radiation fields. This was pointed out first by Gerasimova et al. (1962), unfortunately overestimating the low energy photon field by 3 orders of magnitude. After the discovery of the microwave background in 1965, Gould and Schröder (1967) and Jelley (1966) calculated the opacity of the universe for photons with energies greater than 100 TeV. These calculations were generalised to high redshifts by Fazio and Stecker (1970).

The pair creation cross-section has a maximum for  $h\nu_1 \times h\nu_2 \approx 2(m_e c^2)^2$  (e.g. Stecker et al., 1992). For a given gamma-ray energy  $E_\gamma$ , the wavelength of the corresponding low energy photon follows as

$$\lambda(E_\gamma) \approx hc \frac{E_\gamma}{2(m_e c^2)^2} \approx 2.5 \frac{E_\gamma}{\text{TeV}} \mu\text{m}. \quad (1.22)$$

Gamma-rays in the energy range accessible with current ground based telescopes (mainly the 100 GeV to 10 TeV range) will interact mostly with photons from  $0.25 \mu\text{m}$  to  $25 \mu\text{m}$  (IR - UV). To calculate the opacity for the gamma-rays the exact energy density of the evolving metagalactic radiation field (MRF) at these wavelengths has to be known. Unfortunately, direct measurements are difficult because of the strong foreground radiation, in particular in the IR due to the zodiacal light. The most robust lower limits on the photon flux come from galaxy number counts, measured by the Spitzer telescope between  $3 \mu\text{m}$  and  $10 \mu\text{m}$  (Fazio et al., 2004) as well as between  $24 \mu\text{m}$  and  $160 \mu\text{m}$  (Dole et al., 2006), and by the Hubble Space Telescope (HST) between  $0.35 \mu\text{m}$  and  $2.2 \mu\text{m}$  (Madau and Pozzetti, 2000).

Since photons in that regime are mainly produced by stars, emitted directly or reprocessed to higher wavelengths by dust, the shape of the radiation

field can be further constrained by star evolution models. A review about the achievements in observations and theoretical modelling during the 1990s is given in Hauser and Dwek (2001). Figure 1.11 shows the MRF at present day (commonly referred to as extragalactic background light,  $EBL \equiv MRF$  for  $z = 0$ ) together with the model taken from Kneiske et al. (2004). For the calculation of the opacity for high redshift sources another problem arises from cosmological evolution of the MRF. A semi-empirical model, based on star light produced and reprocessed in evolving galaxies is presented in Kneiske et al. (2002).

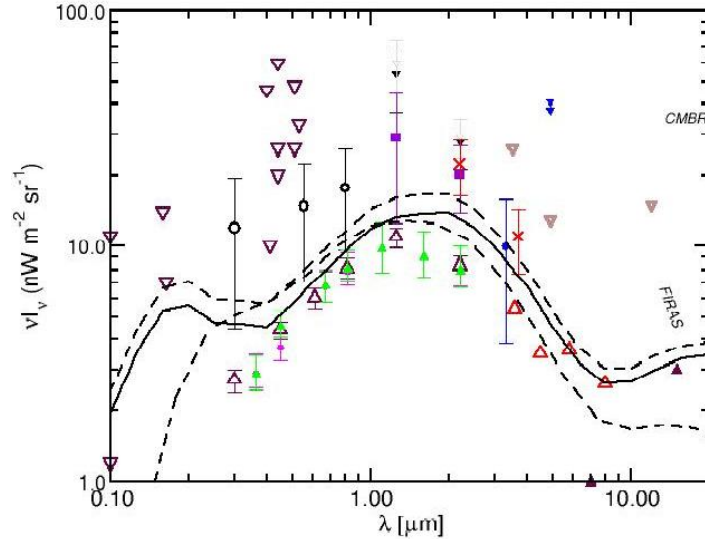


Figure 1.11: The metagalactic radiation field (MRF) at present day. The most robust lower limits come from galaxy number counts measured by HST (green triangles, Madau and Pozzetti, 2000) and Spitzer (open red triangles, Fazio et al., 2004). The solid line shows the best fit model from Kneiske et al. (2004). The dotted lines show a low and a high density model derived by the same author.

Due to the absorption, a cut-off in the energy spectra of distant sources is expected leading to a gamma-ray horizon. The cut-off energy is defined as the energy where the optical depth  $\tau$  is unity. Figure 1.12 shows the cut-off energy vs. redshift, also called the Fazio-Stecker relation (Fazio and Stecker, 1970; Kneiske et al., 2004). It was argued by several authors (e.g. Stecker et al., 1992; Primack et al., 1999) that measured cut-off energies for a set of distant blazars, located at different redshifts, could provide strong constraints on the MRF, in particular for its history where no direct measurements are possible. This in turn requires a good understanding of the intrinsic blazar spectra, which is still not the case. The VHE spectra of recently discovered blazars -

up to a redshift of  $z = 0.212$  - show no hint for a cut-off. Under assumptions on the maximum hardening of the intrinsic spectra of two blazars (1ES 1101-232 and H 2359-309), an upper limit on the energy density of the MRF in the range between  $0.8 \mu\text{m}$  and  $3.5 \mu\text{m}$  was derived by Aharonian et al. (2006e), which is close to the lower limit of the galaxy number counts.

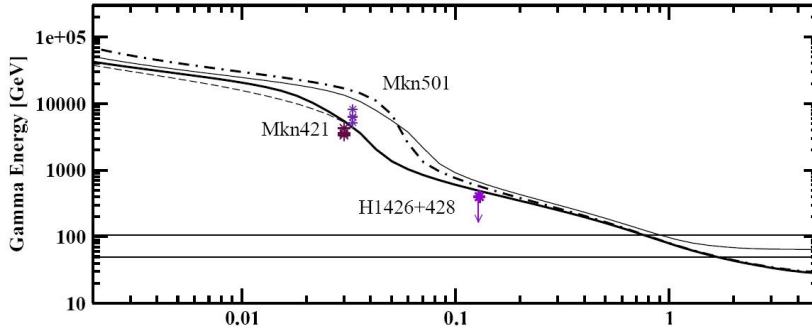


Figure 1.12: Fazio-Stecker relation: cut-off energy vs. redshift. The plot is taken from Kneiske et al. (2004).

In this work, the "best fit 2006" MRF model (Kneiske, in preparation) is employed to calculate the optical depths for the measured gamma-ray energies. This model is an additional model to the ones introduced in Kneiske et al. (2004), but for a new choice of parameters. The result is a high far infrared intensity, while the near infrared intensity stays close to the number counts derived by the Hubble Space Telescope (Madau and Pozzetti, 2000) and above the ones recently published by the Spitzer telescope at higher wavelengths (Fazio et al., 2004; Dole et al., 2006). To achieve this the infrared and optical cosmic star formation rate is reduced to its minimum. The model also includes the warm dust component and excludes the escape of ionising photons from normal galaxies. Figure 1.13 shows the optical depth vs. energy for the redshifts  $z = 0.044$ ,  $z = 0.182$  and  $z = 0.30$ .

The produced electron-positron pairs will comptonise photons from the cosmic microwave background to high energies. These gamma-rays can produce pairs again, which leads to an electro-magnetic cascade where the primary VHE photons are reprocessed to lower energies (Wdowczyk et al., 1972). Depending on the intergalactic magnetic field strength, the secondary radiation could either get fully isotropised or could contribute to the measured flux of the sources, varying the initial spectrum (Protheroe and Stanev, 1993). It was shown by Aharonian et al. (1994) that cascade radiation could form an extended halo ( $R < 1 \text{ Mpc}$ ), observable at energies below a few TeV. So far all detected extragalactic VHE sources are consistent with point sources within their resolution of  $\approx 0.1^\circ$ .

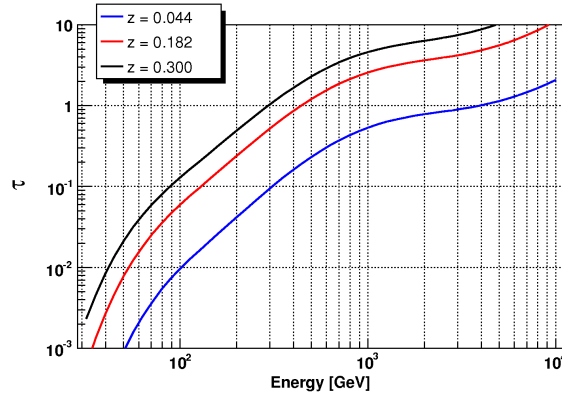


Figure 1.13: Optical depth vs. energy for the redshifts  $z = 0.044$  (blue),  $z = 0.182$  (red) and  $z = 0.30$  (black) using the model from Kneiske et al. (2004)

## 1.5 Astrophysical sources of gamma radiation

It is clear that only extreme objects will be able to accelerate particles to energies of  $10^{12}$  eV to  $10^{20}$  eV. In the Hillas plot (Fig. 1.3) potential objects are already shown with their general possibility of particle acceleration due to the product of the size of the source and its magnetic field. In the following a brief overview of known and possible sources of VHE gamma-ray emission is given. Due to the observations of source candidates in pointing mode and the good spatial resolution, most of the sources detected by ground based gamma-ray telescopes are identified at other wavelength. Recently the H.E.S.S. galactic plane scan discovered a large number of sources where no counterparts at other wavelengths are known.

### 1.5.1 Galactic sources

#### Supernova remnants

Supernovae are powerful explosions with a total energy output of  $\sim 10^{53}$  erg within a few seconds. They are believed to be the sources of the galactic component of the cosmic ray spectrum up to the knee ( $10^{15}$  eV). The explosion builds a shock front where Fermi acceleration of hadrons could take place. So far there are seven VHE gamma-ray sources, identified as supernova remnants (SNR). In 2004 observations of the SNR RX J1713.7-3946 revealed for the first time the morphology of a SNR at VHEs (Aharonian et al., 2004b). The gamma-ray image shows the shell structure of the SNR, which coincides closely with the structures seen in X-rays.

### Pulsars and pulsar wind nebulae

In case of core collapse Supernovae (type II) a neutron star (pulsar) remains. Such pulsars show pulsed emission with periods ranging from 1.4 ms to 11.8 s, masses in the order of 0.1 to 2  $M_{\odot}$  and radii of about 10 km. The extended relativistic outflows from pulsars are called pulsar wind nebulae (PWN). The emission process is still poorly known and it is even unclear if all pulsars exhibit a PWN. As the pulsars are embedded in un-shocked ejecta from the supernova explosion, the wind can form strong shocks in the ejecta at which particles can be accelerated up to  $10^{15}$  eV. Evidence for relativistic electrons and positrons comes from the observation of continuum emission from the radio to the X-ray regime, commonly accepted as synchrotron emission, as well as from detections at HE and VHE gamma-rays. The PWNe are the major galactic source population at TeV-energies with 18 identified objects so far. The most famous example of this source class is the well studied Crab Nebula, which is used as a standard candle in VHE gamma-ray astronomy (and also in X-ray astronomy) because of the high and steady flux. Figure 1.14 shows a X-ray image of the Crab-PWN, taken by the X-ray satellite Chandra. The structure of the PWN is clearly visible.

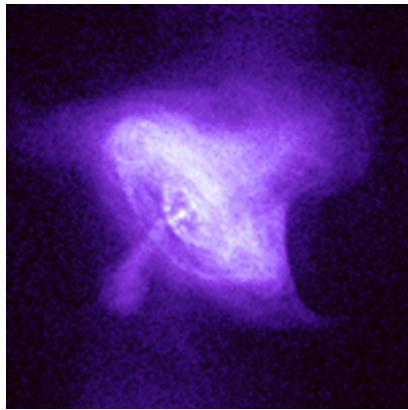


Figure 1.14: The pulsar wind nebula inside the Crab Nebula in X-rays as seen by Chandra (25 arcmin side length, www-06).

Pulsed gamma-ray emission up to several GeV was seen by EGRET from six pulsars. So far no pulsed emission is detected at higher energies. Recently the MAGIC collaboration published an upper limit on the pulsed emission of the Crab pulsar above 60 GeV (Albert et al., 2008a) as well as an upper limit on the pulsed emission of PSR B1951+32 above 75 GeV (Albert et al., 2007h). Compared to the  $\sim 10$  times higher flux detected by EGRET at lower energies, the upper limits require an exponential cut-off below 27 GeV and 34 GeV respectively.

## Binary systems

Among the galactic VHE sources there are by now four binary systems. These systems consist of a compact object like a neutron star or a black hole and a high mass O or Be star (see Fig.1.15). In the case of PSR B1259-63 a young millisecond-pulsar orbits with high excentricity a Be star with a period of 1237 days. The gamma-rays can be produced in the shock where the wind of the pulsar and the Be star collide (Dubus, 2006). For LS I +61°303 and LS 5039 the situation is more complicated. Although the periods are much smaller (26 and 4 days respectively), the behaviour is similar to PSR B1259-63 indicating the same emission mechanism. But the gamma-ray emission could also be related to the compact radio emission, interpreted as a relativistic outflow (jet) driven by accretion of material from the companion star (microquasar-type model, Bosch-Ramon et al., 2006). Both sources show a clear orbital modulation of the VHE emission (Albert et al., 2006f; Aharonian et al., 2006c). Recently the MAGIC collaboration reported the detection of VHE gamma-rays from the microquasar Cygnus X-1 in a 79 min time slice within a 40 hrs observation campaign (Rico et al., 2007).

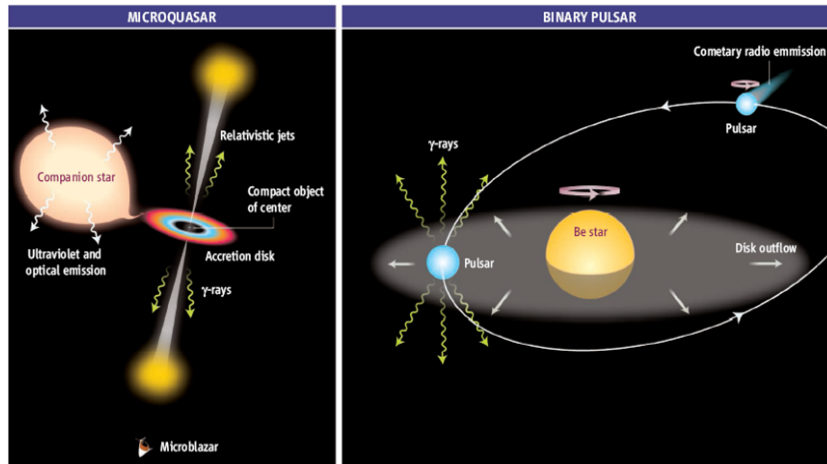


Figure 1.15: Schematic view of the emission models for a binary system (taken from Mirabel, 2006). Microquasar-type (left panel): gamma-rays are emitted from the jet. Binary pulsar (right panel): gamma-rays are emitted by interaction of the pulsar wind with the companion outflow.

## Galactic center

The galactic center (GC) is now confirmed as a VHE gamma-ray source by various experiments (e.g. Aharonian et al., 2006f; Albert et al., 2006a).

Nevertheless the nature of the source remains unknown. The location of the source is consistent with Sgr A\*. Recent studies with the H.E.S.S. array could exclude the SNR Sgr A East by improvements in their pointing uncertainties (van Eldik et al., 2007). The immediate vicinity of the black hole cannot be ruled out, although the steady emission disfavors this possibility. There are also more exotic explanations like gamma-rays from dark matter (DM) annihilation. Most of these models predict curved gamma-ray spectra, which was not seen (Aharonian et al., 2006f); indeed, the spectrum shows a clear power law over two decades in energy.

### Diffuse emission

A diffuse gamma-ray flux is expected from the galactic plane due to interactions of cosmic rays with matter and radiation fields and was measured by EGRET up to 50 GeV. It shows a maximum in the innermost part of galactic plane ( $|b| \leq 2^\circ$  and  $|l| \leq 60^\circ$ ) (Hunter et al., 1997). At higher energies, diffuse emission was reported for the GC ridge by Aharonian et al. (2006d) and the Cygnus region of the galactic plane (Abdo et al., 2007a). Both detections are spatially correlated with molecular clouds.

## 1.5.2 Active galactic nuclei

So far 20 extragalactic sources are known to be VHE gamma-ray emitters. All of them belong to the class of (radio loud) active galactic nuclei, where a supermassive black hole is surrounded by an accretion disc that feeds a bi-polar relativistic outflow (jet). The jet is responsible for the observed non-thermal continuum emission from the radio band up to gamma-rays, where the most energetic radiation is supposed to come out of a small compact region in the vicinity of the black hole, moving with relativistic speed along the jet. A more detailed description is given in the next chapter.

Almost all of the detected sources (17) belong to the subclass of high frequency peaked BL Lac objects (HBL), which show a pronounced peak in their energy output at X-rays and a second one at VHE gamma-rays. Recently the MAGIC collaboration reported the discovery of the first low frequency peaked BL Lac object (BL Lac, Albert et al., 2007d) as well as the first flat spectrum radio quasar (3C 279, Teshima et al., 2007). Both sources are characterised by higher peak-luminosities at lower energies. Quasars are the main extragalactic source class detected by EGRET (Hartman et al., 1999), as they exhibit their peak energies in the EGRET energy range.

Despite all their spectral differences, they all belong to the class of blazars (blazar = **BL** Lac + **quasar**), where the jet is seen under a small angle, lead-

ing to an effective beaming of the observed radiation. With the confirmation of VHE emission from the nearby giant radio galaxy M87, the first extragalactic non-blazar source is established (Beilicke et al., 2004). However, in the context of unified schemes for active galactic nuclei, M87 can be interpreted as a "misaligned" blazar characterised by a larger angle between the jet axis and the line of sight.

### 1.5.3 Unidentified sources

The number of unidentified sources has increased to 21, all of them located in the galactic plane and therefore assumed to have a galactic origin. Beside the evidence for "dark accelerators" (Matsumoto et al., 2007), most of them are supposed to be related with SNRs or PWNe. Intensive multiwavelength studies, mainly at X-rays, are necessary to reveal the counterparts of the gamma-ray sources.

### 1.5.4 Gamma-ray bursts

Gamma-ray bursts (GRB) are the most extreme objects among astrophysical sources, completely dominating the entire sky at high energies for a short moment with luminosities up to  $10^{54}$  erg. The gamma-ray durations range from  $10^{-3}$  s to about  $10^3$  s with a bimodal distribution of long ( $t > 2$  s) and short ( $t < 2$  s) bursts. The first GRB was detected in 1967 by the Vela satellite, but the first step in understanding the GRB phenomena started 1991 with the launch of the Compton Gamma-Ray Observatory (CGRO). The all-sky monitoring with the BATSE instrument showed an isotropical distribution of GRBs. The next major development came after 1997, when the first GRB afterglow was measured in X-rays with the Beppo-SAX satellite. This led to an improvement of the determination of the position and triggered further follow-up observations with ground based telescopes. Measurements in the optical and radio bands could finally confirm the cosmological distance of GRBs. After the demise of CGRO and Beppo-Sax, the HETE-2 satellite provided afterglow positions continuously for several years. By the launch of the Swift satellite in 2004, the number of detected GRBs increased together with an improvement of the localisation and revealed the unexplored afterglow behaviour between minutes and hours from optical to hard X-rays. Nevertheless, the nature of GRBs remains still unknown. The origin is compatible with a merger of two compact stellar mass objects (neutron stars and/or black holes) or with a core collapse model of a massive stellar progenitor (hypernova or collapsar). The sudden energy release would result in a very high temperature fireball, expanding at relativistic speed, which

can account for the observed high energy emission by internal dissipation. This fireball shock scenario has become the leading paradigm for the current understanding of GRBs. A recent review is given in Meszaros (2006).

So far no GRB is detected at VHE gamma-rays. The detection is made difficult by the cosmological distance (strong absorption above 100 GeV) and the expected steep intrinsic spectrum at these energies. The long-duration GRB050713a has been observed by the MAGIC telescope only 40 s after the burst onset, yielding an upper limit for the gamma-ray flux above 170 GeV (Albert et al., 2006c).

### 1.5.5 Dark matter annihilation

An important challenge for gamma-ray astronomy is the search for signatures from dark matter. From recent high precision measurements of the cosmic microwave background it is known that 23% of the matter in the universe is non-baryonic. Possible candidates come from supersymmetric extensions of the standard model, where the most probable particle would be the lightest neutralino ( $\chi_1^0$ ). The neutralino self-annihilation dominantly produces continuum emission of gamma-rays. One of the difficulties in indirect dark matter search is to distinguish possible signatures from an astrophysical origin. It was shown by Elsässer and Mannheim (2005) that the spectral hardening around several GeV in the spectrum of the diffuse extragalactic background light, measured by EGRET, could be explained by a significant contribution of gamma-rays from the annihilation of neutralinos with a mass of  $m_\chi = 515_{-75}^{+110}$  GeV. As the flux produced by a neutralino of this mass peaks between 10 GeV and 20 GeV, it cannot be tested with the current energy threshold of ground based telescopes. With the launch of the GLAST satellite in 2008, a deep search with high sensitivity in the range from a few tens of MeV up to 100 GeV will be possible (Wai, 2007; Morselli et al., 2007).

# Chapter 2

## Active galactic nuclei

The first clear evidence for a new and very unusual kind of extragalactic objects was reported by Seyfert (1943) from the detection of strong and broad emission lines within the nuclei of several spiral galaxies. In addition, the nuclei of these galaxies are generally more luminous than the average of the same Hubble type, containing a large percentage of the total light of the system.

After the second world war, radio astronomy became a fast growing and successful field of astronomy. In the mid-1950s the existence of radio galaxies was widely accepted. One of the early catalogue of radio sources was the Third Cambridge Catalogue (3C) prepared by the Mullard Radio Astronomy Observatory at the University of Cambridge. A major problem was still the optical identification for many of these objects. For 3C273 Hazard et al. (1963) could determine the position with an accuracy of  $\sim 1$  arcsec, using the occultation of the source by the moon. This was sufficient to identify the radio source with a star-like object (Schmidt, 1963). The optical spectrum was very peculiar; four emission lines were detected, each shifted by  $\sim 16\%$ , revealing that the source is located at cosmological distance. The point-like appearance of the high energetic objects lead to the name quasi-stellar object (QSO) or quasar.

In the following chapter a brief overview of the main properties of active galactic nuclei (AGN) are given. Section 2.1 starts with an empirical classification of AGN which is mainly based on line emission and radio loudness. In Section 2.2 the unified model is described with a special emphasis on radio-loud AGN. The last section concentrates on blazars, which are the most extreme objects among AGN and the main class of extragalactic gamma-ray sources.

## 2.1 Empirical classification

The class of AGN shows a huge variety of observational properties. The main characteristics are:

- a nuclear region, brighter than the average of the same Hubble type;
- non-thermal broad-band continuum emission from radio to X-rays, extending to gamma-rays for some sub-classes;
- emission lines produced in non stellar processes in the central region;
- variable flux in nearly all wavebands on time scales from years down to minutes (for the most variable objects).

If an object shows one or more of these characteristics it is referred to as an AGN. Only less than 1% of all known galaxies show an active behaviour. In the following the subclasses are described from an empirical point of view, according to the review given by Urry and Padovani (1995).

The radio to optical flux ratio  $F_R/F_O$  of AGN show a bimodal distribution which divides them into radio-loud and radio-quiet AGN, depending whether  $F_R/F_O$  is above or below ten respectively (corresponding to  $\alpha_{RO} \approx 0.20$ , see Chapter 7). The ratio of radio-loud to radio-quiet AGN is roughly 10% to 15%, although it increases with increasing optical or X-ray luminosity. Table 2.1 gives an overview of the AGN zoo, arranged according to their spectral properties in the optical and ultra-violet (horizontal) and their radio luminosity (vertical). Within the different groups, different types of AGN are listed by increasing luminosity.

Type 1 AGN show bright continua and broad emission lines which are related to hot, high velocity gas, presumably located close to the central black hole (BH). On the low luminosity end of the radio-quiet AGN are the Seyfert 1 galaxies. The high luminosity end build the radio-quiet quasars (QSO). The radio-loud type 1 AGN at low luminosities are called broad-line radio galaxies (BLRG). At higher luminosities there are the radio quasars. Depending on the spectral slope of their photon spectrum  $\alpha_R$  at a few GHz, they are divided into steep spectrum radio quasars (SSRQ,  $\alpha_R > 0.5$ ) and the flat spectrum radio quasars (FSQR,  $\alpha_R < 0.5$ ).

Type 2 AGN show only weak continuum emission and narrow emission lines, leading to the conclusion that either there is no high velocity gas close to the central region or the central region is obscured by an optically thick wall. In the framework of the unified model, the latter conclusion is widely accepted (see next section). At low luminosities the radio-quiet AGN are called Seyfert 2 and narrow emission line X-ray galaxies (NELG). The Seyfert

galaxies don't show a clear bimodal distribution but a sequence including intermediate objects, classified as Seyfert 1.2, 1.5, 1.8 and 1.9 on the basis of the appearance of the Balmer lines as introduced by Osterbrock (1977). The high luminosity end is not clearly identified. Likely candidates are the IR-luminous IRAS<sup>1</sup> AGN (Sanders et al., 1988). Radio-loud type 2 AGN are often referred to as narrow-line radio galaxies (NLRG). They include two distinct morphological types. The less luminous Fanaroff-Riley type I radio galaxies (FR I) and the high-luminosity Fanaroff-Riley type II radio galaxies (FR II), which show higher collimated jets ending in bright radio lobes with prominent hot spots (Fanaroff and Riley, 1974). While the narrow emission lines in FR I are very weak, FR II can show weak as well as strong emission lines (e.g. Laing et al., 1994).

	type 2 (narrow-line)	type 1 (broad-line)	type 0 (unusual)
radio-quiet ( $\sim 90\%$ )	Seyfert 2 NELG IR quasar?	Seyfert 1  QSO	BAL QSO?
radio-loud ( $\sim 10\%$ )	FR I FR II	BLRG SSRQ FSRQ	blazars: BL Lac objects (FSRQ)

Table 2.1: AGN taxonomy, taken from Urry and Padovani (1995)

There is a small percentage of AGN which shows very unusual spectral characteristics, here called type 0. Roughly 10% of the radio-quiet AGN show very broad absorption features in their optical and UV spectra, therefore called broad absorption line (BAL) quasars. In Table 2.1 the BAL QSO is denoted with a question mark. As described in the next section, the spectral classification is related to the orientation of the symmetry axis of the AGN with respect to the observer's line of sight. In that context type 0 refers to small angles, while for the BAL QSO the reason of the absorption feature is unknown and could be either related to polar outflows (small angles) or to edge-on discs with winds.

The radio-loud type 0 AGN are summarised in the blazar class, which consists of BL Lacertae (BL Lac) objects and FSRQs. BL Lacs lack strong emission or absorption features. Although FSRQ are listed also as type 1

<sup>1</sup>The Infrared Astronomy Satellite (IRAS) carried out an all-sky survey in 1983 at 12, 25, 60 and 100 microns.

because of their strong line emission, their continuum emission resembles strongly that of BL Lacs (apart from the "big blue bump" in a few cases). Beside the FSRQ there are also quasars referred to as optically violently variable (OVV) quasars, highly polarised quasars (HPQ) or core-dominated quasars (CDQ). The names reflect different empirical definitions, but show common features like very rapid variability, high and variable polarisation and superluminal motion of compact radio cores; therefore they are here simply referred to as FSRQ.

## 2.2 The unified model

### 2.2.1 The AGN paradigm

Although the objects defined as AGN show very different spectral behaviour, they all are believed to have a common origin. Figure 2.1 shows a schematic diagram of the current AGN paradigm, divided into radio-loud (upper left) and radio-quiet (lower right) AGN. The central engine is a supermassive black hole (SMBH) with  $10^7 M_{\odot}$  to  $10^9 M_{\odot}$  surrounded by a luminous accretion disc. The gravitational potential energy of the SMBH is the ultimate source of the AGN luminosity.

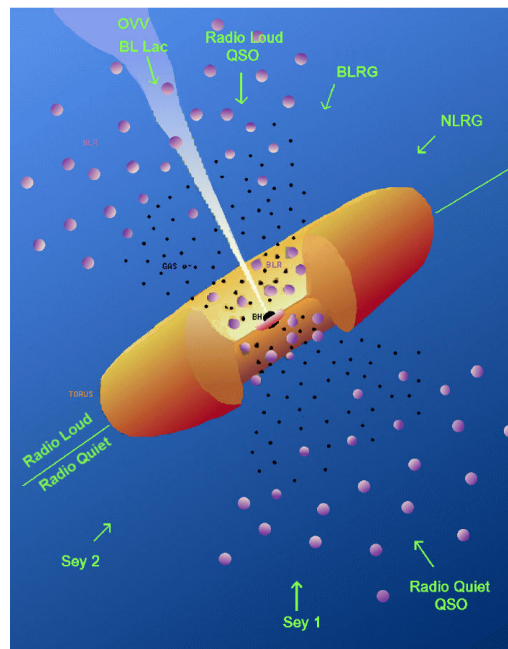


Figure 2.1: The unified AGN model. The upper left part shows the radio-loud, the lower right part the radio-quiet AGN (www-07).

component	size [cm]
SMBH ( $10^8 M_\odot$ )	$\sim 3 \times 10^{13}$
accretion disc	$\sim 1 - 30 \times 10^{14}$
broad-line region	$\sim 2 - 20 \times 10^{16}$
dusty torus (inner radius)	$\sim 10^{17}$
narrow-line region	extending from $10^{18}$ to $10^{19}$
radio jets	up to $10^{24}$

Table 2.2: The sizes of the different AGN components (Urry and Padovani, 1995). For the SMBH and the accretion disc the radii are given. The numbers for the broad- and narrow-line region reflects the distance from the SMBH. The size of the dusty torus is given for the inner radius. For the radio jet the length is given, which can be a factor of ten larger than the largest galaxies.

Strong emission lines are produced in clouds of high velocity gas, located close to the SMBH, the so-called broad-line clouds or broad-line regions (BLR). The BLR is obscured along some lines of sight by a torus (or warped disc) of gas and dust, which is located well outside the accretion disc and the BLR. At larger distance from the SMBH, clouds of lower velocity produce narrow emission lines. Bipolar outflows of highly relativistic particles generate collimated radio jets, extending from the vicinity of the SMBH to Mpc scale. Table 2.2 gives the approximate sizes of the different components.

The paradigm shows that an AGN is far away from being spherically symmetric. In good approximation, a symmetry axis can be defined perpendicular to the accretion disc. If the angle between this axis and the line of sight is small, the nucleus itself is visible together with the accretion disc and the BLRs. At large angles this part is obscured by dust. The orientation can therefore account for many spectral differences among AGN. The radio-loud-radio-quiet dichotomy cannot be explained by orientation effects and is closely related to the formation of a large scale radio jet.

In case of radio-quiet AGN, no jets (or only weak ones) have been formed. The Seyfert 1 galaxies and QSOs show nearly identical spectral behaviour and differ mostly in luminosity. The more luminous QSOs are located at larger distances, which makes (together with their outshining nucleus) the detection of a host galaxy difficult. As they all show broad emission lines and luminous UV to soft X-ray spectra (caused by the accretion disc), they are observed under small and moderate angles. The Seyfert 2 galaxies lack of broad-line features, and are therefore thought to be seen edge on. Intermediate Seyfert galaxies can be interpreted in that context as seen under angles where different contributions change their dominance.

Radio galaxies show large scale radio jets, visible under larger angles, where the BLRs are obscured. Blazars can be interpreted as radio galaxies seen under a small angle with respect to the line of sight. As the emission from the jet is highly Doppler boosted in forward direction, the apparent luminosities are the highest among all AGN. Hereby the apparent variability time scale is reduced by the Lorentz factor of the bulk velocity (see also Section 2.3.1). The unification of the various subclasses of radio-loud AGN is discussed in more detail in the next section.

### 2.2.2 Unified scheme for radio-loud AGN

The dichotomy in FR I and FR II cannot be explained by orientation effects but by physical differences, which are strongly related to the formation of the jet, the relativistic hydrodynamics in the jet itself and the connection to the host galaxy. This also accounts for the differences between FSRQ and BL Lac objects. It is widely accepted that the less luminous FR I build the parent population of BL Lacs (Browne, 1983; Padovani, 1992) and the more luminous FR II are the parent population of FSRQs (Barthel, 1989). In that context SSRQs are connected to luminous radio galaxies and FSRQs by intermediate viewing angles (Browne, 1989).

Several observations support this hypothesis: (i) the host galaxies of blazars are luminous ellipticals (if resolved) like radio galaxies, where the mean luminosity for BL Lacs and FR I, as well as FSRQs and FR II are the same (e.g. McLure et al., 1999; Urry et al., 2000; Dunlop et al., 2003); (ii) the luminosity functions of the beamed object classes fit the expectation derived from the luminosity function of the anticipated parent population, taking into account the beaming effect and the consequential lower number counts (Urry and Padovani, 1995, and references therein); (iii) both the quasars and the BL Lacs show similar environments with respect to their assumed parent population of radio galaxies (Urry and Padovani, 1995, and references therein); (iv) the cosmic evolution of radio galaxies, SSRQs and FSRQs can be described in each case by an increasing luminosity with increasing redshift, roughly as  $(z + 1)^3$  out to  $z \sim 2$ , followed by a comparable decline at higher redshifts (Dunlop and Peacock, 1990). For the BL Lac-FR I connection, the situation is more complicated. While a subclass of BL Lacs, the so-called high frequency peaked BL Lacs shows evidence for a negative evolution<sup>2</sup> like FR Is on a  $2\sigma$ -level, the subclass of low frequency peaked BL Lacs shows a positive evolution, similar to quasars (Beckmann et al., 2003; Rector and

---

<sup>2</sup>Negative evolution means that these objects were less numerous or less luminous in the past.

Stoche, 2001).

Other observational results are still not conclusive. As regards the luminosities of the narrow-line emissions, some discrepancies are found. While FRI and BL Lacs show very weak emission lines, quasars have strong emission lines and FR II can show both (Laing et al., 1994). In case of the extended radio emission, the situation is the opposite. While quasars exhibit extended radio morphologies typical of FR II radio galaxies, BL Lacs can have extended radio emission typical of both FRI and FR II radio galaxies (e.g. Murphy et al., 1993; Fernini et al., 1997; Rector and Stoche, 2001). Although it seems to be evident that blazars are beamed radio galaxies, the simple equalisation of quasars with FR II and BL Lacs with FRI radio galaxies appears to be oversimplified.

### 2.2.3 AGN jets

Most radio jets appear quite linear, but also curved non-linear jets and non-radial motions are observed (e.g. Kellermann et al., 2007). The scales ranging from not much larger than the event horizon of the SMBH<sup>3</sup> (Biretta et al., 2002) up to megaparsecs. One of the closest radio galaxies is M 87 at a distance of 16 Mpc. The linear scale of 1 mas = 0.08 pc is sufficient to resolve the M 87 jet transverse to its extent. The similar morphology at radio, optical and X-rays suggests a common synchrotron radiation mechanism. For the higher energies the radiative cooling length of the electrons is much smaller than the distance to the nucleus, indicating in situ acceleration of the particles (Biretta et al., 1991; Harris and Krawczynski, 2006), occurring at traveling and stationary shocks in the jet.

The recent discovery of VHE gamma-ray emission from M 87 (Beilicke et al., 2004) strongly supports the FRI - BL Lac connection, as almost all other extragalactic objects detected at VHE gamma-rays belong to the class of BL Lac objects. The claim of variability of VHE gamma-rays on a daily time scale from M 87 (Aharonian et al., 2006g) leads to strong constraints on the size of the emission region, raising the question where the VHE gamma-rays are produced. The spatial resolution of current gamma-ray telescopes is not sufficient to rule out any part of the jet. Aharonian et al. (2006g) argued, that the gamma-rays could only come from the nucleus itself (or the close vicinity) because of the required compactness of the emission region. This conclusion is supported by the fact that the variability time scale at VHEs is ten times shorter than observed at any other wavelengths. Cheung et al. (2007) reported superluminal radio features from the HST-1 knot at

---

<sup>3</sup>The Schwarzschild radius of a BH is  $r_s \approx 10^{-4} M_{\text{BH}}/10^9 M_{\odot} \text{ pc}$

a distance of  $\sim 120$  pc from the nucleus. Together with the coincidence of the peak in the VHE gamma-ray and radio-to-X-ray activity in HST-1 in 2005, HST-1 is favored by them as the site of VHE gamma emission. This hypothesis is supported by the problem that the nearest environment of the SMBH is expected to be opaque to TeV photons due to photon-photon interaction on ambient photon fields.

Most compact radio sources are variable on time scales typically of months to years (e.g. Kovalev et al., 2002). Also shorter time scales are observed, the shortest ones at VHE gamma-rays, revealing flux doubling times down to a few minutes in flares of the BL Lac objects Mrk 501 (Albert et al., 2007g) and PKS 2155-304 (Aharonian et al., 2007d).

## 2.3 Blazars

In the following section the main properties and emission models of blazars are described. First the effect of relativistic beaming is briefly discussed. In Section 2.3.2 a classification of blazars is given, based on their spectral energy distribution, and a possible correlation of these subclasses is discussed. In Section 2.3.3 the most important emission models are presented, divided into the nature of the accelerated particles (electrons vs. protons and ions).

### 2.3.1 Relativistic beaming

Based on optical observations of the jets in M87 and quasars, such as 3C 273, Shklovskii (1964) argued that the appearing anisotropy is due to differential Doppler boosting. Radio observations during the past decades showed superluminal motion of compact radio cores in the jets of radio galaxies and blazars (e.g. Kellermann et al., 2007), which can be understood by bulk relativistic motion along the jet (e.g. Blandford and Königl, 1979).

The kinematic Doppler factor of a moving source is defined as:

$$\delta \equiv [\gamma (1 - \beta \cos \theta)]^{-1}, \quad (2.1)$$

where  $\beta$  is the bulk velocity in units of the speed of light,  $\gamma = (1 - \beta^2)^{-1/2}$  the corresponding Lorentz factor and  $\theta$  the angle between the velocity vector and the line of sight. Depending on  $\theta$ , the Doppler factor varies from  $\delta(90^\circ) = \gamma^{-1}$  to  $\delta(0^\circ) = (1 + \beta)\gamma \approx 2\gamma$  (see Fig. 2.2). For large angles a deamplification takes place.

The observed transverse velocity of an emitting blob,  $v_t = \beta_t c$ , is related to its true velocity  $v = \beta c$  and the angle  $\theta$  by

$$\beta_t = \frac{\beta \sin \theta}{1 - \cos \theta}. \quad (2.2)$$

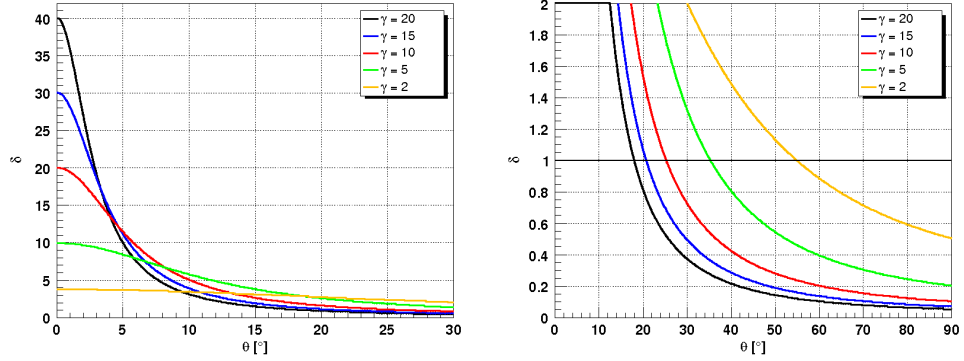


Figure 2.2: Doppler factor  $\delta$  vs. the viewing angle  $\theta$  for different Lorentz factors  $\gamma$ .

The function is plotted in Figure 2.3. The maximum value of the apparent velocity  $\beta_{t,\max} = \sqrt{\gamma^2 - 1}$  occurs for  $\cos\theta = \beta$  (corresponding to  $\sin\theta = \gamma^{-1}$ )<sup>4</sup>, resulting in a Doppler factor of  $\delta = \gamma$ . The Lorentz factor for a measured apparent velocity follows as  $\gamma \geq \sqrt{\beta_t^2 + 1}$ .

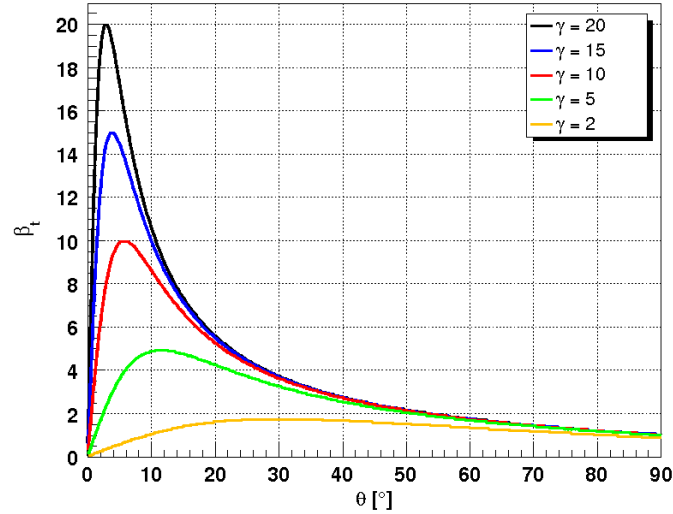


Figure 2.3: The apparent (or transversal) velocity  $\beta_t$  vs. the viewing angle  $\theta$  for different Lorentz factors  $\gamma$ .

The apparent luminosity (observer's frame)  $L_a$  is Doppler boosted and can be related to the luminosity  $L_0$  in the AGN frame by

$$L_a = \delta^n L_0 \quad (2.3)$$

<sup>4</sup>For small angles one gets  $\sin\theta \approx \theta = 1/\gamma$

where  $n$  depends on the geometry of the emission region as well as the spectral index. Typical values are between 2 and 3. With a moderate Lorentz factor  $\gamma \approx 10$  and  $n = 3$ , the Doppler boosting can reach values up to  $\sim 10^4$  for small viewing angles.

As another effect, a time interval  $t_{obs}$  measured by an observer appears shorter:

$$t_{obs} = \delta^{-1} t_0; \quad (2.4)$$

where  $t_0$  is the time interval in the rest frame of the source. The shortest observed variability time scale gives strong constraints on the size of the emission region by the argument of causal connection. Taking into account the Doppler effect one gets the size of the emission region, assuming a sphere with radius  $r$ , as

$$r \leq c \cdot t_0 = c \cdot \delta t_{obs}. \quad (2.5)$$

The apparent velocities measured in quasars reach values up to  $\sim 30$ , leading to a theoretical bound of  $\gamma_{max} \approx 32$  and  $L_{0,max} \approx 10^{26} \text{ W Hz}^{-1}$  (Cohen et al., 2007). BL Lacs show lower values in average. For many blazars also  $\beta_t < 3$  and even subluminal motion is observed. Cohen et al. (2007) argued that the pattern Lorentz factor  $\gamma_p$  has to be much less than the beam Lorentz factor  $\gamma_b$  for these objects, taking into account other observational evidences for a highly relativistic beam in the most of them.

### 2.3.2 Spectral energy distribution

As mentioned at the beginning of this chapter, blazars show broad-band non-thermal emission from the radio band up to VHE gamma-rays. The spectral energy distribution (SED), plotted as  $\nu F_\nu$  vs.  $\nu$  (or the apparent luminosity  $\nu L_\nu$  vs.  $\nu$ ), shows at least two pronounced peaks. The first peak occurs between IR and X-rays and is commonly believed to be caused by synchrotron radiation from relativistic electrons, while the second one is at gamma-rays. In this section a classification of blazars based on their SED is shown and possible correlations are discussed.

#### Classification

Due to the lack of strong emission lines, BL Lacs were mainly discovered in radio and X-rays surveys, leading to the historical separation into RBLs (radio selected BL Lacs) and XBLs (X-ray selected BL Lacs). In the context of the unification of radio galaxies and BL Lac objects, where the latter objects are strongly Doppler boosted, the less luminous XBLs were interpreted as BL Lacs with larger viewing angles than RBLs (Stocke et al., 1985;

Maraschi et al., 1986). This hypothesis was also supported by the stronger polarisation and violent variability observed in the optical band for RBLs. As smaller viewing angles lead to smaller number counts, they concluded, that RBLs will only account for  $\sim 10\%$  of the BL Lac population and X-ray surveys are therefore more representative.

A different scenario proposed by Giommi and Padovani (1994), and now widely accepted, explains the differences with the intrinsic shape of their SEDs. According to this BL Lacs can be separated by their cut-off energies in their synchrotron emission (or peaks in a  $\nu F_\nu$ -plot) into low frequency peaked BL Lacs (LBLs), providing peaks in the IR to optical range, and high frequency peaked BL Lacs (HBLs) with peaks in the UV to X-ray regime (Padovani and Giommi, 1995)<sup>5</sup>. As a dividing line  $F_X/F_R = 10^{-11}$  (with  $F_X$  being the energy density in  $\text{erg cm}^{-2} \text{s}^{-1}$  from 0.3 to 3.5 keV and  $F_R$  the monochromatic radio flux at 5 GHz in Jansky) was originally proposed. Based on a spectral study of X-ray spectra of a large sample of 85 BL Lac objects, observed with ROSAT (White et al., 1994), Padovani and Giommi (1996) changed the value to  $F_X/F_R = 10^{-11.5}$  (corresponding to a broad-band spectral index  $\alpha_{RX} = 0.78$ ).

It was shown by Laurent-Muehleisen et al. (1999) from a large sample of BL Lac objects from the ROSAT All-Sky Survey-Green Bank (RGB) that the apparent dichotomy of BL Lacs into LBL and HBL arose primarily from observational selection effects, rather than reflecting the underlying population. The distribution of  $\alpha_{RX}$  which they derived from their sample peaks around  $\alpha_{RX} = 0.75$ , the previously dividing line of LBL and HBL. They conclude from the existence of intermediate BL Lac objects (IBL) that the synchrotron peak energies are smoothly distributed from IR to X-rays for the complete BL Lac population. So far three objects, Mrk 501, 1ES 2344+514 and 1ES 1426+428, are found with peak energies at very hard X-rays ( $\sim 100$  keV, Costamante et al., 2001), which are also among the small group of blazars detected at VHE gamma-rays.

The FSRQ can reach higher luminosities than BL Lacs in general. While for a long time only high luminosity quasars with low peak energies, comparable or even lower than for LBLs, were known, more sensitive surveys like the Deep X-ray Radio Blazar Survey (DXRBS) vastly extended the coverage of the low luminosity end of the luminosity function, revealing a large amount ( $\approx 25\%$ ) of FSRQs with HBL-like broad-band properties, coined high frequency peaked FSRQs (HFSRQ, Perlman et al., 1998).

---

<sup>5</sup>Originally the names "low" and "high energy cut-off BL Lacs" were proposed, but "low" and "high frequency peaked BL Lacs" is more common due to the presentation of the spectral properties in a  $\nu F_\nu$ -plot.

### The blazar sequence

It was proposed by Fossati et al. (1998) from the study of the broad-band spectrum of 126 blazars, taken from three complete samples (Slew survey, 1-Jy sample of BL Lacs and 2-Jy sample of FSRQ), that the blazars follow a sequence, in which a single parameter, related to the luminosity, governs the physical properties and radiation mechanisms in the relativistic jets. They computed average SEDs of the sample according to the radio luminosity. The main findings are: (i) the first peak in the SED occurs at different frequencies for different luminosity classes, whereas the most luminous sources peak at the lowest frequencies; (ii) the peak frequency of the high energy component correlates with the frequency of the first peak; (iii) the luminosity ratio between the high and low energy peak increases with luminosity.

These phenomenological results were interpreted by Ghisellini et al. (1998) in the framework of leptonic emission models (see also next section). They concluded from their spectral modelling that with increasing luminosity along the sequence, the contribution from external photon fields increase from almost negligible for HBLs up to the dominant part for FSRQs. The decreasing synchrotron peak frequencies can be explained in this model with stronger cooling of the electrons due to the increasing external field. This also results in the observed dominance of the high energy part in the SED of FSRQs. The model is supported by the fact, that quasars show much stronger emission lines than BL Lacs, indicating more circum nuclear material. The results were later extended, finding an important ingredient for the shaping of the spectra of the lowest power objects, namely the role of a finite timescale for the injection of relativistic particles (Ghisellini et al., 2002). The sequence is also in good agreement with the hard X-ray properties investigated for a large sample of blazars by Donato et al. (2001).

An evolutionary sequence of blazars has been proposed by D’Elia and Cavaliere (2001) and Cavaliere and D’Elia (2002) assuming decreasing accretion rates from quasars to BL Lacs. In that picture, the power emitted from FSRQs is dominated by disc components (thermal and electrodynamic jet-like components), while for BL Lacs the radiation is highly non-thermal and the power is partly provided by the rotational energy of the central Kerr black hole. In that context the two populations can be linked if the accretion rate drops in time and the new born BL Lacs are fed by dying FSRQs. This would give a natural explanation for the different observed evolutions, in particular the evidence for negative evolution of HBLs (Beckmann et al., 2003).

The idea of an evolutionary sequence in the framework of a leptonic emission model was further investigated by Böttcher and Dermer (2002). The

evolutionary transition was parametrised by a gradual depletion of the circum nuclear environment (and therefore decline of the accretion rate) and a reprocessing efficiency for the external Compton component (optical depth for the circum nuclear material), assumed to be proportional to the accretion rate. The general features of the blazar sequence could be reproduced in good agreement with Ghisellini et al. (1998).

It was argued by several authors in the recent years that the supposed blazar sequence is not representative for the complete population, rather than a selection effect. Although the samples used in Fossati et al. (1998) were complete above their respective radio and X-ray flux limits, they included very different radio fluxes and not all radio luminosities represented in one survey were above the flux limit of the other sample. Based on new blazar identifications in the Deep X-ray Radio Blazar Survey (DXRBS) Perlman et al. (1998) concluded that all previous samples of blazars, even when taken together, did not representatively survey the blazar population. In particular, the luminosity function of FSRQs was extended to lower luminosities and HBL-like FSRQs (HFSRQ) have been discovered (see also Padovani et al., 2002, 2003).

It was shown by Giommi et al. (2002) that BL Lacs, discovered in the deeper and more homogeneous DXRBS and Sedentary survey, build a population of low radio luminosity and low peak frequency sources, not included in Fossati et al. (1998). The existence of low luminosity blazars (BL Lacs and quasars) with low peak frequencies was also shown by other authors (e.g. Caccianiga and Marchã, 2004; Antón and Browne, 2005). Summarising the observational facts the blazar sequence can, at least in its simplest approach, be ruled out. However, there is still a lack of high luminosity blazars with extreme peak frequencies. If not intrinsically, this effect could arise from the missing determination of the redshift for a large sample of BL Lac objects due to their featureless spectrum. Also the high ratios of the high- to low-energy component seen in many FSRQs, detected by EGRET, is not seen in HBLs (see also Chapter 7). This could still reflect a selection effect, as most of the EGRET blazars were detected in a state of high activity. An increased source statistic at these energies as well as a better coverage of quiescent states will be provided by the GLAST satellite within the next years.

### 2.3.3 Emission models

In the following section the most common emission models, which can account for the observed broad-band spectrum of blazars, are briefly discussed. The general scenario assumes a very compact spherical emission region with a homogeneous magnetic field that moves relativistically along the jet con-

taining relativistic charged particles with a power law energy spectrum. The separation into leptonic and hadronic models here is related to the nature of particles that are responsible for the high energy radiation, depending on whether they are electrons (and positrons, leptonic) or protons (and ions, hadronic). A general problem in modelling blazar SEDs is the lack of high quality multiwavelength data and the sparse coverage of the entire energy range, which often leads to an under-determination of the model parameters.

### Leptonic models

The simplest model is a single zone synchrotron self Compton model (SSC, Ginzburg and Syrovatskii, 1965; Rees, 1967; Maraschi et al., 1992), which naturally produces a two-humped SED. The first peak is related to synchrotron radiation of relativistic electrons, while the second peak is due to inverse Compton scattering of these synchrotron photons. In external Compton (EC) models the seed photons can be dominated by ambient thermal photon fields, which could enter directly into the emission region (Dermer et al., 1992; Dermer and Schlickeiser, 1993) or by scattering on material surrounding the jet (Sikora et al., 1994, see also Figure 2.4).

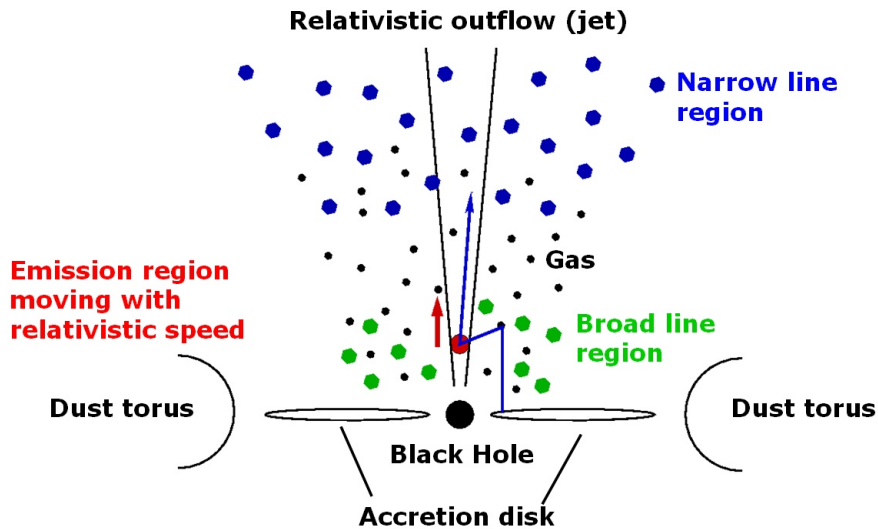


Figure 2.4: Schematic side-view of the inner part of an AGN according to the AGN paradigm. The sizes of the different components are not to scale. The emission region is marked red and moves relativistically along the jet. Ambient thermal photons could enter directly into the jet or can be reprocessed by clouds of gas.

Leptonic models are quite successful in describing the observed SEDs, although there are differences inside the blazar class. While FSRQs gener-

ally require a dominant EC contribution to produce the observed gamma-ray emission (e.g. Sambruna et al., 1997; Hartman et al., 2001), HBLs can be successfully fitted with pure SSC models (e.g. Mastichiadis and Kirk, 1997; Petry et al., 2000).

A strong correlation between the synchrotron and the inverse Compton emission is expected from single zone SSC models. While such correlations were observed, like the X-ray-TeV correlation recently reported by Fossati et al. (2007) from observations of the HBL Mrk 421, a so-called orphan flare (TeV flare with no counterpart at X-rays) has been observed from the HBL 1ES 1959+650 (Krawczynski et al., 2004). Also for Mrk 421 a time lag of days between a high state at TeV energies and X-rays has been reported by Błażejowski et al. (2005). In the context of SSC models an inhomogeneous jet model was proposed by Kusunose and Takahara (2006); in this model X-ray photons, produced in a primary flare, propagate in various directions in the comoving frame of the jet until they reach a dense region, where they can be up-scattered to TeV photons by relativistic electrons, which would be seen as an orphan flare.

Recently distant HBLs with unexpected hard VHE gamma-ray spectra were found (e.g. Aharonian et al., 2007c,b), yielding intrinsic peak energies above several TeV after correction of the measured spectra for the absorption in the MRF. This raises a problem for leptonic models due to the low interaction cross-section in the Klein-Nishina regime. As shown in Section 1.3.3, for  $h\nu \gg mc^2/\gamma$ , the cross section for inverse Compton scattering is reduced by one order of magnitude. This is the case, when photons from the UV to the X-ray band are scattered by electrons with Lorentz factors in the order of  $\sim 10^6$ .

### Hadronic models

It was shown by Mannheim and Biermann (1992) that the high energy emission of blazars (in particular the FSRQ 3C 279) can also be explained by a population of ultra-relativistic protons with Lorentz factors of  $\gamma \sim 10^{10}$ ; these protons produce photons with energies from keV to TeV via pion and pair production and subsequent synchrotron cascade reprocessing (proton initiated cascades, PIC, Mannheim, 1993). The low energy part is hereby synchrotron radiation from co-accelerated electrons like in leptonic models, which also serve as the target radiation field for proton-photon interaction (see also Fig. 2.5). The hadronic model requires in general higher magnetic fields to keep the Larmor radius of the protons inside the compact emission region, leading to rapid radiative cooling of the electrons, and hence negligible contributions from inverse Compton scattering at higher energies. The model

also provides a natural source of ultra high energy cosmic rays, as ultra relativistic neutrons, produced in proton-photon interaction, can escape from the emission region and will decay each into an electron, proton and neutrino. The recent reported correlation between the highest energy cosmic rays and nearby AGN (Abraham et al., 2007) support the picture of AGN as effective proton (and nuclei) accelerators.

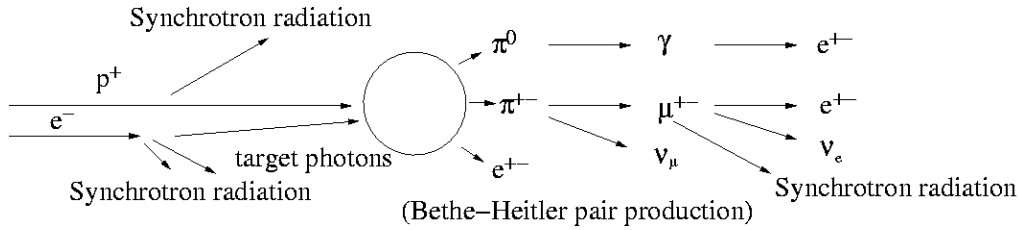


Figure 2.5: The proton blazar: Accelerated electrons and protons produce synchrotron radiation. The electron synchrotron photons serve hereby as target radiation field for proton-photon interaction, leading to pion production and subsequent cascades. While the charged particle will contribute to the spectrum directly via synchrotron radiation, gamma-rays can make pairs in photon-photon interaction, leading to electro-magnetic subcascades.

Based on the PIC model the multiwavelength spectra of Mrk 501 and Mrk 421 were successfully modeled by Aharonian (2000) and Mücke and Protheroe (2001), the latter using a Monte Carlo code. Compared to Mannheim (1993), they concluded that the TeV radiation is completely dominated by proton synchrotron radiation (also known as synchrotron proton blazar, SPB).

Cosmic proton accelerators will produce cosmic rays, gamma-rays and neutrinos with comparable luminosities (Mannheim, 1993). Therefore the detection of neutrinos from an AGN would be the smoking gun for hadronic emission models. Beside point sources, expectations of the diffuse neutrino flux are derived from the cosmic ray spectrum as well as the diffuse extragalactic gamma-ray background (Mannheim et al., 2001; Mücke et al., 2003). Except for solar neutrinos as well as neutrinos from the supernova 1987A no cosmic neutrinos have been detected so far. Nevertheless upper limits from current neutrino telescopes like AMANDA on the diffuse flux as well as stacking analysis of different source classes, can already constrain several prevailing neutrino flux models (Becker et al., 2007). High detection probabilities are predicted for future neutrino telescopes such as ICECUBE and KM3NeT.

# Chapter 3

## The imaging air Cherenkov technique

The atmosphere is opaque for most of the electromagnetic spectrum. Indeed there is only the radio ( $\sim 30$  MHz - 30 GHz) and optical window where the light does not suffer from strong absorption. At VHE, the interaction of the photon with the molecules of the atmosphere initiates a particle cascade whose detection allows to deduce the identity as well as the energy of the primary particle. In the following section the main properties of these particle cascades are introduced. In Section 3.2 it is shown that relativistic charged particles radiate Cherenkov photons which are observable from the ground. The Cherenkov effect and its characteristics are discussed and the expected number of photons on the ground are calculated. These photons can be observed by imaging air Cherenkov telescopes whose detection principle will be explained in Section 3.3. Furthermore, a brief description of the MAGIC telescope is given in Section 3.4.

### 3.1 Air showers

Air showers are particle cascades initiated by charged particles or photons. Photons with energies above several MeV are absorbed in matter by production of electron-positron pairs. The pairs radiate bremsstrahlung in the Coulomb field of atmospheric atoms. These secondary gamma-rays will produce electron-positron pairs again. After  $N$  interactions the particle cascade consists of  $2^N$  particles. While the shower is growing, the energy per particle decreases. Below a critical energy of  $\sim 80$  MeV, ionisation losses become dominant and the shower dies out.

Much more often the primary particle will be an ionised hadron. The schematic development of a hadron induced air shower with its different components is shown in Figure 3.1. Due to the high energies ( $E > 10 \text{ GeV}$ ) the hadron will interact with single nucleons of an atmospheric atom. In multiple scattering inside the nucleus mainly pions but also strange particles (kaons, ...) or anti-nucleons are produced. Neutral pions decay into photons ( $\pi^0 \rightarrow \gamma + \gamma$ , mean lifetime  $\tau = 8.4 \times 10^{-17} \text{ s}$ ) which initiate an electromagnetic cascade. Charged pions are mainly responsible for the muon and neutrino component of the shower ( $\pi^+ \rightarrow \mu^+ + \nu_\mu$ ,  $\pi^- \rightarrow \mu^- + \bar{\nu}_\mu$ , mean lifetime  $\tau = 2.6 \times 10^{-8} \text{ s}$ ). There is also an energy dependent contribution to these components from leptonic decays of kaons. Around 8% of the muons with an energy of 100 GeV are produced in K-decay. This number increases for higher muon energies up to an asymptotic value of 27% (Gaisser, 1990). A part of the muons will further decay before they can reach the ground ( $\mu^+ \rightarrow e^+ + \nu_e + \bar{\nu}_\mu$ ,  $\mu^- \rightarrow e^- + \bar{\nu}_e + \nu_\mu$ , mean lifetime  $\tau = 2.2 \times 10^{-6} \text{ s}$ ) and contribute to the neutrino and the electromagnetic component of the shower.

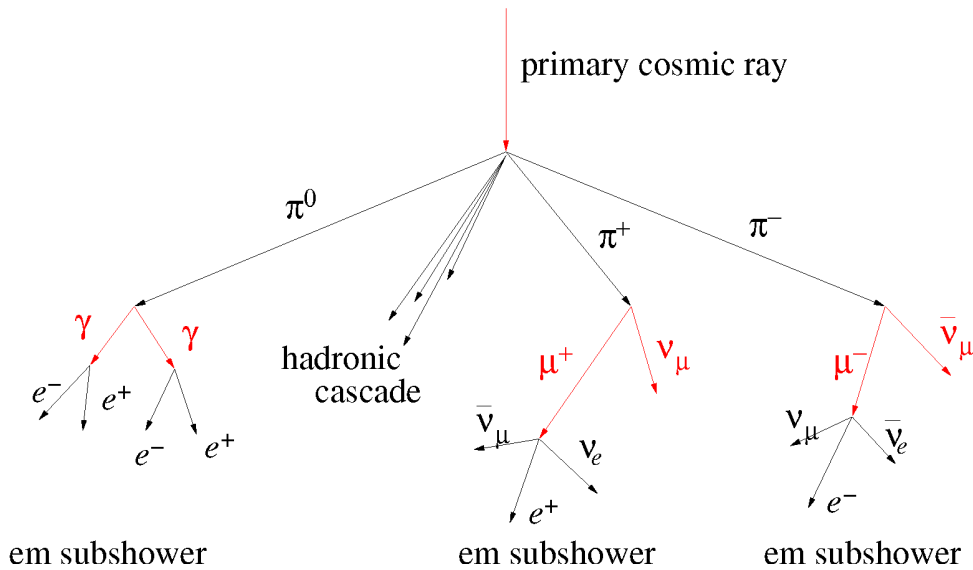


Figure 3.1: Schematic view of the development of a hadron initiated air shower.

Figure 3.2 shows two different air showers simulated with CORSIKA (COsmic Ray SIMulations for KAscade, Heck et al., 1998) using as a primary particle a 100 GeV photon and a 100 GeV proton, respectively. The width of the electromagnetic shower is dominated by multiple scattering of electrons and positrons. In case of the hadron initiated air shower, large transversal impacts due to hadronic interactions result in a wider lateral distribution.

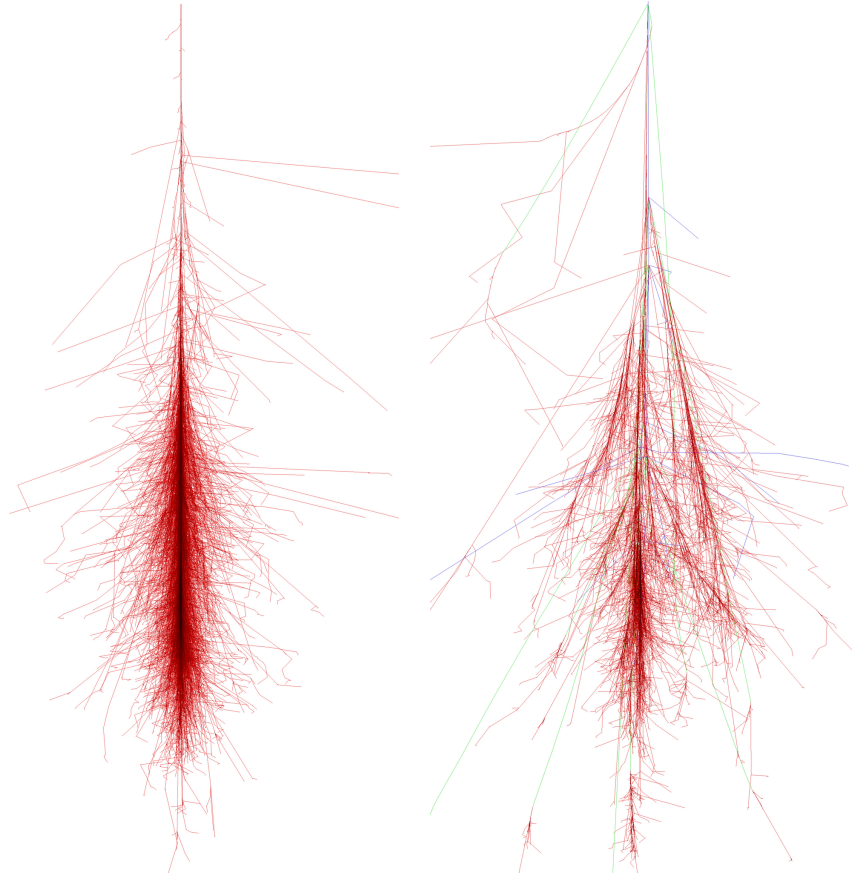


Figure 3.2: Side view of simulated air showers with different primary particles (vertical incidence). Left panel: Photon initiated air shower ( $E_p = 100$  GeV). Right panel: Hadron initiated air shower (proton,  $E_p = 100$  GeV). The red lines mark the tracks of electrons, positrons and gamma-rays, the green lines the tracks of muons and the blue lines the tracks of hadrons (www-08).

Before the longitudinal distributions of the different air showers are investigated, a new quantity is introduced: the column density. It gives the altitude in the atmosphere and is defined as

$$X := \int_h^{\infty} \rho(h) dh, \quad (3.1)$$

where  $\rho$  is the density and  $h$  the altitude above sea level. The radiation length for photons and electrons in air is  $X_0 = 36.66$  g/cm<sup>2</sup>; hence it follows for the atmosphere a depth of  $\sim 27$  radiation lengths in case of vertical inclination (e.g. Grupen, 2000). As the radiation length of hadrons in air is about three times larger, a hadron initiated shower will develop deeper in the atmosphere.

Figure 3.3 shows the height of the shower maximum in units of the column density over the energy of the primary particle for photons and protons as a result of Monte Carlo simulations (Rahman et al., 2001). The height of the shower maximum depends logarithmically on the energy of the primary particle. For a 200 GeV photon this height is  $280 \text{ g cm}^{-2}$  corresponding to  $\sim 10 \text{ km}$  above sea level.

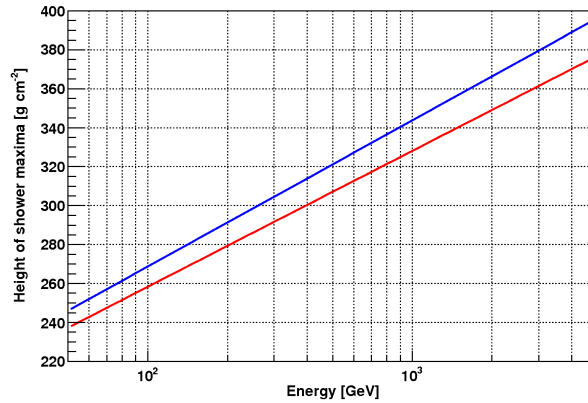


Figure 3.3: Height of shower maximum in units of the column density vs. energy of the primary particle. The blue line denotes protons and the red line gamma-rays as primary particles.

A special attention in this work is given to the muon component (see Chapter 5). Due to the high energies of the muons and the resulting time dilatation, most of the muons above  $\sim 5 \text{ GeV}$  reach the ground before they can decay. Figure 3.4 shows the muon spectrum for an altitude of 2770 m (comparable to the observation level of the MAGIC telescope) and sea level. While the integral flux from 1 GeV to 20 GeV is about 66 % at sea level compared to the mountain altitude, this ratio increases to 84 % for the flux from 15 GeV to 20 GeV. The differential energy spectrum above 20 GeV is well fitted by a power law with a spectral index of -2.71.

As the track through the atmosphere increases with increasing angle of incidence, the muon intensity shows a clear dependence on the zenith distance  $\theta$  as

$$I_{\mu}(\theta) = I_{\mu}(\theta = 0) \times \cos^n(\theta) , \quad (3.2)$$

for zenith distances below  $\sim 60^\circ$ . The exponent  $n$  lies around 2 and varies slightly with energy.

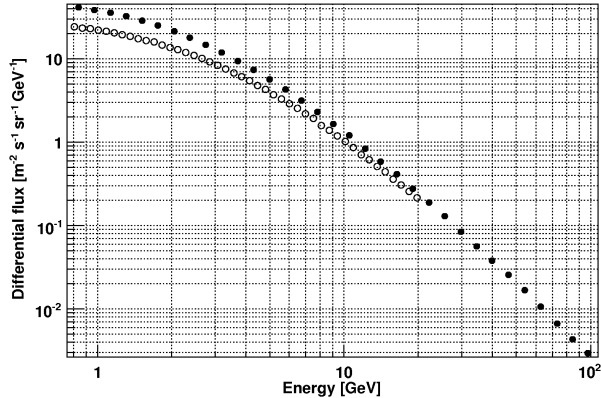


Figure 3.4: Combined spectrum of muons and anti-muons at different altitudes as measured with the BESS instrument for vertical inclination. The full symbols represent a measurement from 1999 on Mt. Norikura (2770 m a.s.l.,  $743 \text{ g cm}^{-2}$ , Sanuki et al., 2002) while the open symbols mark a measurement from 1995 in Tsukuba (30 m a.s.l.,  $1030 \text{ g cm}^{-2}$ , Motoki et al., 2003). The statistical errors are within the size of the symbols.

## 3.2 Cherenkov effect

If a charged particle travels through an electric isolator, the electron shell of the passed atoms gets polarised for a short moment. The induced time-variable dipole-field emits photons isotropically. If the velocity of the particle  $v_p$  is higher than the speed of light  $v_l = c/n$  in the medium (where  $n$  is the index of refraction), the electromagnetic waves are constructively interfered at an angle  $\Theta_C$ , called Cherenkov angle. A wavefront is formed, comparable to the shock front caused by an air plane with supersonic speed (see Fig. 3.5).

The Cherenkov radiation is completely linear polarised in the plane spanned by the line of sight and the particle track. For the discovery of the Cherenkov effect P. A. Cherenkov, I. M. Frank and I. J. Tamm got the nobel prize for physics in 1958<sup>1</sup>. The Cherenkov angle is defined as

$$\cos(\Theta_C) = \frac{v_l}{v_p} = \frac{c}{v_p n(\omega)} = \frac{1}{\beta n(\omega)}; \quad (3.3)$$

where  $c$  is the speed of light in vacuum,  $\omega$  the frequency of the Cherenkov photon,  $\beta$  the velocity in units of the vacuum speed of light and  $n(\omega)$  the frequency dependent index of refraction.

In the following the Cherenkov effect in the atmosphere is investigated. Therefore the approximation of an isothermal atmosphere is used. Also the

<sup>1</sup>The radiation was discovered by P. A. Cherenkov in 1934 and interpreted by I. M. Frank and I. J. Tamm in 1937

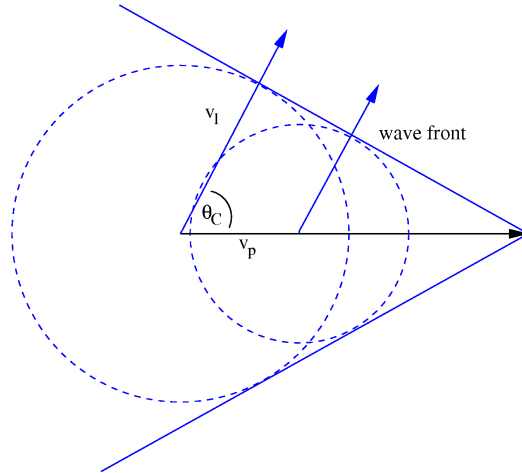


Figure 3.5: Schematic view of the Cherenkov wavefront.  $\Theta_C$  denotes the Cherenkov angle,  $v_l$  and  $v_p$  the speed of light in the medium and the speed of the particle, respectively.

frequency dependence of the index of refraction is neglected. One gets the index of refraction, depending on the altitude  $h$ , as

$$n(h) = 1 + \eta_0 \exp\left(-\frac{h}{h_0}\right) = 1 + \eta, \quad (3.4)$$

where  $h_0 = 8.4$  km is the scaling height and  $\eta_0 = 2.9 \times 10^{-4}$  the value for sea level. At high energies ( $\beta \approx 1$ ) the Cherenkov angle reaches a maximum value that depends only on the index of refraction. Figure 3.6, left panel, shows the maximum Cherenkov angle vs. altitude for the atmospheric model described above.

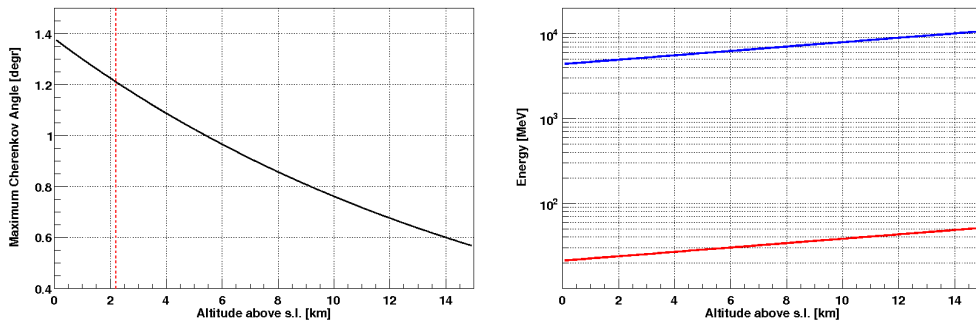


Figure 3.6: Left panel: The maximum Cherenkov angle ( $\beta = 1$ ) vs. altitude. The vertical line indicates the observation level of the MAGIC telescope. Note that the shower maximum is several km above this altitude. Right panel: Minimum energy required for the Cherenkov effect for muons (blue) and electrons (red) vs. altitude.

From the condition  $\beta n \geq 1$  one can calculate the threshold energy which is required for the emission of Cherenkov radiation:

$$\beta n = n \sqrt{1 - \left( \frac{E_0}{E_{min}} \right)^2} = 1$$

$$E_{min} = \sqrt{\frac{E_0^2}{1 - \frac{1}{n^2}}}, \quad (3.5)$$

where  $E_0$  is the energy of the particle at rest. Figure 3.6, right panel, shows the threshold energy vs. altitude for electrons ( $E_0 = 0.511$  MeV) and muons ( $E_0 = 105.66$  MeV). As the threshold energy is directly proportional to the rest mass of the relativistic particle, the threshold energy for muons is a factor 206.8 higher than for electrons.

To estimate the number of observable Cherenkov photons on the ground, first the energy loss due to Cherenkov radiation as well as the number of cherenkov photons emitted per unit path length are calculated. The energy loss per unit distance  $z$  is given by Jackson (1982) as

$$\frac{dE}{dz} = \frac{(Ze)^2}{4\pi\epsilon_0 c^2} \int_{\beta n > 1} \left( 1 - \frac{1}{\beta^2 n^2(\omega)} \right) \omega d\omega, \quad (3.6)$$

where  $Z$  is the atomic number. The  $\omega$  integration extends only over the range where  $\beta n(\omega) \geq 1$ . The integrand shows the differential energy spectrum. In the optical band, the index of refraction in the atmosphere can be considered as nearly constant. In that case the integration yields  $dE/dz \propto \omega^2$ . The Cherenkov spectrum is dominated by radiation in the UV- and blue band. Below  $\lambda \approx 180$  nm abnormal dispersion starts in the atmosphere ( $n(\omega) < 1$ ) so that no Cherenkov radiation can be produced.

In the following the column density instead of the altitude is used as introduced in the last section. Again the index of refraction is considered to be frequency independent. Furthermore  $\beta = 1$  is used as well as the parametrisation  $n = 1 + \eta$ . With  $1 - 1/n^2 \approx 2\eta$  and the differential column density  $dX = -\rho dh$  Equation 3.6 can be rewritten as:

$$\frac{dE}{dX} = \frac{dE}{dh} \frac{dh}{dX} = \frac{2\pi e^2 \eta}{\epsilon_0 \rho} \int_{\lambda_1}^{\lambda_2} \lambda^{-3} d\lambda = \frac{\pi e^2 \eta}{\epsilon_0 \rho} \left( \frac{1}{\lambda_1^2} - \frac{1}{\lambda_2^2} \right). \quad (3.7)$$

Assuming an isothermal atmosphere as described above,  $\eta$  is proportional to the atmospheric density  $\rho$ . Therefore the emitted energy per path length is constant. For the density, standard pressure at sea level ( $1.013 \times 10^5$  Pa)

and the scaling height of 8.4 km are considered. Using  $\eta_0 = 2.9 \times 10^{-4}$ ,  $\rho_0 = 1.23 \times 10^{-3} \text{ g cm}^{-3}$ ,  $\lambda_1 = 180 \text{ nm}$  and  $\lambda_2 \rightarrow \infty$  one gets

$$\frac{dE}{dX} = 4.1 \text{ keV}(\text{g/cm}^2)^{-1}$$

This is relatively low compared to the threshold energy for Cherenkov radiation as shown in Fig. 3.6 as well as compared to the energy loss due to ionisation ( $\sim 1.8 \text{ MeV}(\text{g/cm}^2)^{-1}$ ). Dividing the integrand in Equation 3.7 by  $hc/\lambda$ , the number of emitted Cherenkov photons per column density is given as

$$\frac{dN}{dX} = 4\pi\alpha \frac{\eta}{\rho} \left( \frac{1}{\lambda_1} - \frac{1}{\lambda_2} \right), \quad (3.8)$$

with  $\alpha = \frac{1}{4\pi\epsilon_0} \frac{e^2}{\hbar c}$  being the finestructure constant. Using the same numbers as for the estimation of the emitted energy one gets

$$\frac{dN}{dX} = 1.2 \times 10^3 (\text{g/cm}^2)^{-1}.$$

This corresponds to roughly 140 photons per meter at sea level and 50 photons per meter at an altitude of 10 km.

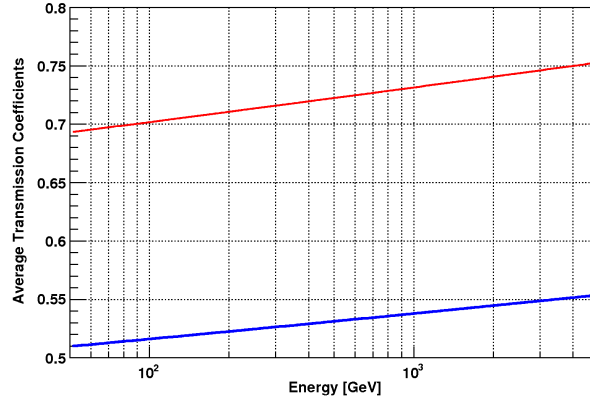


Figure 3.7: The average atmospheric transmission coefficient vs. the energy of the primary gamma-ray for an altitude of 2000 m (red line) and sea level (blue line).

For the detection of Cherenkov radiation with ground based instruments the attenuation in the atmosphere has to be taken into account. Below  $\sim 300 \text{ nm}$  the light is strongly absorbed by atmospheric ozone. Another contribution comes from Rayleigh and aerosol scattering. At higher wavelength one is limited by the bandwidth of the PMTs ( $\leq 600 \text{ nm}$ ). The measured Cherenkov spectrum coming from an air shower depends therefore on the height of its shower maximum and the observation altitude. Figure 3.7 shows

the average transmission coefficient (300 nm - 550 nm), defined as the ratio of produced Cherenkov photons and the number of photons arrived on a certain altitude, vs. the energy of the primary gamma-ray for two different observation levels. The parametrisation is taken from Rahman et al. (2001). The energy dependence of the transmission coefficient reflects the energy dependence of the height of the shower maximum. At an altitude of 2000 m, roughly the observation level of the MAGIC telescope, the transmission coefficient ranges from 0.70 to 0.75 within the observable energy range. Compared to this, an observatory at sea level would see up to 40 % less Cherenkov photons from air showers in the same energy range.

### 3.3 Imaging technique

The superposition of the emitted Cherenkov light of all particles in the shower results in a light pool on the ground (see Figure 3.8 and Figure 3.9). If a telescope is inside the light pool, an image of the shower is projected in the focal plane. Therefore the area of the light pool at the ground is roughly the effective area of the instrument. The area of the light pool depends on the angle of incidence. For a shower maximum at 10 km altitude and an opening angle of  $1^\circ$ , the area of the light pool at an observation level of 2 km ranges from  $6 \times 10^4 \text{ m}^2$  for vertical incidence to  $9.8 \times 10^5 \text{ m}^2$  for a zenith distance of  $60^\circ$ . The large effective area is one of the main advantages of

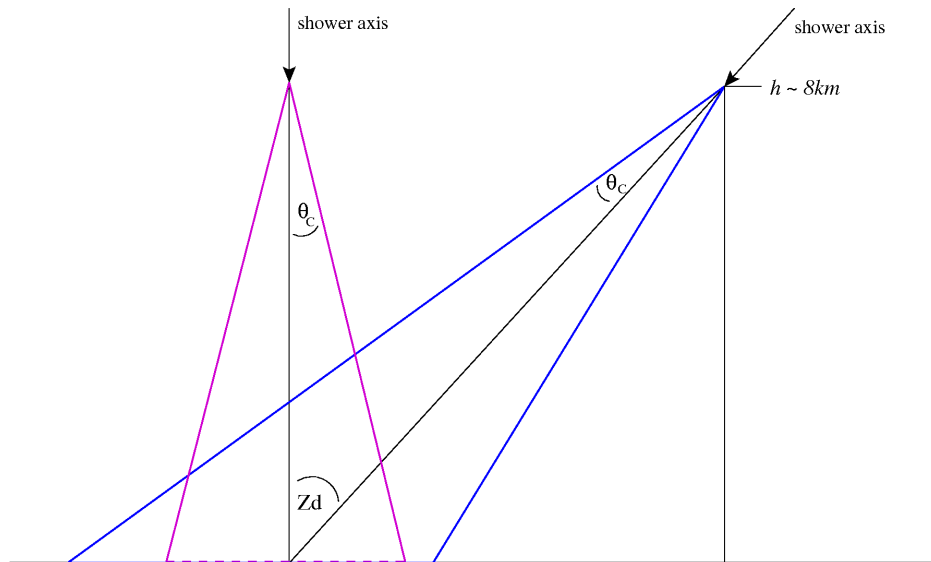


Figure 3.8: Schematic view of the Cherenkov light pool of an air shower for vertical inclination as well as a zenith distance of  $40^\circ$ .

ground based gamma-ray astronomy compared to space born experiments. As the expected photon fluxes at VHEs are quite small ( $\sim 10^{-7} \text{ m}^{-2} \text{ s}^{-1}$ ), a large collection area is needed which is not feasible for the limited size of a satellite experiment.

Since the number of emitted Cherenkov photons will be roughly the same for air showers with different incidence, the photon density of the light pool decreases with increasing zenith distance. This leads to an increasing energy threshold, because the energy of the primary gamma-photon is correlated to the number of secondary particles and therefore to the emitted Cherenkov light.

The number density of Cherenkov photons is very small ( $\sim 5 - 50/\text{m}^2$ ) which requires a large reflector as well as a high-quantum efficiency detector. The number of observed photons is completely dominated by the diffuse light of the night sky. While the night sky is a continuous light source, the time duration of the Cherenkov light flash from an air shower takes only a few nanoseconds. A fast timing with short exposure times can therefore reduce the effect of the night sky background light. In case of a parabolic reflector the time information is conserved and the shower development can be reconstructed.

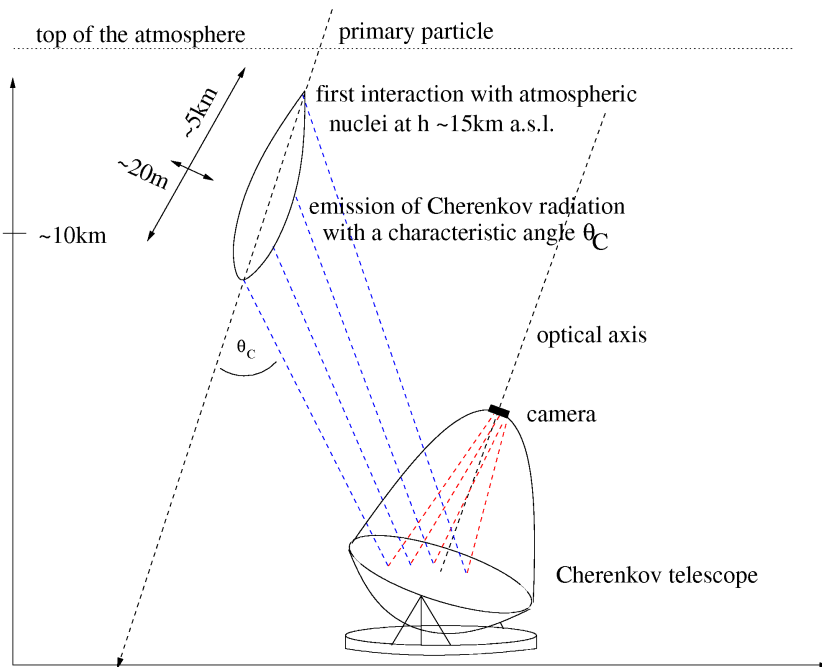


Figure 3.9: Schematic view of the principle of the imaging air Cherenkov technique with the example of a TeV gamma-ray shower. If the telescope is inside the Cherenkov light pool of the shower, a picture of the complete shower is reflected into the focal plane.

The sensitivity of the observation technique is limited by the huge amount of background generated by cosmic rays<sup>2</sup>. As shown in the first section of this chapter, gamma-ray initiated air showers have different morphologies compared to hadron initiated air showers. Based on a parametrised shower image, the identity of the primary particle (gamma-ray or non gamma-ray) can be deduced in a statistical way (see Section 4.3). Figure 3.10 shows images of simulated gamma showers with various primary energies. The shower images are clearly elongated which makes it possible to reconstruct the main axis of the shower. Using the shower axis the origin of the primary gamma-ray in the sky can be reconstructed with an uncertainty of  $\sim 0.1^\circ$ . A main

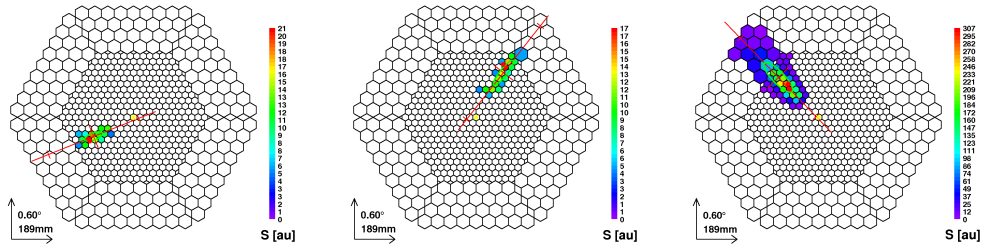


Figure 3.10: Images of simulated photon initiated air showers inside the MAGIC camera. The primary energies are 61 GeV, 187 GeV and 1.8 TeV (from left to the right). The zenith distances are between  $17^\circ$  and  $19^\circ$ . The red line indicates the reconstructed shower axis. As the simulated source position corresponds to the centre of the camera, all showers are pointing to the camera centre. The green ellipse indicates the second moments of the light distribution along and perpendicular to the axis. The colour scale gives the light content of each pixel in arbitrary units.

contribution to the background comes from the Cherenkov light of single mounes. Depending on their impact parameter, the images can look like gamma showers with primary energies mainly below  $\sim 150$  GeV (see also Chapter 5.4).

### 3.4 The MAGIC telescope

The Major Atmospheric Gamma-ray Imaging Cherenkov (MAGIC) telescope is currently the world largest IACT with a single reflector of 17 m in diameter (see Fig.3.11). It is located on the Canary Island of La Palma ( $28.8^\circ$  N,

<sup>2</sup>The ratio of gamma-rays to cosmic rays is roughly 1:1000; compare the flux of the Crab Nebula at 300 GeV ( $6.3 \times 10^{-6}$  photons  $\text{m}^{-2} \text{s}^{-1}$ ) to the flux of cosmic rays at the same energy ( $\sim 2.5 \times 10^{-3}$  photons  $\text{m}^{-2} \text{s}^{-1}$  for a solid angle of  $1.3 \times 10^{-5}$  sr corresponding to the trigger area of the MAGIC telescope).

17.8° W, 2200 m a.s.l.). In the following a brief overview of the main properties of the telescope is given.

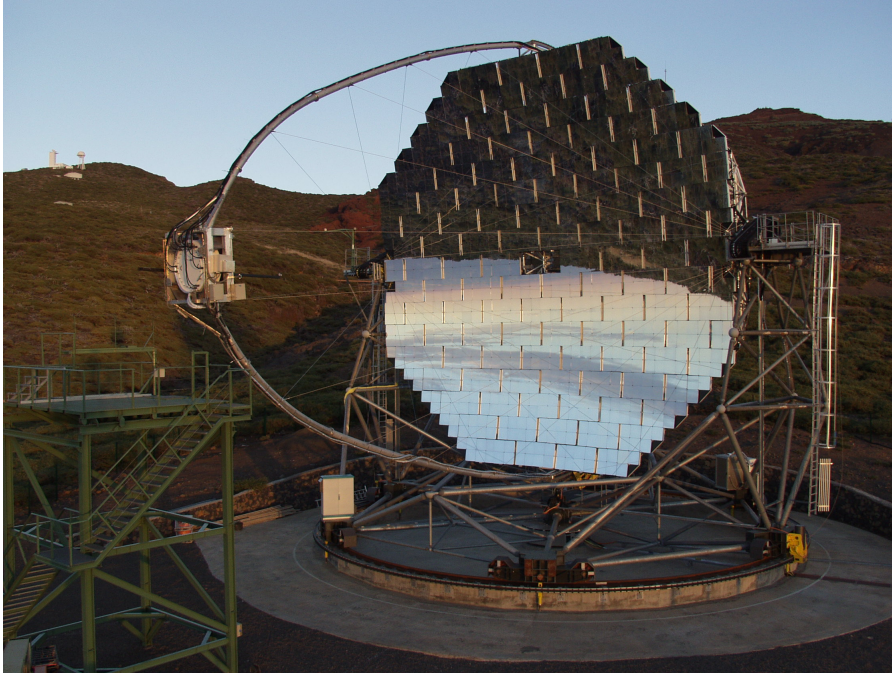


Figure 3.11: The MAGIC telescope, located on the Canary island of La Palma (28.8° N, 17.8° W, 2200 m a.s.l., www-09).

### 3.4.1 Reflector

The reflector with a diameter of 17 m consists of 247 panels with a reflecting surface of 234 m<sup>2</sup> in total. The focal length amounts to 17 m with a focal over diameter ratio of unity. While the single mirrors (four per panel) are spherically, the complete reflector has a parabolic shape to conserve the time information of the Cherenkov light. Each panel comes with an active mirror control (AMC), which allows to correct the focusing for small bendings of the structure depending on the current position. During data taking so-called Look-up tables, giving the correct positions of all panels for a certain elevation, are used to refocus the reflector within a few seconds. The standard deviation of the point spread function of the optical system is well below the size of an inner camera pixel (diameter 0.1°). The mirror segments are aluminium sandwiches with diamond-milled surfaces. The aluminium surface is coated by a hard transparent layer of SiO<sub>2</sub> to protect it against weather damage and ageing, while the sandwich structure ensures stiffness and low

weight. A heating system in each mirror prevents dew deposit and icing. More detailed information can be found in Garczarczyk (2006).

### 3.4.2 Telescope structure and drive system

The reflector is mounted on a space frame structure made of carbon fiber reinforced plastic tubes. Together with the light mirrors the total weight amounts to only  $\sim 60$  t. The telescope is an alt-az mount with two 11 kW servo motors for the movement in azimuth and one for elevation. The pointing accuracy is  $(1.1 \pm 0.7)$  arcmin and the telescope is able to reposition to any sky position in less than 50 s. The fast repositioning was a design goal to be able to search for VHE gamma-ray emission in the prompt emission phase of GRBs which is below 100 s. The tracking is continuously monitored by a CCD-camera, mounted in the centre of the reflector dish. This system, called starguider, compares the sky field around the pointed source with catalogue star positions. The measured mispointing is later used in the analysis to correct for the source position on software basis. For more details see Bretz (2006).

### 3.4.3 Detector

The detector is located in the prime focus of the reflector (distance of 17 m). It consists of 577 PMTs arranged in a hexagonal pattern, divided in an inner part with 397 PMTs with a FOV of  $0.1^\circ$  each and an outer ring of 180 PMTs with a FOV of  $0.2^\circ$  each (see Fig. 3.10). The quantum efficiency (QE) above 350 nm is enhanced by 15 % - 20 % by applying a light scattering lacquer doped with a wavelength shifter, yielding a maximum QE of  $\sim 30$  % at 400 nm (Paneque et al., 2004).

### 3.4.4 Data acquisition

The system for the data acquisition as described below was used until February 2007. All data analysed in this work were taken with this system. The old 300 Msamples/sec digitalisation system has been upgraded in February 2007 by a 2Gsamples/sec digitalisation system (Goebel et al., 2007).

The analogue signals from the PMTs are transmitted via optical fibers over a distance of 162 m to the Receiver boards using Vertical Cavity Surface Emitting Laser (VCSEL,  $\lambda = 850$  nm) drivers. In the Receiver boards, the signal is splitted: one branch goes to a discriminator that generates a signal for the trigger system while the other branch is amplified, stretched to a FWHM of  $\sim 6$  ns and splitted again in a high- and a low-gain. The high-gain

is amplified by a factor of  $\sim 10$  while the low-gain is delayed by 50 ns. If the signal in the high-gain exceeds a certain threshold, a fast GaAs switch combines the low- and the high-gain branch again and both are digitised. If the switch is not activated, only the high-gain branch is digitised. As the Cherenkov light pulse is recorded within the first 50 ns, the second part is used as a measurement of the night sky background light and the electronic noise (Fig. 3.12).

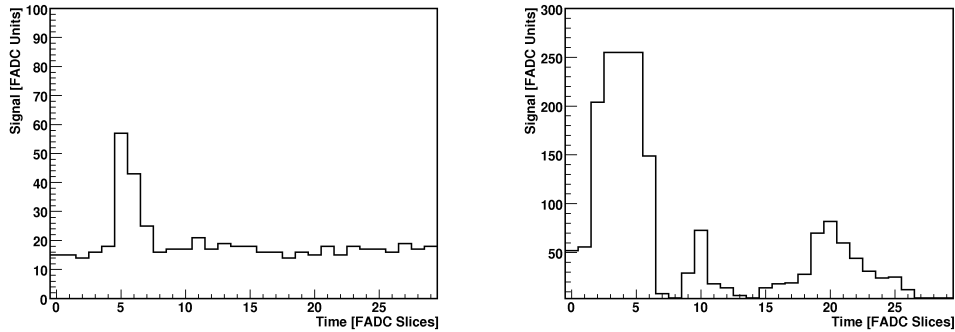


Figure 3.12: Readout for single pixels: digital counts vs. time slices. The left panel shows a pixel where the high-gain is not saturated. All the time slices belong to the high-gain. In the right panel, the high-gain is saturated and the low-gain is also read out (slices 15 to 30).

The analogue signals are continuously digitised with 300 Msamples/sec using a 8 bit Flash Analogue Digital Converter (FADC) and stored in 32 kByte long ringbuffers. If a trigger signal arrives,  $2 \times 15$  samples<sup>3</sup>,  $\sim 3.3$  ns each, is written to a 512 kByte long FiFo (First-in-First-out) buffer with up to 80 MBytes/sec. The readout procedure of the ringbuffer results in a dead time of less than  $1\mu\text{s}$  corresponding to less than 0.03% dead time at a usual trigger rate of 300 Hz. As the signal was stretched before, the time slices of 3.3 ns allow for a time resolution below 1 ns. A scetch of the data stream is shown in Figure 3.13.

### 3.4.5 Trigger

Only 325 inner pixels belong to the trigger, yielding an effective trigger area of  $2^\circ$  in diameter. The signal for the trigger first goes through a discriminator. If the signal exceeds a certain threshold (the so-called discriminator threshold, DT), a digital signal is issued. The DTs are variable: if the individual trigger

<sup>3</sup>15 high-gain and 15 low-gain samples, if the switch was activated, otherwise 30 high-gain samples

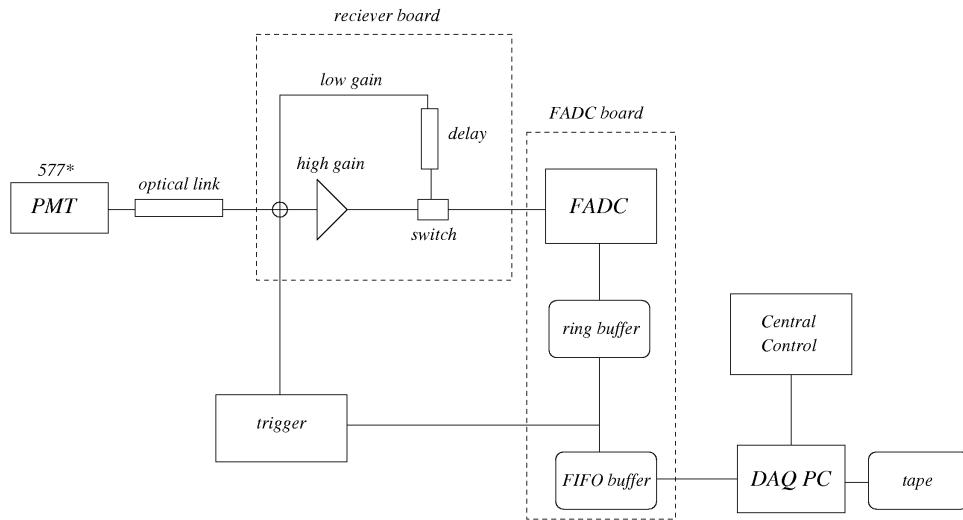


Figure 3.13: Sketch of the data stream of the MAGIC telescope (until Feb. 2007, Goebel et al., 2003).

rate of a pixel exceeds a certain level, the threshold for this pixel is raised. This avoids artificial triggers by bright stars or malfunctioning pixels. The trigger further consists of two levels. The level-1 trigger contains 19 overlapping hexagonal cells with 36 pixels each (see Fig. 3.14). The trigger logic looks for a  $N$ -next-neighbour coincidence within a few nanoseconds in one of the cells. The multiplicity can be variably adjusted; the default value, which has been also used for all the data analysed in this work, is four. The level-2 trigger is widely programmable. It is currently not in use.

The trigger rates depend strongly on weather conditions and zenith distance. The rate is dominated by background events (hadron initiated air showers and single muons) and amounts to  $\sim 250$  Hz for extragalactic and  $\sim 200$  Hz for galactic sources, in case of low zenith distances and good weather conditions. The difference comes from different discriminator thresholds, due to the brighter star field of most of the galactic targets.

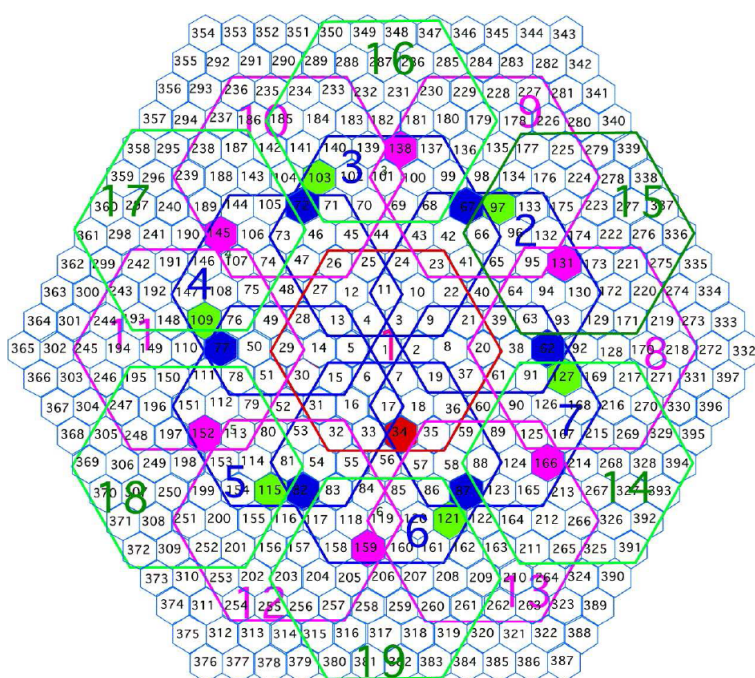


Figure 3.14: The level-1 trigger. Only the inner part of the camera is shown. Note that twelve pixels around every corner do not belong to the trigger region.

# Chapter 4

## The analysis chain

The data taken with the MAGIC telescope are on event basis. A certain number of recorded events are combined in a so-called run. There are three different kinds of runs: pedestal, calibration and data runs. One pedestal run together with a calibration run and a couple of data runs define a sequence.

- Pedestal run: the telescope is pointing to the source but is triggered randomly with 1kHz, 1000 events are recorded. With a pedestal run, the night sky background light (NSB) as well as the electronic noise is measured. One pedestal run is taken before a calibration run. To take into account the change of the NSB during the observation (rotating starfield), the pedestal is updated at regular intervals, using the last time slices of each event of the data run in case the high-gain was not saturated. Note that with the upgrade of the data acquisition system in February 2007, the signal is no longer splitted into a high and a low-gain branch. Therefore pedestal events are recorded with a rate of 25 Hz during data taking.
- Calibration run: the camera is illuminated by ultra-fast UV-light pulses (10 LEDs,  $\lambda = 375$  nm, FWHM of the optical pulses 2-3 ns) with 500 Hz,  $\sim 4000$  events are recorded. The detector is triggered directly by the calibration system. With a calibration run, the response of each PMT is measured to calculate the conversion factors (calibration constants) from FADC counts to photoelectrons. Due to gain fluctuations, it is necessary to update the calibration constants at regular intervals. Therefore calibration events are taken with 50 Hz during the data runs (interleaved calibration events). Further details can be found in Gaug (2006). Since February 2007 the rate of interleaved calibration events is reduced to 25 Hz, yielding a total rate of interleaved events of 50 Hz (including interleaved pedestal events).

- Data run: the detector is triggered if the light content of at least four connected pixels exceeds the discriminator thresholds within a narrow time interval (see also Section 3.4.5).

The data is processed, using the Magic Analysis and Reconstruction Software (MARS), which is based on ROOT<sup>1</sup>. A detailed description can be found in Bretz (2006).

In the following chapter first a brief overview of the data processing from the raw data to the calculation of the image parameters is given. These steps are completely automatised. Section 4.2 explains briefly the two different observation modes and the resulting ways of background determination. In Section 4.3 it is shown how the background is suppressed and how the source position is reconstructed. The method of the reconstruction of the energy spectrum is explained in Section 4.4, including a comparison of the distributions of the most important image parameters between simulated gamma showers and observed events from a strong source after background suppression. In Section 4.5 the analysis is shown for the Crab Nebula, the standard candle in TeV astronomy, together with a brief discussion about the sensitivity of the analysis.

## 4.1 Data preparation

The following part of the analysis is completely automatised in the Würzburg data centre (Dorner et al., 2005). The calibration is done by a program called CALLISTO (CALibrate LIght Signals and Time Offsets); after the calibration the information of the telescope subsystems are combined in a single file by the program MERPP (Merging and Preprocessing Program). Software trigger, image cleaning and the calculation of the image parameters are done by the program STAR (STandard Analysis and Reconstruction). All these program are part of the MARS-package.

### 4.1.1 Calibration

The calibration of an IACT is a crucial task, as no artificial gamma-ray source is available at these energies. The calibration follows two steps: first the response of every pixel is measured based on a uniform illumination with pulsed UV-light (calibration events) and the conversion factors (calibration constants) are calculated. Second, different data sets as well as simulated air shower events are cross calibrated with ring images of recorded muon

---

<sup>1</sup><http://root.cern.ch/>

events, which are sensitive to different atmospheric conditions as well as to the reflector performance (see Chapter 5.3).

The standard calibration for the MAGIC telescope uses the excess-noise factors of the PMTs (also called F-factor) which were measured for a sample of PMTs in the laboratory. The F-factor in general is defined as

$$F = \frac{(\text{Signal/noise}) \text{ at input}}{(\text{Signal/noise}) \text{ at output}} \quad (4.1)$$

The distribution of charges for each pixel from  $\sim 4000$  calibration events is measured and the mean value  $\mu$  as well as the standard deviation  $\sigma$  are calculated from a Gaussian fit. The number of photoelectrons (phe) is then

$$n_{\text{phe}} = F^2 \cdot \frac{(\mu - \mu_{\text{ped}})^2}{\sigma^2 - \sigma_{\text{ped}}^2}, \quad (4.2)$$

where  $\mu_{\text{ped}}$  is the mean and  $\sigma_{\text{ped}}$  the standard deviation of the pedestal. The used F-factor has been measured for a sample of 20 PMTs with the result of  $F = 1.15 \pm 0.02$ . Further details can be found in Doro (2004) and Gaug (2006).

The method is limited by the fact that a global F-factor, based on the measurement of a sample, is used instead of the F-factors of the individual PMTs. In addition the F-factor will change with time due to degradation effects. Furthermore it is only a relative calibration. If the camera changes its global behaviour, it is not recognised by the F-factor method. Since the light source is located in the reflector dish, neither the performance of the reflector nor the atmospheric conditions are taken into account. It is shown in Chapter 5.3 that a global correction of the calibration constants up to 20% has to be made to get the same level of light intensity for data of different periods.

### 4.1.2 Pulse extraction

As mentioned in Section 3.4.4, the Cherenkov light pulses are stretched to a FWHM of  $\sim 6$  ns (high-gain,  $\sim 10$  ns for the low-gain part) which ensures a sampling of four time slices. The broadened light pulse is still narrow compared to the exposure time of 50 ns. To reduce the noise, only the pulse itself shall be extracted. Two methods are used in this work.

1. Spline: the pedestal subtracted FADC slice contents are interpolated by a cubic spline algorithm. At the position of the maximum, 1.5 time slices are integrated

2. Digital filter: an analytic fit to a standard pulse form is used, assuming that both the shape and the noise are independent from the signal amplitude and the arrival time. Further details can be found in Bartko (2006).

### 4.1.3 Detector inhomogeneities

The detector response is not completely homogeneous. The main reason comes from shifted pulse positions due to hardware problems. Usually the mean peak position - averaged over all pixels - is pre-adjusted to lie within the fifth sampling slice. If the peak moves to the edge of the sampling range, the signal can not be extracted correctly. As this happens only in parts of the camera, the efficiency of the detector changes locally. An additional inhomogeneity comes from single malfunctioning pixels in the trigger area. To quantify this effect a parameter, called *inhomogeneity*, has been introduced. From simulations, inhomogeneities well below 10% are expected from fluctuations in the camera. For observational data, values up to 15% are still acceptable.

### 4.1.4 Bad pixel treatment

Pixels where the signal extraction fails are flagged as unsuitable pixels (or "bad" pixels). The reasons can be hardware defects or strong illumination, e.g. by a bright star. Also the central pixel is marked as unsuitable as it is not connected for normal data taking. The light content has to be interpolated for a bad pixel from surrounding pixels, whereas three suitable pixels are required as a minimum for the interpolation.

### 4.1.5 Software trigger

The trigger rate can be artificially increased by random coincidences, generated by fluctuations of the NSB light. This is mainly caused by small variations of gains or delays in the trigger logic. Therefore the trigger is simulated in the software after the calibration, when the signal is corrected for gain fluctuations, requiring at least four neighbouring pixels with a signal above 5 phe and an arrival time inside a coincidence window of  $\pm 0.5$  time slices. This suppression of background fluctuations, early in the analysis, decreases the further analysis time and leads to an unbiased trigger rate, which provides a good quality check of atmospheric conditions.

### 4.1.6 Image cleaning

After calibration and pulse extraction, pixels having a content dominated by NSB fluctuations have to be distinguished from pixels containing Cherenkov light of air showers. This procedure is called image cleaning. Each pixel holds the information of light content and arrival time of the light pulse. For pixels, dominated by NSB light, the arrival time is randomly distributed, whereas the Cherenkov light from an air shower arrives within a small time window. The standard cleaning used mainly in this work takes only the pixels' content into account and ignores the timing information. In a first step all pixels above a certain threshold are defined as core pixels. In a second step every pixel with a content above a second, lower threshold, located next to - at least - one core pixel, is defined as a border pixel. In a final step, isolated core pixels are removed (see Fig. 4.1). In this work an absolute image cleaning with a threshold of 8.5 phe for core and 4.0 phe for border pixels is used.

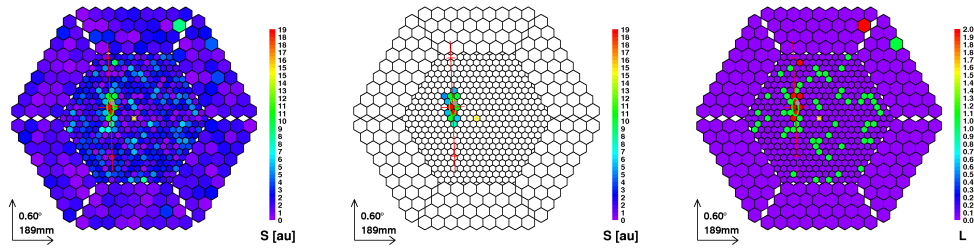


Figure 4.1: One event, recorded by the MAGIC telescope. Left: After calibration and pedestal subtraction. Middle: After image cleaning. Right: The cleaning levels: red indicates the core pixels (pixel contents  $> 8.5$  phe), green the border pixels (pixel contents  $> 4.0$  phe) and violet pixels with contents below 4 phe. Compared to the image in the middle, pixels with more than 4 phe but without connection to a core pixel as well as single core pixels are removed.

At the time of writing, a new image cleaning has been developed by Bretz (2007) using in addition to the light content also the arrival time. This leads to lower threshold values of 6 phe and 3 phe for core and boundary pixels, respectively, without picking up additional NSB noise. The new development is later used for sources of the investigated sample, for which already a signal - or a hint of it - is seen in the standard analysis.

### 4.1.7 Image parameters

In the next step the cleaned shower image is parametrised. First the image axis is determined. It is defined as the line where the signal-weighted sum of squares of perpendicular angular distances is minimised. Afterwards the intensity distribution with respect to the image axis up to the third moments are calculated. The most important parameters used in this work are described below.

- *size*: the sum over all pixel contents that survived the image cleaning. For gamma initiated air showers this parameter is strongly correlated to the energy of the primary gamma-ray.
- *length*: the second moment of the intensity distribution along the shower axis.
- *width*: the second moment of the intensity distribution perpendicular to the shower axis.
- *m3long*: the third moment of the intensity distribution along the shower axis. This parameter is used to discriminate between the head and the tail of a gamma-like shower.
- *leakage1*: the ratio of the pixel content in the outermost camera pixel ring and *size* (or the two outermost rings, referred to as *leakage2*). This parameter is a quantity for the truncation of the shower by the border of the camera.
- *conc*: the concentration, defined as the ratio of the two highest pixel contents and *size*. In addition the ratio of only the highest pixel content and *size* can be used (*conc1*).
- *dist*: the distance between the assumed source position and the centre of gravity of the shower.
- *usedarea*: the area of all pixels which survived the image cleaning.
- *corearea*: the area of all core pixels of the image.

The image parameters *width*, *length*, *conc*<sup>2</sup> and *dist* are called "classical image parameters" or "Hillas parameters", originally proposed by Hillas (1985). A schematic view of the the shower geometry is shown in Figure 4.2. For the analysis of muon ring images, additional parameters are introduced which are described in detail in Chapter 5.

---

<sup>2</sup>The parameter *conc* is called *frac(2)* in the original work of Hillas

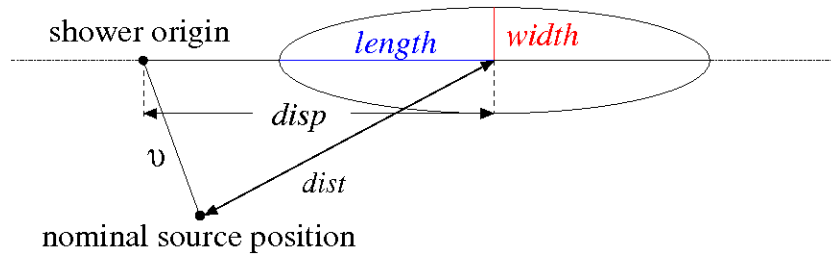


Figure 4.2: Schematic view of an air shower image. Shown are the basic image parameters *width*, *length* and *dist*, as well as the *disp* for the reconstructed shower origin (see Section 4.3.3) and  $\vartheta$  as the distance between the shower origin and the nominal source position.

At the time of writing, a new image parameter, called *slopelong*, has been introduced by Bretz (2007). This new parameter characterises the time development of the shower along its major axis.

## 4.2 Background determination

The determination of the background depends on the observation mode. Two different modes are distinguished: the "on-off" and the "wobble" mode.

### 4.2.1 On-off mode

The telescope is pointing directly at the source so that the starfield is rotating during the observation. To determine the background in the source region, additional observations of sky positions where no gamma-ray source is expected have to be performed. These so-called off data should cover the same range in zenith distance (ZD), a similar NSB, similar atmospheric conditions and the same telescope performance. Since the ratio between on and off data should be at least unity (see Sec. 4.5.7, in particular Fig. 4.13), long observation campaigns require long off exposures, though it is possible to share off data for several sources visible in a certain time window under the same ZD. Nevertheless the off data are never taken simultaneously so that atmospheric differences are unavoidable, leading to systematic uncertainties in the background determination.

### 4.2.2 Wobble mode

The telescope is pointing alternatingly at two opposite sky directions, each  $0.4^\circ$  off the source. The source is therefore rotating in the field of view during

the observation and the position is calculated by a rotation matrix for every shower image. The background in the signal region is estimated from three sky positions placed at the same distance as the source candidate. This provides three times more background events than on events without the need of additional observation time. Compared to off observations, the background in wobble mode is simultaneously recorded which reduces the systematic error of the background determination. A drawback of the wobble mode is the reduced detector acceptance with increasing distance from the camera centre. When comparing the sensitivity to on-off mode, this drawback is more than compensated by the higher background statistics together with the omission of off observations<sup>3</sup>. A systematic error comes from inhomogeneities of the detector response, as the method assumes a symmetric detector acceptance in azimuth. Note that this would also affect on-off observations as long as such inhomogeneities are not locally stable during the observation campaign. But even in the latter case a measured flux would be underestimated because of an overestimation of the detector efficiency.

## 4.3 Gamma-hadron separation

To distinguish between gamma initiated air showers and non-gamma showers, a cut is performed in the parameter space and the origin of the shower is reconstructed. Since hadron initiated air showers are randomly distributed in the sky (and therefore in the camera), a powerful background reduction is achieved if only showers originating close to the assumed source position are taken into account. All calculations described in the following section are done by the program GANYMED, which is also included in the MARS-package.

### 4.3.1 Quality cuts

To get rid of events which are not suited for further analysis or which are caused by detector malfunctions, several cuts are performed. All events surviving the following cuts are selected for further analysis.

- Even with closed camera lids events are recorded with a rate of  $\leq 1$  Hz. These events could be related to single muons traveling through the detector or from sparks in a single PMT. These are very small images characterised by a high pixel content. At least in one pixel, the high-gain

---

<sup>3</sup>This holds for longer observations ( $> 10$  h). In case of short exposure times, on-off observations offer the possibility of very high background statistics.

is saturated. It is easy to select them without affecting a gamma-ray shower image by cutting in the number of saturated high-gain pixels ( $N_h$ ) and the image parameter *area* ( $= width \times length \times \pi$ ) as well as in *conc* vs. *size*.

$$N_h < 1 \quad \text{and} \quad \text{area} > 0.003N_h + 0.0325 \quad (4.3)$$

$$\log_{10}(\text{conc}) < -0.371 \log_{10}(\text{size}) + 0.596 \quad (4.4)$$

- With the following cuts no gamma-like showers are affected, which has been verified on simulated gamma showers:

$$\text{number of pixels surviving image cleaning} > 5 \quad (4.5)$$

$$\text{number of saturating low-gains} > 2 \quad (4.6)$$

$$\text{number of islands} < 3 \quad (4.7)$$

Hereby an island is defined as a cluster of pixels surviving the image cleaning. It is spatially separated from another cluster by pixels which did not survive the image cleaning.

- Images for which the truncation of the shower by the borders of the camera is too large are not suited for further analysis.

$$\text{leakage1} < 0.3 \quad (4.8)$$

### 4.3.2 Dynamical cuts

Figure 4.3 shows the combined parameter *area* ( $width \times length \times \pi$ ) vs. *size* for simulated gamma showers and observational data. It can be seen that above a *size* of 200 phe the distributions can be separated, while below 200 phe they completely overlap. This corresponds to a primary energy for the gamma-ray of roughly 150 GeV. As shown in the next chapter, this is mainly dominated by single muons, the so-called "muon wall". The following parametrisation is used:

$$\text{area} < c_3(1 - c_4(\log_{10}(\text{size}) - c_5))^2 \quad (4.9)$$

where the coefficients  $c_3$ ,  $c_4$  and  $c_5$  are optimised on data from the Crab Nebula (see Section 4.5). The *area*-cut provides an easy, robust and powerful background suppression above  $\sim 150$  GeV.

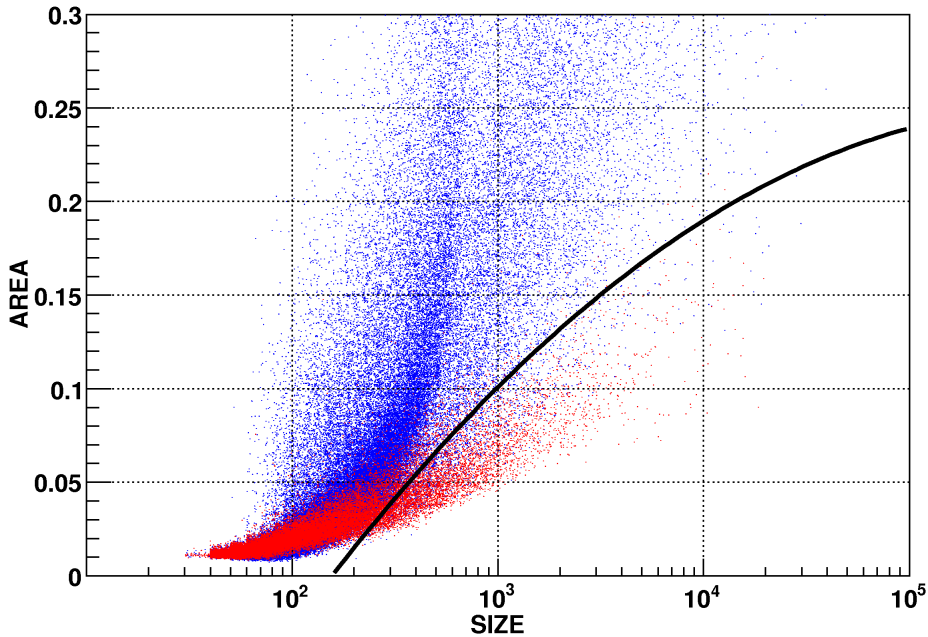


Figure 4.3: Image parameters *area* vs. *size* for simulated gamma showers (red) and observational data (green). The black line marks the standard cut used in this work.

### 4.3.3 Reconstruction of the shower origin

The origin of the gamma shower in the camera plane corresponds to the sky position of the gamma-ray source. The origin is located on the image axis which represents the shower axis. In case of stereoscopic observations, the shower origin results from the intersection of the axes of all images recorded by the different telescopes. It was shown by Lessard et al. (2001) with data from the Whipple IACT that the origin of a gamma shower can also be reconstructed by its geometry. The elongation of the image, expressed as the ratio between the shower width and the shower length, depends on the impact parameter. The distance from the centre of gravity (COG) of the shower to the shower origin, called *disp*, can be described by the following empirical equation:

$$disp = \xi \left( 1 - \frac{width}{length} \right), \quad (4.10)$$

where  $\xi$  is a parameter that has to be adjusted by simulated gamma showers. Here the parametrisation from Rügamer (2006) is used that takes into account the truncation of the shower image by the finite size of the camera.

$$disp = (c_0 + c_6(\log_{10}(leakage1 + 1))^{c_7}) \times \left( 1 - \frac{width}{length} \right) \quad (4.11)$$

The coefficients  $c_0$ ,  $c_6$  and  $c_7$  were optimized with simulated gamma showers (Rügamer, 2006). Since *disp* gives only the distance from the COG to the shower origin, a discrimination between the head and the tail of the shower is necessary for an unambiguous reconstruction. For gamma showers the third moment along the shower axis (*m3long*) is expected to be positive in the direction of the shower development. Due to fluctuations, also slightly negative values can be seen, in particular at low energies. Therefore the shower head is determined as

$$m3long > c_5, \quad (4.12)$$

where  $c_5$  is optimised on data from the Crab Nebula. The resulting spatial resolution is  $\sim 0.1^\circ$ . The *disp*-method offers the possibility of searches for gamma-ray emission from unknown sources in the field of view as well as the reconstruction of extended sources.

With the introduction of the arrival time information in MARS version 2.0, also the parametrisation of  $\xi$  has been changed. It now takes also the time development (*slopelong*) as well as the brightness (*size*) of the shower into account. It is given as

$$\xi = c'_0 + c'_8 \times slope + c'_9 \times leakage1 \quad (4.13)$$

for  $\log_{10}(size) \leq c'_{10}$ . Otherwise the additional term

$$c'_{11} \times (\log_{10}(size) - c'_{10})^2 \quad (4.14)$$

is added. The notation  $c'_x$  marks the coefficients for the new parametrisation of MARS version 2.0. For the head-tail discrimination a further condition additionally to Equation 4.12 is introduced which is based on the time development along the shower axis:

$$slopelong < (dist - c'_7) \cdot c'_6. \quad (4.15)$$

To get the significance of a signal from a source candidate, the distribution of the squared angular distance between the shower origin and the source position ( $\vartheta^2$ ) is compared to the  $\vartheta^2$ -distribution with respect to a background region. In case of a signal an excess at low  $\vartheta^2$ -values is expected. The significance is calculated for  $\vartheta < c_1$ , using Equation 17 from Li and Ma (1983) which takes the number of signal and background events as well as the scaling factor between them into account. In case of on-off observations, the  $\vartheta^2$ -distribution of the off data is scaled to match the on data in a region where no bias from the source is expected. For wobble data, the scaling factor is fixed to 1/3 corresponding to the three background regions.

The exact source position has to be determined for every event, prior to the calculation of the source dependent parameters. To correct the nominal source position for tracking inaccuracies, the deviation measured by the starguider is used. While the relative deviation is well determined, the starguider pointing corrections can introduce a constant fake mispointing. An absolute calibration of the starguider is first introduced in MARS version 2.0. A detailed description can be found in Bretz (2006).

## 4.4 Spectrum

The background events are subtracted from the signal events within the signal region ( $\vartheta < c_1$ ) and divided by the effective observation time, which results in the rate of observed gamma photons. To derive the differential energy spectrum, the energy of each event has to be estimated and the collection area as well as the trigger and cut efficiencies have to be calculated. This is done using simulated gamma showers.

### 4.4.1 Monte Carlo simulations

The gamma-ray initiated air showers are simulated with the Magic Monte Carlo Simulation (MMCS) program which is based on CORSIKA (version 6.019 Heck et al., 1998). The simulated energy ranges from 10 GeV to 30 TeV with a differential energy distribution following a power law with spectral index -2.6. The simulation is separated in different ZD bins, whereas the ZD of bin  $x$  ranges from  $\arccos(1.005 - 0.01x)$  to  $\arccos(0.995 - 0.01x)$ . The impact parameter is equally distributed from 0 to 300 m.

The CORSIKA output (distribution of Cherenkov photons at observation level) is processed with the MAGIC reflector program (version 0.6), which derives the distribution of Cherenkov photons in the focal plane. It also calculates the absorption of Cherenkov photons in the atmosphere. The detector is simulated using the MAGIC camera program (version 0.7). In addition to the detector simulation, an average distribution of photons from the NSB light is added to the Cherenkov photons. The NSB is simulated beforehand for a certain time interval, much longer than the exposure time for a single event, and the results are stored in a database. For each event, the NSB contribution is read from this database for the time interval of the exposure time. The starting time is thereby chosen randomly.

Also the simulation of the optical system can be further adjusted in the camera program: The reflectivity of the mirrors can be changed by a global correction factor. The point spread function (PSF), simulated as a two-

dimensional gaussian distribution, can be increased additionally to the spot size of two times 5 mm, already simulated in the reflector program. The resulting PSF is given as

$$\sqrt{(5 \text{ mm})^2 + (5 \text{ mm})^2 + (\textit{additional spot/mm})^2}.$$

The sample of simulated gamma showers is analysed in the same way as the observational data. For the reconstruction of the energy spectrum, the ZD distribution is weighted to match the ZD distribution of the observation. Also the simulated spectrum can be changed by weights to avoid a bias from an a priori assumption on the spectral shape.

#### 4.4.2 Energy reconstruction

The energy of the primary gamma-ray of each shower image is estimated using correlations between several image parameters. This is done by a statistical learning method called *random forests* (Breiman, 2001). The following image parameters are used in this work: *size*, *dist*, *area*, *usedarea*, *corearea*, *leakage1*, *leakage2*, *conc* and *conc1*. For all parameters the ZD dependence is taken into account. The by far most important image parameter is *size*, which is approximately proportional to the primary energy of the gamma-ray.

From the comparison of the distribution of estimated energy and real energy of simulated gamma showers, correction factors for spillover effects from one energy bin to another are calculated. These factors depend also on the assumed spectral shape. For an example see also Section 4.5.5, Figures 4.7 and 4.8.

#### 4.4.3 Effective collection area

The effective collection area is calculated for each energy bin. It accounts for the trigger and the cut efficiency whereas the latter depends on the particular analysis. It is calculated from the ratio of the number of simulated events surviving all cuts ( $N_c$ ) and the number of simulated events ( $N_{sim}$ ) within a fixed area ( $A_0$ ).

$$A_{eff}(E_n) = A_0 \frac{N_c}{N_{sim}} \quad (4.16)$$

An example of the energy dependend collection area is given in Section 4.5.5, Figure 4.10.

The differential energy flux is finally given by the gamma-rate in each energy bin divided by the effective collection area, multiplied by the spillover factor and divided by the mean energy of the bin.

## 4.5 Observations of the Crab Nebula

In the following section, the performance of the telescope as well as of the analysis method is shown on the basis of observations of the Crab Nebula, the standard candle in TeV-astronomy.

### 4.5.1 The Crab Nebula

The Crab Nebula, located at a distance of  $\sim 2$  kpc, is the remnant of a supernova that occurred in 1054 A.D. (e.g. Collins et al., 1999). It is one of the best studied celestial objects and shows broad-band non-thermal emission from the radio band up to VHE gamma-rays. The remnant is powered by the pulsar PSR B0531+21, a fast rotating neutron star with a period of 33 ms. Pulsed emission has been discovered in all energy bands up to 10 GeV. Figure 4.4 shows the Crab Nebula in the light of different wavelengths. At X-rays the PWN is clearly visible. In the optical band, the filaments indicate shock fronts in the interstellar medium. With decreasing energy the size of the Nebula increases. This can be understood taking into account that the spectrum from X-rays to the radio band is dominated by synchrotron radiation of relativistic electrons. Since the electrons cool radiatively, the critical synchrotron frequency decreases so that electrons at the farthest distance from the central engine are just energetic enough to produce synchrotron photons in the radio band.

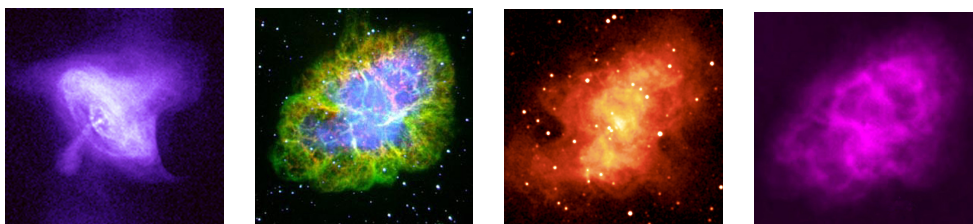


Figure 4.4: The Crab Nebula at different wavelengths. The images are not to scale. From left to the right: X-rays (taken by Chandra), optical (Palomar Obs.), infrared (2MASS), radio (NRAO). The X-ray image is 2.5 arcmin on a side, the other images are three times larger (www-06).

The Crab Nebula was discovered as the first source of VHE gamma-rays in 1989 by the Whipple 10 m reflector (Weekes et al., 1989). Since then detailed studies of the VHE emission have been carried out by various experiments (e.g. Akerlof et al., 1990; Vacanti et al., 1991; Konopelko et al., 1996; de Naurois et al., 2002; Aharonian et al., 2006b; Albert et al., 2008a)), revealing

the nebula to be the strongest steady source of VHE gamma-ray emission, which made it suitable for a standard candle in TeV astronomy.

### 4.5.2 Observations with the MAGIC telescope

The Crab Nebula is regularly monitored by the MAGIC telescope since the end of commissioning in October 2004, mainly to check the performance and the stability of the telescope. The source is located at RA 05 34 31.97 and dec. +22 00 52.1 and is visible from September to March under low ZD ( $6.6^\circ < \text{ZD} < 40^\circ$ ) from the MAGIC site. In this work data from December 2004 to March 2006, both in on-off and wobble (w) mode, are used. All analysed sequences together with the most important quality parameters are listed in Appendix A. Table 4.1 gives a summary of the data.

season	mode	exp. [h]	$\langle \text{ZD} \rangle$ [degr.]
10/2005 - 03/2006	w	8.1	22.0
12/2004 - 03/2006	on	38.7	16.2
12/2004 - 03/2006	off	44.3	20.1

Table 4.1: Observations of the Crab Nebula with the MAGIC telescope: observation summary. The exposure time is given after quality selection. The value for the ZD represents the time weighted mean value.

Only data with ZD below  $40^\circ$  are analysed which covers the ZD range of the observed AGN. The most important quality parameter is the rate after image cleaning, as this rate is very sensitive to atmospheric conditions. The rate after image cleaning for the used data lies between 137 Hz and 224 Hz (for most of the data it lies between 160 Hz and 190 Hz). The pedestal rms is between 1.04 phe and 1.28 phe which corresponds to light conditions without a significant contribution from moon light. These values are slightly higher than for most of the AGN due to the brighter star field around the Crab Nebula. The number of unsuitable inner pixels is below 15 for most of the data, with a few sequences up to 23 bad pixels (without clustering). The inhomogeneity is always below 12.6%.

### 4.5.3 Gamma-hadron separation

Table 4.2 shows the values of all coefficients used in the analysis as defined in Section 4.3. The coefficients for the *disp*-parametrisation ( $c_0$ ,  $c_6$  and  $c_7$ ) are optimised using simulated gamma-showers (Rügamer, 2006). The coefficients of the *area*-cut ( $c_2 - c_4$ ) and the head-tail discrimination ( $m3long$ ,  $c_5$ ), used

coefficient	on-off	wobble	name
$c_0$	1.3245	1.221	<i>disp</i>
$c_1$	0.23	0.23	$\vartheta$ -cut
$c_2$	0.215	0.25	<i>area</i>
$c_3$	5.486	5.74	<i>area</i>
$c_4$	0.0897	0.0795	<i>area</i>
$c_5$	-0.07	-0.04	<i>m3long</i>
$c_6$	8.2957	13.425	<i>disp</i>
$c_7$	0.8677	1.04343	<i>disp</i>

Table 4.2: Coefficients  $c_0$  to  $c_7$  of the analysis, separated into on-off and wobble mode.

for the analysis of the on-off observations, are the values of the standard analysis, which are optimised on a large sample of data from the Crab Nebula (2005 - 2006) as well as data from the HBL 1ES 1218+304 from January 2005 which provides a much steeper spectrum at lower energies. In case of observation in wobble mode, the coefficients are optimised on Crab data from January 2006 to March 2006 which covered a ZD range from  $7^\circ$  to  $40^\circ$ . The value for  $\vartheta$ , which defines the source region, corresponds to two times the PSF of the MAGIC telescope for gamma-rays above 200 GeV.

In the following all analysis plots are shown as examples for the data taken in wobble mode only. The results of both observation are shown in Table 4.3.

mode	$\langle ZD \rangle$ [degr.]	$E_{\text{thres}}$ [GeV]	excess [1/min]	backgr. [1/min]	scale	sign. [ $\sigma/\sqrt{h}$ ]
w	22.0	226	6.39	5.31	0.33	15.4
on	16.2	190	8.80	9.19	0.92	13.5

Table 4.3: Results of the analysis of the Crab Nebula observations.

The left panel of Figure 4.5 shows the two-dimensional background subtracted distribution of reconstructed shower origins centered at the position of the Crab Nebula. Each shower origin is folded with a two-dimensional Gaussian with a standard deviation of  $0.06^\circ$ . The centre of gravity of the observed excess coincides within the systematic pointing uncertainty of  $0.04^\circ$  with the nominal source position. Figure 4.5, right panel, shows the distribution of the squared angular distance with respect to the position of the Crab Nebula and three off-regions (scaled by 1/3). The excess of 3083 events over 2312 scaled background events has a statistical significance of  $45.3\sigma$ .

The background subtracted  $\vartheta^2$ -distribution with respect to the Crab Nebula is well fitted by a Gaussian distribution with a standard deviation of  $0.11^\circ$  which represents the PSF of the MAGIC telescope at VHEs.

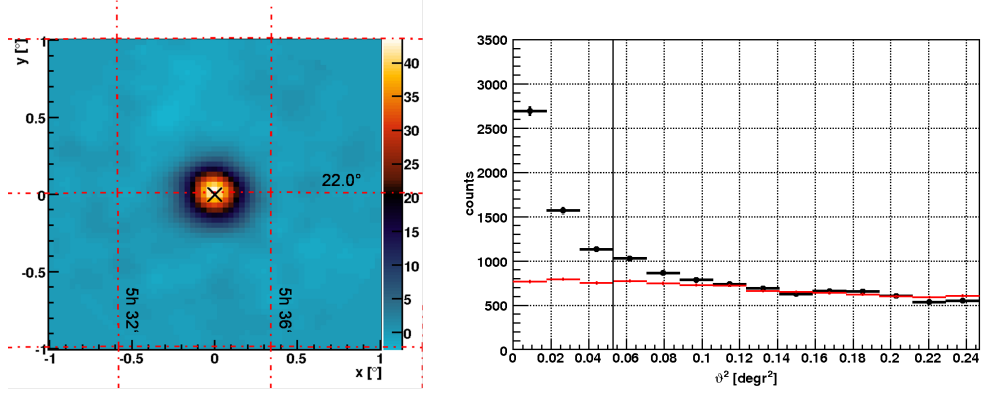


Figure 4.5: Left panel: Distribution of background subtracted shower origins on the sky (sky map) around the position of the Crab Nebula (cross) in units of events/4 arcmin<sup>2</sup>. Right panel: The  $\vartheta^2$ -distribution with respect to the position of the Crab Nebula (black dots) and with respect to three background region (red crosses, scaled by 1/3). The source region is indicated by the vertical line ( $\vartheta < 0.23^\circ$ ).

The energy threshold ( $E_{\text{thres}}$ ) is defined as the peak of the differential energy distribution of simulated gamma showers, as shown in Figure 4.6. It depends on the analysis (cuts) as well as on the spectrum of the source. Here the Crab Nebula spectrum as given in Equation 4.17 is used. The energy threshold lies in the energy bin from 209 GeV to 245 GeV.

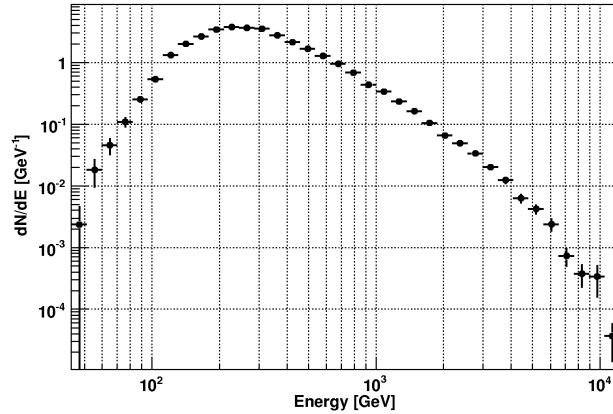


Figure 4.6: Differential energy distribution for simulated gamma showers after cuts assuming a Crab-like spectrum. The distribution peaks at 226 GeV (energy bin from 209 GeV to 245 GeV).

#### 4.5.4 Monte Carlo comparison

Since the calculation of the effective collection area as well as the energy reconstruction depends on simulated air showers, a Monte Carlo (MC) sample of gamma showers is compared to gamma events from the Crab Nebula. The distribution of the image parameters *length*, *width*, *dist*, *size* and *m3long* for a 4.0 h sample of the Crab Nebula (October to December 2005, wobble mode) and simulated gamma showers is shown in Appendix B.1. The ZD distribution of the MC sample is fitted to the ZD distribution of the Crab sample, the simulated spectrum is given by Equation 4.17.

All distributions are in a satisfying agreement. The distributions of the image parameters *length* and *width* show a small systematic shift. These parameters are very sensitive to the PSF of the optical system. Here, a Gaussian PSF with a standard deviation of 15.7 mm (corresponding to an additional spot size of 14 mm in the camera simulation) is used. The analysis of the width of muon ring images (see Chapter 5) results in a slightly smaller PSF for the Crab data. Since the PSF of all data analysed in this work ranges from  $\sim 14$  mm to  $\sim 18$  mm, the 15.7 mm MC-sample is used as an average. For the other image parameters the differences are less systematic. The main reasons for the differences are the atmospheric modelling, which can never reproduce perfectly the atmospheric conditions for a certain data sample as well as the detector simulation, where malfunctioning pixels are not simulated.

#### 4.5.5 Energy spectrum

##### Energy estimation and energy resolution

To reconstruct the differential energy spectrum, first the energy has to be reconstructed for each event. Figure 4.7 shows the distributions of the true and the estimated energy of simulated gamma showers after all cuts. In the energy range from 250 GeV to 3 TeV they agree very well. Above an estimated energy of 4 TeV the number of events is overestimated and below 200 GeV underestimated. The ratio of both distributions for each bin are called spillover factors. For the energy spectrum the flux in each energy bin is corrected for the spillover by multiplying with the spillover factor. The spillover depends on the spectrum and the energy threshold. Below the threshold the number of events is underestimated, while around the threshold the spillover factor is very close to unity. See also Bretz (2006) for a detailed study of the effect of the spillover to the reconstructed spectrum.

Figure 4.8 shows the resolution of the energy reconstruction. The average resolution is 19% above  $\sim 200$  GeV. After the energy reconstruction the  $\chi^2$ -

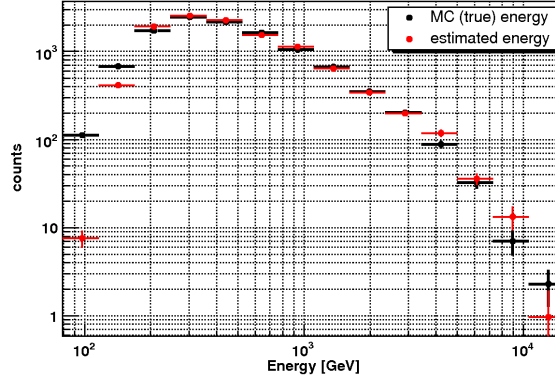


Figure 4.7: Distribution of the true and the estimated energy of simulated gamma showers.

distributions are calculated for all energy bins, yielding the observed energy dependent gamma rate. To calculate the flux, the effective collection area of the detector is still needed.

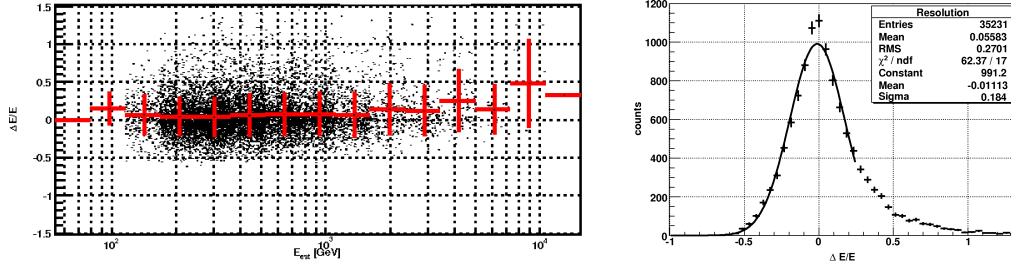


Figure 4.8: Left panel:  $(E_{\text{MC}} - E_{\text{est}})/E_{\text{est}}$  vs.  $E_{\text{est}}$ . Right panel: The distribution of  $(E_{\text{MC}} - E_{\text{est}})/E_{\text{est}}$  with a Gaussian fit ( $\chi^2/\text{n.d.o.f.} = 3.7$ ). The distribution clearly shows a tail towards higher values. The mean value of the distribution is 0.06, which indicates a bias to an underestimation of the energy. The Gaussian fit is restricted to values below 0.25 and gives a mean value of -0.01.

### Effective collection area

Air showers are simulated up to an impact parameter of 300 m which includes more than 99% of all detectable showers. Figure 4.9 shows the MC spectrum as originally simulated, after trigger<sup>4</sup> and after cuts. Again the spectrum as given by Equation 4.17 is assumed. The ratio between the originally simulated distribution and the distribution after cuts yields the total efficiency

<sup>4</sup>“After trigger” means here after image cleaning.

for the detection of gamma showers. The efficiency, multiplied by the simulated area of  $2.8 \times 10^5 \text{ m}^2$ , gives the effective collection area per energy bin (Fig. 4.10, upper panel).

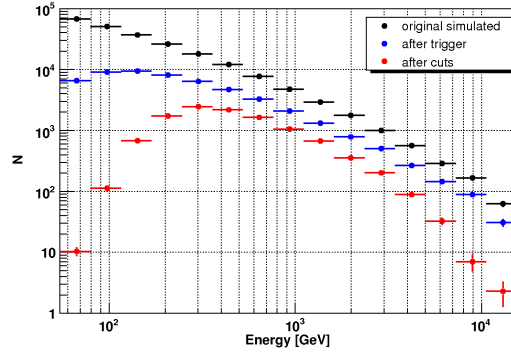


Figure 4.9: MC spectrum as originally simulated (black), after trigger (blue) and after cuts (red).

While the effective area is constant after trigger at energies above 300 GeV, it decreases fast above 4 TeV after the background suppression. The reason is a reduced cut efficiency above  $\sim 2 \text{ TeV}$  (Fig. 4.10, lower panel), which is mainly caused by the truncation of large shower images by the border of the camera.

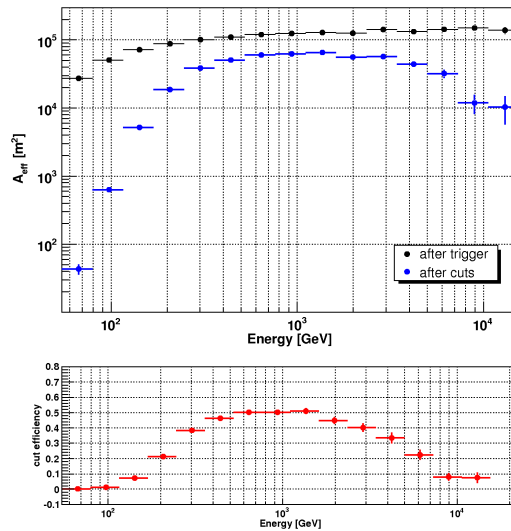


Figure 4.10: Upper panel: Effective collection area after trigger (black) and after all cuts (blue) vs. energy. Lower panel: The cut efficiency, given as the ratio between the upper distributions.

### Differential energy spectrum

Multiplying the excess rate of each energy bin with the spillover factor and the effective area and dividing it by the mean energy results in the differential energy spectrum as shown in Figure 4.11.

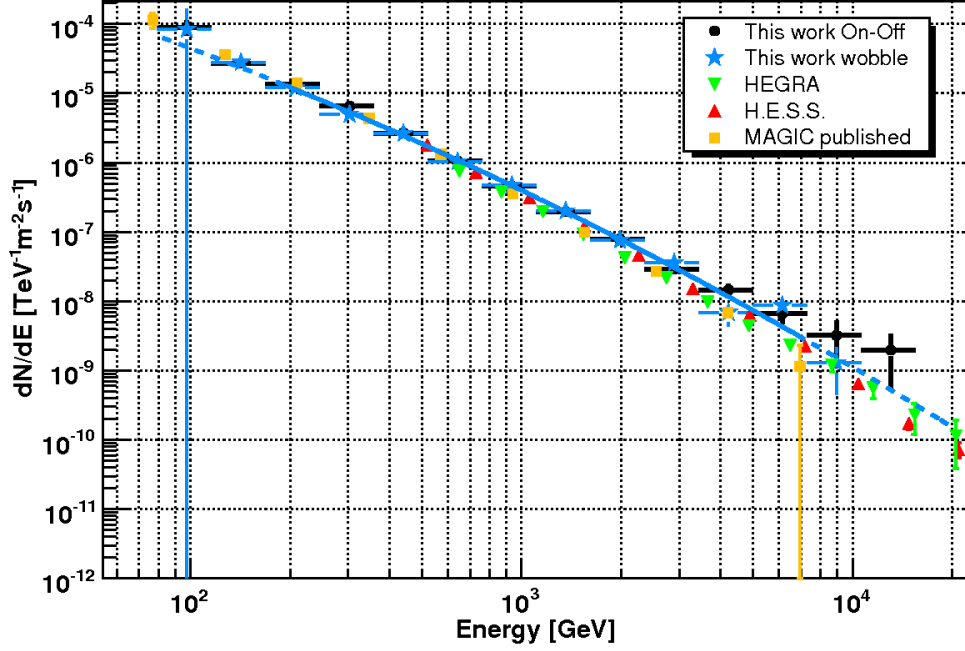


Figure 4.11: Reconstructed differential VHE spectrum of the Crab Nebula together with a fit by a logarithmic parabola. The black and blue data points are the result from this work for observations in on-off and wobble mode, respectively, while the green triangles denote the spectrum as published by HEGRA (Konopelko et al., 1996) and the red triangles as reported by H.E.S.S. (Aharonian et al., 2006b). The yellow squares are the official result from the MAGIC collaboration (Albert et al., 2008a).

A simple power law fit from 190 GeV to 7 TeV results in an acceptable description with  $\chi^2/\text{n.d.o.f.} = 17.3/8 \approx 2.2$ . Nevertheless the spectrum is better described by a logarithmic parabola which results in ( $\chi^2/\text{n.d.o.f.} = 10.9/7 \approx 1.6$ )

$$\frac{dN}{dAdtdE} = (5.43 \pm 0.22) \times 10^{-6} \left( \frac{E}{E_0} \right)^{-a - (b \log(E/E_0))} \text{ m}^{-2} \text{ s}^{-1} \text{ TeV}^{-1} \quad (4.17)$$

with  $a = (2.04 \pm 0.09)$ ,  $b = (0.25 \pm 0.11)$  and  $E_0 = 300 \text{ GeV}$ . The first two points are excluded from the fit. The first one because it is not statistically significant, the second one because of the large systematic error due to the low cut efficiency (the same holds for the last point). The spectrum reconstructed

from the on-off observations is in good agreement with the one from the wobble observations. The last point above 10 TeV in the on-off observations comes from the four times longer observation time with respect to the wobble observations. As the flux at these energies is very low and the collection area has already decreased by one order of magnitude due to the low cut efficiency, the sensitivity of the instrument above 10 TeV is quite poor and affected by a larger systematic error. The spectrum is also in good agreement with measurements from other experiments like HEGRA (Konopelko et al., 1996) or H.E.S.S. (Aharonian et al., 2006b). The spectrum published by the MAGIC collaboration (Albert et al., 2008a) is based on a 15.9 h sample, recorded from October to December 2005 in on-off mode. The analysis was restricted to data with a ZD below  $23^\circ$  to ensure a low energy threshold. A fit by a logarithmic parabola yields a slightly steeper spectrum ( $a = (2.31 \pm 0.06)$ ,  $b = (0.26 \pm 0.07)$ ,  $E_0 = 300$  GeV) with a 10% higher flux at 300 GeV. This analysis is independent from the one which is presented here. They differ in calibration, gamma-hadron separation as well as energy reconstruction and unfolding. Also the used data sample is different. Taking into account a 20% systematic error, both results are in good agreement.

#### 4.5.6 Lightcurve

Investigations from different experiments during the past two decades yield no significant time variability of the VHE flux of the Crab Nebula. Figure 4.12 shows the integral flux from 200 GeV to 5 TeV for all data used in this work, divided into 21 subsamples (5 in wobble mode and 16 in on-off mode). A constant fit results in an integral flux of

$$F(0.2 - 5 \text{ TeV}) = (2.29 \pm 0.03) \times 10^{-6} \text{ photons m}^{-2} \text{ s}^{-1} \quad (4.18)$$

The quality of the fit is quite poor ( $\chi^2/\text{n.d.o.f.} = 101/20$ ). A Gaussian fit to the distribution of the integral fluxes of all subamples (Fig. 4.12, lower panel) yields a mean value of  $(2.36 \pm 0.11) \times 10^{-6} \text{ photons m}^{-2} \text{ s}^{-1}$  with a standard deviation of  $(0.34 \pm 0.11) \times 10^{-6} \text{ photons m}^{-2} \text{ s}^{-1}$ , corresponding to 14.4% of the mean value. Assuming a constant flux, the spread can be interpreted as the systematic error. It is dominated by the uncertainty of changing atmospheric conditions. As the statistical errors of the flux of the different subsamples are quite small compared to the strong signal, the systematic errors become dominant. The average flux reconstructed here is 14% higher than the flux published by the MAGIC collaboration (Albert et al., 2008a), which is still within the systematic error from the lightcurve. Note that the integral fluxes derived from the spectral fits are in very good agreement.

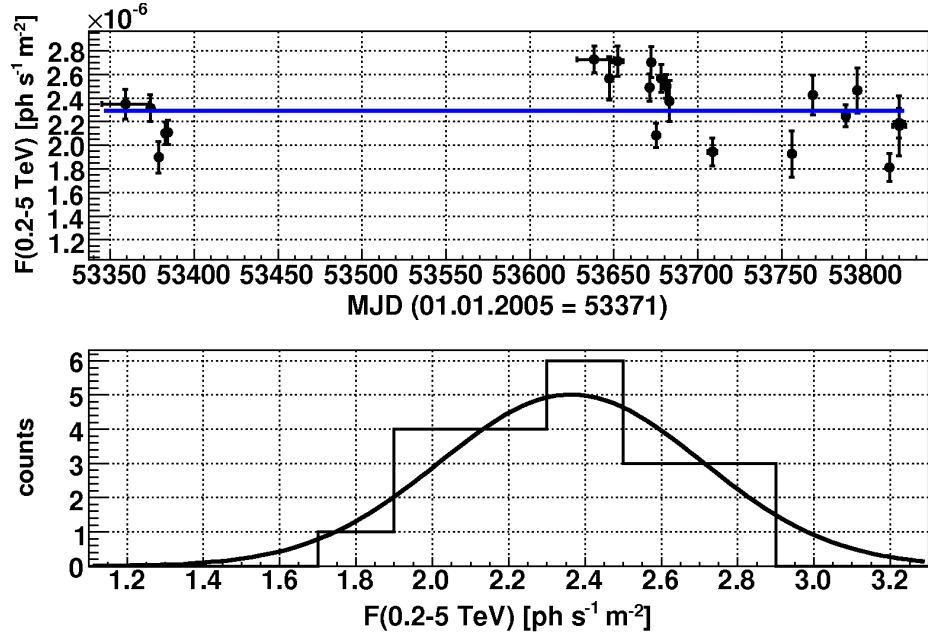


Figure 4.12: Flux of the Crab Nebula from 200 GeV to 5 TeV from on-off and wobble observations in the time from December 2004 to March 2006

#### 4.5.7 Sensitivity

Based on the results of the Crab Nebula observations, the sensitivity of the telescope above  $\sim 200$  GeV is calculated for both observation modes, assuming a Crab-like spectrum.

The sensitivity is defined as the minimal flux that can be detected with a significance of  $5\sigma$  within a certain exposure time above a certain energy threshold. Usually it is calculated by dividing the number of excess events by the square root of the scaled background events. This always overestimates the significance by a factor of  $\sim \sqrt{2}$  compared to Equation 17 from Li and Ma (1983). Here the sensitivity is calculated with both methods. In the first method the significance for the flux level of Crab can be calculated for any exposure time by simply scaling the observed significance with the square root of the exposure time. The resulting flux limit in units of the flux of the Crab Nebula is then calculated by dividing  $5\sigma$  by the total significance. In case of the Li-Ma method, the number of expected excess and background events have to be calculated according to the chosen exposure time and significance. Hereby the number of background events is determined by the measured background rate multiplied by the exposure time. The number of excess events are calculated using the number of background events, the scaling factor and the requested significance ( $5\sigma$ ). The resulting excess rate is finally

compared to the measured excess rate from the Crab analysis.

For wobble observations the scaling factor is 1/3. For on-off observations a scaling factor of unity is assumed. Note that the needed off observation is not taken into account for the calculation of the sensitivity. Table 4.4 shows the sensitivity above 200 GeV for 20 h and 50 h observation time. The scaling factor is only taken into account in the Li-Ma approach.

		$F_{>200 \text{ GeV}}$ [Crab]			
		50 h		20 h	
mode	scale	Li-Ma	$N_e/\sqrt{N_b}$	LiMa	$N_e/\sqrt{N_b}$
wobble	1/3	0.038	0.033	0.061	0.052
on-off	1	0.045	0.031	0.072	0.049

Table 4.4: Sensitivity, defined as the minimum flux detectable with  $5\sigma$  significance above 200 GeV in units of the Crab Nebula flux, calculated with two different methods.

The significance depends on three values: the number of measured signal events, the number of measured background events and the scaling factor, which takes different background statistics into account. Since the significance of a possible signal increases with increasing background statistics, the scaling factor is crucial in the determination of the sensitivity. Figure 4.13 shows the significance for a fixed number of measured signal events and scaled background events for scaling factors ranging from 0.01 to 10. Below 0.1 the significance changes only slightly, while around unity it changes strongly with the background statistics.

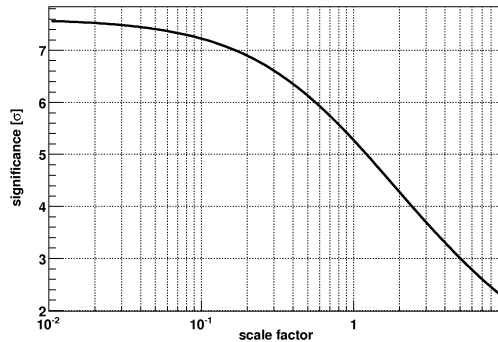


Figure 4.13: The significance calculated by Equation 17 from Li and Ma (1983) vs. the scaling factor for a fixed number of excess events (250) and scaled background events (1000).

# Chapter 5

## Muons

Single muons reach the observation level frequently. Above  $\sim 6$  GeV muons produce Cherenkov light in the atmosphere. For small impact parameters, the Cherenkov light cone of the single muon gives a well defined image in the camera, which can be used to monitor the performance of the telescope. With increasing impact parameter, the image of the muon looks more like the image of a gamma shower, which makes it a strong source of background. In the following chapter first the characteristic properties of muon images are described. In Section 5.2 follows the description of the analysis method, which is mainly an improvement of the method shown by Meyer (2004). In Section 5.3 the implementation of the absolute light calibration as well as of the PSF measurement in the automatic analysis is described. In Section 5.4 the contribution of single muons to the background is investigated.

### 5.1 Muon image in the Cherenkov telescope

#### 5.1.1 Dependence on the impact parameter

Two cases have to be differentiated. Incidence of the muon inside and outside the reflector (see Fig. 5.1). If the muon hits the reflector a complete ring is projected in the focal plane (Fig. 5.2, left panel). Depending on the angle of incidence, the ring can be truncated by the border of the camera. If the impact parameter is larger than the radius of the reflector, only a segment of the Cherenkov light cone is inside the reflector, resulting in an image of a ring segment (Fig. 5.2, right panel). With increasing impact parameter the opening angle of the ring segment decreases and therefore also the curvature of the image. This leads to a shape of the image very similar to the one of a gamma shower at low energies ( $< 150$  GeV, see also Fig. 5.16 in Section 5.4).

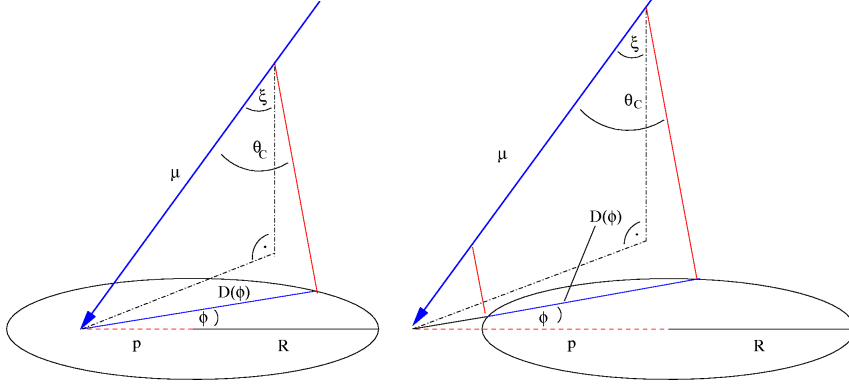


Figure 5.1: Incidence of the muon inside (left panel) and outside (right panel) of the reflector (Meyer, 2004);  $p$  = impact parameter of the muon;  $R$  = radius of the reflector;  $\xi$  = angle of incidence of the muon;  $\theta_C$  = Cherenkov angle;  $\Phi$  = azimuth angle;  $D(\Phi)$  = number of photons hitting the reflector depending on the azimuth angle.

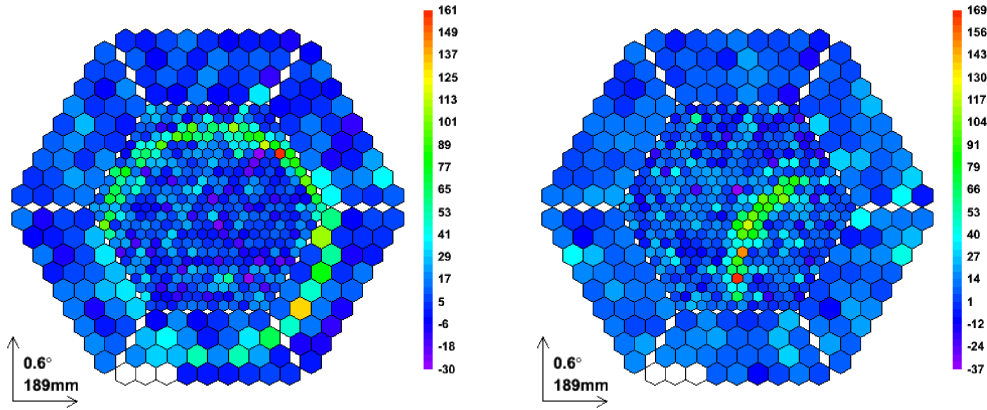


Figure 5.2: Images of muons in the MAGIC camera (after calibration and pedestal subtraction). Left panel: Complete ring. Right panel: Ring segment with an opening angle of  $\sim 90^\circ$ . The colour scale denotes the pixel content in photoelectrons.

Not only the shape of the image, but also the light distribution inside the image depends on the impact parameter. If the muon hits the centre of the reflector, the light distribution  $D(\Phi)$  along the ring is homogeneous (not depending on the azimuth angle  $\Phi$ ). With increasing impact parameter the Cherenkov light cone in a decreasing azimuth range covers an increasing part of the reflector. The azimuthal intensity distribution of the ring image has therefore a maximum and a minimum. Figure 5.3 shows the expected

intensity distribution for different impact parameters. For more details see Vacanti et al. (1994) and Meyer (2004).

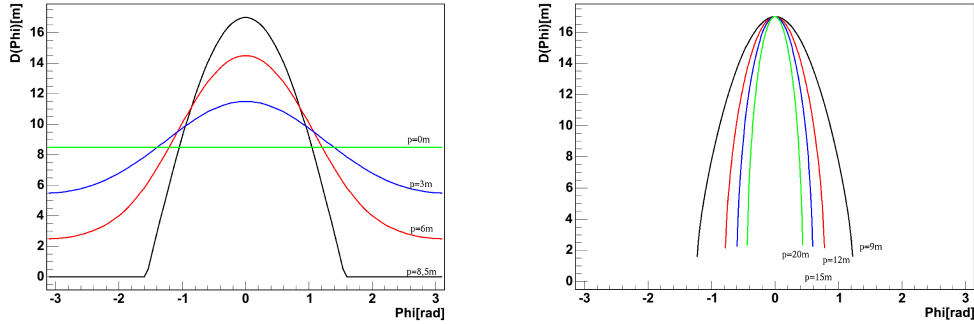


Figure 5.3: Intensity distribution along the ring for different impact parameters  $p$  (Meyer, 2004). The radius of the reflector is  $R = 8.5$  m.

### 5.1.2 Width of muon ring images

If the Cherenkov light of the incoming muon would be exactly parallel and the mirror would be perfect, the width of the muon ring image would be infinitesimal. Several reasons cause a broadening of the ring. They can be differentiated into atmospheric and technical reasons. A detailed description can be found in Vacanti et al. (1994) and Meyer (2004). In the following the main reasons are summarised.

#### 1. Atmospheric reasons:

- dependence of the index of refraction from the altitude.  
With increasing index of refraction in lower altitude the Cherenkov angle increases and the emitted light is no longer parallel. The relative broadening decreases with increasing energy, as the Cherenkov angle itself is increasing up to a limiting value. Above  $\sim 10$  GeV it reaches a constant value of  $\sim 2.5\%$ .
- dependence of the index of refraction from the wavelength.  
Since the index of refraction in air is decreasing with increasing wavelength, photons at longer wavelength are emitted under a smaller angle. The relative broadening depends on the bandpass of the measured Cherenkov spectrum. It decreases fast with increasing energy of the muon and reaches a value of  $\sim 1\%$  for MAGIC.

- multiple scattering.  
Because of Coulomb scattering of the muon in the atmosphere, the Cherenkov photons in the focal plane are scattered around their expected position. It can also happen, that the muon is scattered only once, changing the direction slightly, which leads to the superposition of two ring images. The scattering is strongly energy dependent and dominates the total ring broadening below  $\sim 15$  GeV.
- ionisation losses.  
The muon loses energy by ionisation, which decreases the Cherenkov angle. It gives a significant contribution only at low energies and can be neglected above  $\sim 8$  GeV.

2. Technical reasons:

- finite pixel size.  
There is an uncertainty in the determination of the radius of the muon ring due to the discretisation of the image in the camera. For the MAGIC telescope with a pixel size of  $0.1^\circ$  (inner camera), the contribution to the broadening is negligible.
- aberration.  
As the MAGIC telescope has a parabolic mirror, there is no spherical aberration. However, there is the coma effect, which gets stronger with increasing angle of incidence. In average this leads to  $\sim 6\%$  broadening, which dominates the total broadening at energies above  $\sim 20$  GeV.

Figure 5.4 shows all contributions together with their energy dependence. In addition there can be a dominating broadening from misfocussing of the mirror. Therefore the comparison of the width of simulated and observed muon ring images can be used to determine the total PSF of the optical system.

## 5.2 Analysis of single muon events

The method was developed by Meyer (2004). Here the main steps of the analysis are recapitulated and improvements are shown. The improvements are mainly based on the use of the arrival time information for the image reconstruction.

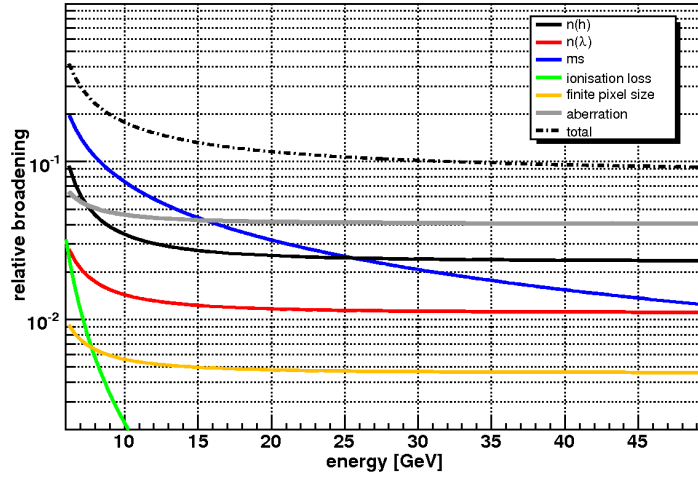


Figure 5.4: Different contributions to the relative broadening of the muon ring vs. the energy of the muon.

### 5.2.1 Image reconstruction

As new image parameters, the radius of the muon ring (*radius*), the width of the ring (*arcwidth*), the light content of the muon events (*muonsize*), and the length of the ring, measured as an angle from the centre of the ring (*arcphi*), are introduced.

First the event is fitted by a ring after the standard image cleaning. To speed up the analysis only events with a *size* above 150 phe are used, as the muon ring images are bright events. Since the radius of the muon ring represents the Cherenkov angle only events with *radius* between  $0.6^\circ$  and  $1.35^\circ$  are used. Below  $0.6^\circ$  the reconstruction gets worse and  $1.35^\circ$  is already larger than the maximum of the Cherenkov angle in the atmosphere at this altitude. Also the quality of the fit is taken into account for the exclusion of events from the further analysis.

To reconstruct the length of the ring, all pixels within a margin of  $0.2^\circ$  around the radius and with a certain time coincidence are taken into account, even if they were removed in the image cleaning before. To define the coincidence window, first the mean arrival time of the core pixel is calculated. Then the difference between the mean arrival time and the arrival time of each pixel, located within the margin around the circle, is filled in a histogram, which is fitted by a Gaussian distribution. The coincidence window is then given as two standard deviations from the mean value. The idea is now to walk along the circle to reconstruct the azimuthal intensity distribution. Starting point is above the circle centre along the y-axis in the

camera plane. For each pixel the angle between the starting point and the position of the pixel, called  $\phi$ , is calculated and its light content is filled in a profile histogram. The ring segment is defined as the successional part of the circle above a certain threshold. The threshold is determined empirically by a test sample. The length of the segment is called *arcphi* and is measured as an angle, where  $360^\circ$  correspond to a complete ring. For *arcphi*  $> 180^\circ$  the impact of the muon has to be smaller than the radius of the reflector. All rings with  $180^\circ < \textit{arcphi} < 360^\circ$  are usually truncated by the border of the camera (or the intensity in a part of the ring is below the threshold). To avoid misassigned muon rings, only events with *arcphi*  $> 190^\circ$  are assumed as "full" rings. The use of a profile histogram makes the threshold value independent from the total brightness of the event. The sum of the light content of all pixels, which do belong to the ring segment defines the *muonsize*. This parameter is usually larger than the *size* calculated after image cleaning, because additional pixels with low intensity are included if their arrival time is within the coincidence window.

The width of the muon ring is determined from a Gaussian fit to the radial intensity distribution with respect to the centre of the ring. In the original approach, a correlation between the width of the ring and the pedestal rms was found using a large sample of sequences. This was due to a pedestal rms-dependent off-set that biased the Gaussian fit. To avoid this effect, the distribution is now fitted by a Gaussian distribution with an additional constant. Also the fit region is now determined by a threshold value. The original histogram is replaced by a profile to make this threshold independent of the total brightness of the event.

### 5.2.2 Monte Carlo simulation

The simulation programs are described in Section 4.4.1. A large sample of  $3.01 \times 10^9$  muons has been simulated with vertical incidence. The energy spectrum follows a power law with a spectral index of -2.71, according to a power law fit of the muon spectrum as measured on mountain altitude by the BESS spectrometer (Sanuki et al., 2002) above 20 GeV, where the hardening of the spectrum due to the decay of muons is almost negligible. The simulated energy ranges from 6 GeV to 200 GeV. Around 6 GeV, muons start to emit Cherenkov radiation in the atmosphere. Above 200 GeV muons contribute less than 0.5% to the integral flux above 6 GeV. The energy spectrum after image cleaning peaks slightly above 10 GeV (see Figure 5.5). At 6 GeV the trigger efficiency is  $< 0.1\%$ .

The starting altitude is  $280 \text{ g cm}^{-2}$ , corresponding to  $\sim 10$  km above sea level, which is roughly the height of the maximal muon flux (e.g. Grupen,

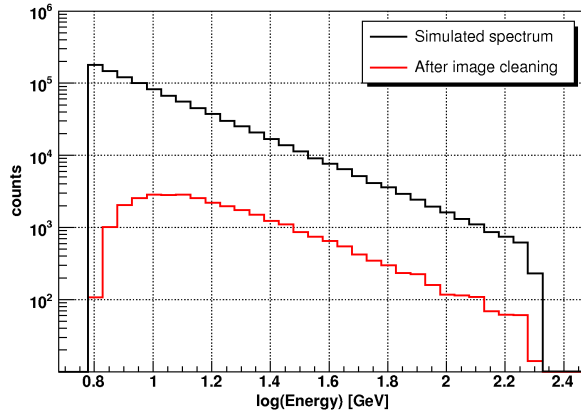


Figure 5.5: The simulated muon spectrum (black) and the spectrum after image cleaning (red) for a subsample of  $1 \times 10^6$  simulated muons.

2000). For the simulation of the atmosphere, the model for the average atmosphere on La Palma during Winter, as developed by Haffke (2007) is used. The goal is to simulate all muons that could trigger the telescope<sup>1</sup>. Therefore the maximum impact parameter as well as the maximum angle of incidence have to be determined beforehand. Figure 5.6, left panel, shows the distribution of the squared impact parameter  $p^2$  after trigger. Above  $p \approx 100$  m a cut-off in the number of triggered muon events can be seen. At the maximal simulated impact  $p = 120$  m, the number is almost zero. The right panel of Figure 5.6 shows the distribution of the squared angle of incidence with respect to the optical axis of the telescope after trigger. The maximal simulated angle was  $2.3^\circ$ . Above  $\sim 2.2^\circ$  the trigger efficiency is already below 1%.

### 5.2.3 Monte Carlo comparison

The distributions of the muon image parameters *radius*, *arcwidth* and *arcphi* of simulated muons are compared with muon events extracted from a data sample of the Crab Nebula (see Appendix B.2). The distribution of *radius* shows a small systematic shift between simulated and observed muons. While the distribution of the simulated muons peaks in the bin from  $1.20^\circ$  to  $1.25^\circ$ , the peak for the observed muons is below  $1.2^\circ$ . This could be related to a systematic difference in the index of refraction. Since the radius of the ring image is equal to the Cherenkov angle, it depends only on the index of refraction for muons above  $\sim 20$  GeV ( $\beta \rightarrow 1$ ). A higher index of refraction would therefore lead to a larger radius. The *arcwidth* distributions are in

<sup>1</sup>Again "after trigger" here means actually after image cleaning.

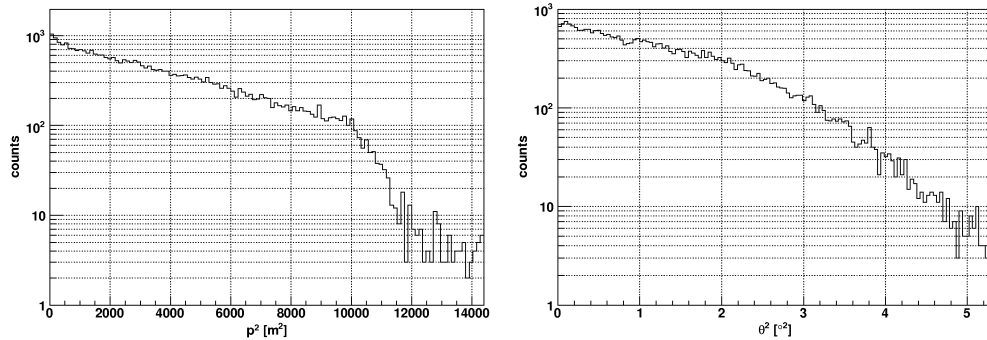


Figure 5.6: Left panel: Distribution of the squared impact parameter  $p^2$  after image cleaning. Right panel: Distribution of the squared angle of incidence  $\theta^2$  after image cleaning.

good agreement. The simulation is made with an additional spot size of 12 mm, resulting in a total PSF of 13.9 mm. Also the *arcphi* distributions agree quite well, yielding a good reconstruction of the ring segment. There is a tendency for a slightly higher number of large ring segments in the simulation compared to the observed muon events.

### 5.3 Calibration and point spread function

There is no absolute calibration for IACTs as there is no artificial VHE gamma-ray source, which one can easily switch on and off. As shown in Chapter 4.1.1, the calibration of the detector response is performed by an artificial light source, mounted in the centre of the reflector dish. This allows to calibrate the relative response of each single PMT in the camera, while the reflector performance and the atmospheric conditions are not taken into account. As first shown by Vacanti et al. (1994), the light content of muon ring images can be used to calibrate the total light response of the detector including the mirrors as well as the current atmospheric conditions.

Since the structure of the telescope is bended depending on the elevation, the mirrors have to be refocussed using the active mirror control (AMC). It was shown by Meyer (2004) with data from the MAGIC telescope that the broadening of muon ring images can be used to calculate the PSF of the optical system.

In the following section, the implementation of the muon ring analysis in the standard analysis is described and the results from the calibration as well as the monitoring of the PSF is shown for all data of cycle 1 (= 12/2004 - 03/2006) of MAGIC observations.

### 5.3.1 Implementation in the automatic analysis

The muon analysis is implemented in STAR, where the image cleaning and the calculation of all image parameters is performed. To speed up the processing time, the calculation is done in several steps, using cuts to keep only possible ring event candidates:

1.  $size > 150$  phe  $\rightarrow$  ring fit
2.  $0.60^\circ < radius < 1.35^\circ$  and standard deviation of the fit below  $0.15^\circ$   
 $\rightarrow$  calculation of  $arcwidth$ ,  $arcphi$  and  $muonsize$
3.  $arcphi > 190^\circ$   $\rightarrow$  classification of complete rings
4.  $0.04^\circ < arcwidth < 0.2^\circ$  to remove outliers

All image parameters (including the standard parameters as described in Section 4.1.7) for muon ring candidates are stored in a separate tree, called "Muons".

### 5.3.2 Monitoring of the point spread function

Since the muon ring image has an intrinsic width, a direct calculation of the contribution from the optical system is difficult. However it can be determined by the comparison of the  $arcwidth$  distribution of observed muons with simulated ones with known PSF. For an automatic analysis it is important to reduce the comparison to a single parameter. Figure 5.7 shows the distribution of the relative broadening  $arcwidth/radius$  vs.  $radius$  in a profile histogram for data of the Crab Nebula (Sequ. 70695).

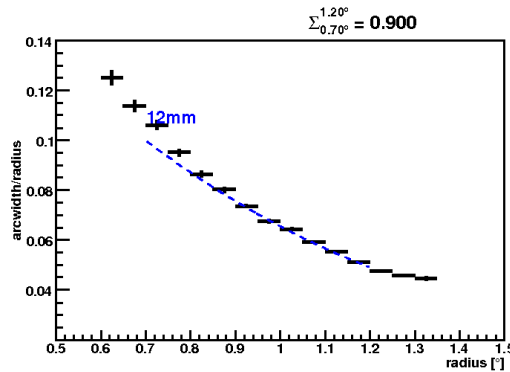


Figure 5.7: The relative ring broadening  $arcwidth/radius$  vs.  $radius$  for data of the Crab Nebula (Sequ. 70695). The blue dashed line represents a fit to the same distribution for simulated muons with an additional spot size of 12 mm (13.9 mm total PSF).

To get a representative quantity the bin contents from  $0.7^\circ$  to  $1.2^\circ$  are summed ( $= \textit{sumpsf}$ ). Since the radius of the rings correlates with the energy of the muon, the influence of spectral changes (e.g. due to higher ZD) to this quantity is minimised. Small and large radii are excluded to avoid border effects from the radius distribution.

Figure 5.8 shows  $\textit{sumpsf}$  over the total PSF of simulated muons (additional spot size: 8 mm, 10 mm, 12 mm, 14 mm and 16 mm) together with a linear regression, yielding:

$$\textit{sumpsf} = (0.0176 \pm 0.0016) \times \left( \frac{\text{PSF}}{\text{mm}} \right) + (0.643 \pm 0.022) \quad (5.1)$$

Using this fit the PSF is calculated for every sequence.

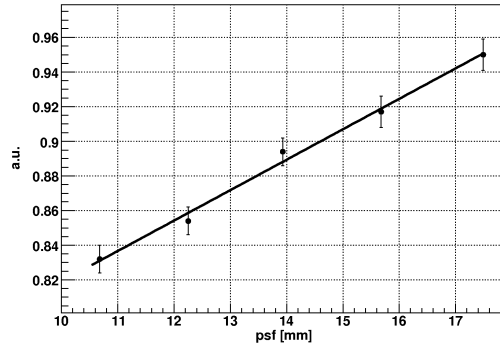


Figure 5.8: The quantity  $\textit{sumpsf}$  vs. the total PSF in mm for five samples of simulated muons with different spot sizes together with a linear regression.

Figure 5.9 shows the PSF for all sequences from December 2004 to March 2006, which contain more than 300 reconstructed muon ring events (corresponding to  $\sim 5$  min observation time). From December 2004 to April 2005 the PSF is around 20 mm, which is 50% more than the intended value. At the end of April 2005 the mirror was completely realigned, resulting in a drop of the PSF from 20 mm to 13 mm. In the following five months, the PSF was continuously increasing again. Until the end of 2005 the mirrors were focussed using the so-called laser adjustment, where each panel is moved to a position which is controlled by a laser beam, mounted in the centre of the panel. It was found that the degradation of the AMC was caused by the lasers themselves, by changing their relative position with respect to the panel. From October 2005 to March 2006 the PSF is stable around 16 mm. After a new calibration of the AMC, so called look-up tables are used instead of the laser adjustment. In that method, the panels move to fixed positions depending on the elevation, which are determined once before. In

the distribution of the PSF over time some outliers can be seen. Most of them are related to data taken under moonlight condition resulting in higher discriminator thresholds and pedestal rms. Since the simulation is performed with dark night conditions, the results for these sequences are not reliable. The usual spread of the PSF measurement in one period (where degradation effects can be neglected) lies around 1.5 mm.

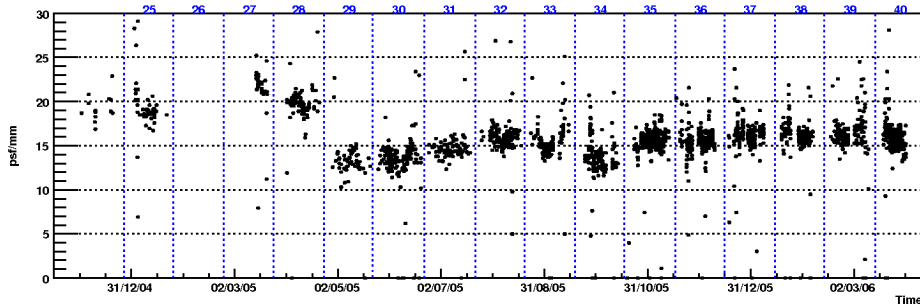


Figure 5.9: The point spread function of the optical system, as calculated from the comparison of the width of observed muons and simulated ones over the complete cycle 1.

Since the simulation is performed for vertical incidence only, it is investigated if there is any dependence of the PSF on the ZD. Figure 5.10, left panel shows the PSF vs. the average ZD of each sequence for the complete cycle 1. In addition to the cut in the number of muons, only sequences with pedestal rms between 0.7 phe and 1.2 phe are taken into account. The left panel indicates a decrease of the PSF with increasing ZD. If compared to Figure 5.9 almost all sequences with  $PSF > 18$  mm are taken before May 2005, when the mirror was in a bad condition. The right panel of Figure 5.10 shows the same distribution as the left one, but for data after April 2005 only. There is still the tendency of a decrease of the PSF with increasing ZD, but much smaller now. Compared to the spread of the distribution it is negligible below  $40^\circ$ .

### 5.3.3 Calibration with muon ring images

For the calibration the distribution of *muonsize* of observational data is compared with the one of simulated muons. The goal is to get the same total detector response for data taken under different conditions and simulated data. Also different signal extractors can lead to differences in the calibrated signal. To reduce the comparison to a single parameter, the bin contents of the profile histogram *muonsize* vs. *radius* are summed from  $0.7^\circ$  to  $1.2^\circ$  (= *sumsize*, see Figure 5.11). Again, the radius dependence minimises effects of spectral changes. For small radii the *muonsize* seems to

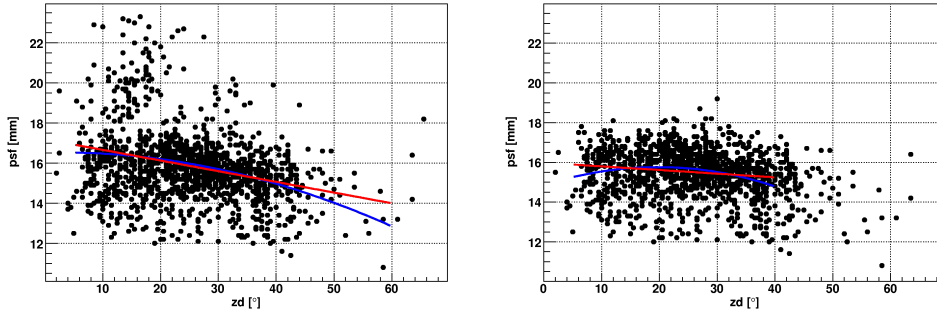


Figure 5.10: The point spread function of the optical system vs. the ZD together with a parabolic and a linear fit. Left panel: For all sequences (12/2004 - 03/2006). Right panel: Sequences after April 2005.

be overestimated. Despite the low statistics at these radii, the fraction of incorrectly reconstructed images is higher. At large radii the *muonsize* is underestimated. This can be understood taking into account a fraction of events with overestimated radii. To avoid these border effects of the *radius* distribution, these bins are not taken into account.

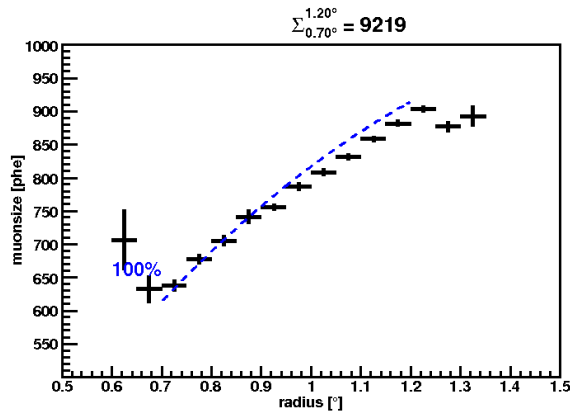


Figure 5.11: The image parameter *muonsize* vs. *radius* for data from the Crab Nebula (sequ. 70695). The blue dashed line represent a fit to the same distribution for simulated muons.

For the simulated muon samples with five different values for the PSF, the average value of *sumsize* is taken as the reference value. The parameter *ratio* gives the ratio of *sumsize* for any sequence of observed data to this reference value (multiplied by 100). The average response is then corrected by this value. Although every sequence could be calibrated separately, this second calibration is at the moment only performed for a complete observation period. The calibration is done in two steps: first the average value of

*ratio* is calculated for a complete period with some sequences, which are calibrated using the F-factor method; afterwards the data are calibrated again, whereas the conversion factor of each pixel is corrected by the average *ratio*. Figure 5.12 shows the *ratio* for all sequences from December 2004 to March 2006 after the second calibration. Again only sequences which contain more than 300 reconstructed muon ring images are shown.

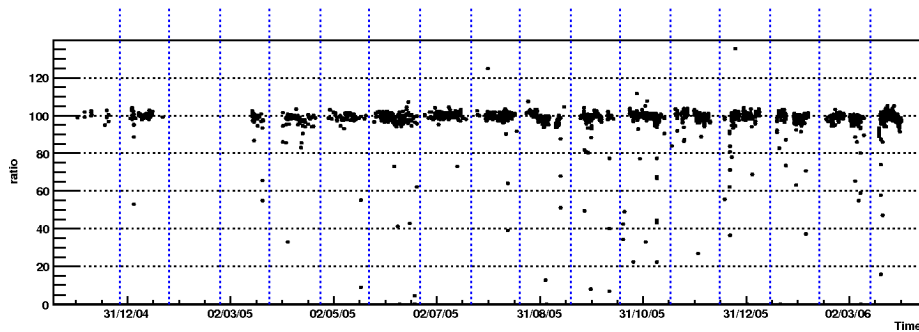


Figure 5.12: Distribution of the ratio between the light intensity of observed muons and simulated ones over time (December 2004 to March 2006) after the second calibration.

Figure 5.13 shows the distribution of *ratio* together with a Gaussian fit for the same time slot. As an additional cut only sequences with pedestal rms between 0.7 phe and 1.2 phe are used. The distribution is slightly asymmetric with more events at lower *ratio* values. The mean of the Gaussian is 99.8 with a fit probability of 0.5%. If the fit range is restricted to a smaller interval around 100, the quality of the fit improves (probability 50% for a fit between *ratio* 98 and 102) and the mean value moves to 100.

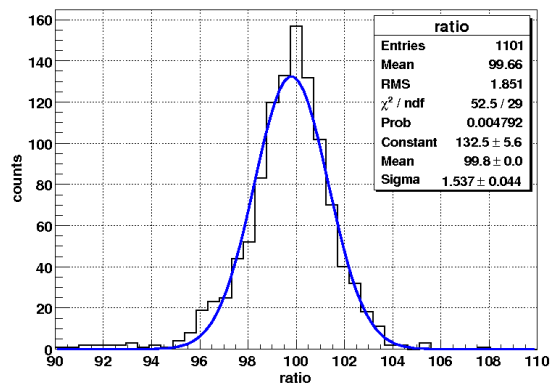


Figure 5.13: The ratio between the light intensity of observed muons and simulated ones for all sequences of cycle 1 with a pedestal rms between 0.7 phe and 1.2 phe, number of muon rings > 300 and rate after image cleaning > 150 Hz together with a Gaussian fit.

Figure 5.14 shows the correction factors ( $100/ratio$ ) from the muon analysis after the first calibration step for each observation period from December 2004 to March 2006. In some periods the pulses arrive so late that the falling edge of the pulse is outside the digitised range. In that case the signal is reconstructed using a spline instead of the digital filter. The muon analysis clearly shows that the extraction with the spline leads to a bias to larger pixel signals.

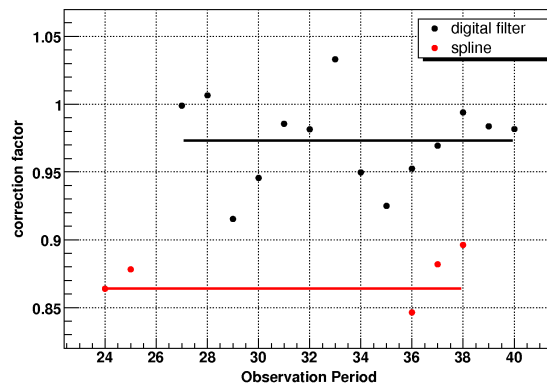


Figure 5.14: The correction factor for the average total light calibration for data extracted with the digital filter (black) and spline (red).

An uncertainty of this method comes from the different altitude of the emission. Unlike gamma showers, the Cherenkov light measured from single muons is emitted close to the telescope and therefore less affected by atmospheric absorption

## 5.4 Muon background

### 5.4.1 Gamma-background separation

In Chapter 4.3.2 it is shown that the background suppression works well above  $\sim 150$  GeV, corresponding to a *size* of roughly 200 phe, while at lower *sizes* the separation between background and signal gets worse. It was argued by Vacanti et al. (1994) that thin muon images, caused by muons with large impact parameters together with unavoidable cosmic electrons set the ultimate sensitivity limit of future single IACTs. In Figure 5.15 *area* vs. *size* is shown for observational data, simulated gamma showers and simulated muons. The muons start to contribute significantly below 500 phe. Below 200 phe they completely overlap with the distribution of the gamma showers. This phenomenon is also called the "muon wall". The black line indicates

the standard *area*-cut for the data taken in wobble mode. The efficiency of the cut is limited by the muon wall at low *sizes*. Note that the sensitivity achieved with the *area*-cut is comparable with other, more sophisticated methods, like the tree classification method *random forests* (Albert et al., 2007f, 2008a), where correlations between several image parameters are deduced from simulated gamma showers and background measurements.

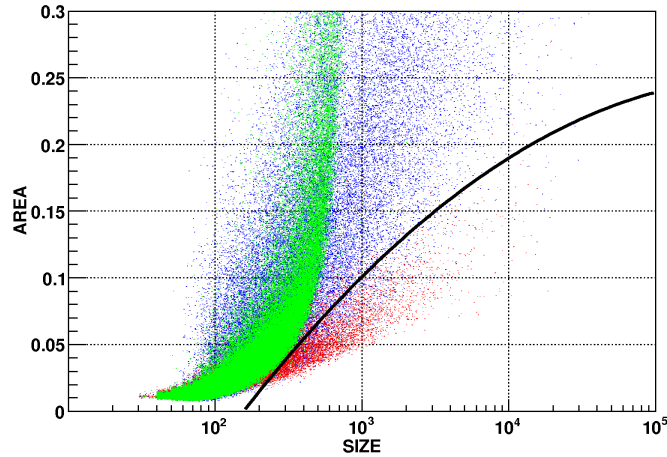


Figure 5.15: The image parameter *area* vs. *size* for simulated gamma showers (red), observational off-data (blue) and simulated muons (green) together with the used *area*-cut (black line).

Figure 5.16 shows the distribution of *width* and *length* for simulated muons and gamma showers below a *size* of 180 phe. Even if the distributions do not completely match, there is a large overlap. Taking into account that the flux of atmospheric muons is much larger than the gamma-ray fluxes, the distributions are not distinguishable.

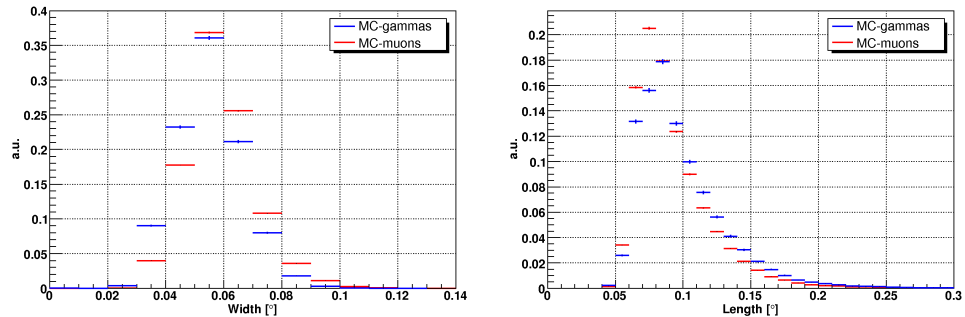


Figure 5.16: Distributions of the image parameters *width* (left) and *length* (right) for simulated muons (red) and gamma showers (blue). The distributions are scaled by their integrals.

### 5.4.2 Estimated muon rate

Based on the simulated muons, the expected muon rate for MAGIC is estimated using two different approaches: (i) the use of muon ring images to estimate the corresponding simulated observation time and (ii) the determination of the expected muon flux by direct measurements taking into account the effective collection area for muons as calculated from the simulation.

Figure 5.17, left panel, shows the rate of muons with a reconstructed ring segment of more than  $180^\circ$ , corresponding to an impact parameter of less than the radius of the reflector, vs. the data rate after image cleaning for the data from December 2004 to March 2006 with a ZD below  $30^\circ$ . Only sequences with more than 300 muons ring events and a pedestal rms between 0.7 phe and 1.2 phe are taken into account. There is some evidence for a linear correlation of both rates. The spread in the data rate is mainly dominated by weather conditions, but also the quality of the optical system can contribute to it, as the data rate is dominated by small events. The discriminator thresholds are higher for galactic than for extragalactic targets because of the usually higher night sky background light in the field of view of the galactic sources. The

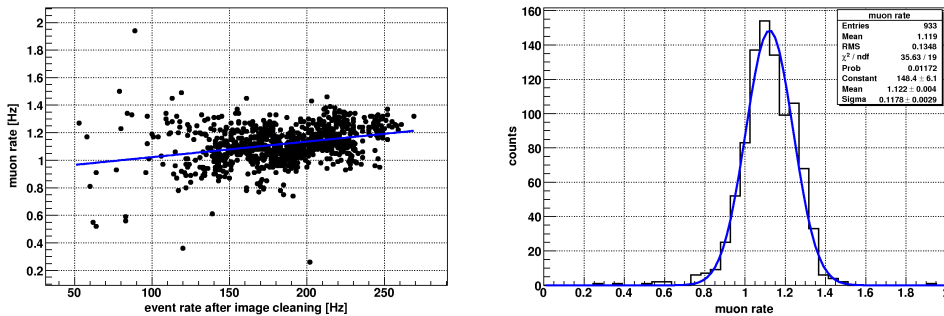


Figure 5.17: Left panel: Muon rate vs. rate after image cleaning for all sequences with more than 300 muon ring images, from December 2004 to March 2006 with ZD below  $30^\circ$  and a pedestal rms between 0.7 phe and 1.2 phe. The distribution is fitted by a linear function, yielding  $muonrate = 1.13 \times 10^{-3} datarate + 0.91$ . Right panel: The distribution of the muon rate together with a Gaussian fit, yielding a mean value of 1.12 Hz with a standard deviation of 0.12 Hz.

average trigger rate is therefore lower for these observations. The muon rate is not affected by changing discriminator thresholds as all ring images are bright events. Figure 5.17, right panel, shows the distribution of the muon rate together with a Gaussian fit. The distribution is not perfectly Gaussian, which could come from a small dependence on the data rate. At least a part of the Gaussian spread arises from the selection criteria: the number of muon events is increasing with decreasing  $arcphi$ . As the  $arcphi$  distribution

spot size [mm]	$N_\mu$ after img. cl.	efficiency	$N_{rings}$
08	944094	0.0314	7084
10	960147	0.0319	7386
12	963180	0.0320	7337
14	949270	0.0315	7222
16	918319	0.0305	6762
average	947002	0.0314	7158

Table 5.1: Number of simulated muons after image cleaning and the number of reconstructed ring images with  $arcphi > 180^\circ$  for five different point spread functions. The total number of simulated muons is  $3.01 \times 10^7$ .

is quite steep around  $180^\circ$  fluctuations in the intensity (e.g. due to weather conditions) cause fluctuations in  $arcphi$ , which lead to fluctuations in the rate of the muon ring images.

To get an estimation for the expected total muon rate, the average number of muon events after image cleaning and the number of reconstructed rings, with  $arcphi > 180^\circ$  are taken from the simulation (see Table 5.1). Taking the average muon rate of 1.12 Hz, the simulated muon sample would correspond to an observation time of  $(7158/1.12) \text{ s} = 6391 \text{ s}$ . This results in an expected total muon rate of 148 Hz. The uncertainty from figure 5.17 is  $\sim 10\%$ . This would mean that the data are completely dominated by muon events. At least for a data rate around 150 Hz, this muon rate is too high. The ratio from muon rings to muons after image cleaning seems to be overestimated. Different weather conditions will lead to different trigger rates. The rate of large muon rings will be less affected, as these are bright events, caused by muons with small impact parameters. However, the muon rate after image cleaning is dominated by faint events, caused by muons with large impact parameters, which will be more sensitive to the weather conditions. Another systematic difference arises from the fact that all muons are produced in hadron showers, while only single muons are simulated. In the observational data, ring images can be overlapped by other parts of the shower and then the ring analysis fails.

In the second approach, the muon spectrum as measured by the BESS spectrometer on an altitude of 2700 m a.s.l. (Sanuki et al., 2002) is used. To be independent from muon decay, the spectrum is fitted by a power law above 20 GeV, 25 GeV and 30 GeV, yielding slopes of -2.71, -2.77 and 2.75, respectively. For the simulation parameters (energy range from 6 GeV to 200 GeV, impact parameters up to 120 m and a solid angle from 0 to 0.005062 sr) this would correspond to a simulated muon rate of  $(6010.8 \pm$

204.4) Hz. Taking the average efficiency of  $(0.0314 \pm 0.0006)$ , the muon rate after image cleaning is  $(170.4 \pm 6.6)$  Hz. The error reflects the pure statistical uncertainty from the fit to the muon spectrum and the spread in the efficiency for the different samples. Again the efficiency can be overestimated, at least for suboptimal weather conditions. Another uncertainty comes from the spectrum itself, as an interpolation from 20 GeV to 6 GeV was used. Due to the steep power law, the total flux is dominated by the extrapolated energy range.

# Chapter 6

## Search for gamma-ray emission

In the following chapter the observation program is described (Sect. 6.1 and 6.2) and the results of the analysis are shown (Sect. 6.3 and 6.4). In total 13 data samples of 12 objects are analysed in this work. The results are discussed in the Chapters 7 and 8.

### 6.1 Sample selection

All HBL objects detected at VHE gamma-rays so far are among the brightest X-ray sources of their class. At least several of them show a comparable luminosity at gamma-rays than in the X-ray regime. In the simplest leptonic model for the broad-band emission, the single zone SSC model, the VHE flux has to be correlated with the X-ray flux, as the photons in both bands are produced by the same population of relativistic electrons. Furthermore the energy density of the magnetic field  $u_B$  should be equal to the energy density of the photon field  $u_{ph}$ , although this can be different in a state of high activity. This would lead, at least for a quiescent state, to the same energy output in the synchrotron as in the Inverse Compton regime and therefore to comparable peak luminosities<sup>1</sup>.

The observed sample is based on the blazar compilation of Donato et al. (2001) which contains 421 X-ray spectra of 268 blazars (136 HBLs). The X-ray data are complemented by the radio flux at 5 GHz, the optical flux in the V-band and the redshift, if available. The purpose of this compilation is to have the most complete ensemble of spectral information (fluxes and spectral indices) in the X-ray band from 0.1 keV to 10 keV for all known blazars. The X-ray fluxes are given as the monochromatic fluxes at 1 keV. If in the literature an integral flux was reported, the flux at 1 keV was calcu-

---

<sup>1</sup>This is only strictly valid in case of Thomson scattering; see also Chapter 8.

lated using the measured spectral index. The compilation includes data from five X-ray satellites: *Einstein*, EXOSAT, ROSAT, ASCA and BeppoSAX. Unfortunately this compilation is not a complete catalogue. This problem is discussed in Chapter 9. The following selection criteria are used to obtain the sample:

$$\begin{aligned} z &< 0.3 \\ ZD(\text{at culmination}) &< 30^\circ \\ F(1 \text{ keV}) &> 2 \mu\text{Jy} \end{aligned}$$

The redshift criterium ensures low absorption at the energy threshold of the telescope. For an object at  $z = 0.3$  the optical depth at 200 GeV is 0.49 (Kneiske in preparation, see also Section 1.4), resulting in 39% absorption. The second criterium is complementary to the first one. As the energy threshold increases with ZD, all observations are performed below  $40^\circ$ . Therefore only objects which culminate at La Palma below  $30^\circ$  are selected. This ensures a trigger threshold below the analysis threshold of  $\sim 200$  GeV. As most of the established TeV sources show comparable luminosities at X-rays and VHE  $\gamma$ -rays, only the X-ray brightest HBLs are selected, leading to the cut at  $2 \mu\text{Jy}$ . Assuming the same luminosity at  $\sim 200$  GeV, it corresponds to  $\sim 7\%$  of the flux of the Crab Nebula which would be detectable for MAGIC within 15 h.

Table 6.1 shows the complete set of objects which satisfy the selection criteria. The total number amounts to 15. The sample includes the well studied TeV sources Mrk 421 and Mrk 501 as well as two other objects, 1ES 2344+514 and 1ES 1426+428, known as TeV sources before the beginning of this campaign.

For the object RX J1725.0+1152 the redshift of 0.018 was recently revised by Sbarufatti et al. (2006) into a lower limit of 0.17. Also the redshift of 1ES 1011+496 was corrected from 0.200 to 0.212 by a recent measurement (Albert et al., 2007e). The redshift of 1ES 1218+304, given as 0.130 by Donato et al. (2001), was corrected to 0.182 (e.g., Véron-Cetty and Véron, 2003). The average flux at 1 keV for RX J0319.8+1845 is slightly below  $2 \mu\text{Jy}$ . This value is based on three measurements, yielding fluxes from  $0.17 \mu\text{Jy}$  to  $3.06 \mu\text{Jy}$ . In addition also the object RX J1058.6+5628 yields one measurement with a flux slightly above  $2 \mu\text{Jy}$ . The average flux from three measurements is  $1.24 \mu\text{Jy}$ . As this object shows also a very bright star in the field of view of the MAGIC camera, the object was skipped from the list of targets. It is a general problem to apply a cut on the flux for an object class, which is characterised by strong variability on different time scales.

source	RA	dec	$z$	F(1keV) [ $\mu$ Jy]	$\Gamma$
1ES 0120+340	01 23 08.9	+34 20 50	0.272	4.34	1.93
RX J0319.8+1845	03 19 51.8	+18 45 35	0.190	1.76	2.07
1ES 0323+022	03 26 14.0	+02 25 15	0.147	3.24	2.46
1ES 0414+009	04 16 53	+01 04 54	0.287	5.00	2.49
1ES 0806+524	08 09 49.2	+52 18 58	0.138	4.91	2.93
1ES 0927+500	09 30 37.6	+49 50 24	0.188	4.00	1.88
1ES 1011+496	10 15 04.2	+49 26 01	0.212	2.15	2.49
Mrk 421	11 04 27.3	+38 12 31.8	0.030	39.4	2.96
1ES 1218+304	12 21 21.9	+30 10 37	0.182	8.78	2.34
RX J1417.9+2543	14 17 56.6	+25 43 25	0.237	3.58	2.25
1ES 1426+428	14 28 32.5	+42 40 25	0.129	7.63	2.09
Mrk 501	16 53 52.2	+39 45 36.6	0.034	20.9	2.25
RX J1725.0+1152	17 25 04.4	+11 52 16	$> 0.17$	3.60	2.65
1ES 1727+502	17 28 18.6	+50 13 11	0.055	3.68	2.61
1ES 2344+514	23 47 04.9	+51 42 18	0.044	4.98	2.18

Table 6.1: Complete set of objects which satisfy the selection criteria as described in the text. In addition to the position, the redshift as well as the flux at 1 keV together with the index of the differential energy spectrum are listed (Donato et al., 2001). In case of several measurements, the given numbers are the average values.

## 6.2 Observations

The observations were performed in cycle 1 of scheduled MAGIC observations, which started in December 2004 and lasted until the beginning of April 2006. Table 6.2 shows all observations with the MAGIC telescope of the objects listed in Table 6.1. The cycle 1 observations of Mrk 421 and Mrk 501 are discussed in detail in Albert et al. (2007c) and Albert et al. (2007g) respectively. Also the discovery of VHE emission from 1ES 1218+304, which is based on the observations in January 2005, is discussed in detail elsewhere (Albert et al., 2006d; Bretz, 2006). The observation of 1ES 1727+502 was postponed to cycle 2. All observation times are after quality selection. All sequences analysed in this work are listed in Appendix C together with the most important quality parameters.

source	mode	$\langle ZD \rangle$ degr.	season	exp. [h]
1ES 0120+340	wobble	12.2	2005 Aug-Sep	14.9
RX J0319.8+1845	on	14.3	2004 Dec-2005 Feb	6.9
	wobble	14.2	2005 Sep-2006 Jan	4.7
1ES 0323+022	wobble	29.0	2005 Sep-Dec	11.4
1ES 0414+009	wobble	29.7	2005 Dec-2006 Jan	17.8
1ES 0806+524	wobble	26.8	2005 Oct-Dec	17.5
1ES 0927+500	wobble	22.1	2005 Dec-2006 Mar	16.1
1ES 1011+496	wobble	23.6	2006 Mar-Apr	14.5
Mrk 421	wobble	9.2 - 55.0*	2004 Nov-2005 Mar	25.6
1ES 1218+304	on	< 13*	2005 Jan	8.2
	wobble	26.6	2006 Jan-Mar	14.6
RX J1417.9+2543	on	9.7	2005 Apr-Jun	13.0
1ES 1426+428	on	16.6	2005 Mar-Dec	6.1
Mrk 501	on	< 30*	2005 May-Jul	31.6
RX J1725.0+1152	on	17.4	2005 Apr	5.3
1ES 1727+502	-	-	-	0
1ES 2344+514	wobble	27.6	2005 Aug-2006 Jan	23.1

Table 6.2: Cycle 1 HBL observations with the MAGIC telescope. The table lists the observation mode as well as the mean ZD of the observation, the season and the effective observation time after quality selection (exp.). Numbers marked by an asterisk refer to the maximum ZD instead of the mean value.

## 6.3 Analysis

If an observation does not result in a significant detection, an upper limit on the integral flux above the energy threshold is calculated.

### 6.3.1 Method of upper limit calculation

First the upper limit (UL) on the excess rate is calculated. This is done with the method of Rolke et al. (2005) in the implementation of the class TROLKE within the ROOT framework. The confidence interval is computed for the number of excess events of a Poisson distributed signal in the presence of background with a fully frequentist treatment of the uncertainties in the background estimate, using the profile likelihood method. It provides seven models, depending on the kind of the background distribution (Gaussian, Poisson, known) and the so-called efficiency (Gaussian, Binomial, known).

In this work, model 4 is used, which makes the following assumptions:

- Poisson uncertainty in the signal (as in all models);
- Poisson uncertainty in the background estimate;
- known efficiency.

The efficiency can be interpreted as a systematic uncertainty. Here the confidence intervals are calculated, taking into account only the statistical uncertainty. The model depends on the following parameters:

- number of observed background events;
- number of events in the signal region;
- ratio of background to signal statistics;
- confidence level (CL).

An advantage of this method is that different statistics of signal and background are taken into account. A higher background statistic can therefore decrease the confidence interval. Another advantage comes from the concept of the confidence intervals. Choosing a confidence level of 99.7%, a signal with a statistical significance of more than three standard deviations would lead to a lower limit that is not consistent with zero. In principle, the confidence interval can be calculated without an a priori selection in detections and non-detections.

To convert the upper limit on the excess rate into a flux, the upper limit is compared to the excess rate of the Crab Nebula. Since the excess rate of different Crab Nebula observations show deviations up to 20% from the mean value, the excess rate is plotted against the background rate to search for possible correlations (Fig. 6.1). For the observations in on-off mode a linear regression yields ( $\chi^2/\text{n.d.o.f.} = 26/14$ ):

$$excess = (0.946 \pm 0.102) \times background + (0.23 \pm 0.93)$$

While the excess rate for on-off observations is indeed correlated to the background rate, a fit to the data taken in wobble mode is quite poor, yielding ( $\chi^2/\text{n.d.o.f.} = 13.5/3$ ):

$$excess = (1.26 \pm 0.30) \times background - (1.51 \pm 1.93).$$

As a fit by a constant is even worse, the linear regression is used to calculate the reference excess rate from the Crab Nebula. The Crab units are converted

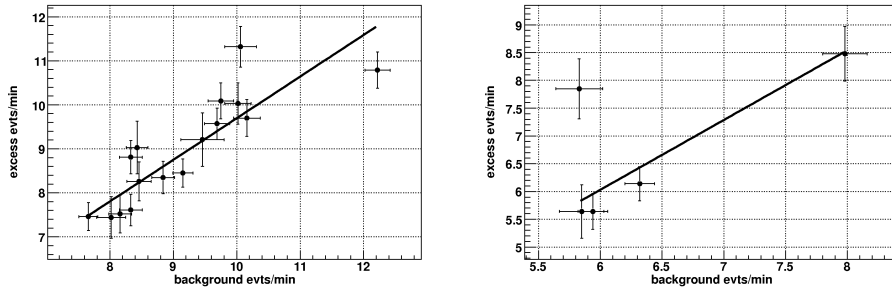


Figure 6.1: Excess rate vs. background rate for observations of the Crab Nebula in on-off (left) and wobble mode (right).

into an integral flux of photons  $\text{cm}^{-2} \text{s}^{-1}$  using the spectrum of the Crab Nebula as given by Equation 4.17.

As an alternative method, the conversion from excess rate to an integral flux can be calculated from simulated gamma showers. Hereby the effective area above a given energy threshold is determined as well as the spillover factor. As an example, the effective area for gamma-rays above 190 GeV is calculated for 1ES 0120+34.0, assuming a Crab spectrum. This results in an upper limit of  $F(> 190 \text{ GeV}) < 7.7 \times 10^{-12}$  photons  $\text{cm}^{-2} \text{s}^{-1}$ , which is 5.5% higher as derived in comparison with the flux from the Crab Nebula (see Table 6.3) and well within the systematic uncertainties of the method.

The energy threshold of the analysis is determined by simulated gamma showers as described in Chapter 4.5.3. The exact ZD distribution is thereby taken into account. Unfortunately, the threshold depends also on the source spectrum which is not known in case of non-detected objects.

The systematic error for the flux level is estimated to be in the order of  $\sim 30\%$ . The main contributions are uncertainties of the atmospheric conditions, the mirror reflectivity and the effective quantum efficiency of the PMTs (see also Albert et al., 2008a, and the discussion therein). In case of the UL determination, there is also the uncertainty of the correct energy threshold due to the unknown spectrum.

### 6.3.2 Analysis results

Within this observation program, VHE gamma-rays have been discovered from 1ES 1218+304 (Albert et al., 2006d) and 1ES 2344+515 has been observed in a low flux state with high significance (Albert et al., 2007b, and this work, Sect. 6.4.3) (see also Sect. 6.4.3). For ten sources of the sample, no significant signal has been detected. The 2006 observations of 1ES 1218+304

result in a weak signal of  $4.0\sigma$  (see Sect. 6.4.2). A refined analysis of 1ES 1011+496 yields a hint for a signal on a  $\sim 3\sigma$ -level (see Sect. 6.4.1). In the meanwhile VHE emission from this object was clearly detected in a second observation campaign in March 2007, which was triggered by an optical high state (Albert et al., 2007e). The results of the analysis are summarised in Table 6.3.

source	mode	exp. [h]	$E_{\text{thres}}$ [GeV]	$N_E$	$N_B$	scale	sig. $\sigma$	UL c.u.	UL f.u.
1ES 0120+340	w	14.9	190	-48	5358	0.33	-0.6	0.032	0.73
RX J0319.8+1845	w	4.7	190	9	2225	0.33	0.2	0.049	1.12
RX J0319.8+1845	on	6.5	190	-95	3257	0.86	-1.2	0.033	0.76
1ES 0323+022	w	11.4	230	55	5262	0.33	0.7	0.064	1.16
1ES 0414+009	w	17.8	230	176	7309	0.33	1.8	0.057	1.05
1ES 0806+524	w	17.5	230	111	6174	0.33	1.2	0.056	1.04
1ES 0927+500	w	16.1	230	72	5721	0.33	0.8	0.052	0.96
1ES 1011+496	w	14.5	230	200	4857	0.33	2.5	0.086	1.58
1ES 1218+304	w	14.6	170	282	3573	0.33	4.0	-	-
RX J1417.9+2543	on	13.0	190	-137	9007	1.03	-1.0	0.023	0.53
1ES 1426+428	on	6.1	190	-7	2561	0.24	-0.1	0.050	1.15
RX J1725.0+1152	on	5.3	190	-69	2001	0.98	-1.1	0.046	1.06
1ES 2344+514	w	26.0	190	927	4980	0.33	11.0	-	-

Table 6.3: Results of the analysis; columns (from left to the right): (1) source name; (2) observation mode, on-off (on) or wobble (w); (3) observation time after quality selection; (4) energy threshold assuming the Crab spectrum as given by Equation 4.17, except for 1ES 1218+304 and 1ES 2344+514 where the spectral indices, derived in the next sections, are used; (5) number of excess events; (6) number of background events after scaling; (7) scale factor; (8) statistical significance of the excess; (9) upper limit on the integral flux above the threshold in units of the flux of the Crab Nebula (crab units, c.u.) on a 99% CL; (10) upper limit on the integral flux above the threshold given in flux units (f.u.) of  $10^{-11}$  photons  $\text{cm}^{-2} \text{s}^{-1}$  on a 99% CL.

The ULs (99% CL) are between 2.3% and 8.6% of the Crab Nebula flux. For a Crab-like spectrum the energy thresholds vary between  $(190 \pm 15)$  GeV and  $(230 \pm 15)$  GeV, depending on the ZD of the observation.

### 6.3.3 1ES 1426+428

A special candidate of the sample is 1ES 1426+426 because it is an established TeV source. Unfortunately the observation campaign suffered from bad weather conditions in February and March 2005 as well as from several technical problems in March and April 2005, reducing the analysed observation time to 6.1 h (where more than 20 h were scheduled). In the following

the upper limit derived in this work is discussed in the context of former observations.

The VERITAS collaboration reported a steep spectrum above 300 GeV for their observations in 2001, well fitted by a power law with spectral index  $-(3.50 \pm 0.35)$  (Petry et al., 2002). Extrapolating the spectral fit to 200 GeV, it yields an integral flux of 0.50 Crab units above 200 GeV, which is by a factor of 10 larger than the UL presented here. Previous measurements yield a marginal detection in 2000 and upper limits for the data taken from 1995 to 1999 with the most stringent one of 0.08 Crab above 350 GeV (Horan et al., 2002).

The HEGRA collaboration published a much harder spectrum at higher energies (above  $\sim 800$  GeV) for their combined 1999 and 2000 data, which is well fitted by a power law with spectral index  $-(2.6 \pm 0.6)$  (Aharonian et al., 2002). An extrapolation of the power law yields an integral flux above 200 GeV of 0.075 Crab. Due to the large extrapolated energy range, combined with the large statistical error of 0.6 for the slope, the statistical uncertainty is a factor of two. Further measurements in 2002 with the HEGRA telescopes showed the source in a 2.5 times lower flux state (Aharonian et al., 2003).

The UL for the flux above 200 GeV presented in this work indicates a lower flux than measured from 1999 to 2001 during several campaigns with different telescopes, whereas it is consistent with the low flux level observed in 2002.

## 6.4 Detections and possible detections

In the following section the analysis of the detected sources (including a possible tentative detection) are described in detail, including the spectra of two sources as well as their lightcurves. For this analysis MARS version 2.0 is used (www-10). Summarised, the main changes are:

- the inclusion of the arrival time information in the image cleaning (time image cleaning) (Section 4.1.6);
- the inclusion of the new image parameter *slopelong* and the resulting new parametrisation of *disp* (Section 4.1.7 and Section 4.3.3);
- the absolute calibration of the starguider (Section 4.3.3).

Table 6.4 lists the coefficients used for this analysis.

coefficient	value	name
$c'_0$	1.15136	<i>disp</i>
$c'_1$	0.23	<i><math>\vartheta</math>-cut</i>
$c'_2$	0.21547	<i>area</i>
$c'_3$	5.58	<i>area</i>
$c'_4$	0.08362	<i>area</i>
$c'_5$	-0.07	<i>m3long</i>
$c'_6$	7.2	<i>slopelong</i>
$c'_7$	0.5	<i>slopelong</i>
$c'_8$	0.06814	<i>disp</i>
$c'_9$	2.62932	<i>disp</i>
$c'_{10}$	1.51279	<i>disp</i>
$c'_{11}$	0.05078	<i>disp</i>

Table 6.4: Coefficients  $c'_0$  to  $c'_{11}$  for the analysis made with MARS version 2.0.

### 6.4.1 1ES 1011+496

The standard analysis shows a hint of a possible signal with a significance of  $2.5\sigma$  (Table 6.3). The sky map derived from this analysis (Figure 6.2, upper left panel) shows a weak excess,  $0.12^\circ$  away from the nominal position of 1ES 1011+496. If the excess is related to a gamma-ray signal from the source, the mispointing correction in the analysis has introduced a constant off-set. Therefore the data are also analysed with MARS version 2.0 which provides an absolute calibration of the starguider. Figure 6.2, lower left panel, shows the sky map for the same data sample but with the new analysis, including the new pointing correction. The excess is still weak, but now located at the position of 1ES 1011+496. The right panels of Figure 6.2 show the  $\vartheta^2$ -distributions for both analyses. The signal region in the second analysis is decreased from  $\vartheta = 0.23$  to  $\vartheta = 0.18$  to increase the signal to noise ratio. It results in 99 excess events over 958 background events (scaled by  $1/3$ ), corresponding to a statistical significance of 2.7 standard deviations. This is still too less to claim a detection. By changing the cut efficiencies the significance reached values from  $1.5\sigma$  to  $3.5\sigma$ . Dividing the data in several subsamples does not yield any hint of a signal.

Further observations with the MAGIC telescope, triggered by an optical outburst in March 2007, show a clear signal of  $6.2\sigma$  within 18.7 h of observation, resulting in an integral flux above 200 GeV of  $(1.58 \pm 0.32) \times 10^{-7}$  photons  $\text{m}^{-2} \text{s}^{-1}$  (Albert et al., 2007e). The spectrum is well described by a power law with index  $(-4.0 \pm 0.5)$ .

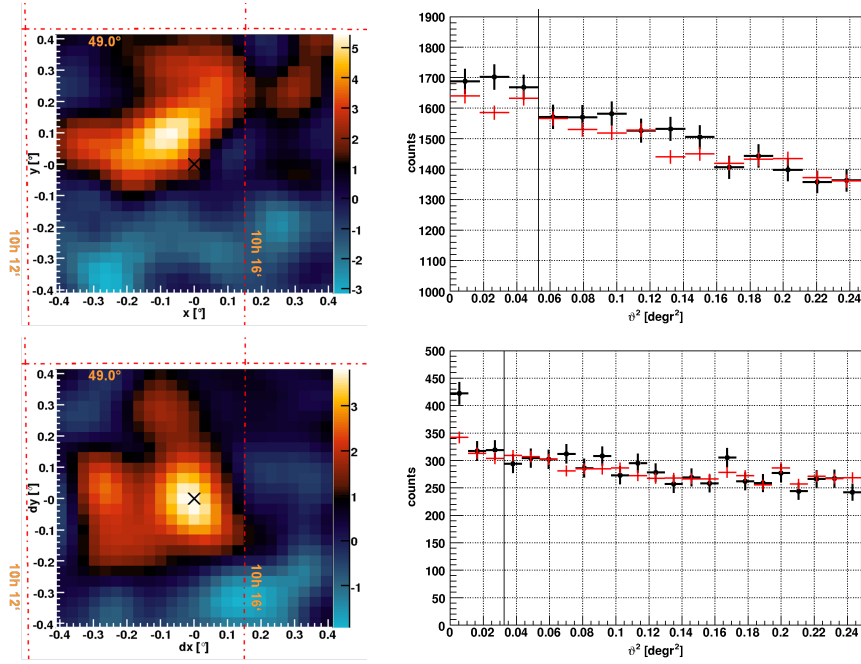


Figure 6.2: Left panels: Sky map around the position of 1ES 1011+496 (cross). The scale is in units of events/4 arcmin<sup>2</sup>. Right panels: Distribution of the squared angular distance with respect to the position of 1ES 1011+496 (black dots) and with respect to three background regions (red crosses). The upper panels show the results from the standard analysis of this work, done with MARS version 1.2 and the lower ones show the same data processed with MARS version 2.0. The vertical lines denote the signal region.

In Albert et al. (2008b) the integral flux above 180 GeV for the 2006 observations is given under the assumption of a detection. The flux is  $\sim 50\%$  smaller than measured in 2007. The reconstruction is based on the analysis with MARS version 1.2 with a smaller signal region ( $\vartheta < 0.20$ ) and a slightly changed coefficient  $c_3$  of the *area*-cut, compared to the result shown in Table 6.3. With the new analysis, this result cannot be confirmed. As the cut efficiencies of the new analysis are higher than in the old one and the measured excess from the direction of 1ES 1011+496 has decreased, the reconstructed flux above 180 GeV from this analysis would be 3.4 times lower than in the old one and 5 times lower than the flux in 2007.

### 6.4.2 1ES 1218+304

The source has been discovered at VHE gamma-rays by the MAGIC telescope in an observation campaign in January 2005 (Albert et al., 2006d). The total observation time was 8.2 h in on mode with additional 6.5 h off observations,

yielding a signal with a significance of  $6.4\sigma$ . The differential energy spectrum from 80 GeV to 700 GeV is well fitted by a power law, yielding

$$F_E(E) = (8.1 \pm 2.1) \times 10^{-7} (E/250 \text{ GeV})^{-3.0 \pm 0.4} \text{ m}^{-2} \text{ s}^{-1} \text{ TeV}^{-1}.$$

Here the analysis results of a second observation campaign from January to March 2006 are shown. The total observation time after quality selection is 14.6 h. The ZD ranges from  $12^\circ$  to  $36^\circ$  with a mean value of  $26.6^\circ$ . All data are taken in wobble mode. Figure 6.3, left panel, shows the sky map around the position of 1ES 1218+304. A clear excess is visible from the direction of 1ES 1218+304. Within the signal region ( $\vartheta < 0.23$ ) an excess of 282 events over 3573 background events are measured, corresponding to a statistical significance of  $4.0\sigma$  (Figure 6.3). By changing the cut efficiencies over a reasonable range, significances from  $3.6\sigma$  to  $4.7\sigma$  can be achieved.

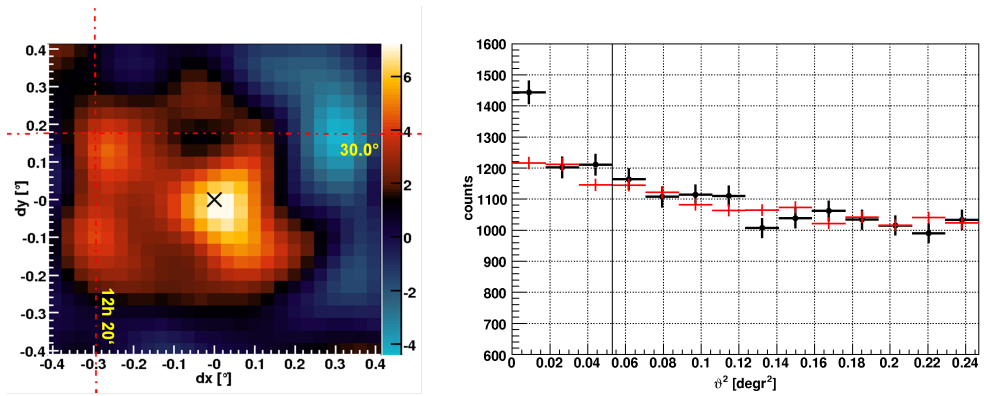


Figure 6.3: Left panel: Sky map around the position of 1ES 1218+304 (cross). The scale is in units of events/4 arcmin<sup>2</sup>. Right panel:  $\vartheta^2$ -distribution with respect to the position of 1ES 1218+304 (black dots) and with respect to three background regions (red crosses). The vertical line denotes the signal region.

Figure 6.4 shows the differential energy spectrum of 1ES 1218+304. The energy threshold is 165 GeV (bin from 150 GeV to 180 GeV). Nearly the complete excess lies in the two energy bins from 150 GeV to 470 GeV. A simple connection of these two spectral points by a straight line results in a spectral slope of -3.7. A power law fit including the spectral point at 630 GeV yields

$$F_E(E) = (9.9 \pm 2.6) \times 10^{-7} \left( \frac{E}{200 \text{ GeV}} \right)^{-(3.6 \pm 0.7)} \text{ m}^{-2} \text{ s}^{-1} \text{ TeV}^{-1}. \quad (6.1)$$

In addition the upper limits on the differential flux at 112 GeV, 632 GeV, 1.12 TeV and 2.0 TeV are calculated on a 99% confidence level. Again the method from Rolke et al. (2005) is used to calculate the UL on the excess

rate from the  $\vartheta^2$ -distribution of each energy bin. The flux is reconstructed by dividing the excess rate by the effective area and the width of the energy bin and multiplying with the spillover factor. A power law with fixed slope is fitted to the data to derive the steepest as well as the hardest possible spectrum that is still consistent with the ULs. The steepest spectrum has a slope of -4.5, constrained by the UL at 112 GeV, the hardest one is -2.5, constrained by the UL at 1.12 TeV.

To investigate a possible time variability, the sample is divided in three subsamples. The first subsample spans from January 29th to February 5th (seven consecutive nights with a gap on February 1st). The second subsample spans from February 22nd to 27th (five consecutive nights) and the last one from March 3rd to 5th. The integral flux from 150 GeV to 5 TeV for all subsamples is shown in Figure 6.5, upper panel. A constant fit yields ( $\chi^2/\text{n.d.o.f.} = 8.77/2$ ):

$$F_E(0.15 - 5.0 \text{ TeV}) = (1.33 \pm 0.33) \times 10^{-7} \text{ m}^{-2} \text{ s}^{-1}.$$

The fit probability is quite low (1.2%). While the first subsample shows a significance of  $4.0\sigma$ , the second one has only  $1.4\sigma$ . In addition also the UL on the integral flux for the second subsample is shown in the plot (99% CL). This UL excludes the flux measured in the first subsample. Furthermore the lower limit on the flux of the first subsample on a 95% CL excludes the UL for

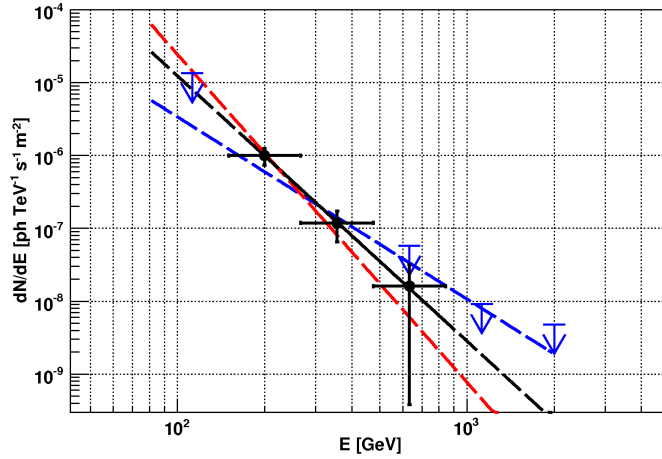


Figure 6.4: Differential energy spectrum of 1ES 1218+304. The arrows mark UL on a 99% confidence level in the energy bins where no significant signal is seen. The black line represents a power law fit to the data, yielding a spectral index of  $-(3.6 \pm 0.7)$ . The dashed lines mark the steepest (-4.5, red) and the hardest (-2.5, blue) possible spectrum, which is still consistent with the upper limits at lower and higher energies. The data points are listed in Table D.1.

the second subsample on the same confidence level. This is the first evidence for time variability at VHE gamma-rays from 1ES 1218+304. The time scale is 17 days. A further division in subsamples on a daily time scale ( $\sim 40$  min per sample) does not reveal any evidences for time variability on smaller time scales, even though it cannot be excluded due to the low flux level. In Albert et al. (2008b) it is stated that the lightcurve of the 2006 observations is consistent with a constant flux. Indeed a second, independent analysis (Prandini, private communication) showed the same tendency as described here but less significant, mainly due to a weaker excess in the first subsample.

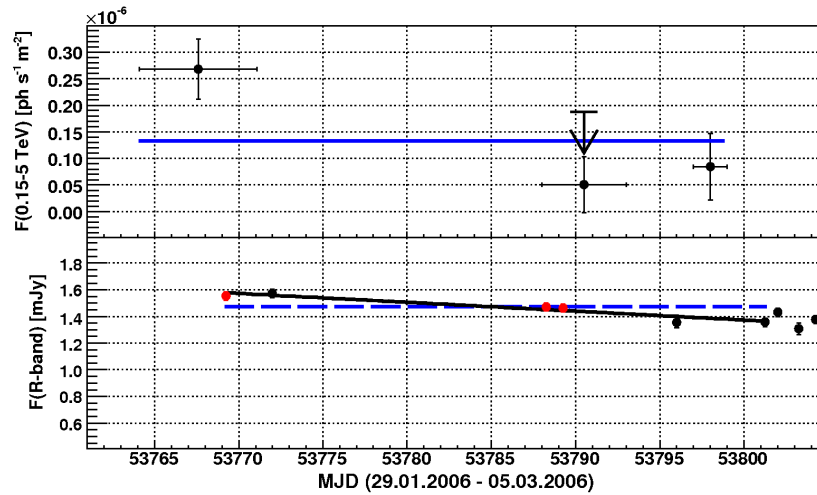


Figure 6.5: Upper panel: Lightcurve above 150 GeV of 1ES 1218+304 divided into three subsamples together with a constant fit. For the second subsample also the ULs on a 99% confidence level is shown. Lower panel: The optical R-band lightcurve as measured by KVA. The red points mark the data taken simultaneously. The dashed line denotes a constant fit ( $\chi^2/\text{n.d.o.f.} = 39.3/5$ ), the solid line a linear regression ( $\chi^2/\text{n.d.o.f.} = 2.8/4$ ).

The lower panel of Figure 6.5 shows the lightcurve of 1ES 1218+304 in the optical R-band, as measured by the 35 cm telescope of the KVA observatory (see also Section 7.1.2). The contribution of the host galaxy is  $(0.41 \pm 0.02)$  mJy (Nilsson et al., 2007). The total average flux is  $(1.474 \pm 0.013)$  mJy during the time of MAGIC observations, though the optical lightcurve is not well described by a constant ( $\chi^2/\text{n.d.o.f.} = 39.3/5$ ). During the observations in 2006 the optical flux decreases continuously from  $(1.144 \pm 0.036)$  mJy on the 3rd of February to  $(0.947 \pm 0.038)$  mJy on the 7th of March (all optical fluxes are host galaxy subtracted), well fitted by a linear regression ( $\chi^2/\text{n.d.o.f.} = 2.8/4$ ). This trend continued until June 2006, where the source remained in a low optical state. Unfortunately, with six nights the sampling

of the optical light curve during the MAGIC observations is quite low, hence an increase of the optical activity on a time scale of days cannot be excluded.

A power law fit to the 2005 data yields an integral flux from 150 GeV to 5 TeV of  $(2.8 \pm 0.6) \times 10^{-7} \text{ m}^{-2} \text{ s}^{-1}$  which is consistent with the flux of  $(2.68 \pm 0.56) \times 10^{-7} \text{ m}^{-2} \text{ s}^{-1}$  of the first subsample and two times higher than the average in 2006. The average optical flux in 2006 was  $\sim 20\%$  lower than in 2005, which is already significant compared to the statistical error of  $\sim 2\%$ .

Figure 6.6 shows the differential energy spectrum for the first subsample. A power law fit from 150 GeV to 850 GeV yields:

$$F_E(E) = (1.5 \pm 0.4) \times 10^{-7} \left( \frac{E}{200 \text{ GeV}} \right)^{-(2.9 \pm 0.5)} \text{ m}^{-2} \text{ s}^{-1} \text{ TeV}^{-1} \quad (6.2)$$

Again the ULs on the differential flux at 112 GeV, 1.12 TeV and 2.0 TeV are calculated (99% CL). Here the constraints on the spectral index derived from the UL are stronger, reducing the possible interval of the spectral slope to the range from -2.8 to -3.3, which is smaller than the statistical error of the fit. The slope is consistent with the one derived for the complete data sample. The spectral hardening with increasing flux as seen from the two fits is not significant.

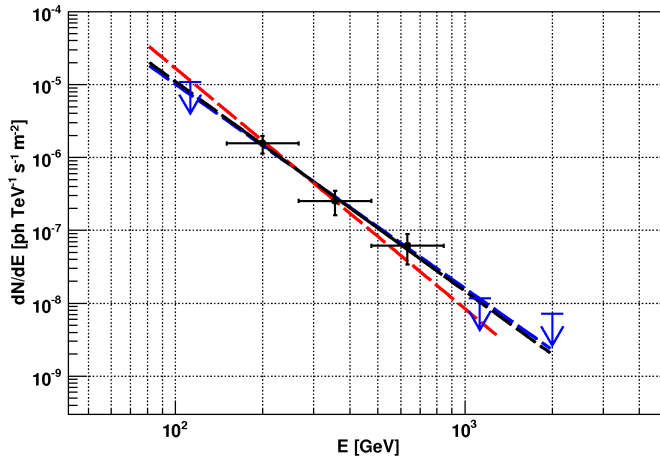


Figure 6.6: Differential energy spectrum of the first subsample of 1ES 1218+304 (January 29th to February 29th 2006). The arrows mark ULs on a 99 % confidence level in the energy bins where no significant signal is seen. The black line represents a power law fit to the data, yielding a spectral index of  $-(2.9 \pm 0.5)$ . The dashed lines mark the steepest (-3.3, red) and the hardest (-2.8, blue) possible spectrum, which is still consistent with the ULs at lower and higher energies. The data points are listed in Table D.1.

The VHE spectrum is discussed in the context of the broad-band spectral energy distribution together with simultaneous optical as well as archival X-ray data in Section 8.3.

### 6.4.3 1ES 2344+514

The source has been observed from August 5th 2005 to January 1st 2006 with a total exposure time of 41.6 h, including 9.6 h where the moon was above the horizon. The analysis presented here is restricted to observations where the moon was below the horizon. From the resulting 32 h, 19 nights with a total of exposure time of 26.0 h are left after quality selection.

Figure 6.7, left panel, shows the sky map around the position of 1ES 2344+514. A clear excess is visible on the nominal position of 1ES 2344+514. The right panel in Figure 6.7 shows the  $\vartheta^2$ -distribution with respect to the source and three background regions (scaled by 1/3). The excess of 927 events over 4980 scaled background events has a statistical significance of  $11.0\sigma$ . The energy threshold for this analysis is 190 GeV.

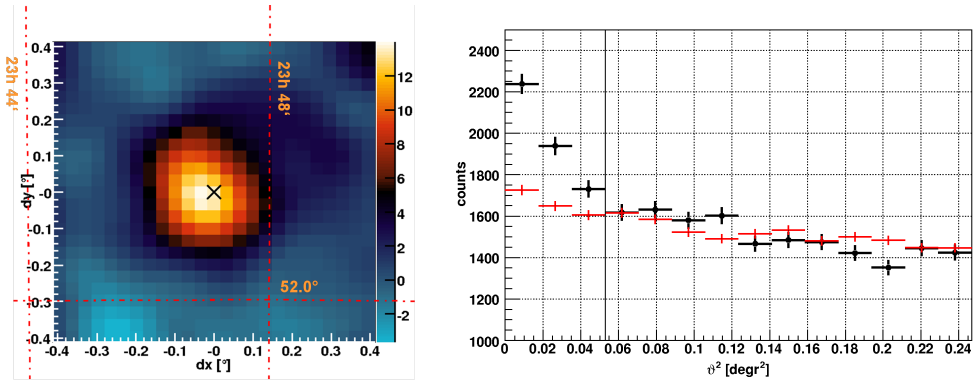


Figure 6.7: Left panel: Sky map around the position of 1ES 2344+514 (cross). The scale is in units of events/4 arcmin<sup>2</sup>. Right panel:  $\vartheta^2$ -distribution with respect to the position of 1ES 2344+514 (black dots) and with respect to three background regions (red crosses, scaled by 1/3). The vertical line denotes the signal region.

To reconstruct the energy spectrum, the cut efficiency is increased by shifting the parabolic cut in *area* vs. *size* to lower *size* values. This usually decreases the significance of the signal, but lowers the energy threshold. Also the systematic error from the comparison of the observational data with the simulation is reduced. The resulting spectrum from 120 GeV to 2 TeV is shown in Figure 6.8. The energy threshold for this analysis is 165 GeV (bin from 153 GeV to 179 GeV). The spectrum is well described by a power law, yielding ( $\chi^2/\text{n.d.o.f.} = 1.3/4$ ):

$$F_E(E) = (6.02 \pm 0.72) \times 10^{-7} \left( \frac{E}{250 \text{ GeV}} \right)^{-(2.60 \pm 0.15)} \text{ m}^{-2} \text{ s}^{-1} \text{ TeV}^{-1}. \quad (6.3)$$

At 2.5 TeV the upper limit on a 99% CL is shown. To investigate the systematic error, caused by different cut efficiencies and spectral assumptions, the

reconstruction is done for different *area*-cuts (coefficient  $c'_3$ ) and for spectral slopes from -2.45 to -2.75, according to the  $1\sigma$ -error of the fit. The result is shown as a grey band in Figure 6.8.

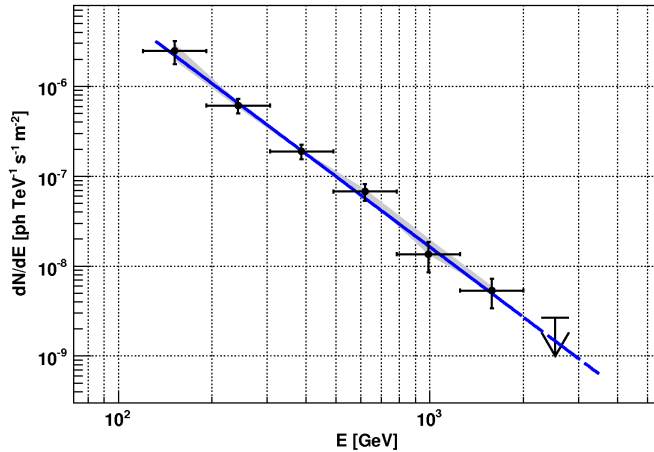


Figure 6.8: Differential energy spectrum of 1ES 2344+514 including an upper limit at 2.5 TeV (99 % CL). The blue line represents a power law fit to the data, yielding a spectral index of  $-(2.60 \pm 0.15)$ . The systematic uncertainties due to the cut efficiencies and spectral assumptions are shown as a grey band. The data points are listed in Table D.2.

The spectrum is harder than the one which is published by the MAGIC collaboration for the same observation campaign (Albert et al., 2007b). The difference of 0.35 in the spectral index is more than expected from the statistical error. Both spectra agree around 1 TeV. The harder spectrum in this analysis results from a lower flux around the threshold. For possible reasons see the next paragraph.

To investigate a possible time variability, the integral flux from 200 GeV to 5 TeV is calculated for each night of observation (see Figure 6.9, upper panel). The average flux from the daily lightcurve yields

$$F_E(0.2 - 5.0 \text{ TeV}) = (1.24 \pm 0.13) \times 10^{-7} \text{ m}^{-2} \text{ s}^{-1}.$$

The probability for a constant flux from a  $\chi^2$ -test is 0.14 %, which shows clear evidence for variability. In Albert et al. (2007b) the lightcurve is consistent with a constant flux. Also the flux level is  $\sim 90\%$  higher than in the analysis presented here. A possible reason arises from the systematic error around the threshold. Because of the steep power law, the integral flux is always dominated by the lowest energies. Around or below the energy threshold, the systematic error increases strongly, with a clear tendency of an overestimation of the flux. There are also differences in the data selection. While single nights are rejected by Albert et al. (2007b) based on a cut in ZD, data are

included there which are rejected here due to quality reason (e.g. calibration failed). Note that also a systematic difference in the energy estimation of a few percent would lead to a much larger difference in the flux. The evidence for variability mainly arises from smaller statistical errors compared to Albert et al. (2007b).

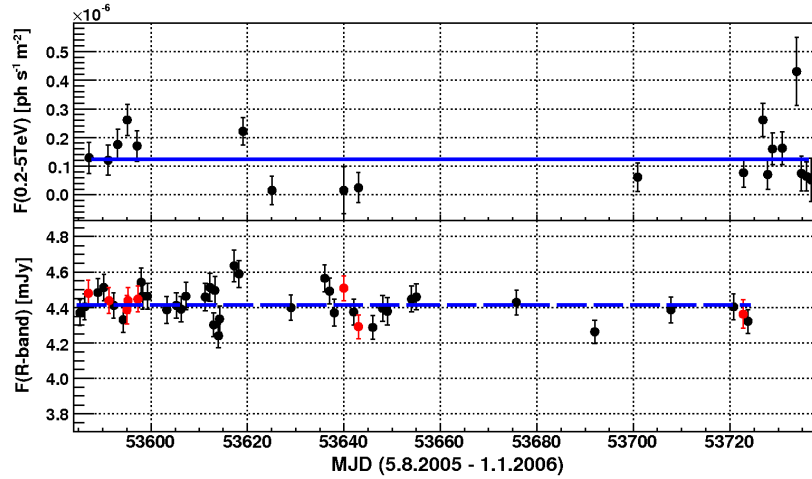


Figure 6.9: Upper panel: Lightcurve above 200 GeV of 1ES 2344+514 on a diurnal basis for 19 nights of observations from August 5th 2005 to January 1st 2006. Lower panel: Lightcurve in the optical (R-band) as measured by KVA. The red data points are taken simultaneously to MAGIC observations.

The source is monitored by the 35 cm optical telescope of the KVA observatory (see also Section 7.1.2). Figure 6.9, lower panel, shows the lightcurve in the R-band for the time of MAGIC observations. The data which are simultaneously taken are marked in red. The average flux over almost five months amounts to  $(4.41 \pm 0.01)$  mJy. The probability for a constant flux from a  $\chi^2$ -test is 5.3%, which gives also a hint of flux variability in the optical. The contribution to the total flux from thermal emission of the host galaxy is  $(3.70 \pm 0.05)$   $\mu$ Jy (Nilsson et al., 2007). The resulting flux of the nucleus shows variability in the order of  $\sim 15\%$ , which is already significant compared to the small statistical errors.

The object is also monitored at X-rays (2-10 keV) by the All Sky Monitor (ASM) onboard the Rossi X-ray Timing Explorer (RXTE). The average count rate for five months of observation is  $(0.140 \pm 0.024)$  cts/s corresponding to 0.19% of the flux of the Crab Nebula, which is also the standard candle in X-ray astronomy. This flux is a factor 15 below the quoted sensitivity of the ASM instrument. From the diurnal lightcurve no variability is seen, but fluxes up to a factor of five above the average cannot be excluded.

Table 6.5 shows the fluxes for three individual months of observations. Only the average fluxes measured in August and September differ significantly. The data of August are in good agreement with a constant flux, while September and December show variability.

month	$F(0.2-5\text{TeV})$		prob.
	$10^{-7} \text{ m}^{-2} \text{ s}^{-1}$	$\chi^2/\text{n.d.o.f.}$	
August	$1.70 \pm 0.24$	4.14/4	38.8%
September	$0.84 \pm 0.28$	11.7/3	0.9%
December	$1.24 \pm 0.19$	18.2/8	2.0%

Table 6.5: Integral flux from 200 GeV to 5 TeV for each individual month of observation together with the  $\chi^2$  and the probability (prob.) of a linear regression.

To find out the shortest time scale of variability two cases are further investigated: the nights from September 6th to 12th (MJD 53619.1 to MJD 53625.1) and from December 22nd to 23rd (MJD 53726.9 to MJD 53727.9). In both cases the first night shows a clear signal on a  $5\sigma$ -level, while the second night shows no signal at all ( $-0.8\sigma$  and  $1.2\sigma$ , respectively) for a comparable observation time. In the first case the lower limit on the flux on a 96% CL excludes the upper limit on the other day on the same CL. The situation is the same for the other two nights on a 91% CL. The shortest variability time scale found here is 24 h.

Figure 6.10 shows the spectrum for four nights with the highest flux ( $F(> 200 \text{ GeV}) > 2.0 \times 10^{-7} \text{ m}^{-2} \text{ s}^{-1}$ , left panel, in the following referred to as "highflux" sample) and for six nights with a flux level around the average for the complete data set ( $1.0 \times 10^{-7} \text{ m}^{-2} \text{ s}^{-1} < F(> 200 \text{ GeV}) < 2.0 \times 10^{-7} \text{ m}^{-2} \text{ s}^{-1}$ , right panel, in the following referred to as "midflux" sample). Both samples are well described by a power law with spectral indices  $-(2.18 \pm 0.18)$  ( $\chi^2/\text{n.d.o.f.} = 5.1/4$ , highflux) and  $-(2.88 \pm 0.25)$  ( $\chi^2/\text{n.d.o.f.} = 0.93/4$ , midflux), respectively. The highflux sample shows evidence for a curvature. A fit by a logarithmic parabola yields ( $\chi^2/\text{n.d.o.f.} = 2.80/3$ )

$$\frac{dN}{dAdtdE} = (8.26 \pm 1.81) \times 10^{-7} \left( \frac{E}{E_0} \right)^{-a - (b \log(E/E_0))} \text{ m}^{-2} \text{ s}^{-1} \text{ TeV}^{-1}, \quad (6.4)$$

with  $a = (1.44 \pm 0.60)$ ,  $b = (1.08 \pm 0.82)$  and  $E_0 = 250 \text{ GeV}$ . This results in a peak energy (the energy where the spectral index of the differential spectrum is equal to -2) of  $(460 \pm 120) \text{ GeV}$ . Note that the spectrum is so far not corrected for the absorption in the MRF. Another evidence for curvature comes from the UL at 2.5 TeV, which is clearly below the extrapolated power

law fit. The spectra are discussed in the context of the broad-band spectral energy distribution together with the simultaneous optical and archival X-ray data in Section 8.2.

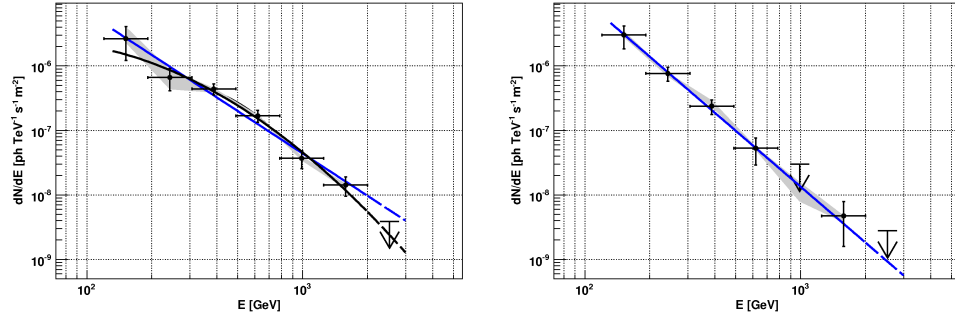


Figure 6.10: Differential energy spectra of 1ES 2344+514 for the highflux (left panel) and the midflux sample (right panel). The upper limits are on a 99% CL. The systematic uncertainties due to the cut efficiencies and spectral assumptions are shown as a grey band. The data points are listed in Table D.2. The blue lines represent power law fits to the data, the black line a logarithmic parabola.

# Chapter 7

## Overall spectral properties

The complete set of observed sources as described in Sect. 6.1 amounts to 14 objects (without 1ES 1727+502) and includes the six established TeV sources 1ES 1011+496, Mrk 501, 1ES 1218+304, 1ES 1426+428, Mrk 421 and 1ES 2344+514. The broad-band spectral properties of this sample are discussed together with all other HBLs detected at VHE so far (which number amounts to 16 in total, November 2007<sup>1</sup>). Note that all established TeV sources, which do not belong to the sample described in Sect. 6.1, fulfil also the criteria on redshift (except of PG 1553+113, where the redshift is not known) and X-ray flux. Therefore they were added to the set of sources considered here, leading to a total of 24 objects.

In Section 7.1 the upper limits on the monochromatic flux at 200 GeV are calculated based on the upper limits on the integral flux, and the simultaneous optical data of the sample are summarised. Different corrections, such as a K-correction as well as corrections for absorption effects, are described in Section 7.2. In Section 7.3 the broad-band spectral indices are defined and the sample is enlarged with all sources detected at VHEs so far. Finally the broad-band spectral properties are discussed for the enlarged sample.

All results of this chapter are also published in Albert et al. (2008b, corresponding author: M. Meyer) in the context of the release of proprietary data of the MAGIC collaboration.

### 7.1 Multiwavelength data

To determine the overall spectral properties, monochromatic fluxes in four different energy bands are taken into account.

---

<sup>1</sup>By the time of writing, VHE emission has been detected from the HBL RGB J0152+017 ( $z = 0.080$ ) by the H.E.S.S. array (Nedbal et al., 2007)

- Radio: 5 GHz.  
The radio fluxes are taken from Donato et al. (2001) and Costamante and Ghisellini (2002) (in case of 1ES 0229+200)
- Optical: R-band (640 nm).  
The simultaneously measured fluxes from KVA are taken if available (see Sec. 7.1.2), otherwise the fluxes from the V-band (550 nm) are taken from Donato et al. (2001). In the latter case, the fluxes are corrected for the different frequency (see Sec. 7.2.1).
- X-rays: 1 keV.  
The X-ray fluxes are taken from Donato et al. (2001) and Costamante and Ghisellini (2002) (in case of 1ES 0229+200). In case of more than one measurement, the mean value is calculated.
- Gamma-rays: 200 GeV.  
The fluxes can be found in Table 7.1, Table 7.4 and the references in Section 6.2. For 1ES 1426+428, beside the UL derived in this work, the extrapolation of the spectrum, measured by HEGRA in 1999/2000, is used to indicate the detected flux level (see Sect. 6.3.3).

### 7.1.1 Upper limits at 200 GeV

To investigate the broad-band properties of the non-detected objects, the ULs on the integral fluxes are converted into monochromatic ULs at 200 GeV. As the Crab spectrum at  $\sim 200$  GeV is quite hard (spectral slope of -2.02 for the differential energy spectrum), first the ULs on the integral flux are calculated for a power law spectrum with index -3.0, which represents quite well the average slope of all HBLs detected at VHE so far. To get the UL on the monochromatic flux, the normalisation factor of a -3.0 power law template is calculated by equating the integral of the power law with the UL on the integral flux. The lower energy thresholds due to the steeper spectrum are hereby taken into account. The results are listed in Table 7.1.

### 7.1.2 Simultaneous optical observations

Except for 1ES 0927+500 and 1ES 0414+009, all objects are monitored by the 35 cm telescope at the KVA observatory<sup>2</sup> on La Palma in the optical R-band. None of the sources showed flaring activity in the optical during the MAGIC observations. The simultaneously taken data, averaged over the

---

<sup>2</sup><http://users.utu.fi/kani/1m/index.html>

source	mode	$E_{\text{thres}}$ GeV	$UL_{200}$ $10^{-12} \text{ erg cm}^{-2} \text{ s}^{-1}$
1ES 0120+340	w	170	3.8
RX J0319.8+1845	w	170	5.9
RX J0319.8+1845	on	170	4.0
1ES 0323+022	w	190	8.5
1ES 0414+009	w	190	7.6
1ES 0806+524	w	190	7.5
1ES 0927+500	w	170	6.3
1ES 1011+496	w	170	10.3
RX J1417.9+2543	on	140	2.3
1ES 1426+428	on	140	5.1
RX J1725.0+1152	on	190	6.2

Table 7.1: Upper limits on the gamma-ray flux at 200 GeV ( $UL_{200}$ ) under the assumption of a power law spectrum with spectral index -3.0.

time of the MAGIC observations, are listed in Table 7.2 together with the fluxes of the host galaxies and the resulting fluxes of the AGN.

## 7.2 Corrections

The data have to be corrected for different kinds of absorption and redshift effects (K-correction). The X-ray data are already corrected for absorption. The optical data are corrected for galactic foreground extinction, using the coefficients from the NASA Extragalactic Database (NED), which are calculated following Schlegel et al. (1998).

### 7.2.1 K-correction

Since the sources are located at different distances with respect to the observer, the detected photons are redshifted differently. Observations at a certain energy therefore correspond to emission at different energies. The observed bandwidth is thereby stretched by a factor of  $(1+z)$ . To compare monochromatic intrinsic fluxes, a K-correction is performed beforehand. In case of continuum emission the observed flux  $F_{\text{observed}}$  is transformed into the intrinsic flux  $F_{\text{source}}$  as

$$F_{\text{source}} = F_{\text{observed}} \cdot (1+z)^{\alpha-1} \quad (7.1)$$

source	$F_{o,total}$ [mJy]	$F_{o,host}$ [mJy]	$\nu F_{o,AGN}$ $10^{-12}$ erg cm $^{-2}$ s $^{-1}$
1ES 0120+340	$0.281 \pm 0.003$	$0.18 \pm 0.01$	$0.47 \pm 0.05$
RX J0319.8+1845 (w)	$0.272 \pm 0.005$	$0.17 \pm 0.02$	$0.48 \pm 0.10$
RX J0319.8+1845 (on)	$0.200 \pm 0.006$	$0.17 \pm 0.02$	$0.14 \pm 0.10$
1ES 0323+022	$0.768 \pm 0.007$	$0.38 \pm 0.04$	$1.82 \pm 0.19$
1ES 0414+009	-	-	-
1ES 0806+524	$2.396 \pm 0.026$	$0.69 \pm 0.04$	$8.00 \pm 0.23$
1ES 0927+500	-	-	-
1ES 1011+496	$2.940 \pm 0.018$	$0.49 \pm 0.02$	$11.49 \pm 0.13$
1ES 1218+304 (on)	$1.718 \pm 0.019$	$0.41 \pm 0.02$	$6.13 \pm 0.13$
1ES 1218+304 (w)	$1.474 \pm 0.013$	$0.41 \pm 0.02$	$4.99 \pm 0.11$
RX J1417.9+2543	$0.960 \pm 0.010$	$0.51 \pm 0.06$	$2.11 \pm 0.29$
1ES 1426+428	$1.278 \pm 0.011$	$0.88 \pm 0.03$	$1.87 \pm 0.15$
RX J1725.0+1152	$2.831 \pm 0.020$	$< 0.008$	$13.27 \pm 0.09$
1ES 2344+514	$4.419 \pm 0.021$	$3.70 \pm 0.05$	$3.37 \pm 0.25$

Table 7.2: Simultaneous optical observations. The average flux as measured by KVA at 640 nm ( $F_{o,total}$ ), the flux of the host galaxy ( $F_{o,host}$ ) only (Nilsson et al., 2007) and the resulting flux of the AGN ( $\nu F_{o,AGN}$ ).

where  $\alpha$  is the spectral slope<sup>3</sup> in the observed energy band, assuming a power law.

In Landt (2003) the spectral indices in the radio band  $\alpha_R$  can be found for ten sources of the sample. For the other 14 objects the average value  $\alpha_R = 0.23$  of these ten sources is used. For the optical data, the spectral indices of nine sources, calculated at slightly higher wavelengths, are taken from Bersanelli et al. (1992). For the other 15 objects the average value  $\alpha_O = 0.65$  of these nine sources is used. With these values, also the optical fluxes taken from Donato et al. (2001) are corrected for the transition from the V-band to the R-band. At 1 keV, the spectral indices are taken from Donato et al. (2001), except for 1ES 0229+200 which is not included in this compilation. Instead the flux is taken from Costamante and Ghisellini (2002) together with the average value for the spectral index  $\alpha_X = 1.36$  of all other sources. At 200 GeV the measured spectral indices are used for the detected sources, while for the non-detected ones the average value  $\alpha_\gamma = 2.0$  is used. The energy dependent attenuation at VHEs causes a hardening of the spectra. Therefore the measured spectral indices are changed by -0.4 for  $0.1 < z < 0.2$ , -0.8 for  $0.2 < z < 0.3$  and remain unchanged for  $z < 0.1$ .

<sup>3</sup>Photon flux  $F \propto \nu^{-\alpha}$  [photons cm $^{-2}$  s $^{-1}$ ]

### 7.2.2 Absorption of gamma-rays

Sizeable attenuation is expected from current models of the metagalactic radiation field (see Section 1.4 for a more detailed description). Therefore all ULs at 200 GeV as well as the measured fluxes of the detected HBLs are corrected for the absorption by multiplying with  $\exp(\tau(200 \text{ GeV}, z))$ ,  $\tau$  being the energy and redshift dependent optical depth. The optical depths for 200 GeV photons for all objects are listed in Table 7.3 and Table 7.4.

source	$z$	$\tau(200 \text{ GeV}, z)$
1ES 0120+340	0.272	0.43
RX J0319.8+1845	0.190	0.25
1ES 0323+022	0.147	0.18
1ES 0414+009	0.287	0.46
1ES 0806+524	0.138	0.17
1ES 0927+500	0.188	0.25
1ES 1011+496	0.212	0.30
Mrk 421	0.030	0.027
1ES 1218+304	0.182	0.24
RX J1417.9+2543	0.237	0.35
1ES 1426+428	0.129	0.15
Mrk 501	0.034	0.031
RX J1725.0+1152	$> 0.17$	$> 0.22$
1ES 2344+514	0.044	0.042

Table 7.3: Optical depths for gamma-rays with an energy of 200 GeV for the redshift of the observed sources.

## 7.3 Broad-band spectral indices

After the corrections described in the previous section, the broad-band spectral indices  $\alpha_{1-2}$  between the different energy regimes as defined by Ledden and Odell (1985) are calculated:

$$\alpha_{1-2} = -\log(F_1/F_2)/\log(\nu_1/\nu_2), \quad \nu_1 < \nu_2, \quad (7.2)$$

where  $F_1$  and  $F_2$  are the fluxes at the frequencies  $\nu_1$  and  $\nu_2$  in units of photons  $\text{cm}^{-2} \text{s}^{-1}$ .

Also the apparent luminosities  $\nu L_\nu$  are calculated, assuming isotropic emission. The following cosmological parameters are used:

$$H_0 = 71 \text{ km s}^{-1} \text{ Mpc}^{-1}, \quad \Omega_\Lambda = 0.73, \quad \text{and} \quad \Omega_m = 0.27.$$

### 7.3.1 Sample enlargement

Table 7.4 lists all HBLs detected at VHE so far, which are not included in the sample described in Section 6.1, together with their fluxes and optical depths at 200 GeV.

source	$z$	$F_\gamma$	$\tau(200 \text{ GeV}, z)$	reference
1ES 0229+200	0.1396	1.6	0.17	Aharonian et al. (2007b)
1ES 0347-121	0.188	4.25	0.25	Aharonian et al. (2007a)
PKS 0548-322	0.069	1.90	0.071	Superina et al. (2007)
1ES 1101-232	0.186	2.93	0.25	Aharonian et al. (2007c)
Mrk 180	0.045	11.0	0.043	Albert et al. (2006e)
PG 1553+113	$> 0.09$	11.5	$> 0.097$	Albert et al. (2007a)
1ES 1959+650	0.047	17.4	0.047	Albert et al. (2006b)
PKS 2005-304	0.071	6.63	0.073	Aharonian et al. (2005b)
PKS 2155-489	0.117	26.3	0.13	Aharonian et al. (2005a)
H 2356-309	0.165	2.78	0.21	Aharonian et al. (2006a)

Table 7.4: HBLs detected at VHE which do not belong to the sample described in Sect. 6.1.  $F_\gamma$  is the measured energy density at 200 GeV in units of  $10^{-12} \text{ erg cm}^{-2} \text{ s}^{-1}$ . In case of PG 1553+113 the lower limit is used for the calculation of the broad-band spectral indices.

A special treatment is necessary to derive the flux at 200 GeV from 1ES 0229+200, recently discovered at VHE gamma-rays (Aharonian et al., 2007b). The spectrum is measured only above 580 GeV. It is well fitted by a power law with spectral index  $-(2.51 \pm 0.19)$ . As the source is located at  $z = 0.1396$ , strong absorption is expected at these energies. Therefore the spectrum is first deabsorbed and afterwards extrapolated to lower energies. The resulting intrinsic spectrum is well described by a power law with a spectral index of  $-(1.09 \pm 0.25)$  (flux normalisation:  $(4.24 \pm 0.81) \times 10^{-12} \text{ cm}^{-2} \text{ s}^{-1} \text{ TeV}^{-1}$  at 1 TeV). This result is in good agreement with the results from Stecker and Scully (2007), yielding model dependent intrinsic spectral indices in the range from  $1.1 \pm 0.3$  to  $1.5 \pm 0.3$ .

### 7.3.2 Discussion

Although the number of gamma-ray emitting HBLs has been increased within the last three years, it is still unclear whether the dominant energy output at VHE is a general characteristic of HBLs or only related to a subclass of them. To search for a pattern in the spectral properties of VHE emitting HBLs, the broad-band spectral index  $\alpha_{\text{RO}}$  vs.  $\alpha_{\text{OX}}$  for all 24 HBLs as described in the previous sections is investigated (see Fig. 7.1).

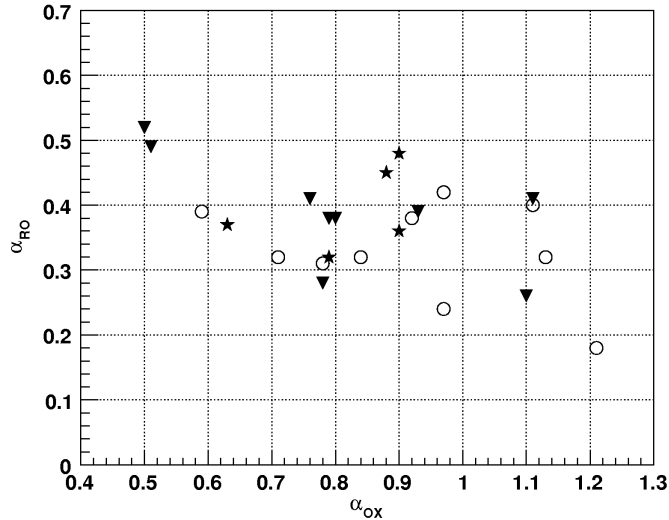


Figure 7.1: The broad-band spectral index  $\alpha_{\text{RO}}$  vs.  $\alpha_{\text{OX}}$  (Albert et al., 2008b). The filled symbols mark the spectral indices of the sources which belong to the sample described in Sect. 6.1. They are further divided into detected (stars) and non-detected sources (triangles). The open circles mark all other HBL objects detected at VHE gamma-rays with published fluxes (see Table 7.4).

The distribution is quite homogeneous. However the time variability makes the study of broad-band spectral indices calculated with non-simultaneously taken data difficult. In the compilation of Donato et al. (2001) the average radio fluxes are given in case there were more than one observation. For the X-ray data several measurements are listed when available in the literature. For some sources like Mrk 421 and Mrk 501 the X-ray data are reduced to a few representative measurements. The typical amplitude of the flux variability at 1 keV amounts to a factor of six. This would lead to a change in  $\alpha_{\text{OX}}$  of 0.29 or less if the X-ray flux is correlated to the optical flux. As the observed variability in the radio and optical band for HBLs is lower than at X-rays or VHE gamma-rays and the spectral index  $\alpha_{\text{RO}}$  is less sensitive to flux variations (because of the larger value of the denominator, see Equ. 7.2) the variation of  $\alpha_{\text{RO}}$  is much lower than for  $\alpha_{\text{OX}}$ . The differences of 0.6 and 0.3 for  $\alpha_{\text{OX}}$  and  $\alpha_{\text{RO}}$ , respectively, shown by the detected VHE sources are therefore related to spectral differences rather than to an accidental scattering. Within the uncertainties, the spectral indices of the non-detected objects are inside the region of the parameter space spanned by the VHE sources.

Figure 7.2 shows the broad-band spectral index  $\alpha_{\text{O}\gamma}$  vs.  $\alpha_{\text{X}\gamma}$ . The parameter space constrained by the upper limits on the gamma-ray flux for

the non-detected objects completely overlap with the region spanned by the VHE sources. Both indices are scattered around unity which represents the case that the energy output in both energy bands is the same. There is a weak tendency for an increasing  $\alpha_{O\gamma}$  with increasing  $\alpha_{X\gamma}$ .

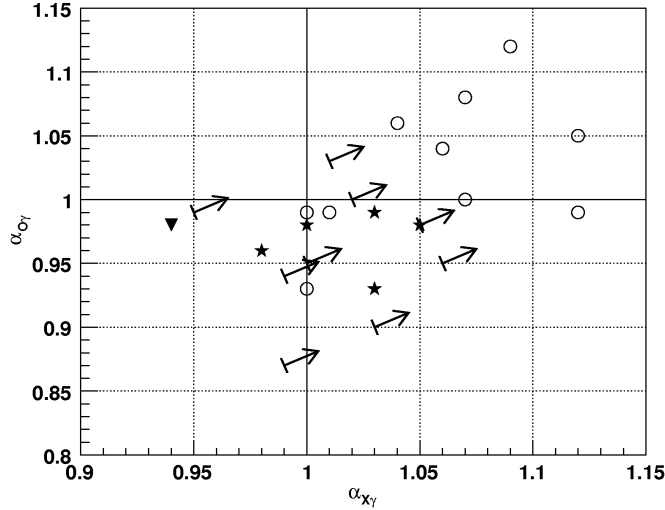


Figure 7.2: The broad-band spectral index  $\alpha_{O\gamma}$  vs.  $\alpha_{X\gamma}$ . The arrows mark the upper limits for the spectral indices, whereas the stars indicate the spectral indices of the detected sources that belong to the sample described in Sect. 6.1. The triangle denotes the value for 1ES 1011+496, based on the flux measured in 2007. The open circles mark all other HBL objects detected at VHE gamma-rays with published fluxes (see Table 7.4).

In the framework of SSC models equal luminosities in the synchrotron and the inverse Compton regime are expected in case of equal photon and magnetic field energy densities. For HBL objects the synchrotron luminosity is dominated by photons in the energy range between the optical and the hard X-ray band (mostly below 1 keV, except for a few extreme cases), depending on the spectral properties of the particular object. The energy output in the inverse Compton regime is mainly generated by VHE gamma-rays. At 200 GeV most of the detected HBLs show steep spectra, indicating much lower peak energies. However, in case of high redshift sources the peak can be masked by absorption in the MRF; indeed a few sources reveal hard intrinsic spectra up to several TeV after correcting for this absorption. From the expectation of a continuous sequence of peak energies, the scattering of  $\alpha_{O\gamma}$  and  $\alpha_{X\gamma}$  around unity could be interpreted as a selection effect due to the observations at fixed energies.

Figure 7.3 shows the broad-band spectral index  $\alpha_{X\gamma}$  vs. X-ray luminosity  $\nu_X L_X$ . The average energy output at 1 keV only exceeds significantly the one at 200 GeV for 1ES 1011+496 ( $\alpha_{X\gamma} = 0.94$ ). This measurement was

triggered by an optical outburst. Unfortunately no simultaneous X-ray data are available. As the upper limit derived from the 2006 observations of 1ES 1011+496 is below the flux detected in 2007, the source was also in an high state at gamma-rays. The value  $\alpha_{X\gamma} = 0.94$  may be therefore taken with caution. For five of the detected sources the energy output in both

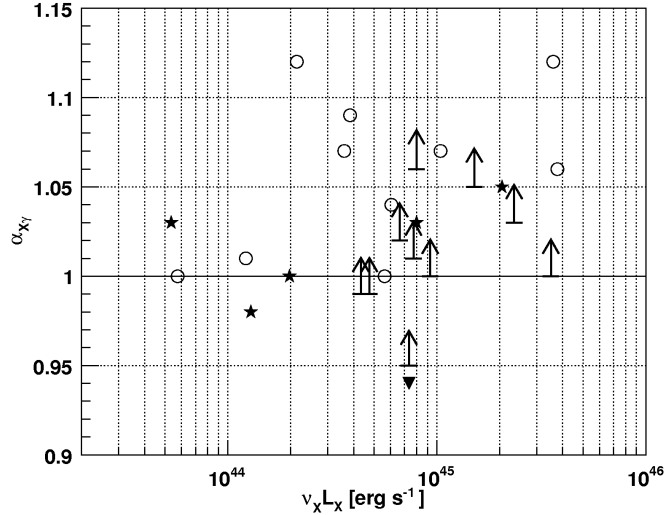


Figure 7.3: The broad-band spectral index  $\alpha_{X\gamma}$  vs. the X-ray luminosity  $\nu_X L_X$ . The arrows mark the upper limits for the spectral indices, while the stars indicate the values for the detected sources that belong to the sample described in Sect. 6.1. The triangle denotes the value for 1ES 1011+496, based on the flux measured in 2007. The open circles mark all other HBL objects detected at VHE gamma-rays with published fluxes (see Table 7.4).

bands is almost the same ( $\alpha_{X\gamma} \cong 1$ ), while for the other ten objects the energy output at 200 GeV is significantly lower with a maximum index of  $\alpha_{X\gamma} = 1.12$ , corresponding to a nine times lower energy output at 200 GeV compared to 1 keV. There is a weak tendency for an increasing  $\alpha_{X\gamma}$  with increasing X-ray luminosity.

In case of the non-detected objects,  $\alpha_{X\gamma} = 1$  can be excluded for five of them. However the upper limits are still in the region occupied by the VHE sources. Further observations of these objects with a more sensitive telescope, such as MAGIC-II, supposed to start regular data taking in 2009, are needed to scan the complete parameter space spanned by the current VHE sources. As the non-detected objects do not deviate in their spectral properties from the gamma-ray emitting objects the detection of all X-ray bright HBLs seems to be only a question of time.

# Chapter 8

## Spectral energy distribution

In the following chapter a single zone synchrotron self Compton (SSC) model is employed to simulate the spectral energy distribution (SED) of 1ES 1218+304 and 1ES 2344+514 (see also Sec.2.3.3). In addition to the simultaneous optical data, archival X-ray data are used. All equations in this chapter are presented in cgs-units.

### 8.1 Single zone SSC model

The emission is simulated using the code from R uger (2007), which also provides a numerical approximation for the complete Klein-Nishina cross section for the inverse Compton scattering. In the following the parameters of the model are briefly described.

The emission region is assumed to be a sphere with radius  $R$  containing a homogeneous magnetic field  $B$ . The emission region, embedded in a much larger radio jet, is supposed to move with relativistic speed along the jet axis. Depending on the angle between the jet and the line of sight, this results in a kinematic Doppler factor  $\delta$ , which effectively boosts the observed emission (see also Sec.2.3.1).

Inside the emission region are relativistic electrons, following a broken power law distribution in momentum with an exponential cut-off at the highest energies. The number density  $n(\gamma)$  of the electrons is given as

$$n(\gamma) = K\gamma^{-s_1} \left(1 + \frac{\gamma}{\gamma_b}\right)^{s_1-s_2} \exp\left(-\frac{\gamma}{\gamma_2}\right), \quad (8.1)$$

where  $\gamma$  is the Lorentz factor of the electron,  $K$  the scale factor of the electron number density,  $\gamma_b$  the Lorentz factor of the electrons at the spectral

break and  $\gamma_2$  the Lorentz factor at the exponential cut-off. The spectral indices  $s_1$  and  $s_2$  are the slopes of the electron spectrum below and above the break, respectively. The broken power law results from the equilibrium of injection of electrons, following a single power law in momentum, and the effect of radiative cooling which is dominated by synchrotron losses. The cut-off takes into account the limited electron energy, which can be reached by the acceleration process. All model parameters are listed in Table 8.1.

environmental parameters	
$R$	radius of the emitting sphere in cm
$B$	magnetic field in the emission region in Gauss
$\delta$	kinematic Doppler factor (dimensionless)
electron spectrum	
$K$	scale factor of the electron density (number electr./cm <sup>3</sup> )
$s_1$	slope of the electr. spectrum below the break
$s_2$	slope of the electr. spectrum above the break
$\gamma_b$	Lorentz factor of the electrons at the break
$\gamma_2$	Lorentz factor of the electrons at the exponential cut off

Table 8.1: The parameters of the SSC model.

The slopes  $s_1$  and  $s_2$  of the electron spectrum are related to the slopes  $\alpha_1$  and  $\alpha_2$  of the photon spectrum<sup>1</sup> below and above the synchrotron peak, respectively:

$$\alpha_i = \frac{-s_i + 1}{2}. \quad (8.2)$$

In case of Thomson scattering, the spectral slopes of the inverse Compton spectrum are the same as for the synchrotron spectrum. From Equation 8.2 one can see that  $\alpha = 1$  for  $s = 3$ , which corresponds to a peak in the energy density ( $\nu F(\nu)$ -plot). Therefore it holds:

$$s_1 < 3 \quad (8.3)$$

$$s_2 > 3 \quad (8.4)$$

Furthermore, the change in the spectral index at the break has to be in the order of unity. In the following  $s_2 = s_1 + 1$  is used, which is valid if synchrotron losses are dominant. This reduces the number of free parameters to seven. Note, that the spectral index of the photon spectrum after the peak can be varied over a wide range by the choice of  $\gamma_2$ .

<sup>1</sup> $F(\nu) \propto \nu^{-\alpha}$  in photons cm<sup>-2</sup> s<sup>-1</sup>

The kinematic Doppler factor  $\delta$  can be generally narrowed down to values below  $\sim 20$  for BL Lac objects from the observations of superluminal motion of radio knots in the jet (Cohen et al., 2007). Indeed most BL Lacs show even much lower apparent velocities indicating lower Lorentz factors (see also Sec. 2.3.1). A model independent lower limit can be set from the opacity condition for gamma-rays avoiding photon-photon pair production, given as (Dondi and Ghisellini, 1995):

$$\delta > \left( \frac{\sigma_{\text{T}}}{5hc^2} d_{\text{L}}^2 (1+z)^{2\beta} \frac{F(\nu_0)}{t_{\text{var}}} \right)^{1/(4+2\beta)}, \quad (8.5)$$

where  $\sigma_{\text{T}}$  is the Thomson cross-section,  $h$  the Planck constant,  $c$  the speed of light,  $d_{\text{L}}$  the luminosity distance of the source,  $z$  the redshift and  $t_{\text{var}}$  the variability time scale.  $F(\nu_0)$  is the differential energy density at  $\nu_0 = 1.6 \times 10^{40}/\nu_{\gamma}$ , the frequency of the target photons. The spectral index of the target photons is  $\beta$  which is equal to  $\alpha_1$  for  $\nu_0 < \nu_s$  and to  $\alpha_2$  for  $\nu_0 > \nu_s$ ,  $\nu_s$  being the frequency of the synchrotron peak.

For Equation 8.5 the relation between the size of the emission region  $R$  and the variability time scale  $t_{\text{var}}$  is used:

$$R \leq t_{\text{var}} \cdot c \cdot \delta \quad (8.6)$$

The model is determined with seven free parameters, which recommend seven independent information from the observation. These are (Tavecchio et al., 1998) the frequencies of the synchrotron and inverse Compton peak as well as the flux at the peaks, the slope of the photon spectrum below and above the peak<sup>2</sup> and the variability time scale. For HBL objects the high energy peak is so far observed only in a few cases, usually in a high flux state (e.g. Albert et al., 2007g). Due to variable flux amplitudes at almost all frequencies, strong constraints can only be made from simultaneous multiwavelength observations. As this requires observations at X-rays by satellite observatories and ground based (weather dependent) gamma-ray observations, successful multiwavelength campaigns are limited so far. Therefore the models are often under-determined, which obviates a unique set of parameters.

The parameter space of the magnetic field and the Doppler factor can be constrained by several conditions. Here the method of Kataoka et al. (1999) is employed which is itself based on Bednarek and Protheroe (1997).

---

<sup>2</sup>In the case of HBLs the slopes at the synchrotron peak are usually taken, as the energy range on the rising edge of the high energy peak is not observed for the most HBLs and the slope above the peak is steeper due to Klein-Nishina effects.

The first constraint combines the condition for a maximum Lorentz factor  $\gamma_{\max}$  of the electron spectrum<sup>3</sup>, derived from the highest energies observed in the Compton regime and the highest synchrotron photons. Following Equation 1.13, the Lorentz factor  $\gamma_{\max}$  of synchrotron photons at the cut-off  $E_{\text{syn,max}}$  can be described as

$$\gamma_{\max} = \sqrt{1.15 \times 10^8 \frac{E_{\text{syn,max}}}{\text{eV}} \cdot B^{-0.5} \cdot \delta^{-0.5}}. \quad (8.7)$$

From the observation of the highest photon energies  $E_{\text{IC,max}}$  it follows

$$\gamma_{\max} \geq \frac{E_{\text{IC}}}{m_e c^2 \delta}. \quad (8.8)$$

The combination of Equation 8.7 and Equation 8.8 yields

$$B \leq 1.15 \times 10^8 \frac{E_{\text{syn,max}}}{\text{eV}} \left( \frac{m_e c^2}{E_{\text{IC,max}}} \right)^2 \cdot \delta. \quad (8.9)$$

This constraint is strict, however in practise it is often very difficult to determine the cut-off energies  $E_{\text{syn,max}}$  and  $E_{\text{IC,max}}$ .

The second constraint uses the ratio of the synchrotron and the inverse Compton luminosities. In case of Thomson scattering the magnetic energy density  $u_B = u_{\text{syn}}(L_{\text{syn}}/L_{\text{IC}})$ , where  $L_{\text{syn}}$  and  $L_{\text{IC}}$  are the apparent synchrotron and the inverse Compton luminosities. The energy density of the synchrotron photon field can be represented as

$$u_{\text{syn}} = \frac{L_{\text{syn}}}{4\pi R^2 c \delta^2}, \quad (8.10)$$

leading to

$$u_B = \frac{d_L^2}{R^2 c \delta^4} \frac{(\nu F_{\text{syn}})^2}{\nu F_{\text{IC}}} = \frac{B^2}{8\pi}, \quad (8.11)$$

where  $d_L$  is the luminosity distance and  $\nu F_{\text{syn}}$  and  $\nu F_{\text{IC}}$  are the measured energy densities at the synchrotron and inverse Compton peak, respectively. Using Equation 8.6 the magnetic field is constrained as

$$B \geq \frac{d_L}{\nu F_{\text{syn}} c} \sqrt{\frac{8\pi}{\nu F_{\text{IC}}}} t_{\text{var}}^{-1} \delta^{-3}. \quad (8.12)$$

Note that this condition is only strictly valid in the Thomson limit. Otherwise Equation 8.11 becomes an inequality and the constraint is shifted to lower values of  $B$  and  $\delta$ .

---

<sup>3</sup>In the model which is applied here,  $\gamma_{\max}$  can be assumed to be identical with  $\gamma_2$ , the Lorentz factor at the cut-off.

The third constraint makes the assumption, that the cooling time  $t_{\text{syn}}$  due to synchrotron losses is smaller than the source crossing time scale  $R/c$ , which is valid for large Lorentz factors ( $\gamma > \gamma_b$ ). The cooling time is represented as

$$t_{\text{syn}} = \frac{3m_e c}{4u_B \sigma_T \gamma} \leq t_{\text{var}} \delta, \quad (8.13)$$

which becomes minimum for the highest Lorentz factors. Using Equation 8.7 for  $\gamma_{\text{max}}$ , the third condition can be expressed as

$$B \geq \left( \frac{6m_e c \pi}{\sigma_T} \right)^{2/3} \left( 1.15 \times 10^8 \frac{E_{\text{syn}}}{\text{eV}} \right)^{-1/3} t_{\text{var}}^{-2/3} \delta^{-1/3}. \quad (8.14)$$

The fourth constraint assumes that also the inverse Compton cooling time scale  $t_{\text{IC}}$  is shorter than the source crossing time  $t_{\text{var}} \delta$ . In case of Thomson scattering, Equation 8.13 can be used replacing the magnetic field density by the synchrotron photon density, yielding

$$B \leq \left( \frac{\sigma_T}{3m_e c^4 \pi} \right)^2 1.15 \times 10^8 \frac{E_{\text{syn,max}}}{\text{eV}} L_{\text{syn}}^2 t_{\text{var}}^{-2} \delta^{-11}. \quad (8.15)$$

The constraints together with the chosen parametrisation are shown at the end of the sections 8.2.3 and 8.3.3 for 1ES 2344+514 and 1ES 1218+304, respectively.

## 8.2 1ES 2344+514

The object 1ES 2344+514 was discovered in the *Einstein* Slew Survey (1ES, Elvis et al., 1992) in the hard X-ray band. It was identified by Perlman et al. (1996) as a BL Lac object at a redshift of  $z = 0.044$  revealing the object as one of the closest blazars (e.g. the sixth closest in the compilation of Donato et al. (2001)). It was the third extragalactic object detected at VHE gamma-rays (Catanese et al., 1998) after the discoveries of Mrk 421 (Punch et al., 1992) and Mrk 501 (Quinn et al., 1996), all of them observed with the Whipple 10 m reflector. The source was later confirmed by the HEGRA collaboration on a  $4\sigma$  level using their stereo system of Cherenkov telescopes (Aharonian et al., 2004a). The mass of the central black hole as derived from stellar velocity dispersion is  $10^{8.80 \pm 0.16} M_{\odot}$  (Barth et al., 2003). Observations with the BeppoSAX satellite in 1996 showed a very hard X-ray spectrum up to  $\sim 50$  keV revealing the object as an extreme blazar (together with Mrk 501 and 1ES 1426+428) with a synchrotron peak in the hard X-ray band (Giommi et al., 2000).

The SED of 1ES 2344+514 will be modeled for three different gamma-ray samples: (i) the average spectrum measured by MAGIC in 2005 as derived in this work; (ii) the "highflux" subsample as defined in Chapter 6.4.3; (iii) the exceptional outburst measured by Whipple in 1995 (Schroedter et al., 2005). For none of the samples are any simultaneous X-ray data available. The object was also not detected by the EGRET instrument yielding a gap from  $\sim 50$  keV to  $\sim 100$  GeV in the SED.

### 8.2.1 Gamma-ray data

First the gamma-ray data have to be deabsorbed. Therefore the optical depth  $\tau$  is calculated for each energy bin (see also Chapter 1.4), and the measured flux is corrected by multiplying with  $\exp(\tau(E,z))$ . Figure 8.1 shows the average spectrum (differential spectrum multiplied by  $E^2$ ) as derived from the complete data sample as well as the midflux subsample before and after deabsorption. Both spectra are in good agreement, which justifies one parametrisation of the SED fitting both spectra. As expected the deabsorbed spectrum hardens significantly. The spectra are well described by power laws with indices  $-(0.31 \pm 0.20)$  and  $-(0.51 \pm 0.30)$  respectively. As the spectra do not become significantly flatter at lower energies, the high energy peak has to be below 100 GeV. In the framework of a SSC model, the high energy spectrum steepens dramatically after the Inverse Compton peak, as the photons get scattered by the electrons in the Klein-Nishina regime. Therefore the high energy peak has to be in the energy range shortly below the observed one.

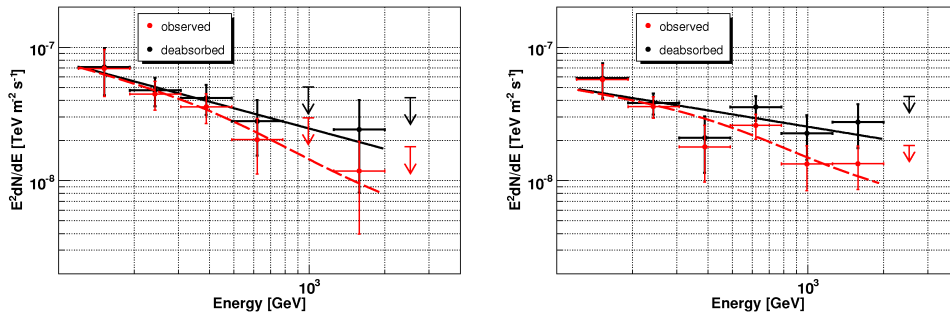


Figure 8.1: Energy spectrum of 1ES 2344+514 multiplied by  $E^2$  for the midflux data sample (left) and the complete sample (right). The red points mark the observed spectrum, the black one after deabsorption. The arrows are ULs on a 99% confidence level. The red dashed lines are derived from the fits to the deabsorbed spectra (solid lines) by multiplying with  $\exp(-\tau(E,z))$ .

As shown in Chapter 6.4.3 the source showed significant flux variations during the observation campaign, coming along with a spectral hardening.

While the differential flux at  $\sim 150$  GeV is the same for the highflux and the complete sample, the spectral hardening causes a more than two times higher integral flux above 200 GeV. Figure 8.2 shows the highflux spectrum in a  $E^2 dN/dE$  plot before and after deabsorption. Both are in good agreement with a power law, the deabsorbed one with an index of  $0.17 \pm 0.17$ . A fit by a logarithmic parabola gives a comparable result ( $\chi^2/\text{n.d.o.f.} = 2.2/3$  vs.  $\chi^2/\text{n.d.o.f.} = 4.0/4$  for the power law fit), yielding a peak at  $650 \pm 190$  GeV.

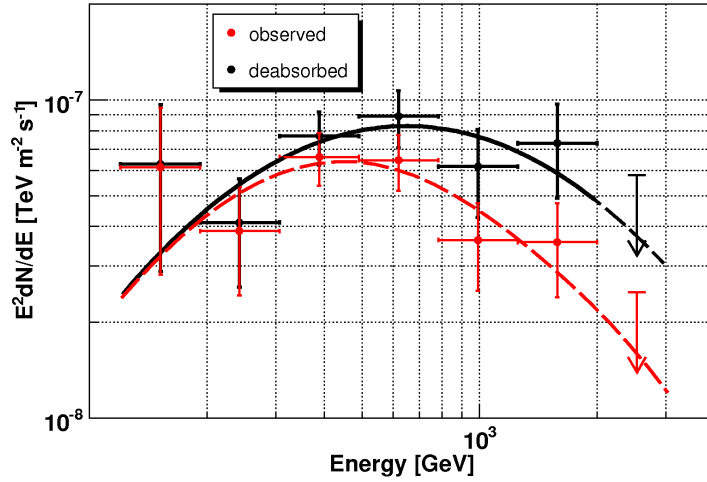


Figure 8.2: Energy spectrum of 1ES 2344+514 multiplied by  $E^2$  for the highflux sample. The red points mark the observed spectrum, the black one after deabsorption. The arrows are ULs on a 99 % confidence level. The fit by a logarithmic parabola yields a peak energy of  $650 \pm 190$  GeV for the deabsorbed spectrum. The red dashed line is derived from the fit to the deabsorbed spectrum (solid lines) by multiplying with  $\exp(-\tau(E, z))$ .

In 1995 the source underwent an exceptional outburst, which led to a clear detection at VHE gamma-rays with the Whipple telescope above  $\sim 0.8$  TeV (Catanese et al., 1998). The differential spectrum between 0.8 TeV and 12.6 TeV can be well described by a power law with index  $-(2.54 \pm 0.17)$  (Schroedter et al., 2005). For an object at a distance of  $z = 0.044$  the energy  $E_c$ , where the optical depth for photon-photon pair production is unity, is about 4.0 TeV. Nevertheless the spectrum up to 12.6 TeV showed no hint for a steepening or a cut-off. This yields a hard intrinsic spectrum. The spectral index for a power law after deabsorption is  $-(2.08 \pm 0.35)$ , which means that the high energy peak should be within or very close to the observed energy range. The deabsorbed spectrum is shown in Figure 8.3.

### 8.2.2 Multiwavelength data - the X-ray properties

Except the measurement in the optical (R-band) from KVA, no simultaneous multiwavelength data are available for the time of the MAGIC observations. For the flare in 1995 observed by Whipple, even no optical data are available. To model the synchrotron spectrum, X-ray observations, performed by the BeppoSAX satellite in 1996 and 1998 are taken (Giommi et al., 2000). These data show strong variability, both in flux and in the spectral behaviour. The integral flux from 2 keV to 10 keV changed by a factor of 4.5 (and even more at the highest energies). The slope of the differential spectrum changed from  $-(2.31 \pm 0.05)$  (steepest spectrum, lowest flux level) to  $-(1.77 \pm 0.04)$  (hardest spectrum, highest flux level), revealing peak energies from below 1 keV to more than  $\sim 50$  keV. All other reported measurements in the X-ray regime are within the wide range of the spectra obtained by BeppoSAX observations. For the simulation of the SED three spectra are taken into account. The one from December 7th 1996, which showed the hardest spectrum with the highest flux level, the one from December 11th 1996, where the source was in an intermediate state with a slope of  $-(2.03 \pm 0.04)$  and an integral flux between the highest and lowest level and the one from June 26th 1998, where the source reached its lowest level and the steepest spectrum. The object was also observed by *Swift* on 19 April 2005 (Tramacere et al., 2007). The spectrum derived from this observation is in good agreement with the one observed by BeppoSAX in 1998. The minimum time scale for flux variations observed in the BeppoSAX campaign in 1996 amounts to  $\sim 5000$  sec (Giommi et al., 2000).

### 8.2.3 Model fit

The shortest time scale for flux variability  $t_{\text{var}}$ , found at VHEs so far is one day (Catanese et al., 1998, and this work). Nevertheless variation on shorter time scales cannot be excluded due to the limited sensitivity of the instruments and the sparse sampling of the lightcurve. At hard X-rays the shortest variability time scale observed so far is 5000 sec (Giommi et al., 2000). Similar (and even lower) time scales were observed at VHE gamma-rays for other HBL objects such as Mrk 421 (Gaidos et al., 1996), Mrk 501 (Albert et al., 2007g) and PKS 2155-304 (Aharonian et al., 2007d).

Taking  $t_{\text{var}} = 5000$  s, the minimal Doppler factor is estimated following Equation 8.5 as  $\delta > 7.7$  for photons with an energy of  $\sim 2$  TeV ( $\nu_{\gamma} = 4.8 \times 10^{26}$  Hz,  $\nu_0 = 3.3 \times 10^{13}$  Hz,  $F(\nu_0) \approx 10^{-12}$  erg cm $^{-2}$  s $^{-1}$  and  $\beta = 0.65$ ). Assuming  $t_{\text{var}}$  fixed from observations, the radius of the emission regions is  $R = \delta \cdot 1.5 \times 10^{14}$  cm; every change in the Doppler factor causes a change

in  $R$  and vice versa. Restricting the Doppler factor to values between 8 and 20, the emission region has to be between  $1.2 \times 10^{15}$  cm to  $3.0 \times 10^{15}$  cm (0.0004 pc to 0.001 pc or 80 to 200 astronomical units).

In all observations the X-ray data are close to the synchrotron peak. On the one hand this gives strong constraints on the position of the peak as well as on the flux at the peak. On the other hand, the spectral index of the electron spectrum can be hardly constrained from the X-ray data only. This is done by the interpolation from the synchrotron peak to the host galaxy corrected optical flux.

Figure 8.3 shows the SED from the optical to VHE of 1ES 2344+514 for all three samples. The radio data are excluded as they are supposed to originate from a different part of the jet. The resulting parameters are listed in Table 8.2. The 1995-flare is modeled twice. One set of parameters using the hardest X-ray spectrum ever measured to determine the synchrotron peak and another set, ignoring all X-ray observations so far with the goal of an inverse Compton peak in the TeV regime. In general the object reveals extremely high peak frequencies, which already push the model to its limit.

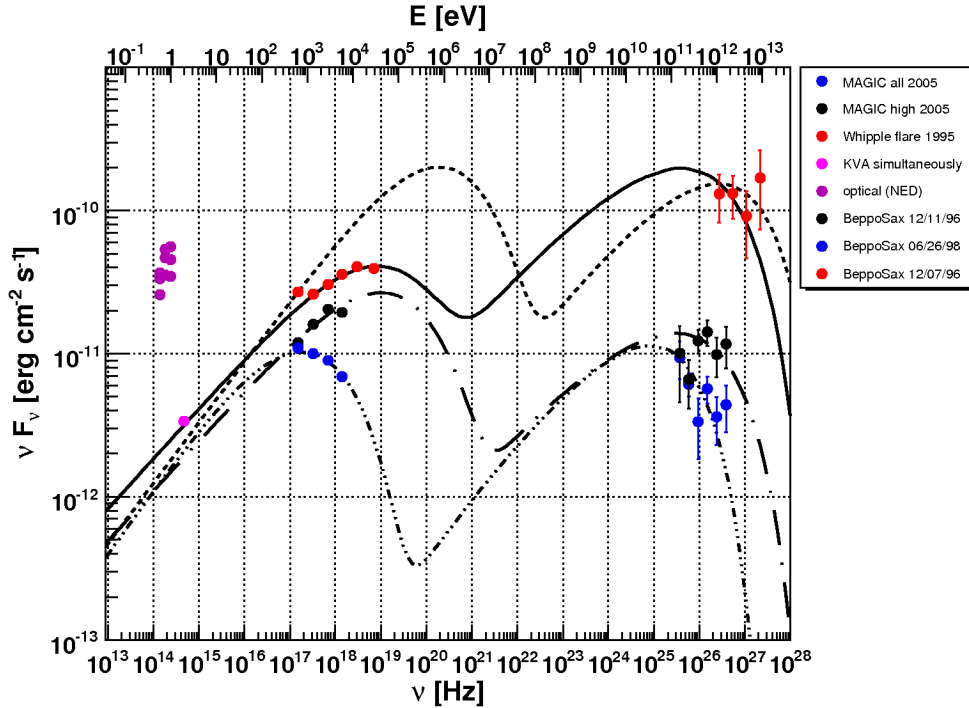


Figure 8.3: Spectral energy distribution of 1ES 2344+514 for different states of activity. The optical data from NED are not host galaxy corrected.

Even with a synchrotron peak at  $\sim 50$  keV, an inverse Compton peak at  $\sim 2$  TeV as suggested from the Whipple observations is not possible for a single zone SSC model. The reason is the strongly reduced scattering cross section at these energies. In case of Thomson scattering the frequency of the inverse Compton peak  $\nu_{\text{IC}}$  is related to the  $\nu_s$  and  $\gamma_b$  as (e.g. Mastichiadis and Kirk, 1997):

$$\nu_{\text{IC}} = \frac{4}{3} \gamma_b^2 \nu_s \quad (8.16)$$

For  $\nu_s \approx 10^{19}$  Hz and  $\gamma_b \approx 10^6$  the inverse Compton peak would be at  $\nu_{\text{IC}} \approx 10^{31}$  Hz, which is apparently not the case. The reason for  $\nu_{\text{IC}}$  being five orders of magnitudes lower than expected from scattering in the Thomson regime, is that the Thomson approximation is not valid already on the rising edge of the inverse Compton bump. This can be quantified by the condition  $h\nu \ll m_e/\gamma_b$  for Thomson scattering. For  $\gamma_b \approx 10^6$ , all synchrotron photons from the optical up to the hard X-ray regime will be scattered in the Klein-Nishina regime. To produce still a reasonable output at TeV energies, the reduced scattering cross section has to be compensated by a larger electron density. By ignoring the X-ray data for the 1995-flare, the parameters were chosen, such that the inverse Compton peak is around 2 TeV. This results in a synchrotron peak at  $\sim 1$  MeV and requires very high Lorentz factors at the break, which is problematic as electrons at high energies suffer more from synchrotron losses.

Assuming  $\nu_s < 100$  keV results in inverse Compton peaks below a few hundred GeV. Due to the larger errors in the VHE regime, this is still consistent with the observation. Note that in that case the last data point is always underestimated by the model. Harder spectra at TeV energies would be a serious problem for SSC models. The recently reported spectra of the distant HBLs 1ES 1101-232 ( $z=0.186$  Aharonian et al., 2007c) and 1ES 0229+200 ( $z=0.14$  Aharonian et al., 2007b) reveal extremely hard spectra after deabsorption ( $\alpha < 1$  up to TeV energies), even with a density of the MRF close to the galaxy number counts. In the context of a multi-component SSC model, additional TeV photons could be produced by a second component with synchrotron radiation up to MeV energies. Other peaks located between the X-ray and the VHE band cannot be excluded at the moment due to the lack of observational data. Future experiments in the medium gamma-ray range (500 keV to 10 MeV) could close this gap.

Another explanation for hard TeV spectra in the framework of leptonic models, avoiding additional peaks, could come from an external target photon field (e.g. Kataoka et al., 1999). In that context IR photons would be important since they can be scattered up to TeV energies without entering the Klein Nishina regime. Because of the anisotropy of an external photon

parameter	1995 flare (Whipple)		MAGIC 2005	
	"with X-ray"	"without X-ray"	highflux	all
$R$	$2.1 \times 10^{15}$	$2.1 \times 10^{15}$	$2.1 \times 10^{15}$	$2.1 \times 10^{15}$
$\delta$	14	14	14	14
$B$	0.095	0.15	0.24	0,225
$K$	$2.7 \times 10^6$	$2.5 \times 10^5$	$3.5 \times 10^5$	$8.0 \times 10^4$
$s_1$	2.30	2.15	2.30	2.10
$s_2$	3.30	3.15	3.30	3.10
$\gamma_b$	$1.5 \times 10^6$	$5.0 \times 10^6$	$1.2 \times 10^6$	$1.0 \times 10^5$
$\gamma_2$	$5.0 \times 10^6$	$1.5 \times 10^7$	$3.6 \times 10^6$	$4.0 \times 10^5$
$\chi^2/\text{n.d.o.f.}$	0.47	-	0.99*	3.33* (1.20)

Table 8.2: Values of the model parameters for the simulated SED of different observations of 1ES 2344+514 together with the reduced  $\chi^2$ -values of the fit. In case of the simulation of the 1995 data without using the X-ray data, the number of degrees of freedom is below the number of free parameters. The values marked by an asterisk are derived without taking the KVA point into account. The value in brackets gives the fit results for the case that also the first X-ray data point is excluded.

field, the comptonisation can be even more efficient as the SSC mechanism (e.g. Sikora et al., 1994; Dermer et al., 1997). These photons can be emitted from dust around the nucleus, at the same time hidden by the strong jet emission in the observer's frame. Also synchrotron photons from other parts of the jet can be considered, assuming a more complex geometry of the jet in which this component is less beamed towards the observer due to a larger viewing angle. A second order inverse Compton scattering can be neglected here, as this would be strongly suppressed by Klein-Nishina effects.

The simulation of the different emission states was performed with the same values for the size of the emission region and the Doppler factor. The different peak energies are primarily produced by shifting Lorentz factors at the break and the cut-off of the electron spectrum. The different flux amplitudes are primarily produced by different electron densities. Similar results for the flaring behaviour of Mrk 421 were found by Mastichiadis and Kirk (1997). The change in the slope of the electron spectrum is maybe surprising, as it slightly steepens with increasing flux. If the synchrotron peak is shifted to higher energies, without a dramatic change in amplitude at lower energies, the spectrum has to be steeper not to underestimate the optical data. It was argued by several authors for 1ES 2344+514 and Mrk 501, that the spectral behaviour in the synchrotron regime could be explained by a two electron populations. One responsible for synchrotron radiation from the far

IR to the X-ray regime with a peak energy below  $\sim 1$  keV and only moderate variations, and a second component producing peak energies up to  $\sim 100$  keV which can completely dominate the synchrotron spectrum in a flaring state (e.g. Giommi et al., 2000; Massaro et al., 2004). In this context a single component SSC model will always produce an effective electron spectrum, which would be a superposition of the two component spectrum.

In Figures 8.4 and 8.5 the constraints on  $B$  and  $\delta$ , as derived at the beginning of this Chapter are shown for all the four simulations of the SED together with the chosen parametrisation. The values for the observational parameters which are used to calculate the constraints are listed in Table E.1. In a few cases, the parametrisation violates the second constraint, while elsewhere they are inside the allowed parameter space. The second constraint is only strictly valid in case of Thomson scattering, otherwise the line is shifted to lower values of  $B$  and  $\delta$ . As already pointed out in this chapter, the Thomson limit does not hold here for a dominant part of the inverse Compton spectrum, due to the high peak frequencies (resulting in high Lorentz factors).

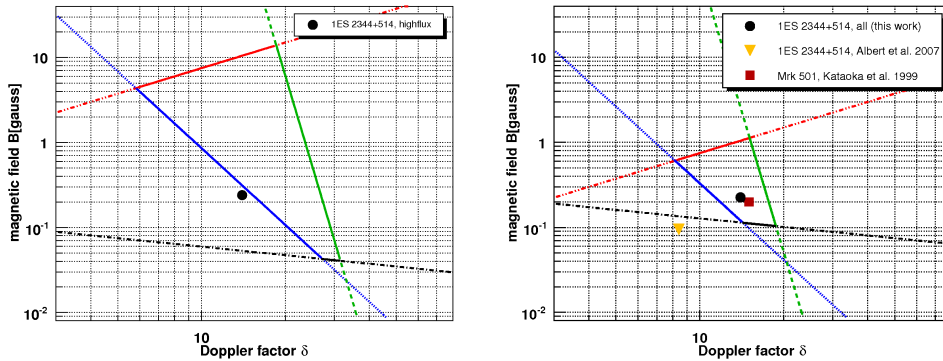


Figure 8.4: The magnetic field  $B$  vs. the Doppler factor  $\delta$  as constrained from a single zone SSC model for 1ES 2344+514 for the highflux data sample (left) and the complete sample (right). The different constraints are marked in red (i, Equ. 8.9), blue (ii, Equ. 8.12), black (iii, Equ. 8.14) and green (iv, Equ. 8.15). The dots show the chosen parameters for the simulation; in the right panel also the values from Albert et al. (2007b), derived for the same observation (triangle), as well as from Kataoka et al. (1999) for the SED of Mrk 501 (square) are shown.

How reliable are the other limits? The first constraint strongly depends on the highest energies which are measured in the synchrotron and the inverse Compton regime. As neither in the hard X-ray nor in the VHE band any intrinsic cut-offs have been seen, the highest energies can be only estimated. In case of the VHE cut-off, the highest observed energies are used. If the intrinsic cut-off is located at much higher energies, the first constraint would

be shifted to larger values of  $B$ . Except the first one, all other constraints depend on the variability time scale, which is not known for many observations. Nevertheless the allowed parameter space (at least for the 2005 data) has a good overlap with the one derived by Kataoka et al. (1999) for observations of Mrk 501 from 1996, yielding a similar magnetic field ( $B = 0.2$  G) and Doppler factor ( $\delta = 15$ ). This is not surprising as both objects show comparable luminosities and spectral properties.

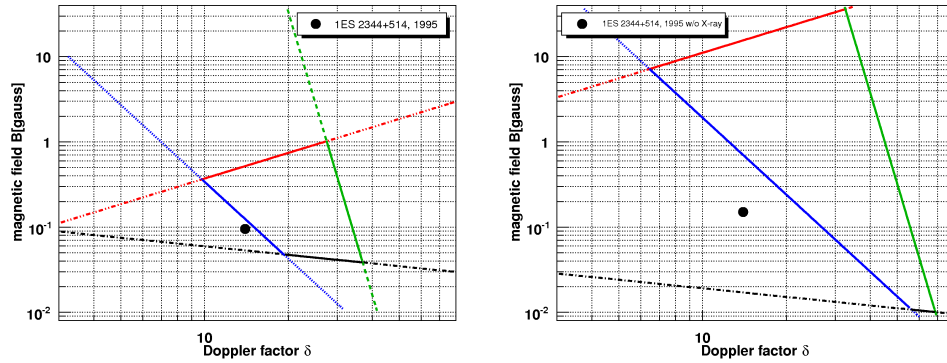


Figure 8.5: The magnetic field  $B$  vs. the Doppler factor  $\delta$  as constrained from a single zone SSC model for 1ES 2344+514 for the 1995 flare modelling including the X-ray data (left) and without the measured X-ray data (right). The different constraints are marked in red (i, Equ. 8.9), blue (ii, Equ. 8.12), black (iii, Equ. 8.14) and green (iv, Equ. 8.15). The dots mark the chosen parameters for the simulation.

The values for the model parameter of the average 2005 spectrum are in reasonable agreement with the ones derived by Albert et al. (2007b) for the same observation using another single zone SSC code. While the electron spectrum is almost identical, they got lower values for the magnetic field ( $B = 0.095$  G) and the Doppler factor ( $\delta = 8.4$ ). These values are clearly outside the region enclosed in Figure 8.4. The apparent mismatch can be explained, taking into account the longer variability time scale, used for their simulation ( $t_{\text{var}} \approx$  one day). Larger values of  $t_{\text{var}}$  shift the constraints two, three and four to lower values of  $B$  and  $\delta$ .

### 8.3 1ES 1218+304

This object was first suggested to be a X-ray emitting BL Lac object by Wilson et al. (1979) from the identification of the former unidentified X-ray source 2A 1219+305, observed by the Ariel V satellite (Cooke et al., 1978), with the radio source RS 4. Optical observations revealed a featureless continuum spectrum, typical for BL Lacertae objects. This result was

confirmed at the same time by Schwartz et al. (1979) based on X-ray observations with the Scanning Modulation Collimator experiment onboard the first High Energy Astronomy Observatory (HEAO 1), which provided a much better spatial resolution than the instrument onboard the Ariel V satellite. In addition the search for historical variability by L. Chaisson in the optical, using the Harvard College Observatory plate stack collection, revealed several events including a  $1.1 \pm 0.2$  mag variation of the optical flux within 120 days in 1941.

VHE gamma-ray emission was first discovered from this object by the MAGIC telescope in an observation campaign carried out in January 2005 (Albert et al., 2006d). The new TeV source was recently confirmed by observations with the VERITAS stereoscopic system, taken place from December 2006 to March 2007, with a significance of  $10.2 \sigma$  (Fortin, 2007). Several observations with the Whipple telescope between 1995 and 2000 resulted in an upper flux limit of  $F(> 350 \text{ GeV}) = 8.3 \times 10^8 \text{ photons m}^{-2} \text{ s}^{-1}$  (corresponding to  $\sim 8\%$  of the Crab Nebula flux) (Horan et al., 2004). The source was also observed by HEGRA between 1996 and 2002. An upper flux limit above 840 GeV of  $2.67 \times 10^8 \text{ photons m}^{-2} \text{ s}^{-1}$  (or 12% of the Crab Nebula flux) is reported by Aharonian et al. (2004a).

The mass of the central black hole is estimated to  $m_{BH} = 10^{8.0} M_{\odot}$  from the tight correlation between black hole mass and central velocity dispersion (Wu et al., 2002). The latter was derived from morphology parameters of the host galaxy (adopting the fundamental plane for ellipticals). The redshift is determined to  $z = 0.182$  (Véron-Cetty and Véron, 2006), which makes it one of the farthest objects, detected at VHE gamma-rays so far<sup>4</sup>.

The SED is modeled for three VHE data samples: (i) the average spectrum for the 2006 January to March MAGIC observations as derived in this work; (ii) the spectrum of the first subsample of the 2006 observations as described in Section 6.4.2; (iii) the 2005 MAGIC observations, taken from Albert et al. (2006d). For each sample, simultaneously taken optical data are available from KVA. Again archival X-ray data are used for the modelling.

### 8.3.1 Gamma-ray data

Due to the large distance of 1ES 1218+304 strong attenuation is expected. The correction is done analogue to Section 8.2.1. Figure 8.6 shows the differential energy spectrum multiplied by  $E^2$  for the complete 2006 sample as

---

<sup>4</sup>More distant VHE sources are 1ES 1101-232 ( $z = 0.186$ ), 1ES 0347-121 ( $z = 0.188$ ), 1ES 1011+496 ( $z = 0.212$ ) and the recently discovered quasar 3C 279 ( $z = 0.538$ ) (Teshima et al., 2007)

well as for the first subsample before and after the deabsorption. Both samples are in good agreement with single power laws. For the complete sample the slope is  $-(0.68 \pm 0.80)$ , from which a peak energy below  $\sim 100$  GeV can be concluded. In case of the first subsample, the energy density seems to increase with increasing energy after deabsorption (slope of the power law fit:  $0.27 \pm 0.79$ ), although this is not significant due to the large error of the last point. With the so far measured synchrotron peak energies an inverse Compton peak in the TeV range seems not feasible for a single zone SSC model (see Section 8.3.3). Instead the peak is assumed to lie within or at slightly lower energies than the measured energy range.

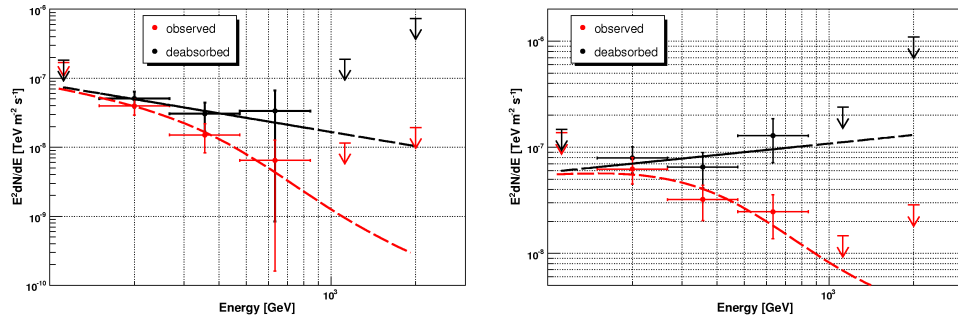


Figure 8.6: Energy spectrum of 1ES 1218+304 multiplied by  $E^2$  for the complete data sample (left) and the first subsample (right). The red points mark the observed spectrum, the black one after deabsorption. The arrows are upper limits on a 99% confidence level. The red dashed lines are derived from the fits to the deabsorbed spectra (solid lines) by multiplying with  $\exp(-\tau(E, z))$ .

The deabsorbed spectrum measured in 2005 is well described by a power law with spectral index  $-(0.34 \pm 0.50)$  ( $E^2 dN/dE$ -plot). Within the errors this is in good agreement with the average 2006 spectrum. By the time of this work no spectrum of 1ES 1218+304 has been published by the VERITAS collaboration from their 2006/2007 observations.

### 8.3.2 Multiwavelength data - the X-ray properties

1ES 1218+304 was observed many times by several X-ray satellites within the last 30 years. A good estimation about the variability can be derived from ROSAT observations (WGACAT2), revealing variations by a factor of  $\sim 6$  for the flux at 1 keV, ranging from 0.8 to 4.2 in units of  $10^{-11}$  erg cm $^{-2}$  s $^{-1}$ . Within the single observations no evidence for short time variability was seen. The spectral behaviour is less extreme than for 1ES 2344+514. Spectral investigations from various instruments (e.g. XMM-Newton (Blustin et al., 2004) and BeppoSAX (Costamante et al., 2001)) showed a steep spectrum

in the hard X-ray band, restricting the synchrotron peak to energies below or close to  $\sim 0.1$  keV.

Except for the measurement in the optical (R-band) from KVA, no simultaneous multiwavelength data are available for the time of the MAGIC observations. In 2005 and 2006 two X-ray observation campaigns were performed on 1ES 1218+304: one by *Swift* on October 30th and 31st 2005 (Tramacere et al., 2007) and one by Suzaku from May 19th to 21st 2006 (Takahashi et al., 2007). While the Swift observations showed the source in a comparable flux state as observed in 1999 by BeppoSAX, the Suzaku measurement gives the first evidence for a peak energy around  $\sim 1$  keV.

For the simulation of the 2005 spectrum as well as the complete sample of the 2006 observation, the BeppoSAX observation from 1999 and the Swift observation from 2005 are used. For the first subsample, which indicates a slightly harder VHE spectrum, the Suzaku data from 2006 are used.

### 8.3.3 Model fit

Again the minimal Doppler factor shall be estimated using equation 8.5. For a variability time scale  $t_{\text{var}} = 5000$  s as used for 1ES 2344+514, one gets  $\delta > 11.1$  for photons with an energy of  $\sim 630$  GeV ( $\nu_{\gamma} = 1.5 \times 10^{26}$  Hz,  $\nu_0 = 1.0 \times 10^{14}$  Hz,  $F(\nu_0) \approx 3 \times 10^{-12}$  erg cm $^{-2}$  s $^{-1}$  and  $\beta = 0.60$ ). The flux

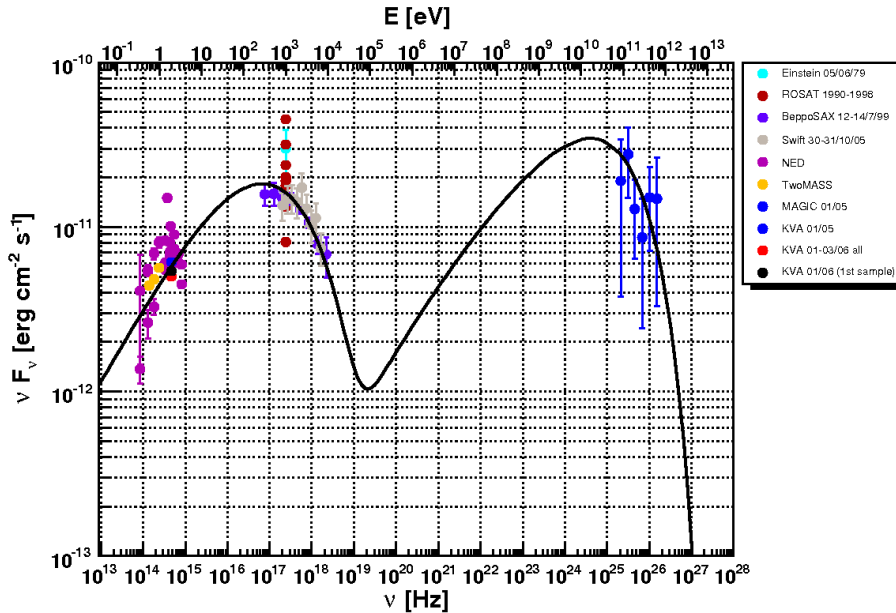


Figure 8.7: Spectral energy distribution of 1ES 1218+304 for the 2005 observation. The optical data from NED are not host galaxy corrected.

level around the peaks of 1ES 1218+304 is comparable to the one of 1ES 2344+514, yielding a 20 times higher apparent luminosity of 1ES 1218+304 due to its larger distance. With the resulting size of the emission region, taking  $t_{\text{var}} = 5000\text{ s}$  and  $\delta = 11$  the observed flux level was not reachable. Instead a Doppler factor of 17 and a blob radius of  $6 \times 10^{15}\text{ cm}$  is used. This choice is somehow arbitrary. The goals were (i) to keep  $\delta$  below 20 and (ii) to reach values of  $t_{\text{var}}$  of a few hours as observed for other HBL objects.

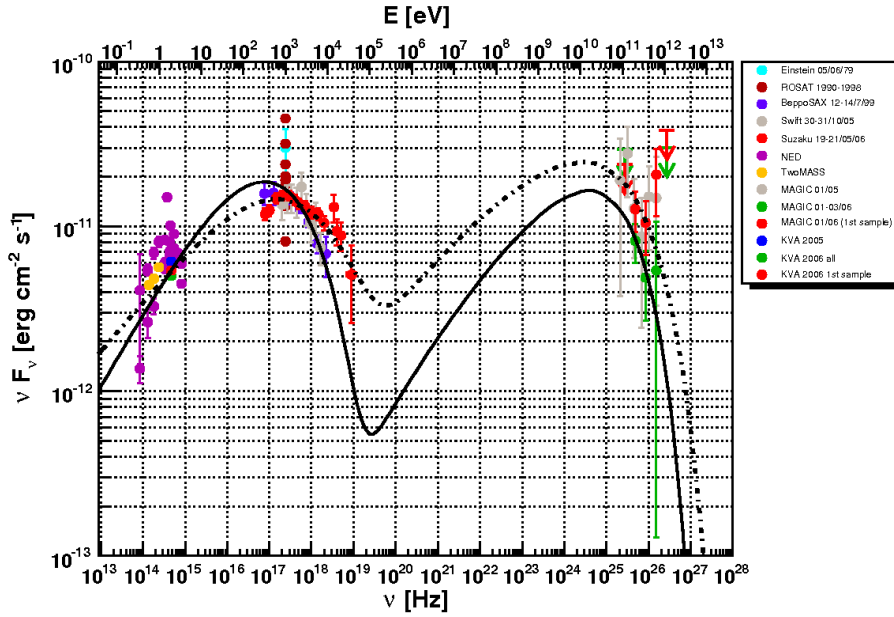


Figure 8.8: Spectral energy distribution of 1ES 1218+304 for the 2006 observation. The 2005 MAGIC observations are shown in the background in grey. The optical data from NED are not host galaxy corrected.

The SED from the optical to VHE is shown in Figure 8.7 for the 2005 and in Figure 8.8 for the 2006 observations. The radio band is excluded as the radiation is supposed to originate from a different part of the jet. The parameters are listed in Table 8.3. The synchrotron peak is around 0.3 keV, at one to two orders of magnitude lower energies than for 1ES 2344+514. This is reflected by the much lower Lorentz factors at the break and at the cut-off. The magnetic field is higher than for 1ES 2344+514. This could be in principle avoided by a larger Doppler factor as the consequences for the SED are similar (shift of the flux level at almost all wavelengths and a shift in the frequencies). The average VHE spectrum in 2005 has a slightly higher flux level than in 2006 with a comparable spectral shape. As for both samples the same X-ray data are used, the electron density in 2005 is two

times higher than in 2006, resulting in a higher energy output in the inverse Compton than in the synchrotron regime. As the first subsample of the 2006 observations shows the hardest spectrum, the Lorentz factors at the break and the cut-off are higher. As a consequence of the higher synchrotron peak frequency, combined with almost the same flux level, the electron spectrum is chosen steeper to fit the optical data. This also results in a higher value for  $K$ , as the density around the break should be similar to the other simulations.

The last data point(s) are always underestimated by the model, although within the errors, the model is still consistent with the observations. Due to the lower synchrotron peak values compared to 1ES 2344+514, inverse Compton peaks above  $\sim 100$  GeV seems not feasible with a single zone SSC model. With  $\gamma_b$  in the order of  $10^{4-5}$ , the condition for Compton scattering in the Thomson limit is no longer valid for photon energies above  $\sim 10$  eV. The case is not as extreme as for 1ES 2344+514, but also for this source, a sharp cut-off is expected due to Klein-Nishina effects above  $\sim$  TeV energies. Future measurements at GeV energies from the LAT onboard the GLAST satellite should reveal the high energy peak of 1ES 1218+304 in the 10 GeV-range. Further measurements at TeV energies would clarify, if the observed increase at the highest energies of the deabsorbed spectrum is real, or just a statistical fluctuation or a so far unknown systematic error from the analysis.

parameter	MAGIC 2005	MAGIC 2006	
		all	first sample
$R$	$6.0 \times 10^{15}$	$6.0 \times 10^{15}$	$6.0 \times 10^{15}$
$\delta$	17	17	17
$B$	0.33	0.45	0.33
$K$	$5.8 \times 10^4$	$3.0 \times 10^4$	$6.3 \times 10^5$
$s_1$	2.10	2.10	2.40
$s_2$	3.10	3.10	3.40
$\gamma_b$	$4.0 \times 10^4$	$4.0 \times 10^4$	$1.0 \times 10^5$
$\gamma_2$	$2.0 \times 10^5$	$2.0 \times 10^5$	$6.0 \times 10^5$
$\chi^2/\text{n.d.o.f.}$	1.16	1.77	1.36

Table 8.3: Values of the model parameters for the simulated SED of different observations of 1ES 1218+304 together with the reduced  $\chi^2$ -values of the fit.

In Figures 8.9 and 8.10 the constraints on  $B$  and  $\delta$ , as derived at the beginning of this Chapter are shown for all the three simulations of the SED together with the chosen parametrisation. The values for the observational parameters which are used to calculate the constraints are listed in Table E.2.

In all cases the chosen parametrisation is well inside the allowed parameter space. In contrast to 1ES 2344+514, even the second constraint, which assumes Thomson scattering, is not violated. Because the spectral properties of 1ES 1218+304 are less extreme, a larger fraction of the high energy output is scattered in the Thomson regime.

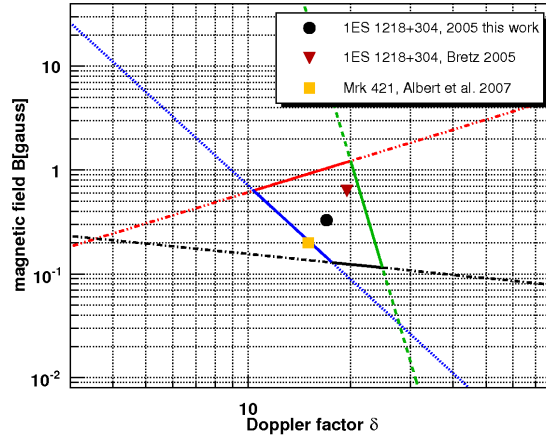


Figure 8.9: The magnetic field  $B$  vs. the Doppler factor  $\delta$  as constrained from a single zone SSC model for 1ES 1218+304 for the 2005 observation. The different constraints are marked in red (i, Equ. 8.9), blue (ii, Equ. 8.12), black (iii, Equ. 8.14) and green (iv, Equ. 8.15). The dot mark the chosen parameters for the simulation presented in this work, the triangle the parameters as derived by Bretz (2006) for the same observation and the square the one for the SED of Mrk 421 as derived by Albert et al. (2007c).

For the 2005 data, the parameters are in good agreement with the ones, derived by Bretz (2006) for the same observation (see Fig. 8.9). As the spectral properties of 1ES 1218+304 are quite similar to those of Mrk 421, it is not surprising that the parameters found here are consistent with the ones derived by Albert et al. (2007c) for observations of Mrk 421 in 2005 with MAGIC telescope. The constraints two, three and four would be shifted towards lower values for a larger variability time scale. In that case, the size of the source region can be larger, which would also allow lower Doppler factors.

## 8.4 Summary and conclusions

The spectral energy distribution from the optical to VHE gamma-rays of the two HBL objects 1ES 2344+514 ( $z = 0.044$ ) and 1ES 1218+304 ( $z = 0.182$ ) is successfully modelled with a single zone SSC model for different states of activity. The set of model parameter found in this work is thereby not

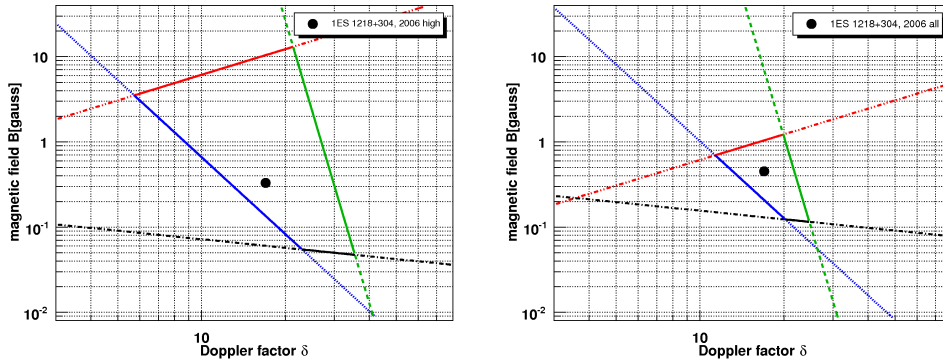


Figure 8.10: The magnetic field  $B$  vs. the Doppler factor  $\delta$  as constrained from a single zone SSC model for 1ES 1218+304 for the 2006 observations as derived in this work (left: highflux sample; right: complete sample). The different constraints are marked in red (i, Equ. 8.9), blue (ii, Equ. 8.12), black (iii, Equ. 8.14) and green (iv, Equ. 8.15). The dots mark the chosen parameters for the simulation.

unique, as the VHE observations lack simultaneously X-ray data. Also the huge spectral gap from  $\sim 100$  keV to  $\sim 100$  GeV is a severe problem, as the high energy peak is not clearly detected and intermediate peaks cannot be excluded. Furthermore the only detected short time variability comes from a X-ray observation from 1996 for 1ES 2344+514. The resulting parameters are in good agreement with other SED simulations (Bretz, 2006; Albert et al., 2007b) of these sources and also with the modelling of similar HBL objects like Mrk 501 (e.g. Kataoka et al., 1999) and Mrk 421 (e.g. Albert et al., 2007c).

One finding of this study is the tendency of steeper electron spectra in case of increasing peak frequencies. As the observed variability is always stronger at X-rays than in the optical, a shift of the peak frequency without a significant increase of the total flux level, requires a steeper electron spectrum to fit the optical data. This problem could be easily solved with a two component model, where one electron population is responsible for the lower, more constant flux level at lower energies, while a second population of electrons with a much larger Lorentz factor at the break and the cut-off can produce the hard component of the synchrotron spectrum, which can dominate the total energy output in case of strong flares. Such a model was already proposed by Giommi et al. (2000) for 1ES 2344+514 and Massaro et al. (2004) for Mrk 501.

A problem raises from the fact, that in every case, the last VHE data points are underestimated by the model, even though they are still consistent within the large errors. As in a single zone SSC model the electron spectrum

is strongly constrained by the synchrotron spectrum, arbitrary high inverse Compton peak energies are not possible. Indeed, a significant part of the photons is scattered in the Klein-Nishina regime, which effectively limits the maximum energy reachable with inverse Compton scattering. One possibility for peaks at TeV energies would be a second component with higher Lorentz factors, which would result in further peaks in the MeV range. Another possibility would be an additional strong IR photon target field, which could produce TeV photons mainly by scattering in the Thomson regime. However such a photon field has to be less luminous in the observer's frame than the boosted synchrotron emission from the electrons. Hard VHE spectra are also observed for other TeV sources like 1ES 1101-232 (Aharonian et al., 2007c). Here the VHE spectrum is even harder and goes up to  $\sim 3\text{TeV}$ . Observations in the X-ray band from *Swift* in 2005 reveal a synchrotron peak slightly below 1 keV for this object (Tramacere et al., 2007). Observations by BeppoSAX in 1997 and 1998 showed also higher peak energies up to a few keV (Donato et al., 2005). Nevertheless these peak values are still too low for a single zone SSC model to produce an inverse Compton peak at several TeV. Multi-component models or a hadronic origin should be investigated for these sources.

As time variability is a defining property of BL Lacs further multiwavelength observation campaigns have to be performed to reveal the emission process of these source class. Beside the recommended simultaneous X-ray and VHE observations, measurements at intermediate energies, as expected to be soon available from the GLAST mission (20 MeV - 200 GeV), but also from future medium gamma-ray telescopes, covering the 100 keV-10 MeV-range, will be crucial for the understanding of the entire SED.

# Chapter 9

## Constraints on the luminosity function

The luminosity function at VHE gamma-rays of HBLs is still poorly known due to the small number of detected objects and the lack of a complete sample. Nevertheless the luminosity function can be constrained by the observations reported in this work.

In the following chapter the expected number of HBL objects at VHE gamma-rays are derived from a complete sample of X-ray BL Lacs making assumptions on the X-ray/gamma-ray flux correlation and on the completeness of the used compilation. An upper limit on the omnidirectional flux at 200 GeV is derived from the investigated sample and compared with model predictions, based on the X-ray luminosity function of BL Lac objects.

### 9.1 Complete BL Lac samples

The compilation of Donato et al. (2001) (in the following referred to as Donato-sample) is not a flux limited sample. The first complete X-ray survey of the entire sky with an imaging X-ray telescope was performed by the ROSAT X-ray satellite. The use of an imaging telescope led to a major increase in sensitivity and source location accuracy compared to former all-sky surveys based on collimated counters (e.g. HEAO-1, Wood et al., 1984). ROSAT was launched in June 1990. The all-sky survey was performed from the end of July 1990 to the end of January 1991. The satellite scanned the sky in great circles whose planes were oriented roughly perpendicular to the solar direction. This resulted in an exposure time varying between  $\sim 400$  s and 40,000 s at the ecliptic equator and the poles respectively. The focal plane of the telescope was hosted by the positional-sensitive propor-

tional counter (PSPC) which detects photons in the soft X-ray range from 0.1 keV to 2.4 keV. In total 145,060 sources have been detected of which the brightest 18,811 form the ROSAT All-Sky Survey Bright Source Catalogue (RASS-BSC, Voges et al., 1999).

A complete flux limited BL Lac sample comprises the Hamburg/ROSAT X-ray bright BL Lac sample (in the following referred to as HRX-sample), including 77 BL Lacs, 65 of them with known redshift (Beckmann et al., 2003). The sample is derived from the X-ray/radio correlation of objects of the Hamburg RASS Catalogue with the NRAO VLA Sky Survey (NVSS, Condon et al., 1998) radio catalogue. For a certain sky region of  $4770 \text{ deg}^2$  ( $= 1.45 \text{ sr}$ ), corresponding to 11.6 % of the sky, 235 objects with an X-ray/radio correlation have been found above the chosen limit on the PSPC count rate of  $0.09 \text{ sec}^{-1}$ . Of these 235 objects, 77 are identified as BL Lacs. The optical identification of the sample is 98 %.

As the sample considered in this work (in the following referred to as HBL-sample) is based on the Donato-sample, the completeness has to be estimated before the number of expected sources can be derived. Of the 77 objects of the HRX-sample, 53 are also included in the Donato-sample (corresponding to 68.8 %). The coverage increases to 85.2 % for objects with an X-ray flux of  $f(1 \text{ keV}) > 1 \mu\text{Jy}$  and to 100 % for objects with an X-ray flux of  $f(1 \text{ keV}) > 2 \mu\text{Jy}$ . Unfortunately the criteria on declination and right ascension of the HRX- and the HBL-sample are not the same. While the HRX-sample ranges mainly from  $20^\circ$  to  $85^\circ$  in declination and from  $7^h$  to  $16^h$  in right ascension, the HBL-sample covers the declination range from  $-1.2^\circ$  to  $58.8^\circ$  and the complete range in right ascension. The sky region of the HRX-sample that is also covered by the HBL-sample is  $1.17 \text{ sr}$  (or 9.3 % of the sky), which is by a factor 4.7 smaller than the complete sky region scanned by the HBL-sample ( $5.51 \text{ sr}$ ). In the HRX-sample seven sources fulfil the selection criteria as described in Section 6.1<sup>1</sup>. If the redshift criterion is rejected, three additional objects have to be added. For two of them, the flux limit would be violated if the absorption of gamma-rays is taken into account<sup>2</sup>.

An extrapolation of the eight candidate sources of the HRX-sample to the  $5.51 \text{ sr}$  patch leads to a total number of 38 objects. Compared to the 14 sources observed from the HBL-sample, a completeness of 37 % is estimated<sup>3</sup>.

<sup>1</sup>One additional object is classified as a LBL in Donato et al. (2001).

<sup>2</sup>Strictly, the flux limit was made on the X-ray flux without taking the absorption for gamma-rays into account. As the redshift was restricted to  $z < 0.3$ , the effect is small. For sources at high redshift an equal intrinsic flux at 1 keV and 200 GeV will result in a much lower observable gamma-ray flux.

<sup>3</sup>For the Donato-sample the completeness is slightly higher ( $\sim 45 \%$ ).

The large discrepancy between the 100% completeness with respect to the HRX-sample and the 37% for the complete set is mainly due to a lack of objects in the right ascension range from  $18^h$  to  $23^h$ .

## 9.2 Redshift distribution

In the following the redshift distribution of the HBL-sample is compared to (i) all HBLs from Donato et al. (2001) with  $f(1 \text{ keV}) > 2 \mu\text{Jy}$ , (ii) all HBLs from Donato et al. (2001) without any flux limitation, (iii) the complete HRX-BL Lac sample from Beckmann et al. (2003) and (iv) all HBLs detected at VHEs so far (Fig. 9.1).

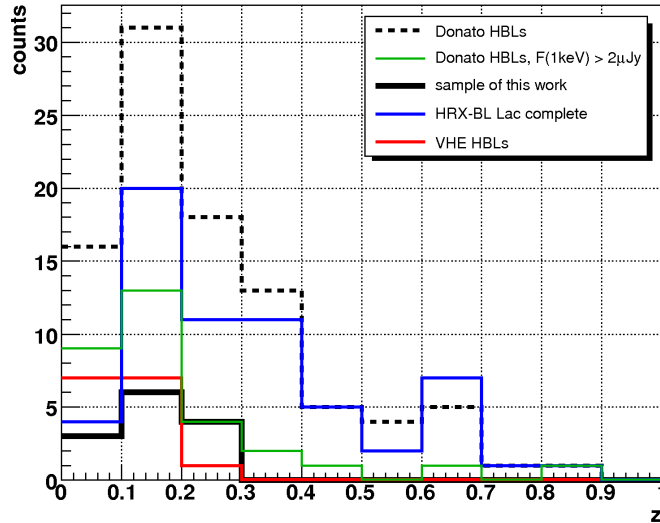


Figure 9.1: Redshift distribution of different BL Lac samples.

All redshift distributions show a maximum in the second bin from  $z = 0.1$  to  $z = 0.2$ . The distribution for the HRX-sample is slightly flatter than the one of the full Donato-sample. While the Donato-sample contains more sources in total, the number of objects in the highest redshift bins is the same or even less. A reason could be that the Donato-sample contains only objects with measured X-ray slope. As this usually requires a certain flux level, the HRX-sample will include also sources with lower fluxes, which are likely located at a higher redshift. This trend is also visible from the comparison between the full Donato-sample and the same sample after the cut in the X-ray flux. In the latter case the number of objects above  $z \approx 0.2$  decreases strongly.

All detected TeV HBLs are located at strikingly low redshift. This has several reasons. (i) The sensitivity in terms of the energy density of current ground based gamma-ray telescopes is much less than the sensitivity of X-ray telescopes. Therefore the VHE HBLs are among the brightest X-ray sources of their class. Since a larger distance requires a higher intrinsic luminosity, the number of sources at high redshifts with a detectable flux is low. This simple geometric effect goes along with (ii), the absorption of VHE gamma-rays in the MRF. (iii) HBLs show evidence for negative evolution on a  $2\sigma$ -level (Beckmann et al., 2003), i.e. HBLs are less numerous or less luminous in the past.

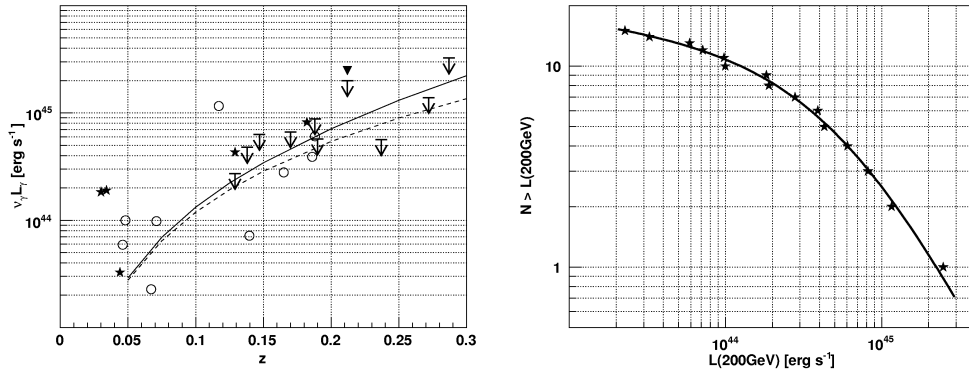


Figure 9.2: Left: The gamma-ray luminosity  $\nu_\gamma L_\gamma$  at 200 GeV vs. redshift. The arrows mark the upper limits calculated in this work, whereas the stars indicate the detected sources that belong to the sample described in Sect. 6.1. The triangle marks the detected flux of 1ES 1011+496 from another observation campaign. The open circles mark all other detected HBL objects with published fluxes. The dashed line indicates a flux of  $4.8 \times 10^{-12}$  erg cm<sup>-2</sup> s<sup>-1</sup> corresponding to  $2 \mu\text{Jy}$  at 1 keV. The solid line corresponds to the same flux taking into account gamma-ray attenuation at 200 GeV. Right: The absolute number of all detected HBLs with known redshift above a the given luminosity at 200 GeV.

Figure 9.2, left panel, shows the luminosity  $\nu_\gamma L_\gamma$  at 200 GeV vs. the redshift. All detected sources are above or within the line that marks the corresponding luminosity to a flux of  $2 \mu\text{Jy}$  at 1 keV. The absorption of gamma-rays by the MRF increases with redshift, so that at a redshift of  $z = 0.3$  the emitted luminosity becomes twice as large as the observable one. In addition, the cumulative number of all HBLs, detected at VHEs so far, above a certain gamma luminosity are shown in the right panel of Figure 9.2. The object PG 1553+113 is excluded from both plots because of its unknown redshift. The distribution is flattening towards lower luminosities. From the X-ray luminosity function as derived by Beckmann et al. (2003), a power-law behaviour with a slope of -0.9 is expected, assuming a comparable luminosity at gamma-rays. The flattening is caused by the limited sensitivity, which

requires low redshifts in case of low luminosity objects, while the accessible volume for high luminosity objects is larger. When calculating a luminosity function, the scaling of the space density by the accessible volume for each object corrects for this effect.

### 9.3 Number counts

Since the HBL-sample is not a complete flux limited sample, the luminosity function at VHEs can not be calculated. However, based on the assumption of a comparable luminosity at 1 keV and 200 GeV and the estimation of the completeness of the HBL-sample, the cumulative number above a certain flux level is compared between the HBL- and the HRX-sample. The HBL-sample includes six detected VHE sources: 1ES 1011+496, Mrk 421, 1ES 1218+304, 1ES 1426+428, Mrk 501 and 2344+514. From the HRX-sample only the 65 objects with known redshift are used. The number counts of the HRX-sample are scaled by multiplying with 4.5 to reach the 44 % patch of the sky spanned by the HBL-sample. To get the monochromatic flux at 1 keV from the HRX-sample, the 0.5 keV - 2 keV fluxes are divided by 1.5 assuming a differential energy spectrum with spectral index -2.0. For a reasonable range of spectral indices the uncertainty in the flux is  $\sim 10\%$ . Assuming the same intrinsic luminosity at 1 keV and 200 GeV, the observed fluxes of the HRX-sample have to be corrected for absorption of the gamma-rays in the MRF. The result is shown in Figure 9.3.

From the differences of the black and red distributions, the effect of absorption is clearly visible. Above the vertical line 37 sources are expected from the red distribution, which is by a factor of 6 more than the number of detected sources. A lack of candidate sources is expected from the incompleteness of the HBL-sample. When correcting for the incompleteness by scaling the number of detected HBLs by a factor of 2.7, the number of expected sources is still twice the one of anticipated detections. This discrepancy can be solved by a different ratio between X-ray and gamma luminosity. A fit to the scaled detections, assuming the shape of the distribution of the red points, results in a 1.4 times less luminosity at 200 GeV than at 1 keV. This value corresponds to a broad-band spectral index of  $\alpha_{X\gamma} = 1.02$ , which is in good agreement with the ones found in Section 7.3.2 (Figure 7.3).

The small number of bright source candidates compared to the expected number from the extrapolation of a complete sample clearly shows the limitations of pointed observations for a Cherenkov telescope. A complete flux limited BL Lac sample over the entire sky is still missing. The upcoming GLAST mission will provide an all sky survey at GeV-energies within the

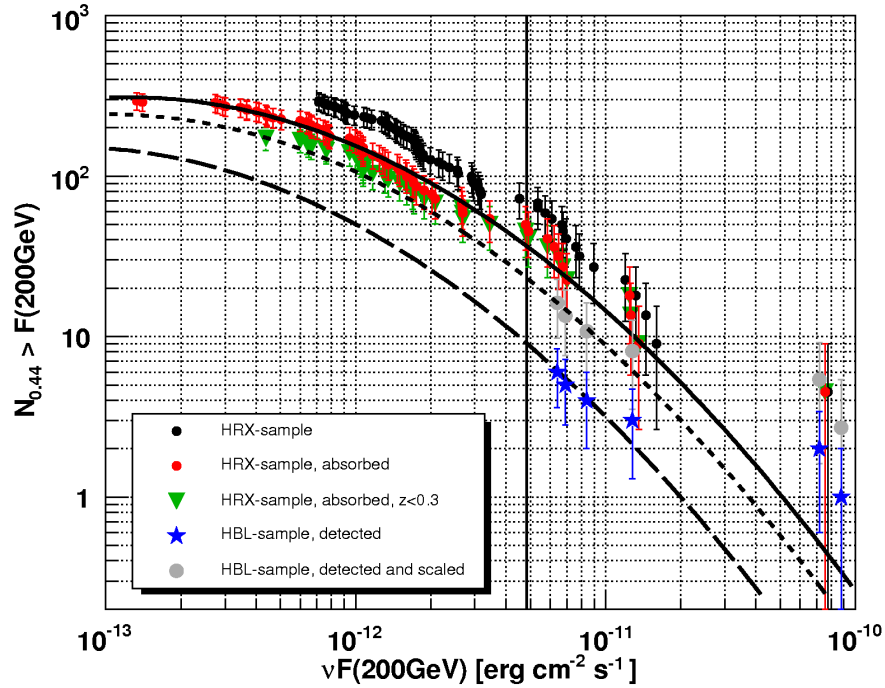


Figure 9.3: Cumulative number over the energy density at 200 GeV. The total number of objects refers to a patch of 44% of the entire sky. The black dots represent the distribution for all objects of the HRX-sample with known redshift (65 out of 77), assuming  $\nu F(1 \text{ keV}) = \nu F(200 \text{ GeV})$ . The red dots show the expected number of BL Lacs at 200 GeV, assuming again the same energy density as at 1 keV but taking the absorption in the MRF into account. The green triangles are a subsample of the red distribution and include only objects with  $z < 0.3$ . The blue stars mark the number counts for the detected objects of the HBL-sample. The grey dots represent the expected detections, based on the real detections, but scaled with 2.7 to account for the incompleteness of the HBL-sample. The vertical line indicates the intended flux limit of the search ( $4.8 \times 10^{-12} \text{ erg cm}^{-2} \text{ s}^{-1}$ , corresponding to  $2 \mu\text{Jy}$  at 1 keV). The solid line represents a fit to the red points. The dashed and dotted lines resemble the solid line, but for a three and 1.4 times lower flux, the latter one from a fit to the grey points.

next two years. This will not automatically lead to a complete sample of BL Lacs, as all the detections have to be identified. The anticipated large number of unidentified sources will ask for follow-up observations with radio, optical, X-ray and ground based gamma-ray telescopes. In addition, the most sensitive energy range of the LAT instrument will favor LBLs and quasars over HBLs. The identification is strongly hampered in the sky region that is covered by the galactic plane.

From the cumulative X-ray number counts, assuming a slightly modified correlation between the X-ray and gamma-ray luminosities, it can be seen

that the current sample of detected VHE BL Lacs is still the tip of the iceberg. Unfortunately the distribution of the expected number of VHE sources is flatter than the corresponding distribution at X-rays due to the absorption of gamma-rays in the MRF. Already with the current sensitivity of MAGIC and an incomplete sample based on compilations, a total number of 20 sources are expected, exploiting the full sensitivity of the instrument in 50 h pointings. With the beginning of regular observations with MAGIC II, scheduled for spring 2009, this goal could be achieved in much less observation time. Also the lower energy threshold will lead to more detections, in particular for high redshift sources. These considerations are based on population statistics. For a single object the X-ray/gamma-ray correlation may be different. Also the variability makes the estimation of a VHE flux, based on archival X-ray data difficult.

## 9.4 Contribution to the extragalactic background

In the following the upper limit on the cumulative omnidirectional flux at 200 GeV from X-ray bright HBLs is derived, noting that GLAST will measure the diffuse extragalactic background up to 200 GeV. The selection criterion for the declination of the sample corresponds to a patch of the sky with a size of 5.51 sr (or 44% of the sky). The sum over the fluxes as well as the upper limits of all 14 sources of the sample and PG 1553+113, which is within the declination range, amounts to  $2.48 \times 10^{-10} \text{ erg cm}^{-2} \text{ s}^{-1}$ . Divided by the 5.51 sr patch, this results in an upper limit on the total intensity at 200 GeV of  $I_{\text{VHE}}(200 \text{ GeV}) = \varepsilon \cdot 2.81 \times 10^{-8} \text{ GeV cm}^{-2} \text{ sr}^{-1} \text{ s}^{-1}$ , where  $\varepsilon$  accounts for the incompleteness of the sample. Assuming  $\varepsilon = 2.7$  as derived in Section 9.1, the upper limit for the total intensity at 200 GeV is calculated as  $I_{\text{VHE}}(200 \text{ GeV}) = 7.6 \times 10^{-8} \text{ GeV cm}^{-2} \text{ sr}^{-1} \text{ s}^{-1}$ . This upper limit is dominated by the two brightest sources, Mrk 501 and Mrk 421. Under the assumption that the HBL-sample is complete for the brightest X-ray sources ( $f(1 \text{ keV}) > 15 \mu\text{Jy}$ ) the factor  $\varepsilon$  counts only for the rest of the sample, resulting in an upper limit of  $I_{\text{VHE}}(200 \text{ GeV}) = 4.5 \times 10^{-8} \text{ GeV cm}^{-2} \text{ sr}^{-1} \text{ s}^{-1}$ .

In a second approach, the omnidirectional flux is calculated using the HRX-sample. Under the assumption of  $f(1 \text{ keV}) = 1.4 \cdot f(200 \text{ GeV})$ , as derived in the last section, and taking into account the pair production optical depth at 200 GeV, the total expected intensity at 200 GeV amounts to  $I_{\text{VHE}}(200 \text{ GeV}) = 7.8 \times 10^{-8} \text{ GeV cm}^{-2} \text{ sr}^{-1} \text{ s}^{-1}$ . Again, a dominant contribution comes from Mrk 421, the brightest source of the sample, which is also

scaled by the same factor than the other sources to cover a sky region of 44%. Assuming only 2 bright sources in this region (Mrk 421 and Mrk 501) results in a total intensity of  $I_{\text{VHE}}(200 \text{ GeV}) = 6.2 \times 10^{-8} \text{ GeV cm}^{-2} \text{ sr}^{-1} \text{ s}^{-1}$ . Note that these numbers decrease by about 40% if only the brightest sources, like in the HBL-sample, are taken into account. In this case, the expected flux is well within the upper limit derived from the HBL-sample. All quoted numbers are summarised in Table 9.1.

Recently Kneiske and Mannheim (2007) showed that HBLs could account for up to  $\sim 20\%$  of the extragalactic background radiation at GeV energies, when including cascade emission from sources at higher redshifts. The luminosity function used for their calculation was derived from the X-ray luminosity function (Beckmann et al., 2003) assuming the same luminosity above 300 GeV as from 0.5 keV to 2 keV. For the HBL contribution of faint point sources at 200 GeV, they obtain (somewhat model-dependent)  $I_{\text{KM}}^{(\text{point})}(200 \text{ GeV}) = (4 - 10) \times 10^{-8} \text{ GeV cm}^{-2} \text{ sr}^{-1} \text{ s}^{-1}$  which is barely within the upper limit obtained here. For the total intensity, including the diffuse component due to electromagnetic cascading, their result is  $I_{\text{KM}}^{(\text{diffuse})}(200 \text{ GeV}) = 1.0 \times 10^{-7} \text{ GeV cm}^{-2} \text{ sr}^{-1} \text{ s}^{-1}$ . This estimate is based on assuming that the emitted VHE spectra generally have peaks at energies well in excess of 200 GeV.

	HBL-sample		HRX-sample	
	(1)	(2)	(1)	(2)
$I_{\text{VHE}}(200 \text{ GeV})$	$< 7.6 \times 10^{-8}$	$< 4.5 \times 10^{-8}$	$7.8 \times 10^{-8}$	$6.2 \times 10^{-8}$

Table 9.1: Estimation of the omnidirectional flux at 200 GeV in units of  $\text{GeV cm}^{-2} \text{ sr}^{-1} \text{ s}^{-1}$ . Two different approaches are shown: one based on the HBL-sample, including the upper limits, and another one based on the X-ray luminosity function (HRX-sample). Note that the upper limits derived with the first approach are below the flux estimation of the second one because only the brightest objects are taken into account in the HBL-sample. For both approaches two numbers are calculated: the first one scales the total flux of all objects to the complete sky taking into account the incompleteness of the HBL-sample (1); for the second value (2) a completeness of 100% is assumed for the brightest objects (like Mrk 421 and Mrk 501).

# Chapter 10

## Conclusions

While the sensitivity of an imaging air Cherenkov telescope above TeV energies is mainly limited by the very low photon fluxes, the sensitivity at lower energies is limited by the large number of background events. It has been shown in this work that the images of single muons with large impact parameters look like showers initiated by gamma-rays with an energy below  $\sim 150$  GeV. The expected rate of muon events has been estimated for the MAGIC telescope in case of ideal observation conditions to lie in the range from 150 Hz to 170 Hz. Compared to an event rate of  $\sim 230$  Hz muons would account for 2/3 of the data taken. Stereo observations in coincidence mode reduce the number of recorded muon events, as these events usually trigger only one telescope. A clone of the MAGIC telescope is currently under construction at the same site. The commissioning phase is planned to start in autumn 2008. A strong improvement in sensitivity is expected from MAGIC-II in particular by reducing the analysis threshold from currently  $\sim 200$  GeV to below 100 GeV.

Beside their role as a strong source of background, the images of single muons with small impact parameters can be used to cross-calibrate different data sets as well as to monitor the point spread function of the optical system. This is achieved by an analysis of well defined ring images in the detector and the comparison of the light intensity of these rings as well as their width with simulated muon events. The method, originally developed by Vacanti et al. (1994) for the Cherenkov telescope of the Whipple observatory and later by Meyer (2004) for the MAGIC telescope, has been improved in this work and implemented in the automatic analysis. The automatised muon analysis revealed a continuous increase of the optical point spread function in 2005. This was explained by a tiny instability of the laser position of the reflector panels which are used by the active mirror control as reference positions. The cross-calibration, based on the muon ring analysis, of data

taken during 14 months yielded differences in the calibrated light intensity up to 20 %.

The search for VHE gamma-ray emission from a sample of twelve X-ray bright HBL objects resulted in the discovery of 1ES 1218+304 as a VHE emitter (Albert et al., 2006d) as well as in the detection of 1ES 2344+514 in a state of low activity with high significance (Albert et al., 2007b, and this work). For ten sources no significant signal has been found. The upper limits on their integral flux above  $\sim 200$  GeV have been calculated on a 99 % confidence level, yielding values between 2.3 % and 8.6 % of the Crab Nebula flux. A hint of a signal has been seen from the direction of 1ES 1011+496 on a  $\sim 3\sigma$  level. The object has been confirmed as a VHE emitter by a second observation in March 2007, triggered by an optical outburst, which led to a clear detection of the source (Albert et al., 2007e).

The broad-band spectral indices, based on the monochromatic radio (5 GHz), optical (640 nm), X-ray (1 keV) and gamma-ray (200 GeV) luminosities of the detected sources, do not deviate from the so far non-detected sources. The X-to-gamma-ray luminosity ratio ( $\alpha_{X\gamma}$ ) significantly exceeds unity for the majority of the objects (the lowest X-to-gamma-ray luminosity ratio of a detected HBL is 1/9) with an indication of an increasing  $\alpha_{X\gamma}$  with increasing X-ray luminosity. In the framework of a single zone SSC model, equal luminosities of the synchrotron emission (here X-rays) and the inverse Compton emission (gamma-rays) are expected for the case of equal energy densities of the synchrotron photons and the magnetic field. In this context, the deviation from unity in the distribution of  $\alpha_{X\gamma}$  could be interpreted as variations of the peak position with respect to the observed energy. As most of the data have not been taken simultaneously, flux variability (e.g. high state X-ray emission vs. quiescent VHE emission) can also account for some deviations from unity. Assuming a short duty cycle for flaring activity compared to the exposure time, fixed observations avoid a bias towards flaring emission states. The detection of 1ES 2344+514 showed that detailed spectral studies become now feasible also in a quiescent state. With the start of regular observations with MAGIC-II, scheduled for 2009, the detection of all known X-ray bright HBLs seems feasible. The lowered energy threshold of MAGIC-II will thereby increase the number of high-redshift sources as well as sources with lower VHE peak energies.

For 1ES 2344+514 and 1ES 1218+304, evidence for time variability on a time scale of 24 h and 17 days, respectively, has been observed, in the latter case for the first time at VHEs. Shorter time scales can not be excluded due to the low flux level and the limited sampling of the lightcurve. The SED of both objects has been successfully modelled for different flux levels with a single zone SSC model using archival X-ray data. The parameter values

are in good agreement with those derived for similar HBLs. In particular the spectral properties of 1ES 1218+304 are quite comparable to the one of Mrk 421 and the spectral properties of 1ES 2344+514 are comparable to the one of Mrk 501 which belongs together with 1ES 1426+428 to a small subclass of extreme BL Lac objects, revealing synchrotron peak energies above  $\sim 10$  keV.

From the comparison of the investigated sample with the complete X-ray BL Lac sample from Beckmann et al. (2003) the expected number of VHE BL Lacs above the sensitivity of the scan is six times higher than the observed one, assuming the same luminosity at 1 keV and at 200 GeV. The discrepancy can be explained taking into account the incompleteness of the investigated sample ( $\sim 37\%$  complete) and a slightly modified 1 keV/200 GeV correlation of 1.4 in average instead of unity. This is also consistent with the values and upper limits found for  $\alpha_{X\gamma}$ . A complete catalogue of HBLs over the entire sky would be important to study them on a much larger statistical basis. This could be provided in the near future by the planned all-sky surveys of the gamma-ray satellite GLAST (launch scheduled for May 2008) and the X-ray satellite eROSITA (launch scheduled for 2011).

# Appendix A

## Observation log: Crab Nebula

In the following tables all data used in this work for the analysis of the Crab Nebula are listed together with the most important parameters.

Abbreviations used in the table headings: seqn. = Sequenz number; start. time = starting time of the first data run; expos. = exposure time in min.; ZD = zenith distance range; BP = number of bad pixels; ped. = pedestal rms in photoelectrons; rate = data rate after image cleaning in Hz; inh. = inhomogeneity;  $\mu$ -rate = rate of muon ring images in Hz; ratio = ratio of light intensity of simulated and observed muon events; PSF = point spread function of the optical system (in mm) as derived from the analysis of muon ring images.

### A.1 Observations in on-off mode

Table A.1: Observations of the Crab Nebula in on mode.

seqn.	start. time	expos.	ZD	BP	ped.	rate	inh.	$\mu$ -rate	ratio	PSF
45636	2004-12-06	16.18	7-9	6	1.24	204	10.1	0.94	99.1	20.8
46068	2004-12-19	23.43	27-31	7	1.20	183	8.1	0.97	99.0	20.2
46533	2005-01-02	38.23	15-22	5	1.14	188	8.9	1.02	103.0	20.2
46575	2005-01-03	12.60	8-9	5	1.15	190	9.0	1.00	103.3	20.9
46581	2005-01-03	16.35	10-12	7	1.18	190	8.9	1.05	102.5	20.1
46693	2005-01-03	150.13	7-21	6	1.14	178	8.8	0.95	100.8	19.6
47585	2005-01-08	23.20	19-23	6	1.15	161	9.6	0.78	97.9	17.3
47621	2005-01-08	69.52	7-17	6	1.15	171	8.7	0.86	98.1	19.1
48471	2005-01-12	192.52	7-28	5	1.15	161	8.9	0.80	99.0	20.6
48786	2005-01-13	10.42	13-14	6	1.11	184	9.4	1.01	102.1	18.4
48791	2005-01-13	8.13	11-12	5	1.11	183	9.0	0.96	100.9	17.6
48796	2005-01-13	5.38	10-10	5	1.10	183	9.1	0.92	101.7	18.6
48800	2005-01-13	42.87	7-9	4	1.11	185	9.5	0.97	99.8	18.2

Table A.1: Observations of the Crab Nebula in on mode (continued).

seqn.	start. time	expos.	ZD	BP	ped.	rate	inh.	$\mu$ -rate	ratio	PSF
48817	2005-01-13	60.23	8-19	6	1.14	180	9.1	0.91	99.5	18.8
49098	2005-01-14	43.08	12-20	6	1.15	170	8.8	0.81	100.8	18.9
68514	2005-09-15	38.68	31-38	8	1.26	203	8.1	1.24	104.7	16.6
68528	2005-09-15	46.90	19-29	9	1.27	215	7.7	1.30	104.7	17.4
70181	2005-10-05	92.75	7-22	12	1.13	218	9.0	1.30	100.2	13.3
70350	2005-10-06	20.67	15-19	6	1.16	208	8.8	1.28	98.8	12.7
70629	2005-10-11	21.48	7-9	12	1.19	169	9.2	1.09	100.1	13.5
70695	2005-10-12	104.50	7-18	15	1.18	163	9.6	1.13	98.8	15.3
71208	2005-10-28	24.58	12-16	12	1.15	169	11.0	1.17	100.2	15.9
71219	2005-10-28	29.38	7-11	12	1.18	169	11.4	1.15	101.4	15.8
71230	2005-10-28	19.62	7-7	12	1.22	169	10.9	1.13	99.9	15.9
71238	2005-10-28	33.27	8-12	10	1.25	167	10.7	1.10	98.6	16.3
71250	2005-10-28	21.38	14-17	12	1.27	169	9.8	1.11	98.1	16.3
71259	2005-10-28	28.38	18-24	13	1.28	162	10.3	1.05	97.6	15.6
71389	2005-10-29	19.42	27-31	8	1.14	205	10.2	1.22	98.7	16.3
71398	2005-10-29	19.75	22-26	12	1.12	157	12.2	1.10	99.4	15.4
71406	2005-10-29	26.12	16-21	11	1.12	158	12.3	1.09	100.2	14.8
71416	2005-10-29	45.12	8-15	12	1.11	160	12.4	1.10	101.2	16.3
71716	2005-11-01	23.63	24-28	8	1.11	149	12.2	1.05	99.1	15.0
71726	2005-11-01	17.97	20-23	8	1.10	154	12.2	1.06	99.7	15.6
71733	2005-11-01	23.82	14-18	8	1.09	155	12.2	1.10	100.0	15.2
71742	2005-11-01	37.25	8-13	8	1.09	154	12.2	1.10	99.5	16.1
71754	2005-11-01	29.83	7-8	8	1.09	156	12.3	1.10	99.1	16.2
71764	2005-11-01	24.18	8-12	8	1.10	152	11.5	1.15	100.3	16.7
71773	2005-11-01	15.10	12-15	8	1.10	159	11.5	1.11	99.9	15.0
73105	2005-11-03	24.92	7-9	10	1.07	158	12.4	1.06	101.3	14.9
73230	2005-11-03	17.05	7-8	9	1.08	158	12.6	1.13	100.4	15.9
73422	2005-11-03	23.17	9-13	9	1.09	158	12.3	1.08	100.6	16.4
74345	2005-11-05	32.85	14-20	12	1.15	162	10.8	1.04	99.2	17.1
74356	2005-11-05	22.00	21-25	13	1.15	159	10.7	1.10	99.7	16.8
74364	2005-11-05	27.13	27-32	12	1.16	155	11.1	1.05	98.7	15.8
74700	2005-11-07	30.57	10-16	11	1.07	159	12.5	1.06	100.0	15.7
74711	2005-11-07	44.53	7-10	11	1.08	161	12.0	1.06	100.1	16.4
74727	2005-11-07	43.18	8-14	11	1.10	161	11.5	1.05	99.3	16.1
74742	2005-11-07	25.45	16-20	11	1.10	158	11.1	1.11	99.8	16.5
74752	2005-11-07	23.65	21-25	11	1.11	157	11.5	1.08	99.5	15.8
74761	2005-11-07	19.77	27-30	10	1.13	156	11.7	1.08	99.1	15.4
74769	2005-11-07	25.23	31-36	11	1.15	149	11.6	0.99	98.4	15.8
77618	2005-12-09	54.13	7-14	17	1.10	151	11.5	0.93	97.6	16.6
81669	2006-02-01	17.52	7-9	14	1.13	205	10.1	1.08	96.8	15.7
81889	2006-02-02	57.20	9-20	12	1.25	175	9.4	1.01	96.9	17.0
82894	2006-02-19	68.72	26-40	21	1.11	186	6.8	1.01	98.2	15.6
82957	2006-02-20	32.92	7-8	20	1.11	199	9.1	1.00	97.8	16.0
83129	2006-02-21	94.92	7-20	23	1.13	191	7.6	1.04	98.5	16.8
83578	2006-02-23	33.30	34-40	14	1.12	185	6.4	1.10	97.4	14.6

Table A.1: Observations of the Crab Nebula in on mode (continued).

seqn.	start. time	expos.	ZD	BP	ped.	rate	inh.	$\mu$ -rate	ratio	PSF
85805	2006-03-22	49.35	28-38	14	1.20	162	11.5	1.06	98.0	16.3
86290	2006-03-24	34.40	31-38	12	1.21	173	9.4	1.08	99.1	16.0
87153	2006-03-28	20.15	35-39	10	1.25	171	9.6	1.03	99.0	14.4

Table A.2: Used off observations for the analysis of the Crab Nebula.

seqn.	start. time	expos.	ZD	BP	ped.	rate	inh.	$\mu$ -rate	ratio	PSF
45604	2004-12-01	31.42	7-14	7	1.12	200	10.4	0.95	99.0	18.7
45729	2004-12-09	59.85	8-19	3	1.02	198	9.2	1.08	102.5	17.7
46078	2004-12-19	27.87	27-32	7	0.98	236	7.4	0.93	102.8	18.9
46638	2005-01-03	123.33	10-27	5	1.04	236	7.6	1.06	102.2	19.6
47403	2005-01-07	160.72	7-25	6	1.16	172	9.1	0.94	99.6	18.6
47988	2005-01-10	96.15	10-22	5	1.07	229	8.1	1.00	100.9	18.9
48663	2005-01-13	71.40	1-12	4	0.90	247	7.5	0.95	102.8	18.8
48694	2005-01-13	10.02	5-6	4	0.91	246	7.2	1.01	101.3	19.1
49329	2005-01-21	92.87	1-15	5	1.20	203	9.7	0.97	99.3	18.5
63403	2005-08-02	24.88	28-29	9	1.11	171	6.8	1.20	99.2	15.4
63911	2005-08-05	43.17	12-16	9	1.00	174	6.4	1.20	100.2	16.8
63936	2005-08-05	27.30	17-22	10	0.99	171	6.3	1.14	100.0	15.7
64789	2005-08-08	46.87	28-30	11	1.11	160	8.2	1.14	99.7	16.0
64817	2005-08-09	38.32	30-35	9	1.12	157	8.1	1.11	99.0	15.7
65234	2005-08-11	34.52	12-13	10	1.02	167	7.0	1.25	101.0	15.1
65252	2005-08-11	36.80	14-20	9	1.03	167	7.5	1.22	100.9	15.6
65434	2005-08-12	55.93	14-20	9	0.95	225	6.7	1.28	101.1	16.1
65471	2005-08-12	30.67	14-14	9	0.96	225	5.5	1.34	102.1	15.8
65607	2005-08-13	12.72	33-34	13	1.14	156	7.3	1.18	99.3	14.7
66784	2005-08-28	29.92	18-22	12	1.17	147	5.0	1.21	102.3	16.6
69689	2005-10-01	34.25	18-22	7	1.05	177	6.7	1.23	99.1	13.1
70600	2005-10-11	25.55	9-12	23	1.12	170	9.6	1.20	100.7	14.6
71431	2005-10-29	76.82	8-12	9	1.17	164	11.7	1.17	99.6	16.2
71455	2005-10-29	40.83	13-20	9	1.22	159	10.3	1.13	98.9	15.7
74116	2005-11-04	55.25	10-20	10	1.12	142	11.4	1.11	99.1	15.9
74134	2005-11-04	8.95	7-8	10	1.10	145	11.4	1.16	98.5	16.6
74374	2005-11-05	31.48	16-20	12	1.14	161	11.3	1.14	100.1	15.6
74386	2005-11-05	31.70	21-25	11	1.09	153	11.7	1.13	99.8	14.5
74397	2005-11-05	17.02	27-29	11	1.06	147	11.6	1.14	99.9	15.0
76312	2005-12-02	29.05	32-37	14	1.06	189	7.7	1.05	100.7	15.1
76606	2005-12-04	49.02	23-26	15	1.02	164	8.6	1.26	100.2	15.1
76787	2005-12-04	28.23	25-30	16	1.08	174	9.9	1.12	98.1	15.9
76804	2005-12-04	14.72	31-33	16	1.06	168	10.0	1.14	99.6	15.2
77523	2005-12-08	43.15	28-32	13	1.04	199	9.2	1.07	99.2	15.2
77542	2005-12-08	118.65	27-36	12	1.05	192	9.2	1.05	98.3	15.2

Table A.2: Used off observations for the analysis of the Crab Nebula (continued).

seqn.	start. time	expos.	ZD	BP	ped.	rate	inh.	$\mu$ -rate	ratio	PSF
79128	2005-12-31	56.55	27-30	13	1.15	175	9.5	1.02	98.4	16.0
79155	2005-12-31	22.22	27-28	13	1.17	172	9.1	1.02	98.2	16.3
79782	2006-01-02	34.55	23-24	13	1.00	179	10.0	1.13	99.5	16.1
79963	2006-01-03	95.58	7-13	17	1.12	144	11.3	1.00	99.8	16.7
82380	2006-02-05	119.85	24-47	16	0.98	200	9.3	1.06	99.0	16.0
83165	2006-02-21	80.58	7-19	21	1.02	215	5.7	1.12	98.6	16.3
84558	2006-03-04	17.93	23-27	20	0.92	228	8.3	0.97	98.1	15.3
84937	2006-03-07	108.25	18-28	20	0.96	214	10.1	1.09	100.5	16.7
85463	2006-03-20	54.93	24-35	17	1.20	161	9.6	1.07	98.0	17.1
86664	2006-03-26	58.98	36-41	18	1.08	178	10.0	1.15	99.4	15.7
86745	2006-03-26	32.18	28-35	11	1.20	163	10.8	1.08	98.0	14.9
87271	2006-03-29	56.20	36-41	13	0.98	192	9.4	1.03	100.0	15.2

## A.2 Observations in wobble mode

Table A.3: Observations of the Crab Nebula in wobble mode.

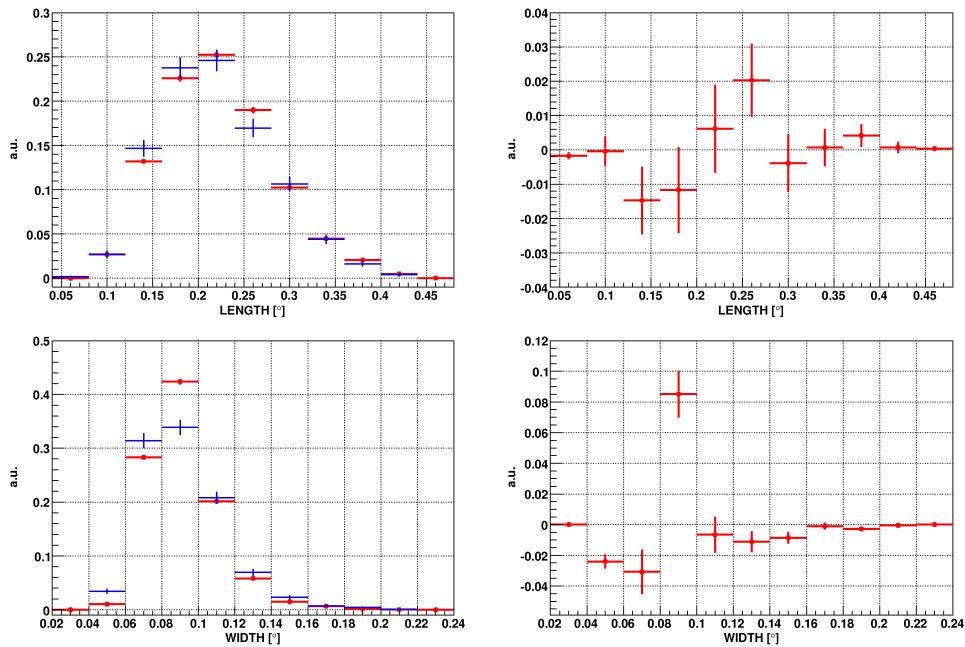
seqn.	start. time	expos.	ZD	BP	ped.	rate	inh.	$\mu$ -rate	ratio	PSF
70006	2005-10-04	16.72	20-23	7	1.11	218	8.0	1.35	101.4	13.5
70015	2005-10-04	23.08	15-19	7	1.11	224	8.1	1.32	101.1	13.8
70025	2005-10-04	24.40	10-14	7	1.11	224	8.0	1.33	101.4	14.4
70035	2005-10-04	18.70	7- 9	6	1.13	221	8.7	1.35	99.3	14.5
76265	2005-12-02	24.83	11-15	14	1.08	144	10.8	0.93	99.0	17.1
76273	2005-12-02	21.45	18-21	13	1.10	143	11.0	0.98	100.0	15.7
76280	2005-12-02	7.52	22-23	15	1.11	144	10.9	0.95	99.9	15.6
76911	2005-12-05	25.77	12-16	16	1.07	142	11.1	0.98	98.0	14.4
76922	2005-12-05	2.32	17-17	14	1.07	146	11.7	1.13	98.7	12.1
76925	2005-12-05	23.63	17-22	14	1.06	140	10.4	0.99	98.6	14.7
77319	2005-12-07	15.32	11-13	14	1.09	144	11.7	0.88	96.2	14.9
77327	2005-12-07	13.67	14-16	14	1.09	143	11.2	0.88	97.0	16.2
77334	2005-12-07	16.63	18-21	13	1.11	140	10.9	0.90	97.5	16.0
77342	2005-12-07	5.60	22-23	14	1.11	137	11.5	0.84	95.0	15.6
80433	2006-01-20	30.82	7-12	12	1.04	217	7.8	1.22	101.8	16.0
80447	2006-01-20	27.20	7- 8	14	1.06	201	8.3	1.30	101.0	16.6
83987	2006-02-26	19.95	25-28	16	1.12	198	7.9	1.14	100.0	16.8
83996	2006-02-26	19.95	30-34	16	1.13	181	8.0	1.07	98.2	15.1
84227	2006-03-02	14.95	34-37	17	1.16	196	7.7	1.06	97.3	16.8
85247	2006-03-19	18.65	36-40	36	1.10	142	13.5	0.68	89.0	15.1
85290	2006-03-19	10.57	42-45	33	1.11	128	16.5	0.68	90.6	15.7
85625	2006-03-21	18.10	29-32	17	1.20	179	9.8	1.09	97.5	16.7
85633	2006-03-21	14.93	34-36	17	1.19	163	9.5	1.00	97.2	16.0
85640	2006-03-21	14.93	37-40	17	1.19	161	10.4	0.97	98.9	14.7
86009	2006-03-23	9.20	29-33	12	1.25	151	9.4	1.15	99.7	16.9
86527	2006-03-25	19.92	32-36	10	1.24	175	11.1	1.01	99.0	15.4
86536	2006-03-25	19.93	36-40	11	1.22	160	10.6	1.00	99.3	14.9
86936	2006-03-27	19.90	35-38	11	1.24	190	9.1	1.06	97.4	16.2
87388	2006-03-29	19.92	37-41	9	1.22	168	10.2	1.03	96.3	15.6

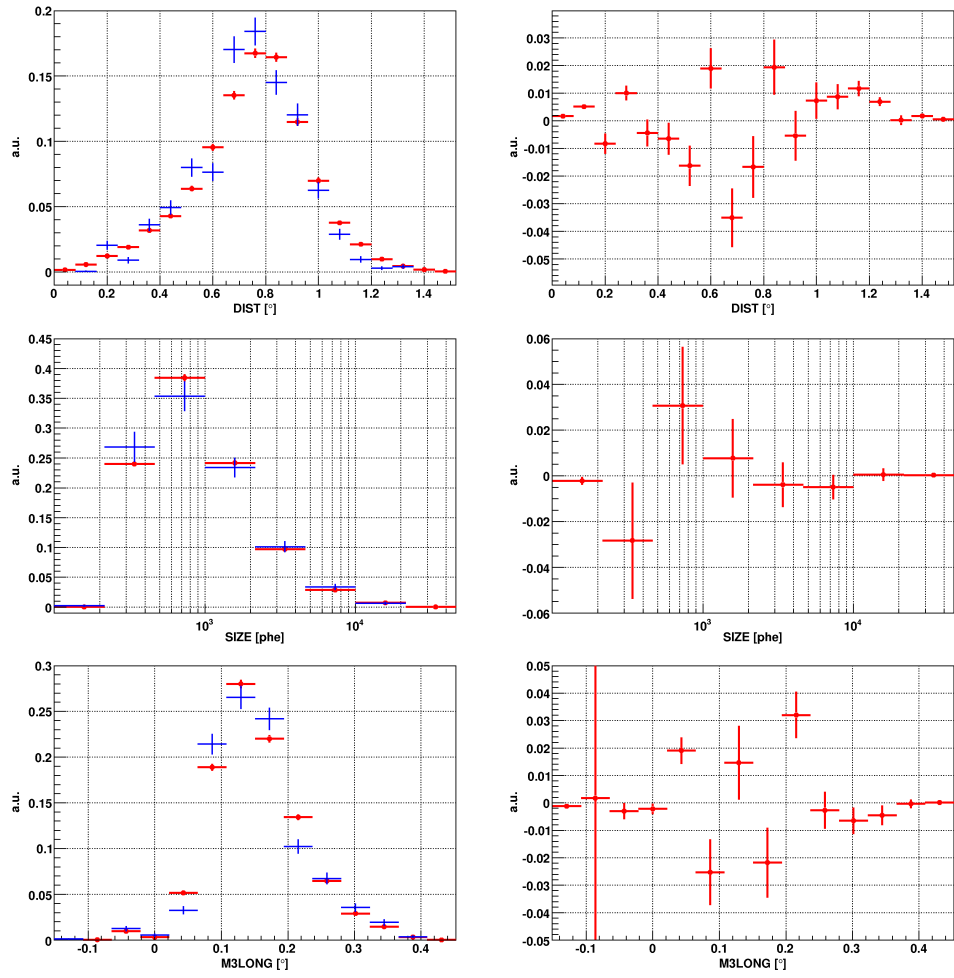
# Appendix B

## Monte Carlo comparison

### B.1 Gamma initiated air showers

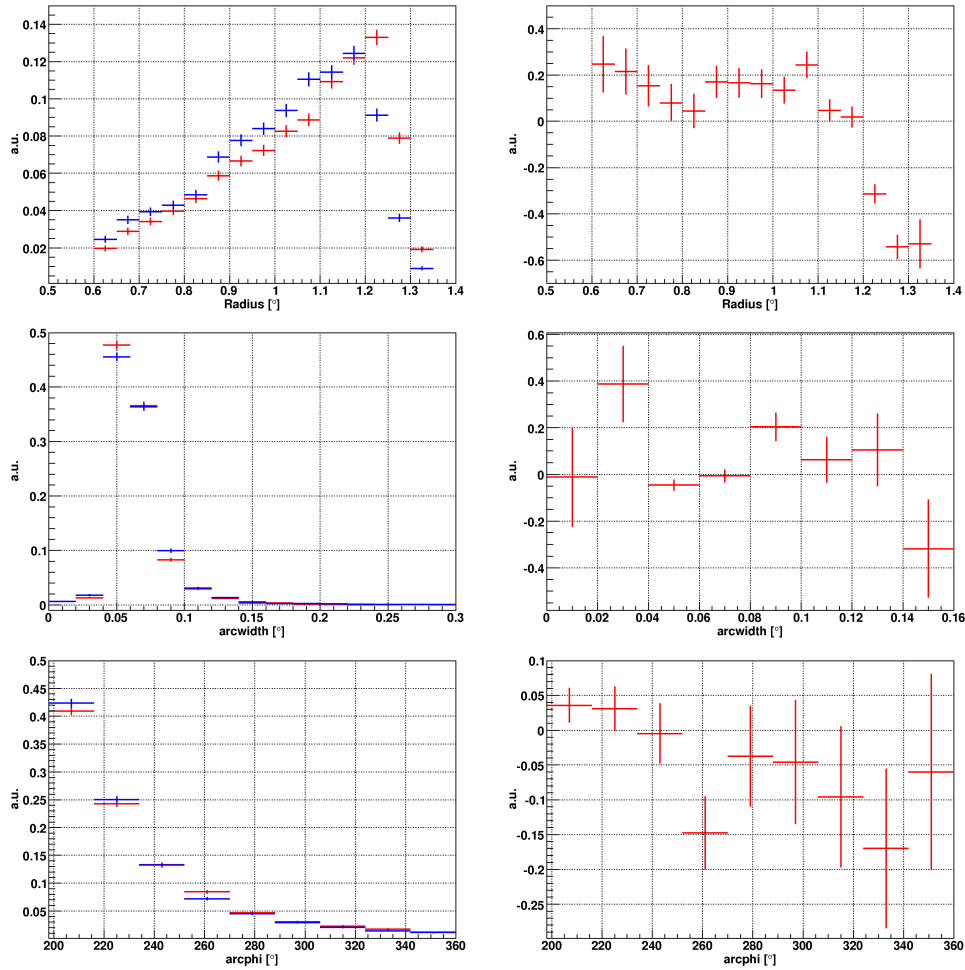
Figure B.1: Left panel: Distribution of the image parameters *length*, *width*, *dist*, *size* and *m3long* of simulated gamma showers (red) and gamma events from the Crab Nebula (blue). Right panel: Distributions of the differences in the same image parameters between simulated and observed gamma showers.





## B.2 Muons

Figure B.2: Left panels: Distribution of the main muon image parameters  $radius$ ,  $arcwidth$  and  $arcphi$  for simulated muon events (red) and muon events extracted from data of the Crab Nebula (sequence 70695, blue). The distributions are scaled by their integrals. Right panels: Differences of both distributions.



# Appendix C

## Observation log: HBL objects

In the following tables all data used in this work for the analysis of the sample of HBL objects as described in Section 6.1 are listed together with the most important parameters.

Abbreviations used in the table headings: seqn. = Sequenz number; start. time = starting time of the first data run; expos. = exposure time in min.; ZD = zenith distance range; BP = number of bad pixels; ped. = pedestal rms in photoelectrons; rate = data rate after image cleaning in Hz; inh. = inhomogeneity;  $\mu$ -rate = rate of muon ring images in Hz; ratio = ratio of light intensity of simulated and observed muon events; PSF = point spread function of the optical system (in mm) as derived from the analysis of muon ring images.

### C.1 1ES 0120+340

Table C.1: Observations of 1ES 0120+340 in wobble mode.

seqn.	start. time	expos.	ZD	BP	ped.	rate	inh.	$\mu$ -rate	ratio	PSF
63776	2005-08-04	10.25	9-12	9	0.92	230	5.4	1.24	100.3	17.4
64025	2005-08-05	24.20	9-12	10	0.92	226	5.6	1.23	101.7	16.9
64713	2005-08-08	30.98	6-13	9	0.91	217	6.9	1.30	101.5	16.1
64943	2005-08-09	45.13	6-13	10	0.93	224	6.0	1.29	101.0	16.3
65142	2005-08-10	46.45	6-13	10	0.90	227	6.0	1.26	102.0	16.5
65333	2005-08-11	38.45	9-15	10	0.90	226	6.3	1.25	101.2	16.4
65356	2005-08-11	12.00	6-7	10	0.89	228	6.3	1.34	103.5	17.8
65531	2005-08-12	51.15	6-16	8	0.89	230	6.4	1.30	101.7	16.5
65563	2005-08-12	9.43	6-6	9	0.89	231	5.2	1.34	102.3	17.0
65695	2005-08-13	44.83	8-16	9	0.93	216	7.1	1.29	101.7	16.4
65716	2005-08-13	30.12	6-8	11	0.92	211	6.6	1.28	101.0	16.2
65778	2005-08-14	44.70	6-10	9	0.91	224	5.8	1.30	101.2	16.8

Table C.1: Observations of 1ES 0120+340 in wobble mode (continued).

seqn.	start. time	expos.	ZD	BP	ped.	rate	inh.	$\mu$ -rate	ratio	PSF
65860	2005-08-15	59.23	7-18	9	0.92	224	6.3	1.28	101.4	16.8
65898	2005-08-15	29.90	6-7	12	0.93	225	5.9	1.26	101.4	16.7
65929	2005-08-16	59.88	6-17	11	0.94	224	6.3	1.29	100.8	16.5
65959	2005-08-16	26.43	6-7	12	0.96	226	4.7	1.29	100.0	15.8
65976	2005-08-17	81.75	6-13	11	0.92	222	6.4	1.26	101.0	16.7
67100	2005-08-30	39.78	16-24	7	0.98	161	7.2	1.45	102.6	15.6
67802	2005-09-04	19.25	23-26	9	1.01	153	11.8	1.20	99.6	14.9
67956	2005-09-05	38.27	8-14	7	0.97	155	13.1	1.22	98.8	15.4
68136	2005-09-10	16.53	27-29	7	1.09	147	11.5	1.11	94.2	15.4
68267	2005-09-11	59.73	19-31	8	1.07	145	8.2	1.12	96.7	15.3
68284	2005-09-11	63.62	6-17	8	1.04	158	8.9	1.16	98.0	15.9
68387	2005-09-12	20.17	20-24	8	1.11	176	9.5	1.19	100.1	17.4

## C.2 RX J0319.8+1845

Table C.2: Observations of RX J0319.8+1845 in wobble mode.

seqn.	start. time	expos.	ZD	BP	ped.	rate	inh.	$\mu$ -rate	ratio	PSF
69286	2005-09-29	20.40	18-21	5	1.04	212	9.2	1.38	99.1	14.4
69301	2005-09-29	6.52	14-14	5	1.06	213	9.6	1.46	98.8	16.7
69807	2005-10-03	22.07	17-21	6	1.00	161	10.7	1.05	100.9	13.8
69815	2005-10-03	25.97	13-17	7	1.00	160	11.0	1.10	100.3	13.8
69824	2005-10-03	19.50	10-12	6	1.00	169	8.9	1.13	100.5	14.2
69831	2005-10-03	18.30	10-10	7	0.99	171	9.0	1.12	101.1	14.4
69838	2005-10-03	17.63	11-12	6	0.99	169	8.8	1.14	100.5	13.3
70133	2005-10-05	20.77	18-22	6	1.05	218	8.3	1.30	100.0	12.2
70142	2005-10-05	23.85	13-17	6	1.06	220	7.9	1.31	100.2	13.3
70153	2005-10-05	20.17	11-13	6	1.04	218	8.9	1.30	99.7	12.5
70162	2005-10-05	18.58	10-10	6	1.02	221	9.8	1.31	101.0	13.9
70170	2005-10-05	22.75	10-12	6	1.02	218	9.0	1.38	100.7	12.9
80727	2006-01-23	20.20	11-13	11	0.99	242	6.4	1.32	101.2	18.1
80738	2006-01-23	28.02	14-19	12	1.03	225	6.2	1.25	101.0	17.6

Table C.3: Observations of RX J0319.8+1845 in on mode.

seqn.	start. time	expos.	ZD	BP	ped.	rate	inh.	$\mu$ -rate	ratio	PSF
45626	2004-12-06	19.32	28-31	5	1.04	189	8.5	1.03	101.8	19.8
45768	2004-12-09	41.37	12-19	6	1.07	257	7.7	1.26	101.9	19.0
47360	2005-01-07	99.73	10-20	4	1.06	228	8.2	1.04	100.5	18.3
47546	2005-01-08	92.68	10-19	7	1.03	227	8.8	0.99	99.6	18.3
47766	2005-01-09	103.93	10-19	6	1.02	168	9.7	0.83	100.1	18.5
48208	2005-01-11	35.02	12-17	7	1.05	235	8.6	0.97	101.2	18.7

Table C.4: Used off observations for the analysis of RX J0319.8+1845.

seqn.	start. time	expos.	ZD	BP	ped.	rate	inh.	$\mu$ -rate	ratio	PSF
45729	2004-12-09	59.85	8-19	3	1.02	198	9.2	1.08	102.5	17.7
46078	2004-12-19	27.87	27-32	7	0.98	236	7.4	0.93	102.8	18.9
46638	2005-01-03	123.33	10-27	5	1.04	236	7.6	1.06	102.2	19.6
47403	2005-01-07	160.72	7 -25	6	1.16	172	9.1	0.94	99.6	18.6
47988	2005-01-10	96.15	10-22	5	1.07	229	8.1	1.00	100.9	18.9

## C.3 1ES 0323+022

Table C.5: Observations of 1ES 0323+022 in wobble mode.

seqn.	start. time	expos.	ZD	BP	ped.	rate	inh.	$\mu$ -rate	ratio	PSF
69474	2005-09-30	19.23	31-33	6	1.10	181	8.9	1.18	97.8	13.1
69483	2005-09-30	19.55	29-31	6	1.11	185	8.5	1.17	98.2	13.3
69491	2005-09-30	23.45	27-28	6	1.10	190	9.0	1.20	98.6	13.4
69502	2005-09-30	16.02	26-27	6	1.09	190	9.7	1.15	97.5	12.1
69510	2005-09-30	18.03	26-27	6	1.10	191	9.1	1.21	97.5	12.8
69518	2005-09-30	2.67	27-27	6	1.10	188	9.2	1.25	98.0	11.3
69959	2005-10-04	15.93	32-34	7	1.00	215	7.8	1.19	101.6	14.1
69967	2005-10-04	22.23	29-31	7	0.98	221	7.8	1.20	100.5	13.7
69976	2005-10-04	24.57	27-29	6	0.98	224	7.4	1.20	100.5	13.6
69987	2005-10-04	21.12	26-27	7	0.97	223	7.6	1.21	100.5	14.7
69997	2005-10-04	20.83	26-27	6	0.97	221	8.0	1.18	102.4	13.2
70731	2005-10-13	18.12	26-27	6	1.01	213	8.5	1.16	100.0	12.6
70739	2005-10-13	22.63	26-27	9	0.99	208	7.8	1.20	99.8	14.2
71105	2005-10-26	14.25	34-36	9	0.99	200	9.9	1.11	101.4	14.4
71112	2005-10-26	17.80	32-34	9	1.00	200	9.3	1.19	101.7	14.6
71165	2005-10-28	16.65	27-28	11	0.98	230	9.1	1.25	100.3	16.1
71173	2005-10-28	21.13	26-27	9	0.99	227	9.2	1.26	102.5	16.4
71352	2005-10-29	31.65	30-34	9	0.98	209	10.6	1.19	99.9	16.0
71366	2005-10-29	24.07	28-30	9	0.99	215	10.7	1.17	100.7	15.4
71377	2005-10-29	22.83	26-28	9	1.00	215	10.0	1.22	100.8	16.4
71510	2005-10-31	28.35	26-28	8	1.07	190	9.4	1.23	100.0	15.7
71679	2005-11-01	21.08	32-34	8	0.94	204	10.4	1.09	99.0	15.7
71688	2005-11-01	20.70	29-32	8	0.96	209	10.2	1.24	100.4	15.4
71697	2005-11-01	19.63	27-29	8	0.97	214	10.5	1.20	100.2	16.1
71706	2005-11-01	14.08	27-27	8	0.98	211	10.0	1.20	100.4	16.0
71936	2005-11-02	22.55	32-36	9	0.93	203	10.1	1.11	100.2	15.1
71946	2005-11-02	22.65	29-31	9	0.92	207	10.0	1.14	101.6	16.0
71962	2005-11-02	20.37	28-29	9	0.93	208	11.0	1.22	105.2	15.5
71971	2005-11-02	15.92	26-27	9	0.93	208	10.6	1.15	99.7	15.6
75753	2005-11-24	26.62	29-32	16	1.05	180	9.8	1.14	101.6	15.6
75768	2005-11-24	36.50	26-29	15	1.04	187	10.0	1.17	101.6	15.4
76128	2005-11-30	25.77	27-29	14	0.96	200	8.8	1.06	102.6	16.2
76139	2005-11-30	19.95	26-27	14	0.96	199	9.2	1.11	101.5	17.0

## C.4 1ES 0414+009

Table C.6: Observations of 1ES 0414+009 in wobble mode

seqn.	start. time	expos.	ZD	BP	ped.	rate	inh.	$\mu$ -rate	ratio	PSF
72012	2005-11-02	19.57	29-31	10	0.94	207	10.1	1.14	101.0	15.3
72021	2005-11-02	22.13	28-29	9	0.94	207	10.2	1.15	101.2	15.3
72036	2005-11-02	22.25	28-28	10	1.01	206	9.6	1.15	99.9	15.8
72047	2005-11-02	20.17	28-29	9	0.94	204	10.0	1.14	100.5	15.9
72056	2005-11-02	23.25	29-31	9	0.96	202	10.8	1.16	100.3	14.7
72066	2005-11-02	23.18	31-34	9	0.98	199	10.7	1.16	100.4	16.0
74319	2005-11-05	23.93	29-30	8	1.03	210	10.2	1.24	100.5	16.3
74881	2005-11-08	23.15	28-29	10	0.94	188	11.0	1.12	99.7	15.3
74891	2005-11-08	23.02	30-32	10	0.95	186	10.7	1.09	96.5	15.6
74901	2005-11-08	15.17	32-34	10	0.94	182	10.5	1.10	98.0	15.7
75271	2005-11-11	20.50	30-32	10	1.00	213	10.1	1.20	100.5	16.4
75282	2005-11-11	16.53	32-34	9	0.99	208	9.9	1.15	99.8	15.8
75793	2005-11-25	25.57	29-31	17	1.01	183	9.6	1.26	103.0	17.0
75803	2005-11-25	23.73	28-29	15	1.04	183	9.1	1.22	101.9	15.8
75813	2005-11-25	20.50	28-28	15	1.05	184	9.4	1.18	101.5	15.4
75824	2005-11-25	19.47	28-29	16	1.07	181	8.5	1.17	102.2	16.2
76148	2005-11-30	22.48	29-30	14	0.98	188	9.5	1.05	102.0	16.5
76157	2005-12-01	20.05	28-28	14	0.97	189	9.2	1.03	102.2	15.2
76165	2005-12-01	27.40	28-28	14	0.97	193	9.7	1.08	102.9	15.6
76176	2005-12-01	17.33	28-29	14	0.96	183	9.8	1.07	100.4	15.8
76432	2005-12-03	21.58	28-28	16	1.02	181	8.8	1.09	99.5	16.5
76441	2005-12-03	26.95	28-30	16	1.04	180	8.6	1.10	99.5	15.7
76869	2005-12-05	23.35	28-28	17	0.93	193	9.6	1.08	99.9	14.9
76879	2005-12-05	22.92	29-30	16	0.93	189	9.5	1.13	100.0	15.3
77272	2005-12-07	18.42	28-29	14	0.96	192	10.1	1.00	98.7	16.5
77281	2005-12-07	20.82	29-30	13	0.96	192	9.8	1.00	98.6	15.8
78105	2005-12-22	21.48	33-36	11	1.03	173	9.6	1.00	99.8	16.2
78117	2005-12-22	22.00	30-33	12	1.02	175	9.8	1.01	99.9	16.5
78130	2005-12-22	22.38	28-30	13	1.04	179	9.3	1.01	101.4	16.8
78145	2005-12-22	21.07	28-28	13	1.03	182	9.5	1.05	100.2	16.7
78160	2005-12-22	18.10	28-28	13	1.02	181	8.8	1.05	100.0	16.1
78386	2005-12-24	20.22	34-36	12	1.02	179	9.5	1.06	102.4	15.1
78394	2005-12-24	20.47	31-34	13	1.01	182	9.2	1.01	102.2	15.3
78403	2005-12-24	17.90	29-30	13	1.03	182	9.1	1.11	100.7	16.1
78411	2005-12-24	18.03	28-29	12	1.03	180	9.7	1.02	101.8	14.9
78419	2005-12-24	17.52	28-28	13	1.02	184	9.3	1.05	101.8	17.0
78428	2005-12-24	14.10	28-28	12	1.03	183	9.4	1.10	101.0	15.8
78513	2005-12-26	18.92	31-32	14	1.02	187	9.1	1.08	100.5	16.5
78521	2005-12-26	25.10	31-31	13	1.03	182	9.1	1.05	102.0	17.4
78532	2005-12-26	23.78	28-28	12	1.01	183	9.5	1.07	101.7	17.2
78542	2005-12-26	18.98	28-28	13	1.00	184	9.7	1.04	100.5	16.4
79014	2005-12-30	20.57	32-35	13	1.04	162	10.3	1.01	99.5	15.0
79035	2005-12-30	16.47	29-31	14	1.06	166	9.7	1.01	100.1	15.2

Table C.6: Observations of 1ES 0414+009 in wobble mode (continued).

seqn.	start. time	expos.	ZD	BP	ped.	rate	inh.	$\mu$ -rate	ratio	PSF
79054	2005-12-30	15.35	28-29	13	1.01	165	9.9	1.03	102.0	16.2
79061	2005-12-30	25.93	28-28	14	0.99	169	10.3	1.01	101.3	15.5
79548	2006-01-01	19.18	33-35	12	0.95	169	11.1	1.00	100.3	17.3
79556	2006-01-01	19.50	31-33	13	0.95	173	11.2	1.07	99.8	15.5
79576	2006-01-01	17.32	28-28	13	0.93	177	10.9	0.98	99.8	16.0
80322	2006-01-19	18.65	31-33	12	1.00	178	10.1	1.13	101.4	17.5
80331	2006-01-19	19.23	30-31	12	0.99	181	10.0	1.15	102.0	16.8
80341	2006-01-19	21.92	28-29	12	1.00	183	9.8	1.17	102.4	17.0
80350	2006-01-19	19.15	28-28	11	1.00	172	10.3	1.08	102.3	16.2

## C.5 1ES 0806+524

Table C.7: Observations of 1ES 0806+524 in wobble mode.

seqn.	start. time	expos.	ZD	BP	ped.	rate	inh.	$\mu$ -rate	ratio	PSF
71567	2005-10-31	23.12	32-34	7	1.07	181	8.0	1.14	100.0	17.4
71576	2005-10-31	25.30	29-32	7	1.05	186	8.7	1.20	100.4	15.1
71586	2005-10-31	9.85	28-29	7	1.05	192	8.8	1.11	99.6	14.8
72079	2005-11-02	16.90	32-34	9	0.96	192	7.2	1.12	100.3	15.3
72087	2005-11-02	21.32	30-32	9	0.95	200	10.4	1.14	99.3	15.9
74524	2005-11-06	21.18	33-35	10	0.98	191	10.4	1.10	99.9	15.9
74533	2005-11-06	22.83	29-31	9	0.98	190	6.4	1.19	100.8	16.8
74543	2005-11-06	23.68	27-29	11	0.97	198	9.6	1.18	101.2	16.9
74553	2005-11-06	4.82	26-26	10	0.97	196	7.3	1.16	101.0	15.4
74557	2005-11-06	21.40	24-26	11	0.98	199	7.9	1.23	100.2	15.9
74567	2005-11-06	32.02	24-24	9	0.98	197	8.4	1.17	100.5	16.5
74911	2005-11-08	24.28	31-34	12	0.90	178	7.3	1.04	98.8	14.9
74921	2005-11-08	23.10	29-31	10	0.87	182	10.0	1.09	98.3	15.7
74930	2005-11-08	22.33	26-28	11	0.88	181	7.1	1.10	98.3	16.7
74939	2005-11-08	23.40	25-26	10	0.86	186	9.9	1.03	99.4	16.6
74949	2005-11-08	22.38	24-24	11	0.88	185	8.9	1.06	101.1	14.2
74958	2005-11-08	17.73	24-24	11	0.91	193	9.0	1.16	98.7	14.2
75290	2005-11-11	24.23	33-36	9	0.96	195	10.3	1.08	100.2	16.2
76188	2005-12-01	24.53	25-27	13	0.97	174	10.5	0.96	100.3	16.1
76197	2005-12-01	24.53	27-29	14	0.98	166	9.1	1.01	101.5	16.8
76474	2005-12-03	26.08	28-30	14	0.97	181	8.6	1.01	100.0	15.2
76484	2005-12-03	22.93	25-26	13	0.99	179	7.5	1.04	99.8	15.1
76494	2005-12-03	25.27	24-24	14	1.00	167	8.6	1.08	99.8	14.5
76505	2005-12-03	24.23	24-24	13	0.98	176	9.0	1.05	100.2	15.2
76523	2005-12-03	22.65	26-28	14	0.97	165	8.9	1.00	100.0	14.4
76943	2005-12-05	21.93	24-25	15	0.96	183	8.5	1.01	99.8	16.4
76959	2005-12-05	22.90	24-24	16	0.95	187	9.8	1.04	99.4	16.7

Table C.7: Observations of 1ES 0806+524 in wobble mode (continued).

seqn.	start. time	expos.	ZD	BP	ped.	rate	inh.	$\mu$ -rate	ratio	PSF
76969	2005-12-05	22.97	24-24	16	0.97	179	10.7	0.98	98.8	15.7
76979	2005-12-05	19.83	24-25	15	0.95	187	9.8	1.04	99.8	15.1
76991	2005-12-05	22.48	26-27	14	0.96	182	10.2	1.05	98.7	15.9
77001	2005-12-05	23.08	27-29	15	0.97	177	8.5	1.01	100.2	15.5
77010	2005-12-05	8.88	30-31	14	0.99	173	9.3	1.01	100.6	14.4
77015	2005-12-05	6.88	32-32	14	1.00	159	8.5	0.93	97.8	14.9
77346	2005-12-07	23.32	24-26	14	0.93	188	9.7	0.92	99.3	15.2
77356	2005-12-07	22.87	24-24	13	0.94	191	10.6	1.00	98.4	16.3
77367	2005-12-07	12.37	24-24	13	0.94	192	8.9	1.01	99.9	15.7
77394	2005-12-07	4.72	24-24	13	0.94	195	9.4	0.94	98.8	15.9
77443	2005-12-07	4.28	24-24	12	0.94	198	9.6	0.93	100.5	18.9
77447	2005-12-07	22.85	24-26	13	0.96	190	10.5	0.96	99.6	15.2
77457	2005-12-07	7.93	26-26	14	0.94	193	10.2	0.92	99.3	15.4
77634	2005-12-09	16.63	27-28	15	0.93	190	7.6	1.00	99.8	15.3
77642	2005-12-09	17.75	26-27	14	0.93	191	9.4	1.03	99.4	16.8
77651	2005-12-09	18.12	24-25	14	0.95	190	7.9	0.95	101.1	15.6
77660	2005-12-09	17.93	24-24	15	0.93	196	9.6	1.04	100.0	15.4
77670	2005-12-09	18.00	24-24	15	0.95	191	10.0	1.07	98.9	15.9
77678	2005-12-09	18.03	24-24	15	0.94	194	9.6	1.07	100.0	16.3
77686	2005-12-09	17.97	24-25	14	0.95	191	10.2	1.01	100.9	15.1
77694	2005-12-09	18.07	25-26	14	0.94	191	9.8	1.05	101.2	16.5
77702	2005-12-09	17.88	27-29	14	0.97	190	9.7	1.09	100.9	15.7
77710	2005-12-09	18.17	29-30	14	0.97	184	9.3	1.02	100.0	15.3
78583	2005-12-27	18.95	27-28	12	1.02	181	6.6	0.96	101.6	17.7
78591	2005-12-27	19.33	25-27	13	1.02	187	8.8	1.00	101.2	17.3
78599	2005-12-27	16.72	24-25	12	1.03	188	8.0	1.06	98.6	15.7
78606	2005-12-27	20.13	24-24	12	1.03	185	8.4	0.98	99.2	15.8

## C.6 1ES 0927+500

Table C.8: Observations of 1ES 0927+500 in wobble mode.

seqn.	start. time	expos.	ZD	BP	ped.	rate	inh.	$\mu$ -rate	ratio	PSF
78615	2005-12-27	19.02	24-26	11	1.02	187	9.0	1.01	100.5	16.5
78623	2005-12-27	15.10	23-24	11	1.02	185	8.8	1.04	100.5	16.2
78872	2005-12-30	21.42	24-26	12	1.02	182	9.8	1.14	102.8	16.2
78881	2005-12-30	19.25	22-24	11	1.02	180	10.3	1.13	103.0	16.1
78889	2005-12-30	18.95	21-22	12	1.02	180	10.0	1.15	101.8	16.4
78897	2005-12-30	21.10	21-21	12	1.01	180	9.4	1.10	101.4	15.5
78905	2005-12-30	18.73	21-22	11	1.01	179	9.2	1.11	100.4	15.9
79168	2005-12-31	12.60	25-26	13	1.02	164	9.7	0.99	97.6	16.0
79175	2005-12-31	19.80	23-24	13	1.03	168	9.9	0.98	99.1	15.7

Table C.8: Observations of 1ES 0927+500 in wobble mode (continued).

seqn.	start. time	expos.	ZD	BP	ped.	rate	inh.	$\mu$ -rate	ratio	PSF
79185	2005-12-31	20.62	22-23	13	1.03	171	9.3	0.95	98.4	15.6
79196	2005-12-31	22.47	21-21	13	1.04	172	9.3	1.00	100.0	16.2
79206	2005-12-31	20.02	21-21	13	1.04	173	9.3	1.02	99.8	16.5
79466	2006-01-01	18.22	21-21	12	0.96	169	9.1	1.09	100.3	16.0
80075	2006-01-06	19.98	24-26	10	0.91	188	9.1	1.11	101.4	16.0
80083	2006-01-06	18.72	22-23	10	0.92	190	9.0	1.14	102.1	16.5
80091	2006-01-06	21.50	21-22	11	0.92	188	8.1	1.08	100.9	17.2
80100	2006-01-06	18.27	21-21	12	0.93	191	8.4	1.15	101.7	16.4
80110	2006-01-06	21.68	21-22	10	0.92	182	8.8	1.07	101.6	17.2
80652	2006-01-23	9.02	23-23	9	0.98	171	6.7	1.18	102.9	18.1
80657	2006-01-23	10.58	22-23	11	0.97	171	7.0	1.18	101.2	17.4
80899	2006-01-29	19.02	23-24	10	0.90	226	7.6	1.11	99.7	16.3
80910	2006-01-29	34.90	21-23	12	0.88	222	7.4	1.14	101.0	17.1
81358	2006-01-31	20.40	21-22	10	0.90	220	7.4	1.13	100.0	16.6
81368	2006-01-31	20.37	21-21	10	0.89	216	7.1	1.05	99.8	16.0
81726	2006-02-02	13.82	22-23	9	0.95	218	7.4	1.12	98.3	16.5
81733	2006-02-02	13.72	21-22	10	0.94	216	7.8	1.10	99.8	15.9
81740	2006-02-02	28.45	21-21	11	0.95	214	8.5	1.14	98.5	15.3
81948	2006-02-03	20.57	22-23	9	0.96	225	8.1	1.14	100.0	16.5
81958	2006-02-03	24.93	21-21	11	0.97	219	8.1	1.13	99.0	16.3
82133	2006-02-04	27.85	22-23	8	0.94	224	8.5	1.20	101.1	16.2
82146	2006-02-04	27.92	21-22	9	0.93	220	8.4	1.17	100.3	15.8
82918	2006-02-19	19.92	22-23	12	0.91	222	5.4	1.07	99.4	17.3
82928	2006-02-20	39.80	21-22	12	0.94	215	7.0	1.10	100.1	16.2
83195	2006-02-21	19.93	22-23	12	0.90	231	5.5	1.08	100.0	15.8
83205	2006-02-22	26.83	21-22	11	0.90	230	6.5	1.10	100.2	16.5
83387	2006-02-22	14.93	22-23	9	0.93	224	6.8	1.13	99.3	16.5
83395	2006-02-22	29.87	21-22	10	0.93	220	6.4	1.17	100.0	15.7
83591	2006-02-23	14.95	22-23	12	0.91	215	5.7	1.13	100.5	17.5
83599	2006-02-23	44.80	21-22	11	0.90	209	5.5	1.11	100.1	16.1
83771	2006-02-24	24.90	22-23	11	0.92	221	6.8	1.18	101.4	16.0
83783	2006-02-25	24.92	21-22	13	0.92	217	7.4	1.20	101.4	17.0
84015	2006-02-26	19.92	22-23	12	0.92	221	7.3	1.10	101.2	15.3
84026	2006-02-26	19.92	21-21	12	0.92	214	7.7	1.11	100.0	16.8
84241	2006-03-02	24.93	22-23	14	0.98	227	7.0	1.13	100.2	16.2
84253	2006-03-02	24.93	21-22	14	0.99	218	7.3	1.19	100.5	16.7

## C.7 1ES 1011+496

Table C.9: Observations of 1ES 1011+496 in wobble mode.

seqn.	start. time	expos.	ZD	BP	ped.	rate	inh.	$\mu$ -rate	ratio	PSF
85481	2006-03-20	19.92	26-28	12	0.92	218	8.6	1.11	100.7	18.7
85491	2006-03-20	19.92	23-25	12	0.93	221	8.8	1.13	100.5	16.4
85501	2006-03-20	19.90	22-23	11	0.90	218	8.6	1.18	101.2	16.5
85512	2006-03-20	19.92	21-21	11	0.91	217	8.7	1.19	101.4	17.4
85522	2006-03-20	19.83	21-21	10	0.90	218	9.0	1.16	100.8	17.5
85534	2006-03-20	19.90	21-22	10	0.92	213	9.1	1.19	101.7	16.6
85647	2006-03-21	19.92	26-28	14	0.91	210	9.0	1.14	100.5	16.5
85658	2006-03-21	19.90	23-25	13	0.91	210	10.0	1.19	100.8	16.9
85670	2006-03-21	19.90	22-23	12	0.89	209	9.8	1.14	99.9	18.2
85682	2006-03-21	19.85	21-21	13	0.92	206	9.5	1.16	100.9	16.8
85695	2006-03-21	19.88	21-21	12	0.91	206	8.3	1.10	101.0	18.1
85705	2006-03-21	19.85	21-22	12	0.96	190	8.9	1.21	99.2	17.3
85822	2006-03-22	19.92	27-29	13	0.90	190	11.8	1.06	101.2	17.3
85831	2006-03-22	19.92	24-26	12	0.91	193	11.6	1.10	101.9	15.9
85840	2006-03-22	19.93	22-24	14	0.88	193	12.0	1.12	102.0	16.9
85849	2006-03-22	19.90	21-22	13	0.89	201	10.6	1.06	100.6	15.4
85862	2006-03-22	33.78	21-21	13	0.89	201	10.9	1.13	101.8	16.7
86088	2006-03-23	19.85	26-28	16	0.94	197	11.0	1.11	103.0	16.3
86106	2006-03-23	19.83	24-26	11	0.91	201	10.8	1.12	102.8	15.8
86118	2006-03-23	24.87	21-23	11	0.91	205	11.3	1.15	103.8	15.2
86304	2006-03-24	19.90	27-29	10	0.92	207	9.9	1.13	101.8	16.9
86313	2006-03-24	19.88	24-25	10	0.92	209	10.2	1.18	102.5	16.9
86325	2006-03-24	19.87	22-24	10	0.89	211	9.9	1.13	101.7	17.4
86338	2006-03-24	9.88	21-22	10	0.89	216	9.9	1.19	100.7	16.1
86545	2006-03-25	19.93	25-27	10	0.92	210	11.1	1.07	101.9	16.9
86554	2006-03-25	19.92	23-24	10	0.92	213	11.2	1.15	100.8	15.9
86563	2006-03-25	19.92	22-23	10	0.90	213	10.5	1.12	101.0	15.6
86757	2006-03-26	20.40	26-28	10	0.97	190	11.3	1.09	100.4	16.8
86776	2006-03-26	15.78	22-24	10	0.95	171	11.4	1.21	101.0	16.3
86784	2006-03-26	9.42	21-22	10	0.93	179	10.4	1.13	99.0	16.7
86946	2006-03-27	19.92	27-29	10	0.94	212	9.3	1.13	101.6	16.2
86956	2006-03-27	19.93	24-26	10	0.95	215	9.2	1.11	100.9	16.7
86965	2006-03-27	14.72	23-24	9	0.92	219	9.6	1.17	103.6	16.8
86973	2006-03-27	13.65	21-22	9	0.94	218	9.6	1.17	101.2	16.6
87162	2006-03-28	19.92	24-26	9	0.96	216	9.4	1.23	100.5	16.1
87172	2006-03-28	15.47	23-24	9	0.94	213	9.8	1.17	101.1	16.6
87180	2006-03-28	11.45	22-22	10	0.95	214	10.0	1.25	100.2	16.3
87397	2006-03-29	18.67	25-27	8	0.91	210	9.1	1.08	100.1	16.7
87407	2006-03-29	10.93	24-24	8	0.92	211	9.7	1.08	98.8	16.6
87413	2006-03-29	24.27	22-23	7	0.91	204	9.4	1.11	100.4	16.9
87608	2006-03-30	18.70	25-27	6	0.92	154	10.3	1.13	99.6	14.8
87616	2006-03-30	18.73	24-25	7	0.91	151	10.4	1.05	100.7	14.8
87624	2006-03-30	18.68	22-23	6	0.94	147	9.9	1.11	100.4	15.1

Table C.9: Observations of 1ES 1011+496 in wobble mode (continued).

seqn.	start. time	expos.	ZD	BP	ped.	rate	inh.	$\mu$ -rate	ratio	PSF
87774	2006-03-31	18.73	21-21	9	0.91	141	9.0	1.04	98.8	16.3
87782	2006-03-31	18.68	21-21	7	0.91	141	10.1	1.10	98.0	16.5
87790	2006-03-31	15.13	21-21	9	0.89	136	11.0	1.09	97.1	15.3
87948	2006-04-01	5.37	21-21	7	0.89	172	10.6	1.11	98.7	15.2

**C.8 1ES 1218+304**

Table C.10: Observations of 1ES 1218+304 in wobble mode.

seqn.	start. time	expos.	ZD	BP	ped.	rate	inh.	$\mu$ -rate	ratio	PSF
80927	2006-01-29	18.37	29-33	19	0.86	210	9.1	0.97	100.5	15.4
80936	2006-01-29	21.72	25-29	21	0.86	219	8.5	1.05	98.8	16.1
81178	2006-01-30	19.60	31-35	19	0.85	184	7.1	0.98	100.1	15.3
81186	2006-01-30	28.97	23-29	21	0.85	194	7.6	0.98	99.1	16.1
81377	2006-01-31	18.88	31-34	16	0.87	207	7.0	1.01	98.2	15.5
81386	2006-01-31	41.80	21-30	16	0.85	214	6.8	0.99	99.1	16.1
81754	2006-02-02	19.17	28-31	18	0.93	214	8.2	0.97	97.7	15.5
81763	2006-02-02	20.23	24-27	17	0.90	215	8.5	1.01	98.9	16.7
81969	2006-02-03	24.93	30-35	17	0.95	203	9.2	1.07	99.1	16.0
81981	2006-02-03	24.93	23-28	20	0.94	210	9.6	1.07	98.7	16.7
82158	2006-02-04	27.93	29-34	20	0.92	216	8.4	1.04	99.4	15.3
82170	2006-02-04	27.88	23-29	21	0.90	218	8.3	1.05	99.4	15.7
82328	2006-02-05	19.93	27-31	21	0.91	211	8.1	1.05	98.8	15.5
82337	2006-02-05	19.93	22-26	16	0.90	214	8.0	1.10	100.1	16.3
83218	2006-02-22	14.92	31-34	20	0.89	222	6.0	1.00	98.9	15.9
83227	2006-02-22	1.73	30-30	21	0.89	213	5.0	0.93	103.3	13.5
83251	2006-02-22	14.88	18-21	21	0.87	226	7.6	1.05	99.9	16.8
83417	2006-02-23	13.57	30-32	21	0.92	214	7.4	1.03	98.4	15.2
83424	2006-02-23	44.77	19-28	21	0.90	221	7.0	1.04	99.6	16.3
83617	2006-02-24	19.90	29-32	20	0.93	193	6.2	1.09	100.5	16.3
83626	2006-02-24	49.78	18-28	22	0.89	216	6.0	1.07	100.4	16.0
83794	2006-02-25	19.93	32-35	30	0.92	210	7.1	1.00	100.4	16.9
83804	2006-02-25	59.98	16-30	21	0.92	220	7.4	1.10	101.1	16.7
84035	2006-02-27	19.93	32-36	22	0.91	212	8.5	0.97	100.9	17.0
84044	2006-02-27	59.77	19-32	21	0.92	203	7.8	1.04	99.4	15.8
84265	2006-03-03	19.95	32-36	28	0.99	218	7.0	1.02	99.3	16.2
84275	2006-03-03	59.77	17-30	27	0.98	223	7.5	1.09	99.0	17.2
84460	2006-03-04	19.92	30-34	20	0.88	221	8.0	0.95	98.5	16.9
84470	2006-03-04	59.70	17-30	19	0.87	232	7.7	0.98	99.3	17.0
84637	2006-03-05	19.87	24-28	21	0.94	229	7.4	1.03	99.7	15.2
84647	2006-03-05	49.78	12-22	21	0.93	229	7.8	1.10	100.7	17.1

## C.9 1ES 1426+428

Table C.11: Observations of 1ES 1426+428 in on mode.

seqn.	start. time	expos.	ZD	BP	ped.	rate	inh.	$\mu$ -rate	ratio	PSF
50126	2005-03-15	19.92	14-15	8	0.99	201	8.3	1.03	102.6	23.1
50424	2005-03-18	45.40	14-17	10	1.02	186	7.8	1.04	100.0	22.0
51322	2005-04-04	88.42	14-17	5	0.87	186	8.8	0.93	99.2	20.1
54181	2005-04-29	19.07	23-25	6	0.94	201	8.9	1.04	103.0	22.7
55221	2005-05-09	96.50	14-24	12	0.94	207	11.7	1.16	99.0	14.1
55472	2005-05-11	44.25	14-17	11	0.84	245	8.5	1.21	100.1	14.5
55572	2005-05-12	56.95	14-20	11	0.95	206	8.4	1.26	100.6	15.2

Table C.12: Used off observations for the analysis of 1ES 1426+428.

seqn.	start. time	expos.	ZD	BP	ped.	rate	inh.	$\mu$ -rate	ratio	PSF
50111	2005-03-15	19.95	17-19	10	1.03	202	8.9	1.05	101.4	22.8
50137	2005-03-15	19.93	15-16	7	0.98	200	8.4	1.04	101.5	23.0
50456	2005-03-18	13.38	20-21	11	1.02	181	8.4	0.98	98.2	21.3
51448	2005-04-05	84.95	14-20	13	0.89	192	9.0	0.98	100.0	20.2
51803	2005-04-07	19.85	14-16	11	0.94	209	8.1	0.98	100.5	21.0
52016	2005-04-08	79.48	13-18	10	0.97	194	9.5	0.95	99.3	19.9
53241	2005-04-18	36.57	17-19	12	1.03	187	7.0	1.03	98.7	19.2
54263	2005-05-01	110.60	1-17	12	0.90	253	9.4	1.25	101.5	14.1
54468	2005-05-03	51.93	3-12	18	0.83	249	11.7	1.18	100.2	13.6
54491	2005-05-03	14.42	4-6	16	0.82	248	11.5	1.18	101.3	12.5
54564	2005-05-03	29.52	17-21	15	0.89	174	11.8	1.22	97.7	12.0
54579	2005-05-04	50.05	14-16	13	0.89	170	8.8	1.23	99.0	12.9
55333	2005-05-10	112.93	14-25	17	0.83	236	12.2	1.14	101.5	14.3
56567	2005-05-29	91.52	3-22	20	0.90	190	7.8	1.15	101.1	14.4
56636	2005-05-30	20.10	17-20	13	0.93	230	5.1	1.28	101.1	14.7
57134	2005-06-02	53.07	7-18	9	0.88	244	6.2	1.26	101.2	14.6
57158	2005-06-02	24.40	3-6	9	0.89	246	6.2	1.26	102.0	13.8
57170	2005-06-02	46.27	7-16	9	0.96	252	6.6	1.33	100.7	13.9
57193	2005-06-03	55.22	5-11	7	0.97	252	6.5	1.37	101.9	13.9
57493	2005-06-05	32.58	9-15	11	0.86	243	6.2	1.26	100.6	14.4
57508	2005-06-05	35.10	3-7	10	0.87	240	6.5	1.21	100.6	14.3
57958	2005-06-09	34.72	14-18	16	0.90	240	6.0	1.22	100.4	13.6
59938	2005-07-01	24.13	16-20	21	0.89	228	7.2	1.22	102.1	15.4
60397	2005-07-05	24.32	17-22	19	0.90	259	7.5	1.22	99.5	14.8
60630	2005-07-07	17.92	15-18	13	0.87	232	7.7	1.19	101.4	16.1

**C.10 RX J1725.0+1152**

Table C.13: Observations of RX J1725.0+1152 in on mode.

seqn.	start. time	expos.	ZD	BP	ped.	rate	inh.	$\mu$ -rate	ratio	PSF
51643	2005-04-06	21.05	17-18	6	1.10	189	8.7	1.12	98.5	20.4
51817	2005-04-07	19.88	17-17	7	1.01	188	9.0	0.96	99.7	21.5
52064	2005-04-08	26.05	17-18	6	1.04	186	9.0	1.01	98.6	20.7
52377	2005-04-09	37.70	17-18	7	1.01	192	8.7	1.02	100.1	20.8
52593	2005-04-10	41.00	17-18	6	1.04	180	8.3	1.08	99.0	20.4
53061	2005-04-14	56.87	17-18	9	1.04	151	7.3	1.08	97.9	19.3
53116	2005-04-15	47.55	17-18	7	1.03	176	8.3	0.95	96.7	19.8
53313	2005-04-19	74.50	17-19	7	1.05	178	7.1	1.00	99.0	20.1

Table C.14: Used off observations for the analysis of RX J1725.0+1152.

seqn.	start. time	expos.	ZD	BP	ped.	rate	inh.	$\mu$ -rate	ratio	PSF
50111	2005-03-15	19.95	17-19	10	1.03	202	8.9	1.05	101.4	22.8
50137	2005-03-15	19.93	15-16	7	0.98	200	8.4	1.04	101.5	23.0
50221	2005-03-16	19.90	21-23	10	1.08	176	9.9	1.04	98.6	22.3
50456	2005-03-18	13.38	20-21	11	1.02	181	8.4	0.98	98.2	21.3
51448	2005-04-05	84.95	14-20	13	0.89	192	9.0	0.98	100.0	20.2
52016	2005-04-08	79.48	13-18	10	0.97	194	9.5	0.95	99.3	19.9
53036	2005-04-14	79.67	13-18	12	0.96	146	7.8	1.02	97.2	19.1
53198	2005-04-17	34.48	17-19	8	1.16	187	7.3	1.11	99.1	21.3

**C.11 1ES 2344+514**

Table C.15: Observations of 1ES 2344+514 in wobble mode.

seqn.	start. time	expos.	ZD	BP	ped.	rate	inh.	$\mu$ -rate	ratio	PSF
63953	2005-08-05	58.30	23-27	13	1.01	217	6.0	1.17	98.5	15.4
63997	2005-08-05	37.90	23-24	15	1.01	216	5.7	1.21	98.8	15.9
64882	2005-08-09	59.63	23-27	10	1.04	210	6.7	1.28	99.9	16.0
64917	2005-08-09	42.92	23-23	17	1.04	204	6.1	1.19	97.6	15.4
65274	2005-08-11	59.98	24-29	11	1.01	209	7.0	1.29	101.1	16.2
65307	2005-08-11	43.48	23-23	11	1.01	206	6.9	1.25	99.7	15.9
65639	2005-08-13	60.00	24-29	16	1.01	209	7.0	1.16	98.1	15.1
65670	2005-08-13	50.03	23-24	14	1.03	205	6.7	1.16	98.0	15.8
65802	2005-08-15	58.45	25-31	17	1.03	204	7.0	1.16	99.2	16.4
65835	2005-08-15	50.73	23-24	19	1.01	201	6.8	1.12	98.2	15.9
68070	2005-09-06	59.70	23-24	22	1.07	160	9.5	1.21	98.4	14.6
68087	2005-09-06	49.80	24-27	18	1.06	156	8.6	1.21	99.4	15.7
68373	2005-09-12	39.78	23-26	13	1.20	179	8.8	1.16	99.5	17.2
68396	2005-09-12	59.75	23-27	15	1.19	172	7.8	1.16	98.8	16.5
68941	2005-09-26	10.30	30-30	5	1.09	144	11.1	1.05	104.2	14.5
68946	2005-09-26	4.65	29-29	6	1.09	148	10.3	1.00	102.2	14.9
68954	2005-09-26	16.68	26-27	5	1.10	149	9.8	1.10	101.3	13.1
68967	2005-09-26	17.80	24-26	5	1.10	149	9.7	1.11	101.6	13.6
69400	2005-09-29	18.88	29-31	6	1.10	178	8.8	1.19	100.0	12.1
69410	2005-09-29	21.27	26-28	7	1.12	179	8.6	1.26	97.2	12.5
69419	2005-09-29	22.22	24-26	7	1.10	178	8.7	1.23	98.5	12.4
69429	2005-09-29	18.75	23-24	7	1.11	177	9.0	1.22	98.4	12.6
69436	2005-09-30	16.98	23-23	7	1.09	174	8.5	1.19	96.5	12.2
76067	2005-11-26	21.95	23-24	14	1.03	156	8.2	1.28	101.3	15.2
76075	2005-11-26	23.82	25-27	13	1.06	156	7.8	1.28	102.4	15.5
77815	2005-12-18	27.58	23-25	13	1.03	183	8.7	1.12	99.3	16.1
77832	2005-12-18	27.80	26-28	13	1.07	152	8.0	1.10	98.9	14.9
77850	2005-12-18	16.75	28-30	14	1.10	158	8.5	1.18	98.0	15.9
77997	2005-12-22	23.80	25-27	13	1.13	182	8.3	1.12	98.9	16.4
78010	2005-12-22	20.60	28-30	13	1.14	179	8.5	1.05	99.7	16.5
78020	2005-12-22	4.23	30-30	12	1.11	175	7.9	1.00	99.8	13.8
78061	2005-12-22	29.60	31-36	21	1.12	169	9.1	1.05	97.4	15.6
78096	2005-12-22	16.12	37-39	12	1.13	162	7.9	1.05	99.6	16.4
78219	2005-12-23	22.58	26-27	12	1.12	182	8.6	1.13	100.6	17.3
78228	2005-12-23	20.33	27-29	12	1.09	175	8.2	1.09	100.1	16.4
78236	2005-12-23	5.40	30-31	11	1.10	175	9.4	1.08	99.9	17.7
78241	2005-12-23	16.47	32-34	11	1.11	169	9.1	1.02	99.5	16.9
78248	2005-12-23	27.02	34-37	11	1.11	165	8.9	0.99	99.6	17.0
78349	2005-12-24	20.85	26-27	12	1.12	179	7.8	1.13	99.9	17.0
78358	2005-12-24	18.80	28-30	12	1.14	177	7.3	1.13	99.9	17.0
78366	2005-12-24	18.67	30-32	12	1.17	176	7.9	1.13	101.1	16.4
78374	2005-12-24	32.17	33-38	14	1.12	171	8.1	1.03	100.1	15.8
78468	2005-12-26	17.42	27-28	12	1.11	188	8.3	1.09	100.5	17.9

Table C.15: Observations of 1ES 2344+514 in wobble mode (continued).

seqn.	start. time	expos.	ZD	BP	ped.	rate	inh.	$\mu$ -rate	ratio	PSF
78476	2005-12-26	19.78	29-31	13	1.19	184	8.2	1.13	102.2	19.2
78485	2005-12-26	21.58	31-34	13	1.13	179	8.4	1.05	101.1	16.0
78494	2005-12-26	27.57	35-39	13	1.14	175	8.2	1.06	100.2	16.6
78699	2005-12-29	14.08	35-37	12	1.15	176	9.3	1.03	101.0	17.3
78706	2005-12-29	13.57	37-38	13	1.13	173	9.5	1.07	99.3	16.3
78958	2005-12-30	19.10	29-31	12	1.15	167	9.1	1.07	98.0	15.9
78966	2005-12-30	18.60	31-33	13	1.11	161	9.3	0.97	100.2	17.2
78973	2005-12-30	15.67	34-36	13	1.12	159	9.6	1.03	100.8	15.6
78980	2005-12-30	12.78	36-38	12	1.10	152	9.9	0.98	100.0	15.9
79273	2005-12-31	19.65	28-31	12	1.07	147	9.7	1.09	98.3	15.7
79286	2005-12-31	20.40	32-34	13	1.06	142	9.5	1.06	98.5	15.3
79294	2005-12-31	13.60	35-36	13	1.04	137	9.7	1.07	99.0	16.4
79300	2005-12-31	10.68	37-38	12	1.05	152	9.8	1.00	99.0	16.8
79525	2006-01-01	20.05	32-34	13	1.06	166	10.7	1.10	100.4	14.0
79533	2006-01-01	19.32	34-37	14	1.04	161	10.9	1.08	99.4	15.6
79542	2006-01-01	9.20	38-39	14	1.06	155	10.7	1.01	98.5	16.5

# Appendix D

## Spectral data points

### D.1 Spectrum of 1ES 1218+304

Table D.1: Differential energy spectrum of 1ES 1218+304 derived from the complete sample and the first subsample of the lightcurve. The flux upper limits are for an 99% confidence level.

energy [GeV]	all data $F_E(E)$ [photons m <sup>-2</sup> s <sup>-1</sup> TeV <sup>-1</sup> ]	first subsample
112	$< 1.35 \times 10^{-5}$	$< 1.09 \times 10^{-5}$
200	$(9.95 \pm 2.60) \times 10^{-7}$	$(1.56 \pm 0.43) \times 10^{-6}$
356	$(1.19 \pm 0.54) \times 10^{-7}$	$(2.54 \pm 0.93) \times 10^{-7}$
632	$(1.61 \pm 1.57) \times 10^{-8}$	$(6.17 \pm 2.74) \times 10^{-8}$
1120	$< 9.18 \times 10^{-9}$	$< 1.17 \times 10^{-8}$
2000	$< 4.82 \times 10^{-9}$	$< 7.19 \times 10^{-9}$

## D.2 Spectrum of 1ES 2344+514

Table D.2: Differential energy spectra of 1ES 2344+514 derived from the complete sample as well as for the highflux and the midflux samples. The flux upper limits are given for an 99% confidence level.

energy [GeV]	all data	highflux $F_E(E)$ [phot m <sup>-2</sup> s <sup>-1</sup> TeV <sup>-1</sup> ]	midflux
152	$(2.48 \pm 0.72) \times 10^{-6}$	$(2.66 \pm 1.44) \times 10^{-6}$	$(3.01 \pm 1.16) \times 10^{-6}$
242	$(6.13 \pm 1.11) \times 10^{-7}$	$(6.61 \pm 2.47) \times 10^{-7}$	$(7.63 \pm 1.85) \times 10^{-7}$
388	$(1.19 \pm 0.54) \times 10^{-7}$	$(4.40 \pm 0.83) \times 10^{-7}$	$(2.38 \pm 0.60) \times 10^{-7}$
619	$(6.77 \pm 1.43) \times 10^{-8}$	$(1.69 \pm 0.34) \times 10^{-7}$	$(5.29 \pm 2.36) \times 10^{-8}$
990	$(1.36 \pm 0.50) \times 10^{-8}$	$(3.70 \pm 1.14) \times 10^{-8}$	$< 3.02 \times 10^{-8}$
1580	$(5.36 \pm 1.93) \times 10^{-9}$	$(1.43 \pm 0.47) \times 10^{-8}$	$(4.73 \pm 3.14) \times 10^{-9}$
2530	$< 2.86 \times 10^{-9}$	$< 3.89 \times 10^{-9}$	$< 2.81 \times 10^{-9}$

# Appendix E

## Parameters for the constraints on $B$ and $\delta$

Table E.1: Observational parameters which are used to derive the constraints on  $B$  and  $\delta$  for 1ES 2344+514.

parameter	1995 flare (Whipple)		MAGIC 2005	
	"with X-ray"	"w/o X-ray"	highflux	all
$E_{\text{syn,max}}$ [keV]	100	3000	100	10
$E_{\text{IC,max}}$ [TeV]	9.0	9.0	2.0	2.0
$t_{\text{var}}$ [s]	5000	5000	5000	5000
$\nu F_{\text{syn}}$ [ $10^{-11}$ erg $\text{cm}^{-2}$ $\text{s}^{-1}$ ]	4.2	20.5	2.8	1.0
$\nu F_{\text{IC}}$ [ $10^{-11}$ erg $\text{cm}^{-2}$ $\text{s}^{-1}$ ]	20.0	15.0	1.4	1.2
$L_{\text{syn}}$ [ $10^{45}$ erg $\text{s}^{-1}$ ]	1.27	3.55	0.54	0.16

Table E.2: Observational parameters which are used to derive the constraints on  $B$  and  $\delta$  for 1ES 1218+304.

parameter	MAGIC 2005	MAGIC 2006	
		all	first sample
$E_{\text{syn,max}}$ [keV]	1.0	1.0	10
$E_{\text{IC,max}}$ [TeV]	0.7	0.7	0.7
$t_{\text{var}}$ [s]	12000	12000	12000
$\nu F_{\text{syn}}$ [ $10^{-11}$ erg $\text{cm}^{-2}$ $\text{s}^{-1}$ ]	1.9	1.9	1.5
$\nu F_{\text{IC}}$ [ $10^{-11}$ erg $\text{cm}^{-2}$ $\text{s}^{-1}$ ]	3.5	1.7	2.5
$L_{\text{syn}}$ [ $10^{45}$ erg $\text{s}^{-1}$ ]	5.77	5.58	8.47

# List of Figures

1.1	The cosmic ray spectrum from $10^8$ eV up to $\sim 10^{20}$ eV. . . . .	16
1.2	The high energy end of the cosmic ray spectrum as measured by the Pierre Auger Observatory. . . . .	17
1.3	Hillas plot. . . . .	18
1.4	Schematic view of a first order Fermi acceleration on a non-relativistic plane shock front. . . . .	19
1.5	The 3rd EGRET catalogue. . . . .	22
1.6	Sky map above 100 MeV as seen by EGRET and as anticipated for GLAST. . . . .	23
1.7	The VHE gamma-ray sky in 2003. . . . .	25
1.8	World map with the locations of the second generation imaging air Cherenkov telescopes. . . . .	27
1.9	The VHE gamma-ray sky in 2007. . . . .	28
1.10	The variation of the Compton scattering cross-section with energy. . . . .	31
1.11	The metagalactic radiation field at present day. . . . .	34
1.12	Fazio-Stecker relation. . . . .	35
1.13	Optical depth vs. energy for different redshifts . . . . .	36
1.14	The pulsar wind nebula inside the Crab Nebula in X-rays. . . . .	37
1.15	Schematic view of the emission models for a binary system. . . . .	38
2.1	Unified model for AGN. . . . .	45
2.2	Doppler factor vs. viewing angle for various Lorentz factors. . . . .	50
2.3	Apparent velocity vs. the viewing angle for different Lorentz factors. . . . .	50
2.4	Schematic side-view of the inner part of an AGN. . . . .	55
2.5	Proton blazar. . . . .	57
3.1	Schematic view of the development of a hadron initiated air shower. . . . .	59

3.2	Side view of simulated air showers with different primary particles. . . . .	60
3.3	Height of shower maximum vs. energy of the primary particle. . . . .	61
3.4	Combined spectrum of muons and anti-muons at different altitudes as measured with the BESS instrument for vertical inclination. . . . .	62
3.5	Schematic view of the Cherenkov wavefront. . . . .	63
3.6	The maximum Cherenkov angle vs. altitude and the minimum energy required for Cherenkov effect for muons and electrons vs. altitude. . . . .	63
3.7	Average atmospheric transmission coefficient vs. the energy of the primary gamma-ray for various altitudes. . . . .	65
3.8	Schematic view of the Cherenkov light pool of an air shower. . . . .	66
3.9	Schematic view of the principle of the imaging air Cherenkov technique. . . . .	67
3.10	Images of simulated photon initiated air showers inside the MAGIC camera. . . . .	68
3.11	The MAGIC telescope. . . . .	69
3.12	Readout for single pixels: digital counts vs. time slices. . . . .	71
3.13	Scetch of the data stream of the MAGIC telescope. . . . .	72
3.14	The level-1 trigger. . . . .	73
4.1	Image of an air shower, recorded by the MAGIC telescope, before and after image cleaning. . . . .	78
4.2	Schematic view of an air shower image. . . . .	80
4.3	Image parameters <i>area</i> vs. <i>size</i> for simulated gamma showers and observational data. . . . .	83
4.4	The Crab Nebula at different wavelengths. . . . .	87
4.5	Sky map around the position of the Crab Nebula and distribution of $\vartheta^2$ . . . . .	90
4.6	Differential energy distribution for simulated gamma showers after cuts assuming a Crab-like spectrum. . . . .	90
4.7	Distribution of the true and the estimated energy of simulated gamma showers. . . . .	92
4.8	Relative error of the estimated energy vs. the simulated energy and the disribution of the relative error with a Gaussian fit. . . . .	92
4.9	MC spectrum as originally simulated, after trigger and after cuts. . . . .	93
4.10	Effective collection area after trigger and after all cuts vs. energy and the cut efficiencies. . . . .	93
4.11	Reconstructed differential VHE spectrum of the Crab Nebula. . . . .	94

4.12	VHE lightcurve of the Crab Nebula. . . . .	96
4.13	Dependency of the significance on the background statistic (scaling factor). . . . .	97
5.1	Incidence of the muon inside and outside of the reflector. . . .	99
5.2	Images of muons in the MAGIC camera. . . . .	99
5.3	Intensity distribution along the ring for different impact parameters. . . . .	100
5.4	Different contributions to the relative broadening of the muon ring vs. energy of the muon. . . . .	102
5.5	The simulated muon spectrum and the spectrum after image cleaning. . . . .	104
5.6	Distribution of the squared impact parameter and the squared angle of incidence after image cleaning. . . . .	105
5.7	Relative broadening of the muon ring vs. its <i>radius</i> for a sample of observed muon events. . . . .	106
5.8	Quantity <i>sumpsf</i> vs. the total PSF in mm for five samples of simulated muons with different spot sizes. . . . .	107
5.9	Point spread function of the optical system, as calculated from the muon ring analysis. . . . .	108
5.10	Point-spread-function of the optical system vs. the ZD. . . . .	109
5.11	Image parameter <i>muonsize</i> vs. <i>radius</i> for observed muon events. . . . .	109
5.12	Ratio between the light intensity of observed muons and simulated ones over time. . . . .	110
5.13	Distribution of the ratio between the light intensity of observed muons and simulated ones. . . . .	110
5.14	Correction factor for the average total light calibration. . . . .	111
5.15	Image parameter <i>area</i> vs. <i>size</i> for simulated gamma showers, observational off-data and simulated muons. . . . .	112
5.16	Distributions of the image parameters <i>width</i> and <i>length</i> for simulated muons and gamma showers. . . . .	112
5.17	Muon rate vs. rate after image cleaning and the distribution of the muon rate. . . . .	113
6.1	Excess rate of the Crab Nebula vs. the background rate. . . . .	121
6.2	Sky map around the position of 1ES 1011+496 and $\vartheta^2$ -plot before and after the starguider calibration. . . . .	125
6.3	Sky map around the position of 1ES 1218+304 and $\vartheta^2$ -plot. . . . .	126
6.4	Differential energy spectrum of 1ES 1218+304. . . . .	127
6.5	Lightcurve of 1ES 1218+304. . . . .	128

6.6	Differential energy spectrum of the first subsample of 1ES 1218+304. . . . .	129
6.7	Sky map around the position of 1ES 2344+514 and $\vartheta^2$ -plot. . .	130
6.8	Differential energy spectrum of 1ES 2344+514. . . . .	131
6.9	Lightcurve of 1ES 2344+514. . . . .	132
6.10	Differential energy spectra of 1ES 2344+514 for two subsamples (highflux and midflux). . . . .	134
7.1	Broad-band spectral index $\alpha_{\text{RO}}$ vs. $\alpha_{\text{OX}}$ . . . . .	141
7.2	Broad-band spectral index $\alpha_{\text{O}\gamma}$ vs. $\alpha_{\text{X}\gamma}$ . . . . .	142
7.3	Broad-band spectral index $\alpha_{\text{X}\gamma}$ vs. the X-ray luminosity $\nu_{\text{X}}L_{\text{X}}$ . . . . .	143
8.1	Energy spectrum of 1ES 2344+514 multiplied by $E^2$ for the midflux and the complete sample. . . . .	149
8.2	Energy spectrum of 1ES 2344+514 multiplied by $E^2$ for the highflux sample. . . . .	150
8.3	Spectral energy distribution of 1ES 2344+514. . . . .	152
8.4	Magnetic field $B$ vs. Doppler factor $\delta$ as constrained for 1ES 2344+514 for the highflux and the complete sample. . . . .	155
8.5	Magnetic field $B$ vs. Doppler factor $\delta$ as constrained for 1ES 2344+514 for the 1995 flare. . . . .	156
8.6	Energy spectrum of 1ES 1218+304 multiplied by $E^2$ . . . . .	158
8.7	Spectral energy distribution of 1ES 1218+304 for the 2005 observation. . . . .	159
8.8	Spectral energy distribution of 1ES 1218+304 for the 2006 observation. . . . .	160
8.9	Magnetic field $B$ vs. Doppler factor $\delta$ as constrained for 1ES 1218+304 for the 1995 flare. . . . .	162
8.10	Magnetic field $B$ vs. Doppler factor $\delta$ as constrained for 1ES 1218+304 for the 2006 observations. . . . .	163
9.1	Redshift distribution of different BL Lac samples. . . . .	167
9.2	The gamma-ray luminosity $\nu_{\gamma}L_{\gamma}$ vs. redshift and the number count above a certain luminosity. . . . .	168
9.3	Cumulative number vs. energy density for a patch of 44% of the sky. . . . .	170
B.1	Distribution of the image parameters <i>length</i> , <i>width</i> , <i>dist</i> , <i>size</i> and <i>m3long</i> of simulated gamma showers and gamma events from the Crab Nebula . . . . .	181
B.2	Distribution of the main muon image parameters <i>radius</i> , <i>arcwidth</i> and <i>arcphi</i> for simulated and observed muon events. . . . .	183

# List of Tables

2.1	AGN taxonomy. . . . .	44
2.2	Size of AGN components. . . . .	46
4.1	Observations of the Crab Nebula with the MAGIC telescope: observation summary. . . . .	88
4.2	Coefficients $c_0$ to $c_7$ used in the analysis. . . . .	89
4.3	Results of the analysis of the Crab Nebula observations. . . . .	89
4.4	Sensitivity of the analysis above 200 GeV for both observation modes. . . . .	97
5.1	Number of simulated muons after image cleaning and the number of reconstructed ring images for different point spread functions. . . . .	114
6.1	List of targets. . . . .	118
6.2	Observation log. . . . .	119
6.3	Analysis results of the investigated HBL sample. . . . .	122
6.4	Coefficients $c'_0$ to $c'_{11}$ for the analysis made with MARS version 2.0. . . . .	124
6.5	Integral flux of 1ES 2344+514 for each month of observation. .	133
7.1	Upper limits on the gamma-ray flux at 200 GeV ( $UL_{200}$ ) under the assumption of a power law spectrum with spectral index -3.0. . . . .	137
7.2	Simultaneous optical observations. . . . .	138
7.3	Optical depths for gamma-rays with an energy of 200 GeV. . .	139
7.4	HBLs detected at VHE which do not belong to the sample. . .	140
8.1	The parameters of the SSC model. . . . .	145
8.2	Values of the model parameters for the simulated SED of dif- ferent observations of 1ES 2344+514 together with the reduced $\chi^2$ -values of the fit. . . . .	154

8.3	Values of the model parameters for the simulated SED of different observations of 1ES 1218+304 together with the reduced $\chi^2$ -values of the fit. . . . .	161
9.1	Estimation of the omnidirectional flux at 200 GeV. . . . .	172
A.1	Observations of the Crab Nebula in on mode. . . . .	176
A.2	Used off observations for the analysis of the Crab Nebula. . . . .	178
A.3	Observations of the Crab Nebula in wobble mode. . . . .	180
C.1	Observations of 1ES 0120+340 in wobble mode. . . . .	184
C.2	Observations of RX J0319.8+1845 in wobble mode. . . . .	185
C.3	Observations of RX J0319.8+1845 in on mode. . . . .	186
C.4	Used off observations for the analysis of RX J0319.8+1845. . . . .	186
C.5	Observations of 1ES 0323+022 in wobble mode. . . . .	187
C.6	Observations of 1ES 0414+009 in wobble mode. . . . .	188
C.7	Observations of 1ES 0806+524 in wobble mode. . . . .	189
C.8	Observations of 1ES 0927+500 in wobble mode. . . . .	190
C.9	Observations of 1ES 1011+496 in wobble mode. . . . .	192
C.10	Observations of 1ES 1218+304 in wobble mode. . . . .	194
C.11	Observations of 1ES 1426+428 in on mode. . . . .	195
C.12	Used off observations for the analysis of 1ES 1426+428. . . . .	195
C.13	Observations of RX J1725.0+1152 in on mode. . . . .	196
C.14	Used off observations for the analysis of RX J1725.0+1152. . . . .	196
C.15	Observations of 1ES 2344+514 in wobble mode. . . . .	197
D.1	Data points of the differential spectrum of 1ES 1218+304 . . . . .	199
D.2	Data points of the differential spectrum of 1ES 2344+514. . . . .	200
E.1	Observational parameters used for the constraints on $B$ and $\delta$ for 1ES 2344+514. . . . .	201
E.2	Observational parameters used for the constraints on $B$ and $\delta$ for 1ES 1218+304. . . . .	201

# Bibliography

- A. A. Abdo, B. Allen, D. Berley, et al. Discovery of TeV Gamma-Ray Emission from the Cygnus Region of the Galaxy. *ApJ*, 658:L33–L36, March 2007a. doi: 10.1086/513696.
- A. A. Abdo, B. Allen, D. Berley, et al. TeV Gamma-Ray Sources from a Survey of the Galactic Plane with Milagro. *ApJL*, 664:L91–L94, August 2007b. doi: 10.1086/520717.
- J. Abraham, M. Abreu, P. Aglietta, et al. Correlation of the highest energy cosmic rays with nearby extragalactic objects. *Science*, 318:938–943, November 2007. doi: 10.1126/science.1151124.
- F. Aharonian, A. Akhperjanian, J. Barrio, et al. TeV gamma rays from the blazar H 1426+428 and the diffuse extragalactic background radiation. *A&A*, 384:L23–L26, March 2002. doi: 10.1051/0004-6361:20020206.
- F. Aharonian, A. Akhperjanian, M. Beilicke, et al. Observations of H1426+428 with HEGRA. Observations in 2002 and reanalysis of 1999 & 2000 data. *A&A*, 403:523–528, May 2003. doi: 10.1051/0004-6361:20030326.
- F. Aharonian, A. Akhperjanian, M. Beilicke, et al. Observations of 54 Active Galactic Nuclei with the HEGRA system of Cherenkov telescopes. *A&A*, 421:529–537, July 2004a. doi: 10.1051/0004-6361:20035764.
- F. Aharonian, A. G. Akhperjanian, K.-M. Aye, et al. H.E.S.S. observations of PKS 2155-304. *A&A*, 430:865–875, February 2005a. doi: 10.1051/0004-6361:20041853.
- F. Aharonian, A. G. Akhperjanian, K.-M. Aye, et al. Discovery of VHE gamma rays from PKS 2005-489. *A&A*, 436:L17–L20, June 2005b. doi: 10.1051/0004-6361:200500113.

- F. Aharonian, A. G. Akhperjanian, K.-M. Aye, et al. Upper limits to the SN1006 multi-TeV gamma-ray flux from HESS observations. *A&A*, 437: 135–139, July 2005c. doi: 10.1051/0004-6361:20042522.
- F. Aharonian, A. G. Akhperjanian, K.-M. Aye, et al. A New Population of Very High Energy Gamma-Ray Sources in the Milky Way. *Science*, 307: 1938–1942, March 2005d. doi: 10.1126/science.1108643.
- F. Aharonian, A. G. Akhperjanian, A. R. Bazer-Bachi, et al. A search for very high energy  $\gamma$ -ray emission from the starburst galaxy NGC 253 with HESS. *A&A*, 442:177–183, October 2005e. doi: 10.1051/0004-6361:20053521.
- F. Aharonian, A. G. Akhperjanian, A. R. Bazer-Bachi, et al. Discovery of very high energy  $\gamma$ -ray emission from the BL Lacertae object H 2356-309 with the HESS Cherenkov telescopes. *A&A*, 455:461–466, August 2006a. doi: 10.1051/0004-6361:20054732.
- F. Aharonian, A. G. Akhperjanian, A. R. Bazer-Bachi, et al. Observations of the Crab nebula with HESS. *A&A*, 457:899–915, October 2006b. doi: 10.1051/0004-6361:20065351.
- F. Aharonian, A. G. Akhperjanian, A. R. Bazer-Bachi, et al. 3.9 day orbital modulation in the TeV  $\gamma$ -ray flux and spectrum from the X-ray binary LS 5039. *A&A*, 460:743–749, December 2006c. doi: 10.1051/0004-6361:20065940.
- F. Aharonian, A. G. Akhperjanian, A. R. Bazer-Bachi, et al. Discovery of very-high-energy  $\gamma$ -rays from the Galactic Centre ridge. *Nature*, 439:695–698, February 2006d. doi: 10.1038/nature04467.
- F. Aharonian, A. G. Akhperjanian, A. R. Bazer-Bachi, et al. A low level of extragalactic background light as revealed by  $\gamma$ -rays from blazars. *Nature*, 440:1018–1021, April 2006e. doi: 10.1038/nature04680.
- F. Aharonian, A. G. Akhperjanian, A. R. Bazer-Bachi, et al. HESS Observations of the Galactic Center Region and Their Possible Dark Matter Interpretation. *Physical Review Letters*, 97(22):221102–+, December 2006f. doi: 10.1103/PhysRevLett.97.221102.
- F. Aharonian, A. G. Akhperjanian, A. R. Bazer-Bachi, et al. Fast variability of tera-electron volt rays from the radio galaxy M87. *Science*, 314:1424–1427, 2006g.

- F. Aharonian, A. G. Akhperjanian, U. Barres de Almeida, et al. Discovery of VHE  $\gamma$ -rays from the distant BL Lacertae 1ES 0347-121. *A&A*, 473:L25–L28, October 2007a. doi: 10.1051/0004-6361:20078412.
- F. Aharonian, A. G. Akhperjanian, U. Barres de Almeida, et al. New constraints on the mid-IR EBL from the HESS discovery of VHE  $\gamma$ -rays from 1ES 0229+200. *A&A*, 475:L9–L13, November 2007b. doi: 10.1051/0004-6361:20078462.
- F. Aharonian, A. G. Akhperjanian, A. R. Bazer-Bachi, et al. Detection of VHE gamma-ray emission from the distant blazar 1ES 1101-232 with HESS and broadband characterisation. *A&A*, 470:475–489, August 2007c. doi: 10.1051/0004-6361:20077057.
- F. Aharonian, A. G. Akhperjanian, A. R. Bazer-Bachi, et al. An Exceptional Very High Energy Gamma-Ray Flare of PKS 2155-304. *ApJL*, 664:L71–L74, August 2007d. doi: 10.1086/520635.
- F. A. Aharonian. TeV gamma rays from BL Lac objects due to synchrotron radiation of extremely high energy protons. *New Astronomy*, 5:377–395, November 2000. doi: 10.1016/S1384-1076(00)00039-7.
- F. A. Aharonian, P. S. Coppi, and H. J. Voelk. Very high energy gamma rays from active galactic nuclei: Cascading on the cosmic background radiation fields and the formation of pair halos. *ApJ*, 423:L5–L8, March 1994. doi: 10.1086/187222.
- F. A. Aharonian, A. G. Akhperjanian, K.-M. Aye, et al. High-energy particle acceleration in the shell of a supernova remnant. *Nature*, 432:75–77, November 2004b. doi: 10.1038/nature02960.
- E.-J. Ahn, P. Bhattacharjee, P. L. Biermann, et al. *Physics and Astrophysics of Ultra-High-Energy Cosmic Rays*. Springer Verlag Berlin Heidelberg, 2001.
- C. Akerlof, J. Dimarco, H. Levy, et al. Detection of High Energy Gamma Rays from the Crab Nebula. In *International Cosmic Ray Conference*, volume 2 of *International Cosmic Ray Conference*, pages 135–+, 1990.
- J. Albert, E. Aliu, H. Anderhub, et al. Observation of Gamma Rays from the Galactic Center with the MAGIC Telescope. *ApJ*, 638:L101–L104, February 2006a. doi: 10.1086/501164.

- J. Albert, E. Aliu, H. Anderhub, et al. Observation of Very High Energy Gamma-Ray Emission from the Active Galactic Nucleus 1ES 1959+650 Using the MAGIC Telescope. *ApJ*, 639:761–765, March 2006b. doi: 10.1086/499421.
- J. Albert, E. Aliu, H. Anderhub, et al. Flux Upper Limit on Gamma-Ray Emission by GRB 050713a from MAGIC Telescope Observations. *ApJ*, 641:L9–L12, April 2006c. doi: 10.1086/503767.
- J. Albert, E. Aliu, H. Anderhub, et al. Discovery of Very High Energy Gamma Rays from 1ES 1218+30.4. *ApJL*, 642:L119–L122, May 2006d. doi: 10.1086/504845.
- J. Albert, E. Aliu, H. Anderhub, et al. Discovery of Very High Energy  $\gamma$ -Rays from Markarian 180 Triggered by an Optical Outburst. *ApJL*, 648:L105–L108, September 2006e. doi: 10.1086/508020.
- J. Albert, E. Aliu, H. Anderhub, et al. Variable Very-High-Energy Gamma-Ray Emission from the Microquasar LS I +61 303. *Science*, 312:1771–1773, June 2006f. doi: 10.1126/science.1128177.
- J. Albert, E. Aliu, H. Anderhub, et al. Detection of Very High Energy Radiation from the BL Lacertae Object PG 1553+113 with the MAGIC Telescope. *ApJL*, 654:L119–L122, January 2007a. doi: 10.1086/511384.
- J. Albert, E. Aliu, H. Anderhub, et al. Observation of Very High Energy  $\gamma$ -Rays from the AGN 1ES 2344+514 in a Low Emission State with the MAGIC Telescope. *ApJ*, 662:892–899, June 2007b. doi: 10.1086/518431.
- J. Albert, E. Aliu, H. Anderhub, et al. Observations of Markarian 421 with the MAGIC Telescope. *ApJ*, 663:125–138, July 2007c. doi: 10.1086/518221.
- J. Albert, E. Aliu, H. Anderhub, et al. Discovery of Very High Energy  $\gamma$ -Ray Emission from the Low-Frequency-peaked BL Lacertae Object BL Lacertae. *ApJ*, 666:L17–L20, September 2007d. doi: 10.1086/521550.
- J. Albert, E. Aliu, H. Anderhub, et al. Discovery of Very High Energy  $\gamma$ -Rays from 1ES 1011+496 at  $z = 0.212$ . *ApJL*, 667:L21–L24, September 2007e. doi: 10.1086/521982.
- J. Albert, E. Aliu, H. Anderhub, et al. Implementation of the Random Forest Method for the Imaging Atmospheric Cherenkov Telescope MAGIC. arXiv:0709.3719v2, 2007f.

- J. Albert, E. Aliu, H. Anderhub, et al. Variable Very High Energy  $\gamma$ -Ray Emission from Markarian 501. *ApJ*, 669:862–883, November 2007g. doi: 10.1086/521382.
- J. Albert, E. Aliu, H. Anderhub, et al. Constraints on the Steady and Pulsed Very High Energy Gamma-Ray Emission from Observations of PSR B1951+32/CTB 80 with the MAGIC Telescope. *ApJ*, 669:1143–1149, November 2007h. doi: 10.1086/521807.
- J. Albert, E. Aliu, H. Anderhub, et al. VHE Gamma-Ray Observation of the Crab Nebula and Pulsar with MAGIC. *to appear in ApJ*, arXiv:0705.3244v2, 2008a.
- J. Albert, E. Aliu, H. Anderhub, et al. Systematic search for VHE gamma-ray emission from X-ray bright high-frequency BL Lac objects. *to appear in ApJ*, arXiv:0706.4453v2, 2008b.
- S. Antón and I. W. A. Browne. The recognition of blazars and the blazar spectral sequence. *MNRAS*, 356:225–231, January 2005. doi: 10.1111/j.1365-2966.2004.08441.x.
- J. R. Arnold, A. E. Metzger, E. C. Anderson, and M. A. van Dilla. Gamma Rays in Space, Ranger 3. *Journal of Geophysical Research*, 67:4878–+, November 1962.
- F. Arqueros, J. Ballestrin, M. Berenguel, et al. Very high-energy  $\gamma$ -ray observations of the Crab nebula and other potential sources with the GRAAL experiment. *Astroparticle Physics*, 17:293–318, June 2002.
- A. J. Barth, L. C. Ho, and W. L. W. Sargent. The Black Hole Masses and Host Galaxies of BL Lacertae Objects. *ApJ*, 583:134–144, January 2003. doi: 10.1086/345083.
- P. D. Barthel. Is every quasar beamed? *ApJ*, 336:606–611, January 1989. doi: 10.1086/167038.
- H. Bartko. *Observation of Galactic Sources of Very High Energy  $\gamma$ -Rays with the MAGIC Telescope*. PhD thesis, Ludwig-Maximilians-Universität München, 2006.
- J. K. Becker, A. Groß, K. Münich, J. Dreyer, W. Rhode, and P. L. Biermann. Astrophysical implications of high energy neutrino limits. *Astroparticle Physics*, 28:98–118, September 2007. doi: 10.1016/j.astropartphys.2007.04.007.

- V. Beckmann, D. Engels, N. Bade, and O. Wucknitz. The HRX-BL Lac sample - Evolution of BL Lac objects. *A&A*, 401:927–938, April 2003. doi: 10.1051/0004-6361:20030184.
- W. Bednarek and R. J. Protheroe. Testing the homogeneous synchrotron self-Compton model for gamma-ray production in MRK 421. *MNRAS*, 292:646–+, December 1997.
- M. Beilicke, W. Benbow, R. Cornils, et al. Observation of the giant radio galaxy M87 at TeV energies with H.E.S.S. In *Texas Symposium on Relativistic Astrophysics*, Texas Symposium on Relativistic Astrophysics, pages 2403–+, December 2004.
- D. R. Bergman and J. W. Belz. Cosmic Rays: The Second Knee and Beyond. *to appear in J. Physics G*, arXiv:0704.3721, 2007.
- K. Bernlöhr, E. Carmona, T. Schweizer, et al. MC Simulation and Layout Studies for a future Cherenkov Telescope Array. *to appear in the Proceedings of the 30th International Cosmic Ray Conference*, 2007.
- M. Bersanelli, P. Bouchet, R. Falomo, and E. G. Tanzi. Homogeneous J, H, K, L photometry of a sample of BL Lac objects. *AJ*, 104:28–39, July 1992. doi: 10.1086/116218.
- P. N. Bhat. Wavefront sampling technique : VHE gamma-ray experiments in India. *Bulletin of the Astronomical Society of India*, 30:135–145, March 2002.
- J. A. Biretta, C. P. Stern, and D. E. Harris. The radio to X-ray spectrum of the M87 jet and nucleus. *AJ*, 101:1632–1646, May 1991. doi: 10.1086/115793.
- J. A. Biretta, W. Junor, and M. Livio. Evidence for initial jet formation by an accretion disk in the radio galaxy M87. *New Astronomy Review*, 46: 239–245, May 2002.
- R. D. Blandford and A. Königl. Relativistic jets as compact radio sources. *ApJ*, 232:34–48, August 1979. doi: 10.1086/157262.
- M. Błażejowski, G. Blaylock, I. H. Bond, et al. A Multiwavelength View of the TeV Blazar Markarian 421: Correlated Variability, Flaring, and Spectral Evolution. *ApJ*, 630:130–141, September 2005. doi: 10.1086/431925.

- G. R. Blumenthal and R. J. Gould. Bremsstrahlung, Synchrotron Radiation, and Compton Scattering of High-Energy Electrons Traversing Dilute Gases. *Reviews of Modern Physics*, 42:237–271, 1970.
- A. J. Blustin, M. J. Page, and G. Branduardi-Raymont. Intrinsic absorbers in BL Lac objects: The XMM-Newton view. *A&A*, 417:61–70, April 2004. doi: 10.1051/0004-6361:20034517.
- V. Bosch-Ramon, J. M. Paredes, G. E. Romero, and M. Ribó. The radio to TeV orbital variability of the microquasar LS I +61 303. *A&A*, 459:L25–L28, November 2006. doi: 10.1051/0004-6361:20065830.
- M. Böttcher and C. D. Dermer. An Evolutionary Scenario for Blazar Unification. *ApJ*, 564:86–91, January 2002. doi: 10.1086/324134.
- Leo Breiman. *Machine Learning* 45(1), 5, 2001.
- T. Bretz. 2007. [http://www.astro.uni-wuerzburg.de/wiki/Image\\_Cleaning](http://www.astro.uni-wuerzburg.de/wiki/Image_Cleaning).
- T. Bretz. *Observation of the Active Galactic Nucleus 1ES1218+304 with the MAGIC telescope*. PhD thesis, Bayerische Julius-Maximilians-Universität Würzburg, 2006.
- I. W. A. Browne. Is it possible to turn an elliptical radio galaxy into a BL Lac object? *MNRAS*, 204:23P–27P, July 1983.
- I. W. A. Browne. BL-Lacertae Objects Optically Violent Variables Hpqs and Unified Models. In L. Maraschi, T. Maccacaro, and M.-H. Ulrich, editors, *BL Lac Objects*, volume 334 of *Lecture Notes in Physics*, Berlin Springer Verlag, pages 401–+, 1989. doi: 10.1007/BFb0031137.
- A. Caccianiga and M. J. M. Marchã. The CLASS blazar survey: testing the blazar sequence. *MNRAS*, 348:937–954, March 2004. doi: 10.1111/j.1365-2966.2004.07415.x.
- M. Catanese, C. W. Akerlof, H. M. Badran, et al. Discovery of Gamma-Ray Emission above 350 GeV from the BL Lacertae Object 1ES 2344+514. *ApJ*, 501:616–+, July 1998. doi: 10.1086/305857.
- A. Cavaliere and V. D’Elia. The Blazar Main Sequence. *ApJ*, 571:226–233, May 2002. doi: 10.1086/339778.
- C. C. Cheung, D. E. Harris, and L. Stawarz. Superluminal Radio Features in the M87 Jet and the Site of Flaring TeV Gamma-Ray Emission. *ApJL*, 663:L65–L68, July 2007. doi: 10.1086/520510.

- M. H. Cohen, M. L. Lister, D. C. Homan, et al. Relativistic Beaming and the Intrinsic Properties of Extragalactic Radio Jets. *ApJ*, 658:232–244, March 2007. doi: 10.1086/511063.
- G. W. Collins, II, W. P. Claspy, and J. C. Martin. A Reinterpretation of Historical References to the Supernova of A.D. 1054. *PASP*, 111:871–880, July 1999.
- J. J. Condon, W. D. Cotton, E. W. Greisen, et al. The NRAO VLA Sky Survey. *AJ*, 115:1693–1716, May 1998. doi: 10.1086/300337.
- B. A. Cooke, M. J. Ricketts, T. Maccacaro, et al. The Ariel V /SSI/ catalogue of high galactic latitude /absolute value of B greater than 10 deg/ X-ray sources. *MNRAS*, 182:489–515, February 1978.
- L. Costamante and G. Ghisellini. TeV candidate BL Lac objects. *A&A*, 384: 56–71, March 2002. doi: 10.1051/0004-6361:20011749.
- L. Costamante, G. Ghisellini, P. Giommi, et al. Extreme synchrotron BL Lac objects. Stretching the blazar sequence. *A&A*, 371:512–526, May 2001. doi: 10.1051/0004-6361:20010412.
- G. Cusumano, G. Agnetta, A. Alberdi, et al. GAW - An Imaging Atmospheric Cherenkov Telescope with Large Field of View. *to appear in the Proceedings of the 30th International Cosmic Ray Conference*, arXiv:0707.4541, 2007.
- A. Daum, G. Hermann, M. Hess, et al. First results on the performance of the HEGRA IACT array. *Astroparticle Physics*, 8:1–2, December 1997.
- M. de Naurois, J. Holder, R. Bazer-Bachi, et al. Measurement of the Crab Flux above 60 GeV with the CELESTE Cerenkov Telescope. *ApJ*, 566: 343–357, February 2002. doi: 10.1086/337991.
- V. D’Elia and A. Cavaliere. The Connection between BL Lacs and Flat-Spectrum Radio Quasars. In P. Padovani and C. M. Urry, editors, *Blazar Demographics and Physics*, volume 227 of *Astronomical Society of the Pacific Conference Series*, pages 252–+, 2001.
- C. D. Dermer and R. Schlickeiser. Model for the High-Energy Emission from Blazars. *ApJ*, 416:458–+, October 1993. doi: 10.1086/173251.
- C. D. Dermer, R. Schlickeiser, and A. Mastichiadis. High-energy gamma radiation from extragalactic radio sources. *A&A*, 256:L27–L30, March 1992.

- C. D. Dermer, S. J. Sturmer, and R. Schlickeiser. Nonthermal Compton and Synchrotron Processes in the Jets of Active Galactic Nuclei. *ApJS*, 109: 103–+, March 1997. doi: 10.1086/312972.
- H. Dole, G. Lagache, J.-L. Puget, et al. The cosmic infrared background resolved by Spitzer. Contributions of mid-infrared galaxies to the far-infrared background. *A&A*, 451:417–429, May 2006. doi: 10.1051/0004-6361:20054446.
- D. Donato, G. Ghisellini, G. Tagliaferri, and G. Fossati. *A&A*, 375:739, 2001.
- D. Donato, R. M. Sambruna, and M. Gliozzi. Six years of BeppoSAX observations of blazars: A spectral catalog. *A&A*, 433:1163–1169, April 2005. doi: 10.1051/0004-6361:20034555.
- L. Dondi and G. Ghisellini. Gamma-ray-loud blazars and beaming. *MNRAS*, 273:583–595, April 1995.
- D. Dorner et al. Data Management and Processing for the MAGIC Telescope. In *International Cosmic Ray Conference*, volume 5 of *International Cosmic Ray Conference*, pages 175–+, 2005.
- M. Doro. The Commissioning and Characterization of the Calibration System of the MAGIC Telescope. Master’s thesis, Universita Degli Studi di Padova, 2004.
- G. Dubus. The gamma-ray binaries LS 5039, LS I +61 303 and PSR B1259-63. *Proceedings of the Vulcano workshop*, arXiv:astro-ph/0608262, 2006.
- J. S. Dunlop and J. A. Peacock. The Redshift Cut-Off in the Luminosity Function of Radio Galaxies and Quasars. *MNRAS*, 247:19–+, November 1990.
- J. S. Dunlop, R. J. McLure, M. J. Kukula, et al. Quasars, their host galaxies and their central black holes. *MNRAS*, 340:1095–1135, April 2003. doi: 10.1046/j.1365-8711.2003.06333.x.
- D. Elsässer and K. Mannheim. Supersymmetric Dark Matter and the Extragalactic Gamma Ray Background. *Physical Review Letters*, 94(17): 171302–+, May 2005. doi: 10.1103/PhysRevLett.94.171302.
- M. Elvis, D. Plummer, J. Schachter, and G. Fabbiano. The Einstein Slew Survey. *ApJS*, 80:257–303, May 1992. doi: 10.1086/191665.

- B. L. Fanaroff and J. M. Riley. The morphology of extragalactic radio sources of high and low luminosity. *MNRAS*, 167:31P–36P, May 1974.
- G. G. Fazio and F. W. Stecker. Predicted High Energy Break in the Isotropic Gamma Ray Spectrum: a Test of Cosmological Origin. *Nature*, 226:135–+, April 1970.
- G. G. Fazio, M. L. N. Ashby, P. Barmby, et al. Number Counts at  $3 \mu\text{m} < \lambda < 10 \mu\text{m}$  from the Spitzer Space Telescope. *ApJS*, 154:39–43, September 2004. doi: 10.1086/422585.
- I. Fernini, J. O. Burns, and R. A. Perley. VLA Imaging of Fanaroff-Riley II 3CR Radio Galaxies.II.Eight New Images and Comparisons with 3CR Quasars. *AJ*, 114:2292–+, December 1997. doi: 10.1086/118649.
- P. Fortin. Observations of the high-frequency-peaked BL Lac object 1ES 1218+304 with VERITAS. *ArXiv e-prints*, 709, September 2007.
- G. Fossati, L. Maraschi, A. Celotti, A. Comastri, and G. Ghisellini. A unifying view of the spectral energy distributions of blazars. *MNRAS*, 299: 433–448, September 1998.
- G. Fossati, J. H. Buckley, I. H. Bond, et al. Multiwavelength Observations of Markarian 421 in March 2001: an Unprecedented View on the X-ray/TeV Correlated Variability. *to appear in ApJ*, arXiv:0710.4138, October 2007.
- J. A. Gaidos, C. W. Akerlof, S. D. Biller, et al. Very Rapid and Energetic Bursts of TeV Photons from the Active Galaxy Markarian 421. *Nature*, 383:319–+, 1996. doi: 10.1038/383319a0.
- T. K. Gaisser. *Cosmic Rays and Particle Physics*. Cambridge University Press, 1990.
- M. Garczarczyk. *First Observations of the GRB Prompt and Early Afterglow Emission Phase at  $\sim 100$  GeV Energy Regime with the 17m  $\emptyset$  MAGIC Imaging Atmospheric Cherenkov Telescope*. PhD thesis, Universität Rostock, 2006.
- M. Gaug. *Calibration of the MAGIC Telescope and Observation of Gamma Ray Burst*. PhD thesis, Universitat Autònoma de Barcelona, 2006.
- N. M. Gerasimova, A. I. Nikishov, and I. L. Rosenthal. Interaction of Nuclei and Photons of High Energies with a Thermal Radiations in the Universe. *Journal of the Physical Society of Japan, Vol. 17, Supplement A-III, Proceedings of the International Conference on Cosmic Rays and the*

- Earth Storm, held 5-15 September, 1961 in Kyoto. Volume III: Cosmic Rays. Published by the Physical Society of Japan, 1962., p.175, 17:C175+, 1962.*
- L. Gerhardt et al. Multi-year Search for UHE Diffuse Neutrino FLux with AMANDA-II. *to appear in the Proceedings of the 30th International Cosmic Ray Conference*, arXiv:0711:0353, 2007.
- P. L. Ghia. WG II Report on UHE cosmic rays. *Journal of Physics Conference Series*, 60:84–89, March 2007. doi: 10.1088/1742-6596/60/1/014.
- G. Ghisellini, A. Celotti, G. Fossati, L. Maraschi, and A. Comastri. A theoretical unifying scheme for gamma-ray bright blazars. *MNRAS*, 301:451–468, December 1998.
- G. Ghisellini, A. Celotti, and L. Costamante. Low power BL Lacertae objects and the blazar sequence. Clues on the particle acceleration process. *A&A*, 386:833–842, May 2002. doi: 10.1051/0004-6361:20020275.
- V. L. Ginzburg and S. I. Syrovatskii. Cosmic Magnetobremstrahlung (synchrotron Radiation). *ARA&A*, 3:297–+, 1965. doi: 10.1146/annurev.aa.03.090165.001501.
- P. Giommi and P. Padovani. BL Lac Reunification. *MNRAS*, 268:L51+, May 1994.
- P. Giommi, P. Padovani, and E. Perlman. Detection of exceptional X-ray spectral variability in the TeV BL Lac 1ES 2344+514. *MNRAS*, 317:743–749, October 2000.
- P. Giommi, P. Padovani, M. Perri, H. Landt, and E. Perlman. Parameter Correlations and Cosmological Properties of BL Lac Objects. In P. Giommi, E. Massaro, and G. Palumbo, editors, *Blazar Astrophysics with BeppoSAX and Other Observatories*, pages 133–+, 2002.
- F. Goebel, H. Bartko, E. Carmona, et al. Upgrade of the MAGIC Telescope with a Multiplexed Fiber-Optic 2 GSamples/s FADC Data Acquisition system. *to appear in the Proceedings of the 30th International Cosmic Ray Conference*, arXiv:0709.2363, 2007.
- F. Goebel et al. The Data Acquisition of the MAGIC Telescope. In *International Cosmic Ray Conference*, volume 5 of *International Cosmic Ray Conference*, pages 2939–+, July 2003.

- R. J. Gould and G. P. Schröder. Opacity of the Universe to High-Energy Photons. *Physical Review*, 155:1408–1411, March 1967. doi: 10.1103/PhysRev.155.1408.
- K. Greisen. End to the Cosmic-Ray Spectrum? *Physical Review Letters*, 16: 748–750, April 1966. doi: 10.1103/PhysRevLett.16.748.
- K. Grupen. *Astroteilchenphysik*. vieweg, September 2000.
- M. Haffke. Berechnung und Implementierung neuer Atmosphärenmodelle in die MAGIC-Monte-Carlo-Kette. Master's thesis, Universität Dortmund, 2007. [http://app.uni-dortmund.de/download/Arbeiten/Dip\\_Haffke.pdf](http://app.uni-dortmund.de/download/Arbeiten/Dip_Haffke.pdf).
- D. S. Hanna, D. Bhattacharya, L. M. Boone, et al. The STACEE-32 ground based gamma-ray detector. *Nuclear Instruments and Methods in Physics Research A*, 491:126–151, September 2002.
- D. E. Harris and H. Krawczynski. X-Ray Emission from Extragalactic Jets. *ARA&A*, 44:463–506, September 2006.
- R. C. Hartman, D. A. Kniffen, D. J. Thompson, et al. Galactic plane gamma-radiation. *ApJ*, 230:597–606, June 1979. doi: 10.1086/157118.
- R. C. Hartman, D. L. Bertsch, S. D. Bloom, et al. The Third EGRET Catalog of High-Energy Gamma-Ray Sources. *ApJS*, 123:79–202, July 1999. doi: 10.1086/313231.
- R. C. Hartman, M. Böttcher, G. Aldering, et al. Multiepoch Multiwavelength Spectra and Models for Blazar 3C 279. *ApJ*, 553:683–694, June 2001. doi: 10.1086/320970.
- M. G. Hauser and E. Dwek. The Cosmic Infrared Background: Measurements and Implications. *ARA&A*, 39:249–307, 2001. doi: 10.1146/annurev.astro.39.1.249.
- W. C. Haxton. The Solar Neutrino Problem. *ARA&A*, 33:459–504, 1995. doi: 10.1146/annurev.aa.33.090195.002331.
- C. Hazard, M. B. Mackey, and A. J. Shimmins. Investigation of the Radio Source 3C273 by the method of Lunar Occultations. *Nature*, 197:1037–+, March 1963.
- D. Heck, J. Knapp, J. N. Capdevielle, G. Schatz, and T. Thouw. CORSIKA: A Monte Carlo code to simulate extensive air showers. *Wissenschaftliche Berichte, FZKA-6019*. Forschungszentrum Karlsruhe, 1998.

- V. F. Hess. Über Beobachtungen der durchdringenden Strahlung bei sieben Freiballonfahrten. *Physikalische Zeitschrift*, 13:1084–1091, November 1912.
- A. M. Hillas. The Origin of Ultra-High-Energy Cosmic Rays. *Ann. Rev. Astron. Astrophys.*, 22:425–444, 1984. doi: 10.1146/annurev.aa.22.090184.002233.
- A. M. Hillas. Cerenkov light images of EAS produced by primary gamma. In F. C. Jones, editor, *International Cosmic Ray Conference*, volume 3 of *International Cosmic Ray Conference*, pages 445–448, August 1985.
- K. Hirata, T. Kajita, M. Koshiba, M. Nakahata, and Y. Oyama. Observation of a neutrino burst from the supernova SN1987A. *Physical Review Letters*, 58:1490–1493, April 1987.
- D. Horan and T. C. Weekes. Extragalactic sources of TeV gamma rays: a summary. *New Astronomy Review*, 48:527–535, April 2004. doi: 10.1016/j.newar.2003.12.057.
- D. Horan, H. M. Badran, I. H. Bond, et al. Detection of the BL Lacertae Object H1426+428 at TeV Gamma-Ray Energies. *ApJ*, 571:753–762, June 2002. doi: 10.1086/340019.
- D. Horan, H. M. Badran, I. H. Bond, et al. Constraints on the Very High Energy Emission from BL Lacertae Objects. *ApJ*, 603:51–61, March 2004. doi: 10.1086/381430.
- K. Hoshina, J. Hodges, C. H. Garry, et al. Searches for a diffuse flux of extra-terrestrial muon neutrinos with AMANDA-II and IceCube. *to appear in the Proceedings of the 30th International Cosmic Ray Conference*, arXiv:0711.0353, 2007.
- S. D. Hunter, D. L. Bertsch, J. R. Catelli, et al. EGRET Observations of the Diffuse Gamma-Ray Emission from the Galactic Plane. *ApJ*, 481:205–+, May 1997. doi: 10.1086/304012.
- C. Itoh, R. Enomoto, S. Yanagita, et al. Evidence of TeV gamma-ray emission from the nearby starburst galaxy NGC 253. *A&A*, 462:67–71, January 2007. doi: 10.1051/0004-6361:20066244.
- J. D. Jackson. *Klassische Elektrodynamik*. de Gruyter, 2nd edition, 1982.

- J. V. Jelley. High-energy  $\gamma$ -ray absorption in space by a 3.5 k microwave field. *Phys. Rev. Lett.*, 16(11):479–481, Mar 1966. doi: 10.1103/PhysRevLett.16.479.
- A. Karle et al. IceCube - construction status and performance results of the 22 string detector. *to appear in the Proceedings of the 30th International Cosmic Ray Conference*, arXiv:0711:0353, 2007.
- J. Kataoka, J. R. Mattox, J. Quinn, et al. High-Energy Emission from the TEV Blazar Markarian 501 during Multiwavelength Observations in 1996. *ApJ*, 514:138–147, March 1999. doi: 10.1086/306918.
- U. F. Katz. Neutrino telescope in the Mediterranean Sea. *Progress in Particle and Nuclear Physics*, 57:273–282, July 2006. doi: 10.1016/j.pnpnp.2006.01.006.
- K. I. Kellermann, Y. Y. Kovalev, M. L. Lister, et al. Doppler boosting, superluminal motion, and the kinematics of AGN jets. *Ap&SS*, 311:231–239, October 2007. doi: 10.1007/s10509-007-9622-5.
- A. K. Kembhavi and J. V. Narlika. *Quasars and Active Galactic Nuclei: An Introduction*. Cambridge University Press, 1999.
- T. M. Kneiske and K. Mannheim. BL Lac Contribution to the Extragalactic Gamma-Ray Background. *to appear in A&A*, arXiv:0705.3778, 2007.
- T. M. Kneiske, K. Mannheim, and D. H. Hartmann. Implications of cosmological gamma-ray absorption. I. Evolution of the metagalactic radiation field. *A&A*, 386:1–11, April 2002. doi: 10.1051/0004-6361:20020211.
- T. M. Kneiske, T. Bretz, K. Mannheim, and D. H. Hartmann. Implications of cosmological gamma-ray absorption. II. Modification of gamma-ray spectra. *A&A*, 413:807–815, January 2004. doi: 10.1051/0004-6361:20031542.
- A. Konopelko, F. Aharonian, A. Akhperjanian, et al. Detection of gamma rays above 1 TeV from the Crab Nebula by the second HEGRA imaging atmospheric Cherenkov telescope at La Palma. *Astroparticle Physics*, 4: 199–215, February 1996.
- A. Kouchner et al. The ANTARES neutrino telescope: a status report. *to appear in the Proceedings of the 30th International Cosmic Ray Conference*, arXiv:0710.0272, 2007.

- Y. Y. Kovalev, Y. A. Kovalev, N. A. Nizhelsky, and A. B. Bogdantsov. Broad-band Radio Spectra Variability of 550 AGN in 1997-2001. *Publications of the Astronomical Society of Australia*, 19:83–87, 2002. doi: 10.1071/AS01109.
- W. L. Kraushaar, G. W. Clark, G. P. Garmire, et al. High-Energy Cosmic Gamma-Ray Observations from the OSO-3 Satellite. *ApJ*, 177:341–+, November 1972.
- H. Krawczynski, S. B. Hughes, D. Horan, et al. Multiwavelength Observations of Strong Flares from the TeV Blazar 1ES 1959+650. *ApJ*, 601:151–164, January 2004. doi: 10.1086/380393.
- M. Kusunose and F. Takahara. A Structured Leptonic Jet Model of the “Orphan” TeV Gamma-Ray Flares in TeV Blazars. *ApJ*, 651:113–119, November 2006. doi: 10.1086/507403.
- R. A. Laing, C. R. Jenkins, J. V. Wall, and S. W. Unger. Spectrophotometry of a Complete Sample of 3CR Radio Sources: Implications for Unified Models. In G. V. Bicknell, M. A. Dopita, and P. J. Quinn, editors, *The Physics of Active Galaxies*, volume 54 of *Astronomical Society of the Pacific Conference Series*, pages 201–+, 1994.
- H. Landt. *Classification of Blazars*. PhD thesis, Universität Hamburg, 2003.
- S. A. Laurent-Muehleisen, R. I. Kollgaard, E. D. Feigelson, W. Brinkmann, and J. Siebert. The RGB Sample of Intermediate BL Lacertae Objects. *ApJ*, 525:127–143, November 1999. doi: 10.1086/307881.
- J. E. Ledden and S. L. Odell. The radio-optical-X-ray spectral flux distributions of blazars. *ApJ*, 298:630–643, November 1985. doi: 10.1086/163647.
- R. W. Lessard, J. H. Buckley, V. Connaughton, and S. Le Bohec. A new analysis method for reconstructing the arrival direction of TeV gamma rays using a single imaging atmospheric Cherenkov telescope. *Astroparticle Physics*, 15:1–18, March 2001.
- T.-P. Li and Y.-Q. Ma. Analysis methods for results in gamma-ray astronomy. *ApJ*, 272:317–324, September 1983. doi: 10.1086/161295.
- P. Madau and L. Pozzetti. Deep galaxy counts, extragalactic background light and the stellar baryon budget. *MNRAS*, 312:L9–L15, February 2000.
- K. Mannheim. The proton blazar. *A&A*, 269:67–76, March 1993.

- K. Mannheim and P. L. Biermann. Gamma-ray flaring of 3C 279 - A proton-initiated cascade in the jet? *A&A*, 253:L21–L24, January 1992.
- K. Mannheim, R. J. Protheroe, and J. P. Rachen. Cosmic ray bound for models of extragalactic neutrino production. *Phys.Rev.D*, 63(2):023003–+, January 2001.
- L. Maraschi, G. Ghisellini, E. G. Tanzi, and A. Treves. Spectral Properties of Blazars. II. an X-Ray Observed Sample. *ApJ*, 310:325–+, November 1986. doi: 10.1086/164685.
- L. Maraschi, G. Ghisellini, and A. Celotti. A jet model for the gamma-ray emitting blazar 3C 279. *ApJL*, 397:L5–L9, September 1992. doi: 10.1086/186531.
- D. Martello et al. First results from the ARGO-YBJ experiment. *to appear in the Proceedings of the 30th International Cosmic Ray Conference*, 2007.
- E. Massaro, M. Perri, P. Giommi, R. Nesci, and F. Verrecchia. Log-parabolic spectra and particle acceleration in blazars. II. The BeppoSAX wide band X-ray spectra of Mkn 501. *A&A*, 422:103–111, July 2004. doi: 10.1051/0004-6361:20047148.
- A. Mastichiadis and J. G. Kirk. Variability in the synchrotron self-Compton model of blazar emission. *A&A*, 320:19–25, April 1997.
- H. Matsumoto, M. Ueno, A. Bamba, et al. Suzaku Observations of HESS J1616-508: Evidence for a Dark Particle Accelerator. *PASJ*, 59:199–208, January 2007.
- R. J. McLure, M. J. Kukula, J. S. Dunlop, et al. A comparative HST imaging study of the host galaxies of radio-quiet quasars, radio-loud quasars and radio galaxies - I. *MNRAS*, 308:377–404, September 1999.
- P. Meszaros. Gamma-ray bursts. *Reports of Progress in Physics*, 69:2259–2322, 2006.
- M. Meyer. Kalibrierung des MAGIC-Teleskops mit Myonen. Master's thesis, Bayerische Julius-Maximilians-Universität Würzburg, 2004.
- I. F. Mirabel. Very energetic gamma-rays from microquasars and binary pulsars. *Science*, 312:1759–+, June 2006.

- A. Morselli et al. Search for point-like Dark Matter with the GLAST Large Area Telescope. *to appear in the Proceedings of the 30th International Cosmic Ray Conference*, 2007.
- M. Motoki, T. Sanuki, S. Orito, et al. Precise measurements of atmospheric muon fluxes with the BESS spectrometer. *Astroparticle Physics*, 19:113–126, April 2003.
- A. Mücke and R. J. Protheroe. A proton synchrotron blazar model for flaring in Markarian 501. *Astroparticle Physics*, 15:121–136, March 2001.
- A. Mücke, R. Engel, J. P. Rachen, R. J. Protheroe, and T. Stanev. Monte Carlo simulations of photohadronic processes in astrophysics. *Computer Physics Communications*, 124:290–314, February 2000. doi: 10.1016/S0010-4655(99)00446-4.
- A. Mücke, R. J. Protheroe, R. Engel, J. P. Rachen, and T. Stanev. BL Lac objects in the synchrotron proton blazar model. *Astroparticle Physics*, 18:593–613, March 2003.
- D. W. Murphy, I. W. A. Browne, and R. A. Perley. VLA Observations of a Complete Sample of Core-Dominated Radio Sources. *MNRAS*, 264:298–+, September 1993.
- D. Nedbal, W. Benbow, L. Costamante, et al. H.E.S.S. discovers VHE gamma-rays from the BL Lac RGB J0152+017. *The Astronomer's Telegram*, 1295:1–+, November 2007.
- K. Nilsson, M. Pasanen, L. O. Takalo, et al. Host galaxy subtraction of TeV candidate BL Lacertae objects. *A&A*, 475:199–207, November 2007. doi: 10.1051/0004-6361:20077624.
- D. E. Osterbrock. Spectrophotometry of Seyfert 1 galaxies. *ApJ*, 215:733–745, August 1977.
- P. Padovani. A statistical analysis of complete samples of BL Lacertae objects. *A&A*, 256:399–407, March 1992.
- P. Padovani and P. Giommi. The connection between x-ray- and radio-selected BL Lacertae objects. *ApJ*, 444:567–581, May 1995. doi: 10.1086/175631.
- P. Padovani and P. Giommi. The ROSAT X-ray spectra of BL Lacertae objects. *MNRAS*, 279:526–534, March 1996.

- P. Padovani, L. Costamante, G. Ghisellini, P. Giommi, and E. Perlman. BeppoSAX Observations of Synchrotron X-Ray Emission from Radio Quasars. *ApJ*, 581:895–911, December 2002. doi: 10.1086/344406.
- P. Padovani, E. S. Perlman, H. Landt, P. Giommi, and M. Perri. What Types of Jets Does Nature Make? A New Population of Radio Quasars. *ApJ*, 588:128–142, May 2003. doi: 10.1086/373899.
- D. Paneque, H. J. Gebauer, E. Lorenz, and R. Mirzoyan. A method to enhance the sensitivity of photomultipliers for Air Cherenkov Telescopes by applying a lacquer that scatters light. *Nuclear Instruments and Methods in Physics Research A*, 518:619–621, February 2004. doi: 10.1016/j.nima.2003.11.101.
- E. S. Perlman, J. T. Stocke, J. F. Schachter, et al. The Einstein Slew Survey Sample of BL Lacertae Objects. *ApJS*, 104:251–+, June 1996. doi: 10.1086/192300.
- E. S. Perlman, P. Padovani, P. Giommi, et al. The Deep X-Ray Radio Blazar Survey. I. Methods and First Results. *AJ*, 115:1253–1294, April 1998. doi: 10.1086/300283.
- D. Petry, M. Böttcher, V. Connaughton, et al. Multiwavelength Observations of Markarian 501 during the 1997 High State. *ApJ*, 536:742–755, June 2000. doi: 10.1086/308955.
- D. Petry, I. H. Bond, S. M. Bradbury, et al. The TeV Spectrum of H1426+428. *ApJ*, 580:104–109, November 2002. doi: 10.1086/343102.
- J. R. Primack, J. S. Bullock, R. S. Somerville, and D. MacMinn. Probing galaxy formation with TeV gamma ray absorption. *Astroparticle Physics*, 11:93–102, June 1999.
- R. J. Protheroe and T. Stanev. Electron-Photon Cascading of Very High-Energy Gamma-Rays in the Infrared Background. *MNRAS*, 264:191–+, September 1993.
- M. Punch, C. W. Akerlof, M. F. Cawley, et al. Detection of TeV photons from the active galaxy Markarian 421. *Nature*, 358:477–+, August 1992. doi: 10.1038/358477a0.
- J. Quinn, C. W. Akerlof, S. Biller, et al. Detection of Gamma Rays with  $E > 300$  GeV from Markarian 501. *ApJL*, 456:L83+, January 1996. doi: 10.1086/309878.

- M. A. Rahman, P. N. Bhat, B. S. Acharya, et al. Gamma Ray and Hadron generated Čerenkov Photon Spectra at Various Observation Altitudes. *Experimental Astronomy*, 11:113–131, April 2001.
- T. A. Rector and J. T. Stocke. The Properties of the Radio-Selected 1 Jy Sample of BL Lacertae Objects. *AJ*, 122:565–584, August 2001. doi: 10.1086/321179.
- M. J. Rees. Studies in radio source structure-III. Inverse Compton radiation from radio sources. *MNRAS*, 137:429–+, 1967.
- J. Rico, M. Rissi, P. Bordas, et al. Observations of microquasars with the MAGIC telescope. *to appear in the Proceedings of the 30th International Cosmic Ray Conference*, arXiv:0709.2288, 2007.
- W. A. Rolke, A. M. López, and J. Conrad. Limits and confidence intervals in the presence of nuisance parameters. *Nuclear Instruments and Methods in Physics Research A*, 551:493–503, October 2005. doi: 10.1016/j.nima.2005.05.068.
- S. Rügamer. Systematische Studien zur Verwendung der Zeitstruktur von Luftschauern zur Reduktion des Untergrundes in MAGIC-Daten. Master's thesis, Bayerische Julius-Maximilians-Universität Würzburg, 2006.
- M. Rügner. Modellierung der Gamma-Emission in Jets von aktiven Galaxienkernen an Hand des Synchrotron-Self-Compton Modells. Master's thesis, Bayerische Julius-Maximilians-Universität Würzburg, 2007.
- R. M. Sambruna, C. M. Urry, L. Maraschi, et al. The High-Energy Continuum Emission of the Gamma-Ray Blazar PKS 0528+134. *ApJ*, 474: 639–+, January 1997. doi: 10.1086/303493.
- D. B. Sanders, B. T. Soifer, J. H. Elias, et al. Ultraluminous infrared galaxies and the origin of quasars. *ApJ*, 325:74–91, February 1988. doi: 10.1086/165983.
- T. Sanuki, M. Fujikawa, K. Abe, et al. Measurements of atmospheric muon spectra at mountain altitude. *Physics Letters B*, 541:234–242, 2002.
- B. Sbarufatti, A. Treves, R. Falomo, et al. ESO Very Large Telescope Optical Spectroscopy of BL Lacertae Objects. II. New Redshifts, Featureless Objects, and Classification Assessments. *AJ*, 132:1–19, July 2006. doi: 10.1086/503031.

- D. J. Schlegel, D. P. Finkbeiner, and M. Davis. Maps of Dust Infrared Emission for Use in Estimation of Reddening and Cosmic Microwave Background Radiation Foregrounds. *ApJ*, 500:525–+, June 1998. doi: 10.1086/305772.
- M. Schmidt. 3C 273 : A Star-Like Object with Large Red-Shift. *Nature*, 197:1040–+, March 1963. doi: 10.1038/1971040a0.
- V. Schönfelder, K. Bennett, J. J. Blom, et al. The first COMPTEL source catalogue. *A&AS*, 143:145–179, April 2000.
- M. Schroedter, H. M. Badran, J. H. Buckley, et al. A Very High Energy Gamma-Ray Spectrum of 1ES 2344+514. *ApJ*, 634:947–954, December 2005. doi: 10.1086/496968.
- D. A. Schwartz, R. E. Griffiths, J. Schwarz, R. E. Doxsey, and M. D. Johnston. X-ray emitting BL Lacertae objects located by the scanning modulation collimator experiment on HEAO 1. *ApJL*, 229:L53–L57, April 1979. doi: 10.1086/182929.
- C. K. Seyfert. Nuclear Emission in Spiral Nebulae. *ApJ*, 97:28–+, January 1943.
- I. S. Shklovskii. Nature of Jets in Radio Galaxies. *Soviet Astronomy*, 7: 748–+, June 1964.
- G. Sigl. Ultra High Energy Cosmic Radiation: Experimental and Theoretical Status. In C. Manzo and G. Yepes, editors, *The Dark Side of the Universe*, volume 878 of *American Institute of Physics Conference Series*, pages 405–411, November 2006. doi: 10.1063/1.2409112.
- M. Sikora, M. C. Begelman, and M. J. Rees. Comptonization of diffuse ambient radiation by a relativistic jet: The source of gamma rays from blazars? *ApJ*, 421:153–162, January 1994. doi: 10.1086/173633.
- F. W. Stecker and M. H. Salamon. The Gamma-Ray Background from Blazars: A New Look. *ApJ*, 464:600–+, June 1996. doi: 10.1086/177348.
- F. W. Stecker and S. T. Scully. The Spectrum of 1ES0229+200 and the Cosmic Infrared Background. *to appear in A&A*, arXiv:0710.2252, 2007.
- F. W. Stecker, O. C. de Jager, and M. H. Salamon. TeV gamma rays from 3C 279 - A possible probe of origin and intergalactic infrared radiation fields. *ApJ*, 390:L49–L52, May 1992. doi: 10.1086/186369.

- J. T. Stocke, J. Liebert, G. Schmidt, et al. Optical and radio properties of X-ray selected BL Lacertae objects. *ApJ*, 298:619–629, November 1985. doi: 10.1086/163646.
- G. Superina, W. Benbow, T. Boutelier, G. Dubus, and B. Giebels. Discovery of VHE gamma-rays from the BL Lac object PKS 0548-322 with H.E.S.S. *to appear in the Proceedings of the 30th International Cosmic Ray Conference*, 2007.
- B. N. Swanenburg, K. Bennett, G. F. Bignami, et al. Second COS B catalog of high-energy gamma-ray sources. *ApJ*, 243:L69–L73, January 1981. doi: 10.1086/183445.
- T. Takahashi, R. Sato, M. Ushio, et al. Suzaku Satellites and Observations of High Energy Jet Sources. In *High Energy Phenomena in Relativistic Outflows*, 2007.
- F. Tavecchio, L. Maraschi, and G. Ghisellini. Constraints on the Physical Parameters of TeV Blazars. *ApJ*, 509:608–619, December 1998. doi: 10.1086/306526.
- M. Teshima, E. Prandini, R. Bock, et al. Discovery of Very High Energy Gamma-Rays from the Distant Flat Spectrum Radio Quasar 3C 279 with the MAGIC Telescope. *to appear in the Proceedings of the 30th International Cosmic Ray Conference*, arXiv:0709.1475, 2007.
- A. Tramacere, P. Giommi, E. Massaro, et al. SWIFT observations of TeV BL Lacertae objects. *A&A*, 467:501–508, May 2007. doi: 10.1051/0004-6361:20066226.
- C. M. Urry and P. Padovani. Unified Schemes for Radio-Loud Active Galactic Nuclei. *PASP*, 107:803–+, September 1995.
- C. M. Urry, R. Scarpa, M. O’Dowd, et al. The Hubble Space Telescope Survey of BL Lacertae Objects. II. Host Galaxies. *ApJ*, 532:816–829, April 2000. doi: 10.1086/308616.
- G. Vacanti, M. F. Cawley, E. Colombo, et al. Gamma-ray observations of the Crab Nebula at TeV energies. *ApJ*, 377:467–479, August 1991. doi: 10.1086/170376.
- G. Vacanti, P. Fleury, Y. Jiang, et al. Muon ring images with an atmospheric Cherenkov telescope. *Astroparticle Physics*, 2:1–11, February 1994. doi: 10.1016/0927-6505(94)90012-4.

- C. van Eldik, O. Bolz, I. Braun, et al. Localising the H.E.S.S. Galactic Centre point source. *to appear in the Proceedings of the 30th International Cosmic Ray Conference*, arXiv:0709.3729, 2007.
- M.-P. Véron-Cetty and P. Véron. A catalogue of quasars and active nuclei: 11th edition. *A&A*, 412:399–403, December 2003. doi: 10.1051/0004-6361:20034225.
- M.-P. Véron-Cetty and P. Véron. A catalogue of quasars and active nuclei: 12th edition. *A&A*, 455:773–777, August 2006. doi: 10.1051/0004-6361:20065177.
- J. I. Vette, D. Gruber, J. L. Matteson, and L. E. Peterson. A New Component of Cosmic Gamma Rays Near 1 MeV Observed by the ERS-18. *ApJ*, 160:L161+, June 1970.
- W. Voges, B. Aschenbach, T. Boller, et al. The ROSAT all-sky survey bright source catalogue. *A&A*, 349:389–405, September 1999.
- L. L. Wai. GLAST LAT Searches for Particle Dark Matter: An Experimental Point of View. In S. Ritz, P. Michelson, and C. A. Meegan, editors, *American Institute of Physics Conference Series*, volume 921 of *American Institute of Physics Conference Series*, pages 139–141, July 2007. doi: 10.1063/1.2757286.
- J. Wdowczyk, W. Tkaczyk, and A. W. Wolfendale. Primary cosmic gamma rays above  $10^{12}$ eV. *Journal of Physics A Mathematical General*, 5:1419–1432, 1972.
- T. C. Weekes, M. F. Cawley, D. J. Fegan, et al. Observation of TeV gamma rays from the Crab nebula using the atmospheric Cerenkov imaging technique. *ApJ*, 342:379–395, July 1989. doi: 10.1086/167599.
- WGACAT2. . <http://www.asdc.asi.it>.
- N. E. White, P. Giommi, and L. Angelini. WGACAT. *IAU Circ.*, 6100:1–+, November 1994.
- A. S. Wilson, M. J. Ward, D. J. Axon, M. Elvis, and E. J. A. Meurs. On the identification of the high-latitude X-ray source 2A 1219 + 305. *MNRAS*, 187:109–115, April 1979.
- K. S. Wood, J. F. Meekins, D. J. Yentis, et al. The HEAO A-1 X-ray source catalog. *ApJS*, 56:507–649, December 1984. doi: 10.1086/190992.

- X.-B. Wu, F. K. Liu, and T. Z. Zhang. Supermassive black hole masses of AGNs with elliptical hosts. *A&A*, 389:742–751, July 2002. doi: 10.1051/0004-6361:20020577.
- www-01. <http://www.chicos.caltech.edu/collaboration/education/spectrum1.jpg>, 2008.
- www-02. <http://www.pi1.physik.uni-erlangen.de/~kappes/lehre/WS05-VAT/V9/Hillas-plot.png>, 2008.
- www-03. [http://heasarc.gsfc.nasa.gov/docs/cgro/images/egret/3rd\\_EGRET\\_Cat.gif](http://heasarc.gsfc.nasa.gov/docs/cgro/images/egret/3rd_EGRET_Cat.gif), 2008.
- www-04. <http://glast.gsfc.nasa.gov/science/resources/sims/>, 2008.
- www-05. [http://www.mppmu.mpg.de/~rwagner/sources/TeV\\_Skymap\\_nolabels.png](http://www.mppmu.mpg.de/~rwagner/sources/TeV_Skymap_nolabels.png), 2008.
- www-06. <http://chandra.harvard.edu/photo/0052/what.html>, 2008.
- www-07. <http://www.cv.nrao.edu/course/ast534/images/unifiedmodel.jpg>, 2008.
- www-08. <http://www.ast.leeds.ac.uk/~fs/showerimages.html>, 2008.
- www-09. <http://wwwmagic.mppmu.mpg.de/>, 2008.
- www-10. <http://magic.astro.uni-wuerzburg.de/mars/>, 2008.
- T. Yamamoto for the Pierre Auger collaboration. The UHECR spectrum measured at the Pierre Auger Observatory and its astrophysical implications. *to appear in the Proceedings of the 30th International Cosmic Ray Conference*, arXiv:0707.2638, 2007.
- G. T. Zatsepin and V. A. Kuzmin. Upper Limit of the Spectrum of Cosmic Rays. *ZhETF Pis ma Redaktsiiu*, 4:114–+, August 1966.

# List of Publications

## Refereed Articles

- Albert, J. et al. (MAGIC collaboration)  
"MAGIC Observations of Very High Energy  $\gamma$ -Rays from HESS J1813-178", 2006, ApJL, 637, L41
- Albert, J. et al. (MAGIC collaboration)  
"Observation of Gamma Rays from the Galactic Center with the MAGIC Telescope", 2006, ApJL, 638, L101
- Albert, J. et al. (MAGIC collaboration)  
"Observation of Very High Energy Gamma-Ray Emission from the Active Galactic Nucleus 1ES 1959+650 Using the MAGIC Telescope", 2006, ApJ, 639, 761
- Albert, J. et al. (MAGIC collaboration)  
"Flux Upper Limit on Gamma-Ray Emission by GRB 050713a from MAGIC Telescope Observations", ApJL, 641, L9
- Albert, J. et al. (MAGIC collaboration, corresp. author: Markus Meyer)  
"Discovery of Very High Energy Gamma Rays from 1ES 1218+30.4", 2006, ApJL, 642, L119
- Albert, J. et al. (MAGIC collaboration)  
"Observation of VHE Gamma Radiation from HESS J1834-087/W41 with the MAGIC Telescope", 2006, ApJL, 643, L53
- Albert, J. et al. (MAGIC collaboration)  
"Variable Very-High-Energy Gamma-Ray Emission from the Microquasar LS I +61 303", 2006, Science, 312, 1771
- Albert, J. et al. (MAGIC collaboration)  
"Discovery of Very High Energy  $\gamma$ -Rays from Markarian 180 Triggered by an Optical Outburst", 2006, ApJL, 648, L105

- Albert, J. et al. (MAGIC collaboration)  
"Signal Reconstruction for the MAGIC Telescope", 2006, submitted to NIM, astro-ph/0612385
- Albert, J. et al. (MAGIC collaboration)  
"Detection of Very High Energy Radiation from the BL Lacertae Object PG 1553+113 with the MAGIC Telescope", 2007, ApJL, 654, L119
- Albert, J. et al. (MAGIC collaboration)  
"Very High Energy Gamma-Ray Observations During Moonlight and Twilight with the MAGIC Telescope", 2007, submitted to Elsevier, astro-ph/0702475
- Albert, J. et al. (MAGIC collaboration)  
"First Bounds on the Very High Energy  $\gamma$ -Ray Emission from Arp 220", 2007, ApJ, 658, 245
- Albert, J. et al. (MAGIC collaboration)  
"VHE  $\gamma$ -Ray Observation of the Crab Nebula and its Pulsar with the MAGIC Telescope", 2007, accepted for publication in ApJ, astro-ph/0705.3244
- Albert, J. et al. (MAGIC collaboration)  
"Observation of Very High Energy  $\gamma$ -Rays from the AGN 1ES 2344+514 in a Low Emission State with the MAGIC Telescope", 2007, ApJ, 662, 892
- Albert, J. et al. (MAGIC collaboration, corresp. author: Markus Meyer)  
"Systematic search for VHE gamma-ray emission from X-ray bright high-frequency BL Lac objects", 2007, accepted for publication in ApJ, arXiv:0706.4453
- Albert, J. et al. (MAGIC collaboration)  
"Observations of Markarian 421 with the MAGIC Telescope", 2007, ApJL, 663, 125
- Albert, J. et al. (MAGIC collaboration)  
"Discovery of Very High Energy Gamma Radiation from IC 443 with the MAGIC Telescope", 2007, ApJL, 664, L87
- Albert, J. et al. (MAGIC collaboration)  
"Very High Energy Gamma-Ray Radiation from the Stellar Mass Black Hole Binary Cygnus X-1", 2007, ApJL, 665, L51

- Albert, J. et al. (MAGIC collaboration) and Ellis, J., Mavromatos, N. E., Nanopoulos, D. V., Sakharov, A. S. and Sarkisyan, E. K. G.  
"Probing Quantum Gravity using Photons from a Mkn 501 Flare Observed by MAGIC", 2007, submitted to Phys. Rev. Lett., arXiv:0708.2889
- Albert, J. et al. (MAGIC collaboration)  
"Discovery of Very High Energy  $\gamma$ -Ray Emission from the Low-Frequency-peaked BL Lacertae Object BL Lacertae", 2007, ApJL, 666, L17
- Albert, J. et al. (MAGIC collaboration)  
"MAGIC Upper Limits on the Very High Energy Emission from Gamma-Ray Bursts", 2007, ApJ, 667, 358
- Albert, J. et al. (MAGIC collaboration)  
"Discovery of Very High Energy  $\gamma$ -Rays from 1ES 1011+496 at  $z = 0.212$ ", 2007, ApJL, 667, L21
- Albert, J. et al. (MAGIC collaboration)  
"Implementation of the Random Forest Method for the Imaging Atmospheric Cherenkov Telescope MAGIC" 2007, accepted by NIM A, arXiv:0709.3719A
- Albert, J. et al. (MAGIC collaboration)  
"Variable VHE  $\gamma$ -Ray Emission from Markarian 501", 2007, ApJ, 669, 862
- Albert, J. et al. (MAGIC collaboration)  
"Constraints on the steady and pulsed VHE gamma-ray emission from observation of PSR B1951+32 / CTB 80 with the MAGIC Telescope", 2007, ApJ, 669, 1143
- Albert, J. et al. (MAGIC collaboration)  
"Upper Limit for  $\gamma$ -Ray Emission above 140 GeV from the Dwarf Spheroidal Galaxy Draco", 2007, accepted for publication in ApJ, astro-ph/0711.2574
- Albert, J. et al. (MAGIC collaboration)  
"Observation of VHE gamma-rays from Cassiopeia A with the MAGIC telescope", 2007, A&A, 474, 937
- Albert, J. et al. (MAGIC collaboration)  
"MAGIC Observation of the Unidentified TeV Gamma-Ray Source TeV J2032+4130", 2008, accepted for publication in ApJ, astro-ph/0801.2391

## Conference Contributions

- Meyer, M. & Mase, K., "Analysis of muon events recorded with the MAGIC telescope" in AIP Conf. Proc. 745, High Energy Gamma-Ray Astronomy, ed. F. A. Aharonian, H. J. Völk, & D. Horns (New York: AIP), 774 gamma-2004-Heidelberg
- Meyer, M., Mannheim, K., Bretz, T. et al. "MAGIC observations of high-peaked BL Lacertae objects", 2005, Proc. 29th Int. Cosmic Ray Conf. (Pune), Vol. 4, 335-338
- Meyer, M., "Observations of high-peaked BL Lacs above 100GeV", talk at the "Herbsttagung der Astronomischen Gesellschaft", Köln, 2005
- Meyer, M., Bretz, T., Dorner, D. et al. "Discovery of VHE gamma-rays from the BL Lacertae object 1ES 1218+304", talk at the "Frühjahrstagung der Deutschen Physikalischen Gesellschaft", Dortmund, 2006
- Meyer, M., Bretz, T., Dorner, D., Prandini, E., "Observations of a systematic selected sample of X-ray bright HBL objects with the MAGIC telescope", 2007, to appear in Proc. 30th Int. Cosmic Ray Conf. (Merida)
- Meyer, M, Bretz T. & Dorner, D., "Systematic search for VHE gamma-ray emission from X-ray bright HBL objects", poster at the "80th Annual Meeting of the Astronomische Gesellschaft jointly with the 5th biennial Workshop on Astroparticle Physics in Germany", Würzburg, 2007

# Abbreviations

2MASS	Two Micron All-Sky Survey
3C	Third Cambridge Catalogue
AGN	Active Galactic Nucleus
AMC	Automatic Mirror Control
BAL	Broad Absorption Line (quasars)
BLR	Broad Line Region
BSC	Bright Source Catalogue (ROSAT All-Sky Survey)
CANGAROO	Collaboration of Australia and Nippon for a GAMMA-Ray Observatory in the Outback
CAT	Cherenkov Array at Themis
CCD	Charged Coupling Device
CDQ	Core-Dominated Quasar
CGRO	Compton Gamma-Ray Observatory
CL	Confidence Level
CMB	Cosmic Microwave Background
CT	Cherenkov Telescope (HEGRA)
CTA	Cherenkov Telescope Array
DXRBS	Deep X-ray Radio Blazar Survey
EBL	Extragalactic Background Light
EC	External Compton
EGRET	Energetic Gamma-Ray Experiment Telescope
FADC	Flash Analogue Digital Converter
FSRQ	Flat Spectrum Radio Quasar
FOV	Field Of View
FR	Fanaroff & Riley
FWHM	Full Width Half Maximum
GLAST	Gamma-ray Large Area Space Telescope
GZK	Greisen-Zatsepin-Kuzmin
HBL	High frequency peaked BL Lac
HE	High Energy
HEGRA	High Energy Gamma-Ray Array

H.E.S.S.	High Energy Stereoscopic System
HPQ	High Polarised Quasars
HST	Hubble Space Telescope
IACT	Imaging Air Cherenkov Telescope/Technique
IR	Infra Red
IRAS	Infrared Astronomy Satellite
LAT	Large Area Telescope
LBL	Low frequency peaked BL Lac
MAGIC	Major Atmospheric Gamma-ray Imaging Cherenkov (Telescope)
MRF	Metagalactic Radiation Field
NED	NASA Extragalactic Database
NLR	Narrow Line Region
NRAO	National Radio Astronomy Observatory
NVSS	NRAO VLA Sky Survey
OVV	Optically Violently Variable (quasar)
PIC	Proton Initiated Cascades
PMT	Photomultiplier Tube
PSF	Point Spread Function
PWN	Pulsar Wind Nebula
QSO	Quasi-Stellar Object
RASS	ROSAT All-Sky Survey
RBL	Radio selected BL Lac
SED	Spectral Energy Distribution
SMBH	Supermassive Black Hole
SNR	Supernova Remnant
SPB	Synchrotron Proton Blazar
SSC	Synchrotron Self Compton
SSRQ	Steep Spectrum Radio Quasar
UL	Upper Limit
VCSEL	Vertical Cavity Surface Emitting Laser
VERITAS	Very Energetic Radiation Imaging Telescope Array System
VHE	Very High Energy
VLA	Very Large Array
XBL	X-ray selected BL Lac

# Lebenslauf

Name	Markus Meyer
Geburtsdatum	5. April 1979
Geburtsort	Dettelbach
Nationalität	deutsch
Adresse	Gosbertsteige 8 97082 Würzburg Telefon: 0931/4653006 email: meyer@astro.uni-wuerzburg.de
Schulausbildung	1985 - 1989: Albert-Schweitzer-Grundschule, Albertshofen 1989 - 1998: Armin-Knab-Gymnasium, Kitzingen
Schulabschluss	Allgemeine Hochschulreife (26.06.1998)
Zivildienst	09/1998 - 09/1999: Arbeiterwohlfahrt in Marktbreit
Hochschulstudium	01.11.1999 - 18.11.2004: Studium der Physik an der Julius-Maximilians-Universität Würzburg
Hochschulabschluss	Diplom (18.11.2004)
Lehrtätigkeit	Betreuung des physikalischen Grundpraktikums (März 2004) Leitung einer Übungsgruppe zur Vorlesung "Introduction to Space Physics" (WS 2005/06 und WS 2006/07) Betreuung von Diplomarbeiten (2005 – 2007)
Wiss. Tätigkeit	01.12.2004 - 30.09.2005: Wissenschaftlicher Mitarbeiter am Lehrstuhl für Astronomie der Universität Würzburg. 01.10.2005 - 31.12.2007: Stipendiat im Graduiertenkolleg "Theoretische Astrophysik und Teilchenphysik" am Lehrstuhl für Astronomie der Universität Würzburg. Seit 18.01.2008: Wissenschaftlicher Mitarbeiter am Lehrstuhl für Astronomie der Universität Würzburg.

# Acknowledgements

First of all, I want to thank my supervisor Prof. Dr. Karl Mannheim. He gave me the opportunity to perform this interesting study inside the MAGIC collaboration and supported me during the last three years. The dialogue and the discussions with him influenced my work significantly.

Next I want to thank all my colleagues from the Würzburg MAGIC group, in particular: Thomas Bretz, for all the advise in the analysis of MAGIC data and for the development of a powerful analysis software package; Daniela Dorner, for all her work on the automatisisation of the MAGIC data analysis as well as the database, which made it possible to perform such a study in time; Stefan Rügamer and Daniel Höhne for proofreading the manuscript and enjoyable lunch breaks.

Furthermore, I want to thank Felix Spanier, Dominik Elsässer and Sebastian Huber for fruitful discussions. Special thanks go to Michael Rüger for providing his SSC code and to Tanja Kneiske for providing her MRF model.

I would like to thank the MAGIC collaboration for the provision of proprietary data of the telescope. Moreover, the friendly atmosphere inherent in the whole collaboration and the opportunity to work with people from all over the world made this time to a pleasurable experience. In particular, I want to thank Abelardo Moralejo for all the help in simulation related questions; Pratik Majumdar and Elisa Prandini for cross-check analysis; Florian Goebel for all his effort on the telescope and his kind support in all the after-midnight calls during my time as a shift leader at the telescope.

Apart from my colleagues, I want to thank my family, in particular my mother, Jutta Heger, for her support during the last 28 years.

This work received financial support by the *Bundesministerium für Bildung und Forschung* (BMBF) and the *Deutsche Forschungsgemeinschaft* (DFG).